STATE UNIVERISTY OF MOLDOVA

DOCTORAL SCHOOL OF NATURE SCIENCES

Manuscript
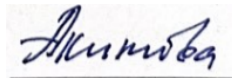C.Z.U: 535.42:535.317.2:621.385.833.2(043)

CAZAC Veronica

DEVELOPMENT OF DIGITAL HOLOGRAPHIC MICROSCOPE FOR THE INVESTIGATION OF DIFFRACTIVE OPTICAL ELEMENTS RECORDED ON CHALCOGENIDE GLASSES AND AZOPOLYMER THIN FILMS
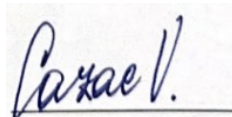
134.01-Physics and technology of materials

Doctoral Thesis in Physics

PhD supervisor: ACHIMOVA Elena,
doctor habilitate in
physical sciences, research
associate

Author: CAZAC Veronica

CHIȘINĂU, 2023

UNIVERSITATEA DE STAT DIN MOLDOVA
ȘCOALA DOCTORALĂ ȘTIINȚE ALE NATURII

Cu titlu de manuscris
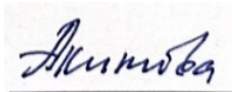C.Z.U: 535.42:535.317.2:621.385.833.2(043)

CAZAC Veronica

DEZVOLTAREA MICROSCOPULUI HOLOGRAFIC DIGITAL PENTRU INVESTIGAREA ELEMENTELOR OPTICE DE DIFRACȚIE ÎNREGISTRATE PE STRATURI SUBȚIRI DE STICLE CALCOGENICE ȘI AZOPOLIMERI

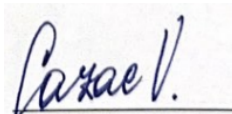**134.01-Fizica și tehnologia materialelor**

Teză de doctor în științe fizice

PhD supervisor: ACHIMOVA Elena, doctor habilitate in physical sciences, research associate

Author: CAZAC Veronica

CHIȘINĂU, 2023

OUTLINE

AKNOWLEDGEMENTS

ANNOTATION

to the thesis „Development of digital holographic microscope for the investigation of diffractive optical elements recorded on chalcogenide glasses and azopolymer thin films", presented by Veronica Cazac for conferring the scientific degree of Ph.D. in Physics, Specialty 134.01 Physics and technology of materials, Chişinau, 2023.

The thesis has been written in English language and consists of the introduction, 5 chapters, general conclusions and recommendations, and the list of 214 references. The thesis contains 128 pages of basic text, 74 figures and 61 formulas. The results presented in the thesis are published in 17 scientific publications and presented at 16 international conferences.

Key words: digital holographic microscope, diffractive optical elements (DOEs), chalcogenide glasses (ChGs), azopolymers (APs), liquid crystal spatial light modulator and variable retarder, phase mask.

The goal: Quantitative analysis of key parameters of different types of diffractive optical elements, patterned on ChGs nanomultilayers and AP thin films by polarization holographic recording via improved hardware and software configuration of digital holographic microscope (DHM).

Research objectives: The development of numerical algorithms for phase reconstruction from acquired digital holograms of DOEs recorded on photosensitive ChGs nanomultilayers and AP thin films and subsequent mapping of their surface relief and refractive index; the modification of the optical part of the DHM in the off-axis and phase-shifting configurations and integration of liquid crystal devices; the calibration of phase and polarization of the liquid crystal devices implemented in digital holographic setups; the development of analog and digital holographic techniques for one-step polarization holographic recording (PHR) of different types of DOEs on nanomultilayers structures from ChGs and carbazole-based APs; the application of the developed DHM with the integrated tools for characterization of the created DOEs.

Scientific novelty and originality of the results: the improved version of the DHM software and hardware configuration has been demonstrated as a versatile instrument for the investigation of DOEs on ChG nanomultilayers and AP thin films; analog and digital PHR are new methods that allowed the photo-induced formation of complex DOEs on ChG nanomultilayers and azopolymer thin films.

The main scientific problem solved consists in elaborating of multifunctional DOEs patterned on ChGs nanomultilayers and azopolymer thin films via analog and digital PHR, and nanoscale investigation of their optical and physical parameters by high performance digital holographic microscope.

Theoretical significance and applicative value: of the work is that continuous enhancement of microscopic tools is mandatory in order to support efficient investigations in different fields as photonics, material science, biomedicine, etc. Therefore, the optical system of DHM including hardware and software components was improved for efficient investigation of the diffractive optical elements on a nanometer scale. The capability to create and perform quantitative analysis of multifunctional DOEs make them attractive in a variety of applications, including aberration correction, sensitive microscopy, augmented reality, imaging systems, solar energy and more.

The implementation of the scientific results: the research presented in this thesis has been successfully implemented in the framework of the EU project nr. 687328 (2016-2018), bilateral moldo-belarous project ANCD 19.80013.50.07.04A/BL (2020-2021), national project ANCD 20.70086.16/COV (2020-2021), national project 20.80009.5007.03 (2020-2023) and international project ANCD 21.80013.5007.1M (2021-2023), and may be further used for educational purposes.

ADNOTARE

la teza „Dezvoltarea microscopului holographic digital pentru investigarea elementelor optice de difracție înregistrate pe straturi subțiri de sticle calcogenice și azopolimeri”, elaborată de Veronica Cazac pentru conferirea gradului științific de doctor în științe fizice la specialitatea 134.01 Fizica și tehnologia materialelor, Chișinău, 2023.

Teza este scrisă în limba engleză și constă din introducere, 5 capitole, concluzii generale și recomandări, și bibliografia din 214 titluri. Teza conține 128 pagini de text de bază, 74 figuri și 61 formule. Rezultatele prezentate în teză sunt publicate în 17 lucrări științifice și prezentate la 16 conferințe.

Cuvinte cheie: microscop holografic digital (MHD), elemente optice de difracție (EOD), sticle calcogenice (SC), azopolimeri (AP), modulator spațial de lumină cu cristale lichide și retarder variabil, mască de faza.

Scopul tezei: Analiza cantitativă a parametrilor cheie a diferitor tipuri de EOD, înregistrate pe nanomultistraturi de SC și straturi subțiri de AP utilizând metoda holografică cu lumina polarizată (HLP) cu ajutorul configurației hardware și software îmbunătățite a MHD.

Obiectivele tezei: Dezvoltarea algoritmilor de reconstrucție numerică pentru reconstrucția fazei din holograme digitale ale EOD înregistrate pe nanomultistraturi fotosensibile de SC și straturi subțiri de AP și măsurarea topografică a suprafeței precum și a indicelui de refracție a acestora; modificarea schemei optice a MHD în afara axei precum și în configurația „"phase-shifting" (din *engl.* cu deplasare de fază) și integrarea dispozitivelor cu cristale lichide; calibrarea fazei și polarizării dispozitivelor cu cristale lichide implementate în configurații holografice digitale; dezvoltarea tehnicilor analogice și digitale pentru înregistrarea HLP printr-o singură etapă a diferitelor tipuri de EOD pe nanomultistraturi din SC și AP pe bază de carbazol; aplicarea MHD dezvoltat cu instrumentele integrate pentru caracterizarea EOD create.

Noutatea științifică și originalitatea rezultatelor: versiunea îmbunătățită a configurației software și hardware a MHD a fost demonstrată ca un instrument versatil pentru investigarea EOD pe nanomultistraturi de SC și a straturilor subțiri de AP; Înregistrarea HLP analog și digitală sunt metode noi care au permis formarea foto-indusă a EOD complexe pe nanomultistraturi de SC și straturilor subțiri de AP.

Problema științifică soluționată constă în elaborarea EOD multifuncționale înregistrate pe nanomultistraturi de SC și straturi subțiri de AP prin înregistrarea HLP analog și digitală precum și investigarea la scară nanometrică a parametrilor optici și fizici a acestora folosind MHD de înaltă performanță.

Semnificația teoretică și valoarea aplicativă: a tezei de doctor constă în îmbunătățirea continuă a microscopului ca instrument pentru efectuarea cercetărilor eficiente în diferite domenii precum fotonica, știința materialelor, biomedicină etc. În acest scop, sistemul optic al MHD, inclusiv componentele hardware și software, au fost îmbunătățite pentru investigarea eficientă a EOD la scară nanometrică. Posibilitatea de a crea și de a efectua analize cantitative a EOD multifuncționale le face atractive pentru o gamă largă de aplicații, inclusiv corectarea aberațiilor (erorilor), microscopia sensibilă, realitate augmentată, sisteme de imagistică, energie solară și multe altele.

Implementarea rezultatelor științifice: studiile prezentate în această teză au fost cu succes implementate în cadrul proiectului European nr. 687328 (2016-2018), proiectului bilateral moldo-belorus ANCD 19.80013.50.07.04A/BL (2020-2021), proiectului național ANCD 20.70086.16/COV (2020-2021), proiectului național 20.80009.5007.03 (2020-2023) și proiectului internațional ANCD 21.80013.5007.1M (2021-2023), și pot fi utilizate cu scop didactic pentru studenții ciclului universitar și post-universitar.

АННОТАЦИЯ

к диссертации « Разработка цифрового голографического микроскопа для исследования дифракционных оптических элементов на тонких пленках халькогенидных стекол и азополимеров», представленной Вероникой Казак на соискание ученой степени доктора физических наук по специальности 134.01 Физика и технология материалов, Кишинев, 2023

Диссертация написана на английском языке и состоит из введения, пяти глав, общих заключений и рекомендаций, и списка цитируемой литературы из 214 источников. Диссертация содержит 128 страниц базового текста, 74 графиков и 61 формул. Результаты диссертационной работы опубликованы в 17 научных публикациях и представлены на 16 конференциях.

Ключевые слова: цифровой голографический микроскоп (ЦГМ), оптические дифракционные элементы (ДОЭ), халькогенидные стекла (ХС), азополимеры (АП), жидкокристаллический пространственный модулятор света и фазовая пластинка, фазовая маска, цифровая обработка изображений.

Цель диссертации: Количественный анализ ключевых параметров различных типов дифракционных оптических элементов, нанесенных на многослойные наноструктуры ХС и тонкие пленки АП, методом поляризационной голографической записи (ПГЗ) с использованием усовершенствованной аппаратной и программной конфигураций ЦГМ.

Задачи диссертации: Разработка алгоритмов для реконструкции фазы из цифровых голограммам ДОЭ записанных на ХС и тонких пленках АП, и последующего картографирования их поверхностного рельефа и показателя преломления; модификация ЦГС во внеосевой и со сдвигом фазы конфигурациях и интеграция жидкокристаллических устройств; калибровка фазы и поляризации жидкокристаллических устройств; разработка аналоговых и цифровых методов одноэтапной ПГЗ; применение разработанного ЦГС с интегрированными инструментами для иследования харахтеристик созданых ДОЭ.

Научная новизна и оригинальность результатов: усовершенствованная версия программного и аппаратного обеспечения ЦГС была продемонстрирована как универсальный инструмент для исследования ДОЭ, записанных на наномногослойных ХС и тонких пленках АП; аналоговая и цифровая ПГЗ - это новые методы, которые позволили фотоиндуцированное формирование сложных ДОЭ.

Основная научная задача, решаемая диссертацией, заключается в разработке многофункциональных ДОЭ, нанесенных на наномногослойные ХС и тонкие пленки АП с помощью аналоговых и цифровых ПГЗ, и в исследовании их оптических и физических параметров в наномасштабе с помощью высокоэффективного ЦГС.

Теоретическая значимость и прикладная ценность: заключается в том, что постоянное совершенствование микроскопических инструментов является обязательным для поддержки исследований в различных областях, как например фотоника, материаловедение, биомедицина и т. д. Оптическая система ЦГС была усовершенствована для эффективного исследования ДОЭ. Возможность создания и проведения количественного анализа многофункциональных ДОЭ делает их привлекательными для различных применений, включая микроскопию, системы визуализации, солнечную энергетику и многое другое.

Внедрение научных результатов: представленные в настоящей диссертации результаты были успешно применены в рамках Европейского проекта нр. 687328 (2016-2018), в молдавско-белорусском двустороннем проекте ANCD 19.80013.50.07.04A/BL (2020-2021), в национальном проекте ANCD 20.70086.16/COV (2020-2021), в национальном проекте 20.80009. 5007.03 (2020-2023) и международном проекте ANCD 21.80013.5007.1M (2021-2023).

SHORTCUTS

AFM - Atomic force microscope
AP - Azopolymer
BM3D - Block-matching and 3D
DH - Digital holography
DHM - Digital holographic microscope
DOE - Diffractive optical element
DE - Diffraction efficiency
ChG - Chalcogenide glasses
CMOS - Complementary metal–oxide–semiconductor
CCD- Charge coupled device
PHR - Polarized holographic recording
LC - Liquid crystal
LCVR - Liquid crystal variable retarder
SRG – surface relief grating
SPAR - Sparse phase and amplitude reconstruction
SLM - Spatial light modulator
FT - Fourier transform
FFT - Fast Fourier transform
FOV - Field of view
RIG – Refractive index grating

INTRODUCTION

In recent years, increasing attention has been paid to the computerization of scientific experiments, including both hardware and software components. The digital holographic microscope (DHM) is a metrological tool used for 3D imaging of fine structures of microscopic objects based on the interference phenomenon. The history of holographic 3D imaging technologies has been shaped by three main breakthroughs that are the corner stones of the field in the last century: the holographic principle invented by Denis Gabor in 1947 [1], the first built laser by Theodore H. Maiman in 1960 [2], and 3D visual presentation schemes developed simultaneously by Juris Leight and Emmett Upatnieks, and Yuri Denisyuk in 1962 [3]. These great ideas lead to the establishment of holography as a new branch of optics.

A hologram is the medium containing the information originating from the light interference between the wave passing through the sample and the reference wave usually coming from a high spatial and temporal coherent source.

At the origins of the field, the hologram was being recorded on a photographic plate that required time-consuming processing including chemical treating and mechanical focusing for the image reconstruction. Later, digitalization opened the door for the development of computer technology, optoelectronics and nanotechnology and today it is possible to record digital holograms (DH) within a tenth of second directly on digital sensor arrays of a *charge coupled device* (CCD) or a *complementary metal–oxide–semiconductor* (CMOS) camera. In DHM, an enlarged image of the sample is obtained by the microscope objective (MO) and the imaging sensor, thus increasing the spatial resolution of an obtained image. Now, it is possible to reconstruct numerically the recorded wavefield from the digitally stored hologram on the computer.

Direct access to the phase information allowed by DHM gave rise to a new concept for microscopic investigations [4-6]. This technique has a wide range of outstanding applications for both 3D and quantitative phase imaging in different fields including biology, condensed matter physics, and material science. The main problem solved by DHM is the investigation of the objects that do not absorb or scatter light significantly. In other words, DHM can perform investigations of transparent objects. Another strength of this technique is that it allows to digitally focus on different layers of the sample and reconstruct a 3D profile of the optical thickness of the sample using the quantitative phase value. This is mostly due to the quantitative phase and amplitude information of the object wavefront that can be digitally obtained along the depth of the object [7]. Being a non-destructive and label-free technique, DHM was used to extract the 3D information

11

of live cancer cells dynamics [8], stem-cell derived induced human neurons [9], opaque micro-fibers at different depths [10], light-induced surface deformation of thin films [11] and many other fascinating implementations [12].

The main problem encountered during DHM investigations, similar to traditional optical imaging systems, is the limited spatial resolution imposed by the magnification and aperture size of its MO as well as by the size of the imaging sensor. DHM resolution limit is described by the Abbe criterion which states that the smallest point that can be resolved is proportional to the wavelength of the light being gathered, divided by the numerical aperture number. Ultimately, a larger CCD chip or a shorter wavelength corresponds to a greater ability to resolve small objects [13]. Another important issue that corrupts the DHM performance is the increased sensitivity of the instrument to the noise and external vibrations.

In the last decade, many hardware and software solutions have been proposed to enhance the DHM performance with current available digital sensor array dimensions and unideal imaging conditions. [14-16].

Hardware solutions presume the utilization of synthetic aperture techniques which include integration of different mechanical components such as rotating and shifting stages, as well as optical components as short wavelength lasers, pulsed lasers, diffractive optical elements (DOEs) or scanning galvo mirrors. These devices and tools were introduced in order to perform image sensor shifting, sample rotation or beam scanning [17]. The positions and directions of an object acquired using such methods contain high-frequency information and the frequency spectrum can be extended using passband superposition and then employed to reconstruct super-resolution imaging.

Recently, Faridian et. al. [13] implemented oblique illumination with short wavelength to design an off-axis digital holographic microscope in deep UV, capable of recording 3D image from nanostructures. The setup allowed to detect structures down to 250 nm. Despite being very interesting, this method is relatively expensive and has a limited range of applications as it presents possible photo-damage and phototoxicity to certain types of specimens (e.g., biological tissues). Another approach is coherent speckle field illumination where a random phase mask (a diffuser) is used to diminish the periodic pattern noise. The resolution enhancement has been achieved by time-consuming procedure of averaging the object waves under hundreds of different speckle illuminations [14].

Modern DHM configurations also take advantage of the advanced optical components such as liquid crystal spatial light modulators (SLM). SLMs are devices capable of modulating the amplitude, phase, or polarization of light waves in space and time. In recent works, the SLM was

applied to DHM to enable synthetic aperture imaging by splitting the light beams or angular-multiplexing [18].   Software solutions proposed to overcome the experimental constraints of the DHM imaging system imply the development of existing digital hologram processing algorithms. Typically, Fourier-transform methods can be applied for the numerical reconstruction of the complex object wavefront [19]. Lately, the principal component analysis algorithm was introduced in the reconstruction process of the phase-shifting DHM with structured illumination to remove the redundant the quadratic phases of the imaging system [20]. Different iterative algorithms were developed to compensate the noise or improve the reconstruction by alternatively updating the amplitude and phase of the object. Moreover, the computational reconstruction of the complex optical wavefront diffused by the object permits a post-acquisition numerical refocus and a quantitative phase and amplitude measurement of the sample by utilizing the Fresnel-Kirchoff theory of diffraction of light [16]. Iterative techniques were applied to perform artificial focusing on the sample by means of Angular Spectrum propagation function [21]. This class of algorithms mainly helps to bring under computational control the experimental conditions.

Despite intense research efforts, there still exists an increased demand in the improvement of DHM especially for obtaining high-precision, full-field depth mapping as well as 3D surface and shape measurements of DOEs pattern on photo-sensitive materials.

DOEs, as the name suggests, are compact optical components capable of tailoring the light in complicated ways via diffraction phenomenon. The first idea of the DOE as a diffraction grating for practical applications was reported by Fraunhofer in 1821. Photo-induced surface-relief formation was discovered in 1995 and extensively applied for both fundamental and applied research. Two centuries of research on fabrication of DOEs on optical materials gave rise to several techniques as photolithography [22], focused ion beam writing [23], and holography [24]. Most of these techniques provide good quality DOE, however time-consuming procedures involving numerous processing stages is the main problem, especially when encumbering etching procedures are required. Although conventional/analog holographic recording is a direct and precise interferometric approach exclusive of extra post-processing steps, theoretically it does not ensure creation of DOE with high diffraction efficiency and deep modulation of the surface relief. In contrast, polarization holographic recording (PHR) operating with different polarization states of the recording beams makes it possible to reveal the phase features of DOEs [25]. PHR triggers the mass-transport mechanism that leads to deeper photo-induced surface-relief formation without additional post-processing stages. It implies recording of the interference between a reference beam and an object beam with orthogonal polarizations. PHR enables one-step formation of sophisticated phase structures on the submicron scale without amplitude interference.

The advance of this fabrication technique is important for understanding how light interference can cause macroscopic movements of different types of photo-sensitive optical materials and for its efficient use in photonic applications. For this purpose, new digital recording approaches must be developed along with the analog ones. The design of the PHR setup allows the operation of a SLM, useful for controlling of the geometry and phase of DOEs via computer generated holograms. In this context, it is important to highlight the advantages of both methods.

The quality of the DOEs is determined not only by the fabrication techniques but also by the properties of optical light-responsive materials. High photo-sensitivity, high-resolution, low cost and wide spectral and frequency range are the key requirements for the optical materials. In some cases, the sensitivity to polarization also must be considered. Furthermore, it is very important that the recording media provides temporal stability of the obtained DOE. Chalcogenide glasses (ChG) and azopolymer (AP) thin films are optical materials that possess the above-mentioned characteristics including polarity and match the PHR as a patterning technique.

Among the other groups of special glasses, chalcogenide glasses have triggered great attention thanks to their rich photo-induced properties, low values of phonon energies and higher values of refractive indices if compared to other glasses. The unique electronic and atomic structure of ChGs reveal the presence of various photo-induced phenomena. Chalcogenide glasses behave as semiconductors, with the optical energy band gap dependent on the existence of short-range atomic order, thus photo-excitable by the light in the visible spectrum [26]. The rigidity of ChGs inter-atomic bonds is strong relative to organic polymers (one-dimensional chain structure) and weak relative to oxide glasses (consisting of three-dimensional networks). The chemical bonding on atomic scale of amorphous chalcogenides glasses can be described by the different length scales: in the range 2 - 5 Å is defined the short-range order and in the range 5 - 20 Å is defined the medium-range order. Amorphous materials by default do not present long-range order structures, in the range ≥ 20 Å [27]

The complicated structure of amorphous ChGs is best described as a continuous random network, usually characterizing noncrystalline solids (solids with lack of atom periodicity). For example, in the well-known structure of binary arsenic trisulfide or triselenide, the As-S, As-Se networks are locally two-dimensional with weak van der Waals bonding between layers while the - and Se structure is similar to a chain [28].

It is presumed that the mechanism behind photosensitivty of ChGs implies the creation of electron-hole pairs, which influence the structural transformations by changing the valence of the neighboring atoms and their inter-atomic bonds. As a consequence, geometrical coordination defects are created. This transformation process is reversible due to the fact that the photo-induced

states are positioned close to each other thus, allowing restoration of the original bonding. The photoinduced phenomena exhibited/manifested particulary by ChG thin films result in modifications of the physical properties of the material, producing scalar phenomena that include photodarkening, photorefraction, photodiffusion and photocrystallization, as well as vectorial phenomena such as - photoinduced birefringence and photo-induced dichroism.

For photonic applications, a certain contribution presents the formation of nanostructures from ChG. Particularly, artificially obtained multilayer structures with controlled geometrical parameters allow to study their characteristics as thin films. Latest investigations show that synthetic formed ChGs nano-multilayers (NML) become sensitive to the polarization of light. Polarization sensitivity of the materials offers an additional degree of freedom for pattern/ DOE recording. Moreover, it provides additional information about the glassy structure. Besides, the overall photo-sensitivity of ChGs NML is higher if compared to conventional ChGs because in the NML structure more medium-range order bonds are preserved [29]. The refractive index modulation greatly depends on the type of bond (short-range or medium-range order) that prevails the ChG structure. Nevertheless, photo-structural transformation dependence of artificial nano-structured ChG is still a great point of concern in the scientific society.

For this reason, with an aim to extend the understanding of ChGs nano-multilayers photo-induced polarization behavior, a part of this thesis is focused on design, fabrication and investigation of DOEs patterned on ChGs nanomultilayers. Specifically, this work highlights relevant insights on light-induced relief formation of two types of diffraction gratings: surface relief gratings (SRG) and refractive index gratings (RIG) patterned on ChGs nano-multilayers constituencies. In addition, the application of the enhanced DHM technique for quantitative investigations of the DOEs designed on ChGs provides essential information about anisotropy and birefringence properties of these optical materials.

Amorphous azopolymers is another class of photosensitive optical materials that proved efficient DOE formation. The molecular architecture of azopolymers contains a backbone and azobenzene-containing chromophores. The polymer backbone consists of atoms (C, N, O, H) and are linked by covalent bonds. One of the most attractive types of photo-polymers are carbazole-based azopolymers which meet state-of-the-art requirements for photonic applications. Since we live in the information technology era, among most relevant applications of carbazole-based azopolymers can be listed optical data storage, data security and identity documents protection.

Remarkable optical and structural proprieties of amorphous azopolymer thin films allow one-step formation of complex surface relief structures. It is possible to arrange SRGs on top of

another SRG, which allows one to create sophisticated DOEs. Complex structures can be created below the glass transition temperature by applying multiple interference patterns mainly because azopolymers are sensitive to a wide wavelength band of light and exhibit tolerance to overexposure. In azopolymers, DOE formation is driven by anisotropic movements of azo materials perpendicular the polarization direction of the incident light, that is one of the paramount criteria for successful PHR.

The origin of the light-induced phenomenon in azopolymers is based on two properties of azo dyes. Specifically, it is believed that the azo dyes exposure to light within ultraviolet (λ=365 nm) to visible (λ=570 nm) spectrum enables reversible *trans-to-cis* and *cis-to-trans* isomerization. This property makes it possible to erase them by shifting the polarization patterns. The second property is the anisotropy of the molecular absorption because the transition dipole moment is oriented approximately along the molecular axis. Photo-isomerization of the azo dye molecule leads to mass transfer of matter and modulation of the surface at the molecular and macro-levels. Based on azopolymer thin films, it is possible to obtain various types of micro and nanoscale optical elements, ranging from linear diffraction gratings to sophisticated optical elements.

High sensitivity to the polarization state of light is the key feature of azopolymers. Different types of DOEs are recorded when the interference pattern is formed by two polarized beams with S:S, P:P, right circular polarizations (RCP) or left circular polarization (LCP) geometries. Recent investigations revealed that due to photo-isomerization expansion of the material in the S:S polarization state, the peaks of the surface relief formation coincide with the intensity maxima, however in the P:P geometry the peaks slowly move from the intensity maxima to the intensity minima thanks to the phase transformations exhibited by DOE during inscription process [30].

Similar to ChG, in azopolymers three kinds of phenomena govern the formation of DOEs: 1. Volume birefringence due to photo-induced modulation of the refractive index; 2. Surface relief modulation caused by the mass movement, triggered by structural photo-induced modifications in the bulk of the material [31]. In practice, the contribution of the birefringence grating to the overall diffraction efficiency of thin films of amorphous azopolymers is relatively small. Still, it is important to account for the input arising from these different gratings. Although there exists a generalized theory describing the mechanisms behind surface pattern formation for many amorphous azopolymers (the light creates a photoinduced excited state in which the charge is redistributed), it is important to emphasize the fact that these mechanisms can vary for different combinations of azo dyes (Disperse Yellow, Disperse Orange, Disperse Red, etc.) with polymers materials. Therefore, a study of DOE parameters on different combinations of azo-chromophores

with polymer materials would bring significant knowledge on the origins of photo-induced phenomena in azopolymers.

Problem statement

Analog PHR presumes direct projection of the interference pattern on the recording media. It allows the creation of DOEs with a high resolution because the resolution in this case is limited by the material resolution. Thus, analog approach permits to exploit the full resolution potential of the recording media which riches today 5000 pl/mm. However, the main drawbacks of analog PHR of DOEs are common to all analog technology: the difficulties of recording complex multifunctional DOEs, limited capabilities for optical processing and storage of holograms, complex optical setups and their adjustments to various recording objects and conditions. The digital PHR provides more opportunities for processing the material with a wide variation for the shape, refractive index or absorption coefficient of the DOEs. The main disadvantage of the digital PHR compared to the analog counterpart is a lower resolution associated with the digital matrix of the SLM, which depends on the size of the matrix and the size of the pixels themselves. The technology at the present time does not permit to produce the pixels and spacing between them smaller than one micrometer.

In this thesis, we implement and develop digital and analog PHR approaches for recording DOEs on azopolymers thin films and ChGs nanomultilayers. The advantages of using the analog approach include the high speed for material processing, absence of computational complexity and energy efficient method for material processing. On the other side, the digital approach to PHR provides graphical modification of the patterns that can be printed on these materials, the ability to implement several mathematical functions in one DOE, in addition to possible changes in the optical characteristics of the shape of the diffracted beam. Furthermore, digital PHR involves direct operation to the wavefront modulation by digital handling of computer-generated holograms, which includes numerical calculation of the pattern rather than producing it photographically.

As mentioned above, DOEs obtained on these materials can be classified based on the origin (digital, analog) of produced light modulation as amplitude-only, phase-only and hybrid DOEs containing both amplitude and phase components. Phase DOEs possess high efficiency and generate diffraction patterns due to the refractive index and thickness modulation of the optical material, compared to their amplitude counterparts with lower efficiency caused by absorption. The diffraction efficiency (DE) of the DOEs is the main parameter determining their possibility to be used for practical applications. Since the DE of phase DOEs is defined both by refractive index and thickness modulations, it is very important to determine accurately the map of these changes.

A topography surface map of DOEs is conventionally measured by atomic force microscope (AFM), but this is a point-by-point scanning technique with restricted field of view. Moreover, revealing the refractive index map of DOEs is still a problem. Optical techniques such as refracted near-field measurements [32], imaging ellipsometry [33,34], and lateral shearing interferometry [35] are used for refractive index mapping. The drawback of these methods is the complicated mechanical arrangement required.

Current advances in photonics and optoelectronics are leading to more sophisticated, complex, and miniaturized optical devices. This boosts the development of new materials as well as methods of their research. *The research topic of the thesis is oriented to elaboration of DOEs on ChG nanomultilayers and azopolymer thin films by the implementation of polarization holography, and advancement of DHM optical system for investigating the recorded DOEs. It is of particular scientific interest because three-dimensional digital images obtained using DHM play an important role in the scientific push forward of a number of practical applications in many fields, including the condensed matter, materials science and biological sciences.*

The purpose of the thesis

The main goal of this work is to improve the design and performance of DHM, including its hardware and software components, for an accurate quantitative description of key parameters of different types of DOEs, patterned on ChGs nanomultilayers and azopolymer thin films by polarization holographic recording.

The objectives of the thesis

In order to accomplish the aim of the thesis, it is necessary to fulfill several objectives:

- Develop numerical reconstruction algorithms for accurate phase reconstruction from acquired digital holograms of DOEs recorded on photosensitive ChGs nanomultilayers and azopolymer thin films and subsequent mapping of their surface relief and refractive index mapping.

- Modify the optical part of the DHM in the off-axis and phase-shifting configurations by introducing liquid crystal devices. Phase and polarization calibration of the liquid crystal devices implemented in digital holographic setups. Compare the effectiveness of these approaches.

- The development of analog and digital holographic techniques for one-step polarization holographic recording of different types of DOEs based on NML structures from ChG and carbazole-based azopolymers.

- Apply the developed imaging – DHM - system with all the integrated tools for characterization of the created DOEs.

The methods implemented in this thesis

1.   The sensitive nature of optical signals to medium changes or inhomogeneities makes light a promising tool to study or process of medium. In recent decades, the features of light have been exploited in many optical techniques and instrumentation, which has contributed significantly to the advancement of modern science and technology. **Analog and digital PHR** were applied to record different types of DOEs on ChGs nanomultilayers and azopolymer thin films. Analog approach offers several advantages such as high speed for material processing, high resolution, absence of computational complexity and energy efficient method for material processing. The digital approach to PHR provides graphical modification of the patterns that can be printed on these materials, the ability to implement several mathematical functions in one DOE, in addition to possible changes in the optical characteristics of the shape of the diffracted beam.

2.   **The DHM** evolution is emerging continuously together with modern photonic technologies contributing to the further development of a wide variety of alternative digital holographic approaches and set-ups proposed to solve weaknesses of the conventional configurations. For the investigation of many variety objects there is space for further enhancement of DHM resolution as the "phase problem" is inherent to optical imaging in material sciences, medicine, crystallography and astronomy, or more general, to all scattering measurements independent of object nature and the wavelength used [36-38]. The scattered wave distribution is complex-valued (contains phase and amplitude components). The phase part carries information about random scattering in objects. Phase information provided by DHM is particularly useful for the real-time, 3D investigation of scattering of disordered media such as biological tissues or engineered surfaces, because it allows to make visible tiny details of their internal structure otherwise completely invisible with current commercial white light microscopes [39, 40]. This feature could allow the DHM to become a game changer in many application fields, from biology to nanoparticles, because it can guarantee an unprecedented level of imaging precision. However, scattering effects provoked by refractive-index inhomogeneities present in complex media corrupt the focus, resolution and sensitivity of DHM. [41].

3.   **Wavefront shaping techniques by digital modulation of light.** Many research groups have exploited the deterministic nature of elastic light scattering and demonstrated the coherent control of multiple scattering in complex media using *state of the art* wavefront shaping methods. Wavefront shaping techniques [42-46] promise to overcome diffusion (scattering) of light by tailoring an optical wavefront to constructively interfere at a target location deep inside scattering

media. Wavefront shaping aims to overcome the limits of optical diffusion by optimizing the optical wavefront to compensate for phase differences imparted as photons travel along differing optical paths in scattering media. By aligning the phase of the diffused light, a focus can be formed inside or beyond the scattering media through constructive interference. Scattered light is not non-informative and often useful. Instead of being filtered out, the scattered light could be reshaped to undo the scattering effects and enable focusing of light in a scattering medium. Mathematically, the input and output properties of the scattering medium can be modeled through different wavefront shaping approaches such as iterative wavefront optimization [47-51], measuring the transmission matrix of the scattering medium [52, 53], and optical time reversal via phase conjugation [54-56]. The basic principle of these methods is to extract information from scattered light by measuring the spatial phase profile of an optical field exiting the sample and computationally recovering an ideal wavefront shape that, when sent back into the object under study, will focus to a micrometer scale spot. To find such a wavefront solution, a "guidestar" mechanism is required to identify the target location [43].

Until now, only a few guidestar mechanisms have been reported. These can be categorized based on their controlling mechanisms. The first category is using light itself to control the guidestar, and includes fluorescence [57, 58], second-harmonic generation [59], absorption [60-63], and coherence gating [64]. A second category employs ultrasound and includes ultrasound [65-69] and ultrasound microbubble guidestars [70]. Measurement and manipulation of the light field have been realized through the utilizations of spatial light modulators (SLMs). Block-Matching and 3D (BM3D) algorithm is a powerful image denoising method showing state-of-the-art denoising performance. For microscopic investigations, it is especially important to minimize the noise but to preserve important image details. This is possible due to filtering in 3D transform domain by combining sliding-window transform processing with block-matching and by applying a shrinkage operator (e.g. hardthresholding or Wiener filtering) on the transform coefficients. The image blocks are processed in a sliding manner so that blocks that exhibit similarity are matched together to form a 3D array. The high correlation induced along the dimension of the array is operated by applying a 3D decorrelating unitary transform which produces a sparse representation of the true signal in 3D transform domain. The final estimate is the weighted average of all matching local block-estimates. Consequently, during the matching process the artifacts are blocked and the estimation ability is improved [71, 72].

4.   The variational algorithm **Sparse Phase and Amplitude Reconstruction (SPAR)** proposed in [73] and Fast Fourier Transform (FFT) methods were adjusted and applied in the numerical algorithms for reconstruction of the amplitude and phase from off-axis digital

holograms. Both methods were used for calibration of the SLM. The algorithm based on SPAR technique was adopted as a noise minimizing approach. The contradictory conditions such as limited resolution of DHM optical setup and meticulous observations of sample under study require precise modulation of light. First, we perform the digital modulation of light by introducing Spatial light modulator (SLM) with appropriate software in the DHM optical setup. Therefore, it is proposed to investigate various phase masks, acting as Bessel beam, blazed grating, object adjusted masks, displayed on SLM as adaptive illumination elements for modulating the amplitude and phase of light propagating through the object. DHM systems run sophisticated numerical algorithms to process large volumes of digital image data, calculate optical phase shifts, and determine the thickness and refractive index of material samples.

The main scientific results submitted for defense:

1.   Analog and digital PHR are direct approaches that can be applied for one-step fabrication of multifunctional DOEs on the surface of ChGs nanomultilayers and azopolymer thin films. It is the result of the mass transfer induced by the vectorial character of holography in polarized light (vectorial). Analog PHR produces DOEs with a high diffraction efficiency with a maximum of 33% achieved in this thesis, while digital PHR enabled designing of DOEs with vortex geometries capable of generating spatially multiplexed beams with phase singularities, but the diffraction efficiency of these DOEs is no more than 1%.

2.   Phase imaging enhancement can be obtained by adopting a sinusoidal phase grating mask to the off-axis lens less DHM setup. The root mean square error values of the phase reconstruction decreased with about 20%. At the same time, the error of the phase reconstruction decreases by approximately 72% when a blazed diffraction grating is inserted in the optical setup of phase-shifting DHM configuration. Both results are proved by computational simulations.

3.   Integration of liquid crystal devices in digital holographic optical systems presumes the mandatory and important procedure of detailed phase and polarization calibration for each specific configuration.

4.   Off-axis and phase-shifting DHM configurations with integrated liquid crystal devices are applicable for the effective investigation of refractive index and surface relief maps of multifunctional DOEs recorded on azopolymers thin films and ChGs nanomultilayers.

The solved scientific problem

As a result of the work, it was shown that the digital holography technique increases both the possibilities of polarization holographic recording of multifunctional DOEs on NML from chalcogenide glasses and thin-film azopolymers, and the perceptivity of digital approach to research of the obtained DOEs. The current work constitutes an important step towards increasing

the availability of computational imaging methods from the hardware-side, which has been typically a bottleneck.

Thesis structure

In the **first Chapter,** presents a general overview of the existing DHM technologies. The main challenges encountered during hologram recording and computational processing are described. Important advantages and limitations of different DHM configurations are highlighted. State-of-the-art methods proposed for improving the resolution and overall DHM performance are discussed. ChGs nanomultilayers and azopolymer thin films are described as photo-sensitive media for DOE recornding. Chapter one ends with description of the novelty and contribution of the doctoral thesis.

In the **second Chapter**, the theoretical framework for the improvement of the DHM by computational processing is addressed. FFT and SPAR phase reconstruction methods are described for the off-axis digital hologram processing. Different phase masks are investigated for improving the DHM performance in both, off-axis and phase-shifting configurations.

In the **third Chapter**, the implementation of the liquid crystal devices in digital holography is discussed. The pixel-wise phase calibration of the SLM is described in the first paragraph of this chapter. Two different algorythms were used for the phase reconstruction, an FFT based method and a LLS method. In addition, the retardance calibration of the SLM is perfomed in order to understand how the deviced changes the polarization of the outcoming beam. The calibration of the liquid crystal variable retarder is presented in the second paragraph of this chapter.

The **fourth Chapter** is dedicated to the design of various DOEs on ChGs nanomultilayers and azopolymer thin films. For a broad understanding of the photo-sensitivity of this materials analog and digital PHR were exploited. The DE kinetics was monitored and analised for DOEs obtained with different exposure doses and recording approaches.

The **fifth chapter** presents the developed DHM for the investigation of DOEs obtained on ChGs nanomultilayers and azopolymer thin films. The chapter considers the off-axis configuration for the 3D imaging and characterization of the surface relief and refractive index parameters of the DOEs. The second chapter describes the implemented phase-shifting DHM configuration for the study of DOEs. The thesis ends with the conclusion and recommendations of the research work.

1. DIGITAL HOLOGRAPHY FOR MICROSCOPY AND RECORDING OF DIFFRACTIVE OPTICAL ELEMENTS. LITERATURE REVIEW

1.1 State-of-the-art in digital holographic microscopy

A hologram, in a general sense, is the resulting intensity at the interference of two waves and contains information about their phase difference, as long as these two waves are not mutually polarized in perpendicular directions. The hologram registration process requires high accuracy and is associated with a number of conditions. First of all, high mechanical stability is required when recording holograms and protection of the DHM optical imaging system from vibrations. Slightest vibrations can make the interference pattern noticeably less clear, or even disrupt it.

The essential components of the DHM imaging system are a light source, a beam splitter to create an interferometer, a complementary metal–oxide–semiconductor (CMOS) or a charge-coupled device (CCD) imaging sensor/digital camera, and a computer with appropriate software needed for recording and processing the digital holograms. Typically, the concept of DHM is associated with acquisition of the amplitude and phase information about the object via a coherent illumination, mandatory for producing an interference pattern. In the last years, however, incoherent light source has been implemented for DHM investigations in order to reduce speckle and interference noise. In this case, for achieving interference it is important to provide very accurate control over the optical path difference between the object and reference beams.

The main DHM configurations can be distinguished depending to the angle between the reference and object beams, the number of recorded holograms (also known as interferograms) and the numerical reconstruction algorithm.

The off-axis configuration enables to reconstruct the information using a single hologram acquisition [36, 37]. It implies that there is set a few degrees angle between the object and references beam to avoid overlap of the zero-order and holographic images, as shown in Fig. 1.1. The established angle α_{max} must fulfill the sampling theorem. The maximal value, leading to a correct sampling of the interference pattern is given, under paraxial conditions, by:

$$\alpha_{max} = \frac{\lambda}{2\Delta x}, \tag{1.1}$$

where Δx denotes the sampling rate of the recording camera. The reconstruction efficiency of the image in the off-axis arrangement strongly depends on the CCD or CMOS pixel size used to transmit the content of the hologram as well as on a clear separation of the conjugate images from the zero-order.

The complex amplitude distribution of the sample under study is reconstructed from off-axis holograms and includes several steps: selection of only one of the twin images (presuming a

twin image and the zero-diffraction order elimination), numerical reference calculation, a refocusing algorithm. In some cases, the reconstruction includes the compensation of the spherical phase distortion produced by the microscope objective (MO) via a numerical phase mask [38]. Quantitative phase-contrast imaging has used phase retrieval to compensate the aberrations introduced by the spherical phase via the MO. However, the residual phase is not only the result of the numerical processing but also the digital hologram recording conditions. Recently, various research papers have been reported on numerical as well as physical compensation of the phase aberrations [39–41]. The spherical distortion introduced by the optical components in DHM systems are commonly compensated via computational processing of the holograms [74, 75].
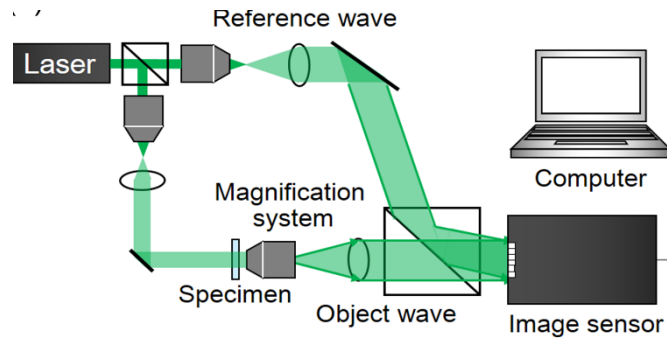
Fig. 1.1. The off axis DHM with Mach-Zehnder optical configuration [76].

Appropriate physical configurations were proposed to eliminate the spherical phase of DHM imaging system. In these configurations, the quadratic phase factor is eliminated during hologram recording, consequently the number of calculations and the computational processing time is reduced [77, 78]. The same result is obtained if identical MOs are introduced in the object and reference arm (both producing a spherical phase) of the microscope system. Other approaches for compensating the spherical distortions are based on the utilization of the optical components such as liquid crystals devices, aspherical lenses, or deformable mirrors.

The **in-line DHM configuration** permits to exploit all the pixels of the hologram because the object and reference waves are aligned. This is a lensless laser microscope arrangement in which a single beam illuminates the object through a small pinhole with diameter of the order of a wavelength. Both waves are forming the hologram.
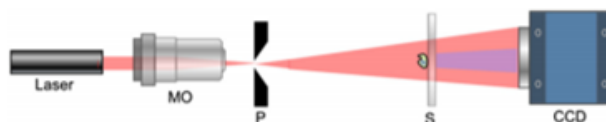
Fig. 1.2. In-line DHM configuration, M- mirror, BS-beam splitters, MO-microscope objectives, S-sample object [79].

24

The object is several thousand wavelengths away from the pinhole and is usually, placed closer to the image sensor, as shown in Fig. 1.2. The object beam is considered to be the light scattered by the object while the reference beam is the part of the incident light that remains undisturbed. Both waves are reciprocally aligned with the interference angle equal to 0^0 that is forming the hologram. The 3D reconstruction of the object can be obtained from a single hologram and the full pixel count is considered leading to higher resolution. It is a simple DHM setup that is especially useful for particle investigations. However, the drawback of this scheme is that the phase image is corrupted by the out-of-focus twin-image. Consequently, the real, virtual and zero order images are overlapped in the spectrum [80-82]. Thus, it requires digital filtering to suppress the conjugate image. For example, in the numerical reconstruction algorithm a high-pass filter near the zero-frequency can be applied to the Fourier transform of the hologram. The spectral properties of the object strongly influence the efficiency of high-pass filtering [4].

The phase-shifting configuration is another possible approach to DHM with a Mach-Zehnder optical configuration. This method was first introduced by Yamaguchi in [83] and implies in-line acquisition (the angle between the reference and object beams is almost 00) of multiple holograms. Typically, four-step phase-shifting is performed where four holograms are acquired, with the phase-shift equal to $\pi/2$, as shown in Figure 1.3. However, three-step and two-step PS-DHM were also reported [84, 85]. Furthermore, phase reconstruction via unknown or random phase shifts were demonstrated in [86, 87].

PS-DHM configuration is more effective and precise if compared to its off-axis and in-line counterpart as it employs entire pixel count along with high-quality reconstruction of the object phase achieved thanks to the twin image and zero-order terms removal.
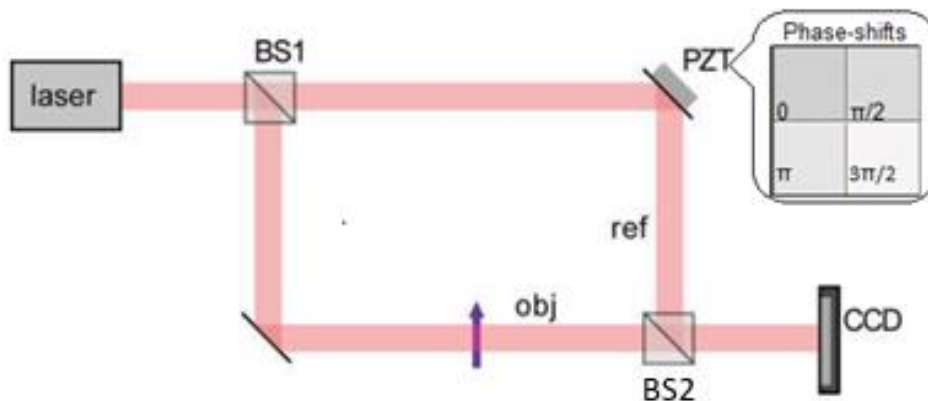

Fig. 1.3. The phase-shifting DHM configuration, BS1, BS2-beam-splitter, PZT-piezoelectric transducer, obj- object, CCD-digital camera [4].

The classical PS-DHM optical system contains a mirror mounted on a piezoelectric transducer (PZT) to shift the reference wave and record four shifted interference patterns. Complex-valued

holograms are formed by a linear combination of these interferograms. Nanometer scale precision of phase-shifting digital holographic microscope (PS-DHM) was proved during the measurement of the out-of-plane displacement of a cantilever [88]. Nevertheless, owing to the fact that the linearity of the PZT is dependent on the applied driving voltage phase-shifting errors may be introduced in the holograms. In addition, the phase fluctuations of the commercial lasers and environmental perturbations may also decrease the phase-shifting accuracy.

To manage phase-shifting errors, various self-calibrating numerical algorithms based on statistical methods have been developed [89-92]. However, the assumption that the diffraction field of the object is fully random or zero mean restricts the application of these methods in case of an experiment where the averaging operator cannot be approximated to a constant.

In the last decade, advanced DHM configurations mostly take advantage of the computational reconstruction to perform impossible optical processes, e.g. the numerical subtraction of zero-order diffraction, and interferometric comparison of the wave fields generated and reconstructed with different wavelengths [93,94]. However, the low-resolution problem still remains because of the limited size of the CCD sensitive chip and the magnification by MOs that increases the resolution concurrently with the coherent speckle noise. From Abbe equation $R = \lambda/2NA$ for the resolution it is known that the smallest point that can be resolved by a DHM objective is proportional to the λ- wavelength of the light being gathered, divided by the NA-numerical aperture number. Ultimately, a larger CCD chip or a shorter wavelength corresponds to a greater ability to resolve small objects [11].

Nowadays, many solutions have been proposed to enhance the DHM resolution with current CCD chip dimensions by using a shorter wavelength thus creating a larger NA or by phase modulation of the object beam with a phase mask (random or periodic pattern) projected onto the object. Recently, Faridian et. al. [13] implemented **oblique illumination with short wavelength** to design an off-axis digital holographic microscope in deep UV, capable of recording 3D image from nanostructures. The setup allowed to detect structures down to 250 nm. Despite being very interesting, this method is relatively expensive and has a limited range of applications as it presents possible photo-damage and phototoxicity to certain types of specimens (e.g., biological tissues). Another approach is coherent **speckle field illumination** where a random phase mask (a diffuser) is used to diminish the periodic pattern noise. The resolution enhancement has been achieved by time-consuming procedure of averaging the object waves under hundreds of different speckle illuminations [7]. Furthermore, the spatial resolution of microscopy can also be improved by mean of the **structured illumination** coming from a periodic phase mask in order to increase the depth of field and to compensate aberrations and image distortion introduced by the optical components

of the setup (microscope objective, lenses, etc.). For this experiment, two types of diffraction gratings were placed in front of the studied sample [95]. When the diffraction grating was applied the wavefront reaching the CCD sensor became more diverse due to diffraction on the grating and in case of linear diffraction only the resolution of the x direction could be improved, because only a one-dimensional grating is used. The enhancement along three different directions was obtained in case of the hexagonal diffraction grating. Even though the super-resolution of the DHM in combination with diffraction grating was proved numerically, from Fig. 2 it can be pointed out that visually there is still place for an enhancement, as speckle noise and blurriness remain noticeable.

(a)   (b)
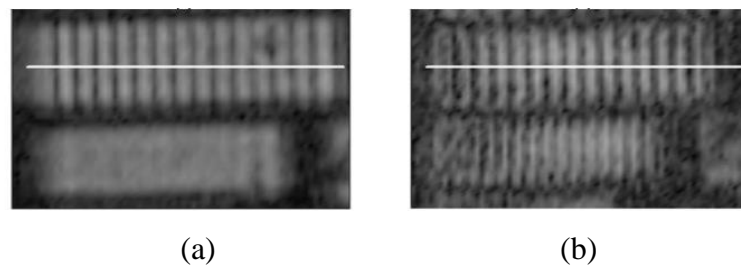
Fig. 1.4. (a) Reconstructed image without a grating in the setup and (b) with a grating in the setup [95].
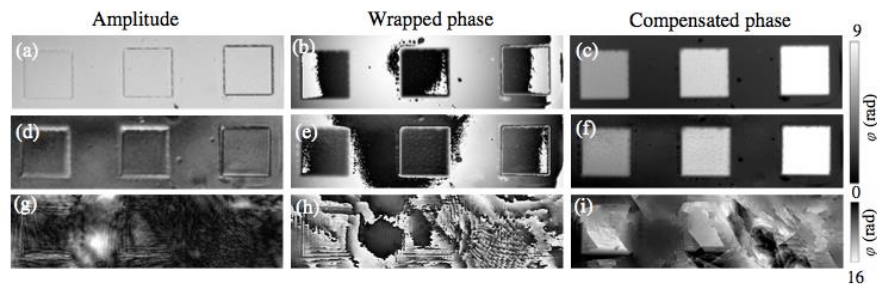
Fig. 1.5. Experimental verification of amplitude imaging and quantitative phase imaging through a weak diffuser in dependence on the spatial coherence of light. (a)-(c) Amplitude, wrapped phase, and compensated unwrapped phase observed without the diffuser. (d)-(f) Amplitude, wrapped phase, and compensated unwrapped phase observed with the diffuser in spatially incoherent light (g)- (i) Amplitude, wrapped phase, and compensated unwrapped phase observed with a diffuser and spatially coherent light [93].

In [93], a **coherence-controlled holographic microscope** (CCHM) was simulated numerically for imaging of a two-dimensional object through a static scattering layer. For comparison, coherent and incoherent illumination scenarios as well as strongly and weakly scattering were considered. It is proved that the quality of imaging process depends on the spatial

light coherence. However, the method demonstrated poor resolution and quality of the revealed phase information for the case of the fixed, strongly scattering layer Fig. 1.5.

To sum up, all the latest emerged DHM approaches have pros and cons, and obviously have their role in progress of the field but it is certain that the random spatial inhomogeneities still remain as a constraint for the high-resolution and high-accuracy phase reconstruction that is required especially for photonic applications. From the experiments performing structured illuminations by periodic or random modulation of light it can be concluded that the improvement was not significant, in addition, the parameters of the phase mask (diffraction grating) were not investigated and optimized. Since, scattering of light vary from object to object it is assumed that the modulation of light should be sample-adapted. Therefore, it is intended to investigate the parameters of the phase masks (diffraction gratings) and apply optimal control over the optical wavefront within DHM in off-axis and phase-shifting configurations.

1.2 DOEs on chalcogenide glasses nanomultilayers

Research into the optical properties of ChGs started around seventy years ago when Frerichs reported the properties and characteristics of As_2S_3 [96, 97]. For several decades, chalcogenide glasses have been known as a group of amorphous non-crystalline materials that exhibit various important optical and electrical properties such as photosensitivity, infrared transparency or significant changes in the refractive index (up to 10 %) upon exposure. The basic composition of these glasses consists of chalcogen elements S, Se and Te covalently bounded with Ge, As, Sb, Ga, Si or P. The transparency to infrared and low phonon energy make ChGs potential hosts for rare-earth dopants such as Nd, Yb, Er, Gd, etc by enabling higher quantum efficiency of photoluminescence, and higher lifetime of the excited states. The possibility to create a wide variety of glass-forming systems with optimized optical properties permits to exploit ChG for different photonic applications for example fabrication of DOEs, waveguides or fiber structures. ChGs is a class of amorphous solids/materials also suitable for the registration of phase holograms, computer synthesis of kinoforms, and the creation of photonic crystal structures, mostly due to the refractive index transformations as a result of interaction with light.

As mentioned above, chalcogenide glasses are known for their high transmittance in the near- and mid-infrared range of the spectrum. Specifically, large masses of ChGs constituent atoms influence the vibrational energies of the chemical bonds to be low, which lead to a broad transparency window from the middle infrared up to ~ 20 µm. In other words, the wide transparency window is determined by the constituent chalcogen element from the glass, as shown in the transmission spectrum in Figure 1.6. It is approximately 11 µm, 15 µm and 20 µm for

sulphides, selenides and tellurides, respectively [98]. In the visible range of the spectrum the glasses based on sulfur are partially transparent, while glasses on selenium or tellurium are opaque. A necessary prerequisite for extending the transparency window of ChGs to the long wavelengths is the addition of more massive chalcogen elements and thus modifying the phonon vibrations. For extending the transmission range to shorter wavelengths it is necessary to vary the electronic band gap, which is a more sophisticated procedure. Therefore, it is imperative to investigate the structure of glasses on a microscopic level for allowing the control of the gap between the valence band and the conduction band.
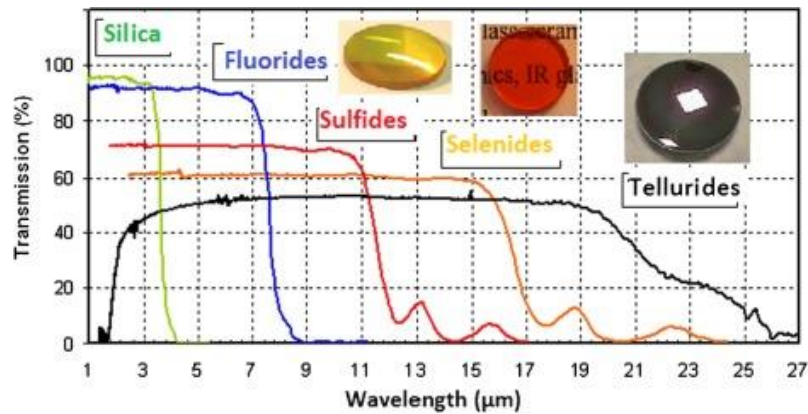
Fig. 1.6. Presentation of windows of transparency of S, Se, Te-based chalcogenide glasses. The insets are examples of sulfide As_2S_3 (yellow), selenium As_2Se_3 (red) and tellurium $Te_{20}As_{30}Se_{50}$ (black) glasses [99].

The transmission spectrum of the material permits to analyze quantitatively the optical properties of amorphous thin films, as shown in the pioneering work of J. C Manificer, et al. [100] and later extended for uniform and inhomogeneous thin films by R. Swanepoel in [101, 102]. The absorption coefficient (α), linear refractive index (n) and optical bandgap ($E_{g\,opt}$) are the parameters included in the linear optical properties of chalcogenide glasses. The optical absorption coefficient of ChGs can be calculated from the transmission spectra of a sample using the formula:

$$\alpha = \frac{1}{d}\ln\left(\frac{1}{T}\right), \tag{1.2}$$

where d is the thickness of the ChGs sample and T is the transmission from the transmission spectrum. However, it is important to note that ChGs possess large linear and nonlinear refractive indices due to their highly polarizable chemical bonds [103].

The refractive index of ChGs has the values in the range between 2 to 3. When the amorphous chalcogenide is illuminated by near bandgap light the optical absorption edge yields a red shift that corresponds to the increase in the refractive index. The determination of the optical constants using Swanepoel's method for several chalcogenide glasses, including As_2Se_3 are described thoroughly in [104-107]. The Swanepoel's method is non-destructive and provides the

dispersion relation over a large range of wavelengths without knowledge of the film's thickness as a prerequisite.

The exposure-dependent refractive index change in As_2Se_3 across a broad spectral range is reported (Fig.1. 7), as is the following theoretical determination of refractive index changes and film thickness [108].
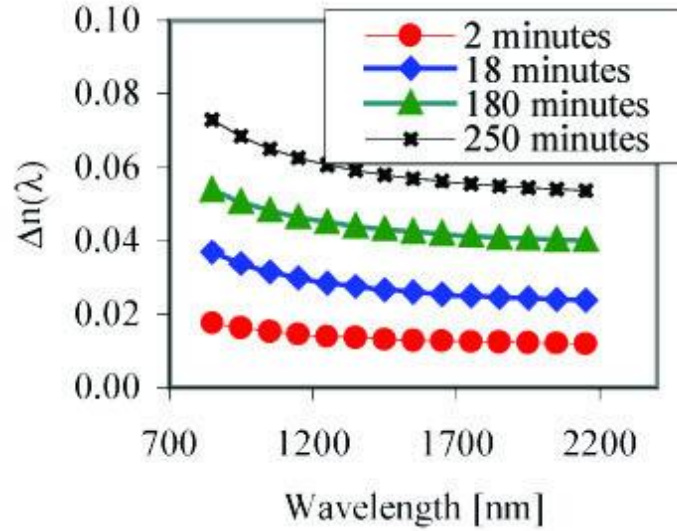
Fig. 1.7. Refractive index changes as a function of wavelength of As_2S_2 in dependence of illumination doze [108].

The model of a thin film deposited on a transparent substrate is shown in Fig 1.8. The film and substrate are surrounded by air with the refractive index $n_0 = 1$ the incident light from the spectrophotometer falls normal to the substrate. The refractive index of the film is $n = n_0 - ik$ and a has the coefficient of absorption $\alpha = 4\pi k/\lambda$. The refractive index of the substrate is denoted by $s(\lambda)$. The thickness of the substrate must ensure the separation of any resonant modes from those within the film. It is presumed that the shape of the film profile ensures linear variation in thickness of the exposed area according to:

$$d = d \pm \Delta d, \tag{1.3}$$

Interference fringes order can be obtained from the transmission spectrum obey the following formula:

$$m\lambda = 2nd, \tag{1.4}$$

where: m = 1, 2, 3, ... at maximum points in the transmission spectrum and m $=^1/_2, ^3/_2, ^5/_2$, at minimum points in the transmission spectrum.

Swanepoel's method [101, 102] requires the separation of the peaks and troughs of the transmission spectrum. Let $T_M(\lambda)$ describe cover all the maxima in the transmission spectrum and

30

let $T_m(\lambda)$ describe all the minima; both are considered to be continuous functions of λ. By setting the conditions $(n^2 \gg k^2)$ and $\alpha = 0$, two equations are obtained:

$$T_M(\lambda) = \frac{\lambda}{2\pi n \Delta d} \frac{a}{(1-b^2)^{\frac{1}{2}}} \tan^{-1}\left[\frac{1+b}{(1-b^2)^{1/2}} \tan\frac{2\pi n \Delta d}{\lambda}\right],$$ (1.5)

Incident light

Δd

$\overline{d}$

Film

$n(\lambda)$

Substrate

$s(\lambda)$
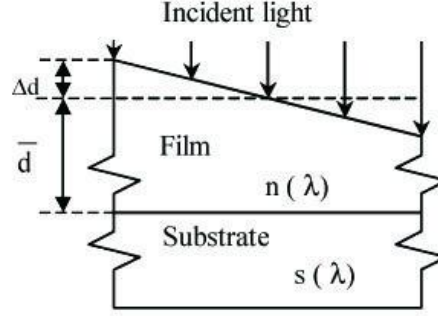
Fig. 1.8. The thin film model deposed on a transparent substrate, with wedge shaped profile [108].

$$T_m(\lambda) = \frac{\lambda}{2\pi n \Delta d} \frac{a}{(1-b^2)^{\frac{1}{2}}} \tan^{-1}\left[\frac{1+b}{(1-b^2)^{1/2}} \tan\frac{2\pi n \Delta d}{\lambda}\right],$$ (1.6)

where $a = A/(B+D)$ and $b = C/(B+D)$. Also, $A = 16n^2 s$, $B = (n+1)^3(n+s^2)$, $C = 2(n^2 - 1)(n^2 - s^2)$, and $D = (n-1)^3(n-s^2)$.

From, Eq. (1.5) and (1.6) is obtained the unique solution for both n and Δd in the region $0 < \Delta d < \lambda/4n$. The average thickness of the film can be found by solving Eq. (3) for a two adjacent maxima or minima described by (n_1, λ_1) and (n_2, λ_2):

$$d = \frac{\lambda_1 \lambda_2}{\lambda_1 n_2 - \lambda_2 n_1},$$ (1.7)

Having calculated the film thickness and refractive index, the accuracy of the results can be greatly improved by using Eq. (1.4) to evaluate the fringe order. The film thickness can be recalculated, averaged, and used to recalculate n, via Eq. (1.4) by rounding off m to its exact integer. The Cauchy dispersion formula can be used to fit $n(\lambda)$:

$$n^2(\lambda) = \frac{E}{\lambda^2} + F,$$ (1.8)

The atomic chemical bonding is an important parameter necessary to determine the correlation between the physical properties and composition of amorphous chalcogenide materials. The structural characterization of these non-crystalline materials is not trivial because the disordered atomic spatial arrangement in amorphous chalcogenides falls somewhere between that of an ideally periodic and a completely random structure. Therefore, the chemical bonding on

atomic scale of amorphous chalcogenides glasses can be described by the different length scales: in the range 2 - 5 Å is defined the short-range order and in the range 5 - 20 Å is defined the medium-range order. Amorphous materials by default do not present long-range order structures, in the range $\geq$ 20 Å [27], however the discovery of the intermediate phase in chalcogenide glasses is noteworthy [109].

The tendency of the chemical bonds to change when exposed to light at a wavelength close to the band edge of the material is known as photosensitivity. The prominent photoinduced phenomena in ChGs are observed because ChGs are regarded as semiconductors with a flexible structure and a band gap of 1-3 eV, in comparison to oxide glasses which have a rigid structure and a wide band gap of 4–9 eV that require intense pulsed lasers for exhibiting these changes. Research streams on photoinduced phenomena in amorphous ChG suggests at least seven distinct effects, including: photocrystallization (or amorphization), photopolymerzation, photodecompozition, photocontraction(or expansion), photovaporization, photodissolution and light-induced changes in local atomic configuration[110].
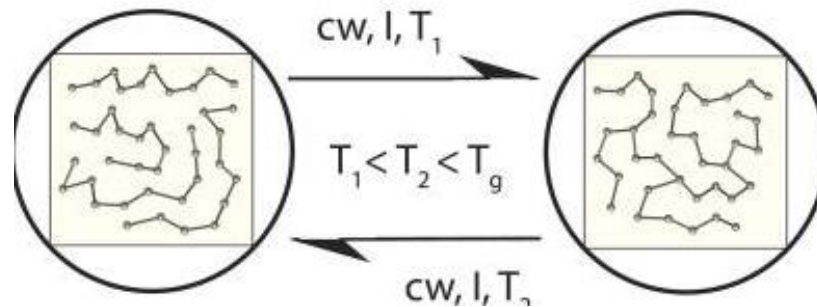
Fig. 1.9. Reversible photo-structural change in a chalcogenide glasses [111].

In [112], K. Tanaka classifies photoinduced phenomena into heat and photon induced, depending on the degree of temperature rise. The heat-mode process represents an optical phase-change occurred when non-radiative recombination of photoexcited carriers triggers atomic structural changes such as transmittance oscillation. The most known heat-mode process may be the phase change between crystalline and amorphous phases, which was first implemented in 1968 by Ovshinsky [113], and now applied to erasable optical memories as digital versatile disks (DVDs). This process is depicted in Fig. 1.9.

The photon-mode process may appear during and after illumination thus can be divided into the transitory and memory phenomena, respectively. The memory phenomena may be bulk effects as photodarkening representing red-shifts of optical absorption edge, or chemical reactions,

such as photodoping, photochemical modification, photo-oxidation. The bulk effects can be irreversible and reversible.
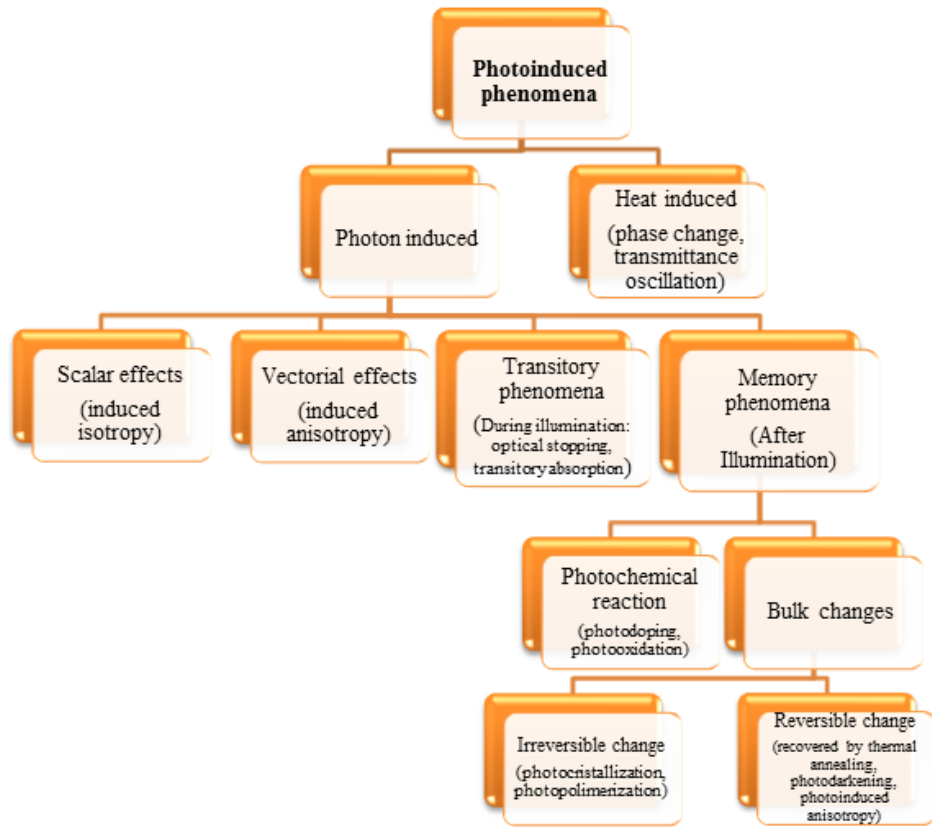
Fig. 1.10. The classification of photoinduced phenomena in amorphous ChGs.

Photo-crystallization and photo-polymerization are considered irreversible changes. When the photoinduced change can be recovered by thermal annealing as for example reversible photodarkening or photoinduced middle gap absorption it is known as reversible change, and it usually appears at glass-transition temperature T_g [114]. Depending on the polarization of the illuminating light source, the photon-mode effects may be scalar or vector when an induced change is isotropic or anisotropic, respectively. The diagram in figure 10 illustrates the classification of photoinduced phenomena.

Many scientists endeavored to develop a model that could explain the mechanism behind photosensitivity on a microscopic level. At the present time, there exist several contradictory models [115-120]. Some researchers believe in the existence of defect centers in ChGs (which are either occupied or empty) to which energy levels in the forbidden gap corresponds [118]. Street and Mott [119] and Kastner et al in article [120] proposed the charged–defect and valence–alternation pairs model for As_2S_3. However, this theory remains unproven. In addition, Tanaka doubts the existence of such centers by providing experimental measurements of ChG in [112].

On the other side, the presence of photo-mid-gap effects in pure materials suggests the existence of mid-gap states. Furthermore, some researchers relate the presence of weak absorption ratio to the impurities despite maximal purity of the ChGs [121,122], while empirical evidence described by Tanaka proves the opposite. To sum up, the principal mechanism that drives the photoinduced effects in ChGs is debatable and not fully understood up to date and further study is necessary.

An interesting review made by Hellmut Fritzsche [123], one of the first researchers that investigated photo-induced transformations in chalcogenide glasses, highlighted two kinds of effects inducing changes in ChGs. The vectorial effect of the first type is fast, repeatable, dynamic, and optically reversible and is supposed to be related to the reconstruction of bistable centres having anisotropic structure. This effect underlies the models proposed by Tikhomirov, Adriaenssens, and Elliott in [124]. For example, dichroism or birefringence can be qualified as vector effects since that depend on the polarization state of the light source [125, 126]. Second type is related to the scalar effect, such as photo-darkening or photo-refraction, which represent photoinduced changes that do not depend on the light polarization [127, 128]. In other words, on a macroscopic level glasses are isotropic even though their atoms are covalently bonded in a locally anisotropic manner due to random orientation and distribution of these anisotropic micro-volumes. The photoinduced changes involve creation of electron– hole pairs, which changes the valence of neighboring atoms and creates coordination defects. The interatomic bonds align with the direction of light polarization and a new network of chemical bonds is formed. On a macroscopic level, this process demonstrates photoinduced material movement [128-133].

1.3 DOEs on azopolymer thin films

The polymers that have -N=N- groups within the polymer structure are called azopolymers. Azopolymers can be classified as main-chain or side-chain depending on the position of the -N=N- groups. Side groups azopolymers can be divided further into polyesters [134], polyamines [135], or various other groups. The unique and striking optical properties of azopolymers have attracted great attention of scientific society.

Synthesis of polymer-containing azobenzenes can be done by two main methods. The direct polymerization of monomers that already contain the azobenzene moiety is the first approach [136,137]. The main advantage of this method is the possibility to control the sequence distribution in the polymer. Chemical modification of the polymers is the second approach. Although it may include multiple steps, one of the main benefits of this method is the commercial availability of the prime materials.

The history of azopolymers begins in 1834, when E. Mitscherlich first described the

azobenzene [138]. Azobenzene is a photoswitchable chemical compound characterized by an azo linkage that connects two phenyl rings. Generally, the term 'azo' is related to the azobenzene structure, though the physical and chemical properties of the azos may change when various substituents are added.
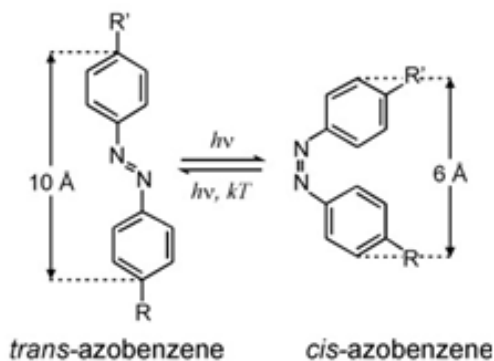
Fig. 1.11. Reaction of *trans-cis* isomerization of azobenzene [140].

After almost one century, in 1937, G. S. Hartley discovered the property of azobenzene to undergo *trans-cis-trans* transitions on illumination in the range between the ultraviolet (UV) and blue part of the electromagnetic spectrum [139]. This property is known as photoisomerization which comprises a decrease in the distance of the para-carbon atoms from about 10 to 6 Å, as shown in Fig.1.11. A fascinating characteristic of azobenzenes is the efficient and completely reversible photoisomerization. It is interesting that by adding different substituents the absorption spectrum can be tailored to have values from the UV ($\lambda=365$ nm) to the visible ($\lambda=570$ nm) region. In *cis* configuration azobenzenes are metastable while in the *trans* state become thermally stable. The absorption of a phonon causes azo chromophore to change from the *trans* to *cis* state. The reversed process or return to the initial state can be achieved via visible light or thermal relaxation which would lead to a transform or a more stable *trans* state, respectively. Nowadays, photoisomerisation and its applicability in the design of functional materials represents the key of azopolymer research [140].

About half a century later, in 1984 T. Todorov et al. discovered the sensibility of azobenzene compounds to the polarization of light. It was determined that the birefringence (Δn) or dichroism (ΔD) can be induced by the action of light at a macroscopic level by a series of *trans-cis-trans* isomerizations cycles when their chromophores reorient perpendicularly to the electric vector of linearly polarized light [141], as shown in Fig.1.12. However, the concept of azopolymers emerged only when it was revealed that the stability and rigidity of the recording can be increased by incorporating the azochromophores in a polymer chain [142].

Efficient formation of a SRG is closely linked to a correct proportion of the azopolymer constituents. In [143] it was proven that the SRG depth is small (<10nm) when an insufficient amount of azo dye was used. Therefore, a high amount of dye (up to 30%) must be incorporated into the polymer [144].
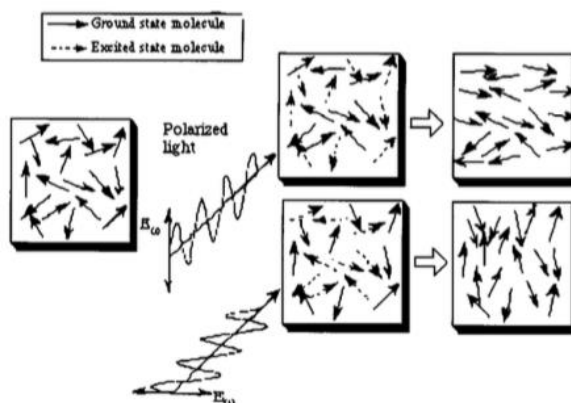
Fig. 1.12. Optical generation of anisotropy. The molecules of azopolymer excited with polarized light tend to align in direction perpendicular to the polarization. [145]

Incorporating azobenzenes into polymers provides certain advantage for the azo moiety as well. In this combination, the azo compound becomes soluble in water, a property it would otherwise not have [146]. Kinetic studies on several azo polymers reveal the effect of the polymer properties on the photochemical and thermal isomerization [147]. Furthermore, these investigations prove that the structural properties of the polymer matrix influence the rate of isomerization of the azo groups which are attached covalently to the polymers [148]. These breakthroughs greatly influenced the development in the area of polarization holography, since it was discovered that azopolymers represent effective media for polarization recording. Among various potential applications of azopolymer films are listed: DOEs with exclusive polarization properties [149–151], surface relief gratings (SRG) [152–154], optical data storage [155,156], or even biological applications [157, 158].

The light-induced azopolymer movements are highly sensitive to the polarization state of the incident light [159]. Weak surface relief displacement is observed when the two interfering waves are S:S polarized. In contrast, P:P polarized and RCP-LCP generate much stronger gratings. An earlier report [160], established that the molecular weight of the azopolymer influences the relative efficiency of the S:S versus P:P geometries. A recent work of Tsutsumi et al. proves that the circular polarization of light utilized in holographic recording systems has a higher response in azopolymer materials if compared to linear polarization of light, as shown in Figure 1.13 [161]. The paper describes the investigations on an azo-carbazole monolithic dye dispersed acrylate

matrix. Particularly, it demonstrated that circular polarization of light produces DOEs that have four times higher diffraction efficiency in comparison with linear polarization, as illustrated in Figure 1.13(b).
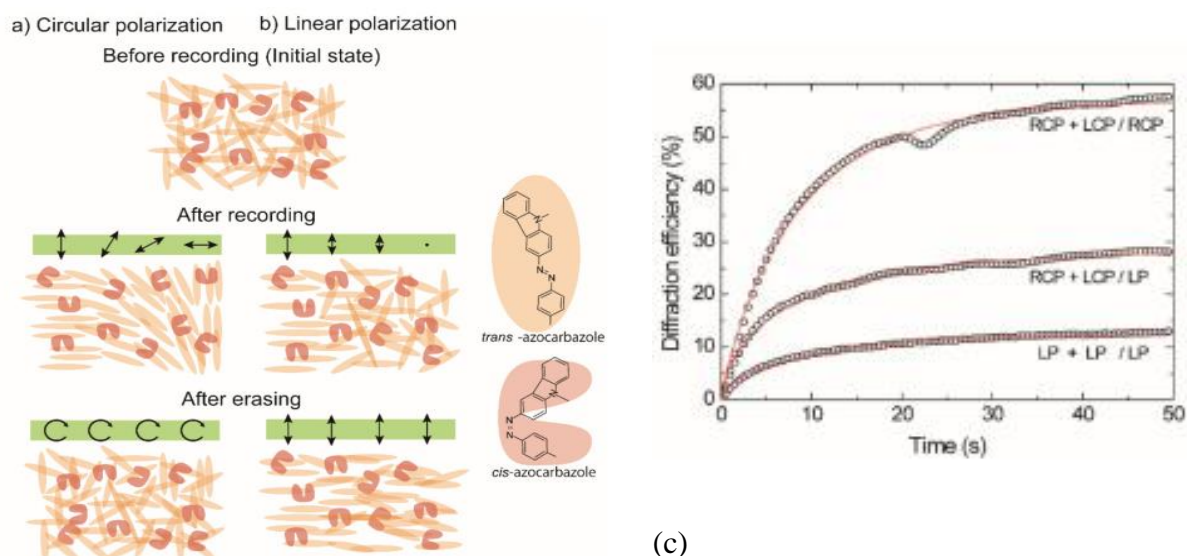
Fig. 1.13. Schematic pictures of morphological change in assembled azo-carbazole molecules during recording. (a) Orthogonal circular polarization recording and (b) parallel linear polarization recording, (c) Diffraction efficiency growth of holographic diffraction grating recorded with orthogonal circularly polarized beams [161].

The in-situ observations of the azopolymer surface topography during the PHR in the s-geometry indicate that due to material photoexpansion the intensity maxima correspond with the peaks of the grating [162,163]. For the p-polarization of the inscribing beams it was demonstrated that the pattern passes a phase shift while the crests migrate from the intensity maxima to the minima.

One of the most intriguing property of azobenzene-containing polymer films is the formation of surface relief patterns upon illumination [164]. The possibility to fabricate periodic microstructures on azopolymer thin films was discovered and described in 1995 [165]. Transmissive and reflective diffraction gratings can be created on azopolymer surface. A transmissive SRG is formed when an optical interference pattern irradiates the azopolymer film. During this one-step process, the material starts to move in order to create a copy of the interference fringes according to the incident illumination as illustrated in Fig. 1.14. As an example, when a thin amorphous azopolymer film is irradiated with an optical interference pattern, the material starts to migrate and move away from high-intensity areas to form a replica of the incident irradiation in the form of a surface-relief grating (SRG), as shown in Fig. 1.14. A reflective grating can be obtained by coating a photo-inscribed pattern with a reflective material [166].
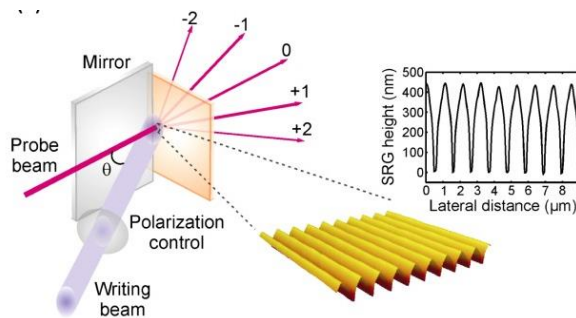
Fig. 1.14. Schematic representation of the SRG recording process. An AFM surface profile measurement of an inscribed grating is shown on the right side [140].

It is a relatively simple procedure that allows the control of the surface topology including the erasure or reconfiguration if needed. The process within the azopolymer material is triggered by the *trans–cis* photoisomerization. The lifetime of the patterns under ordinary storage conditions is several years. The changes on the molecular scale can be related to the photoactuation and photoalignement of azobenzene molecules inside the polymer matrix [167, 168]. As mentioned earlier and illustrated in Fig. 1.13(b) azobenzene molecules change their orientation perpendicular to the direction of the polarization plane of the incident linearly polarized light. Consequently, optical anisotropy can be observed or erased by means of circularly polarized or unpolarized light [164, 169].

It is important to consider the multiple effects that influence the DE values of the patterns inscribed on azopolymer films.
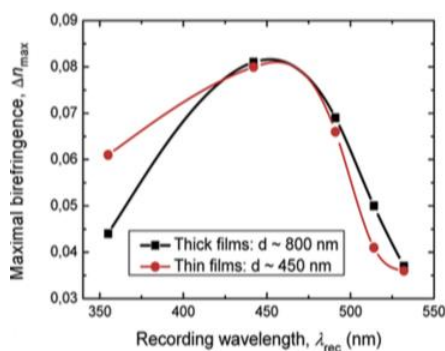
Fig. 1.15. Dependence of the maximal birefringence _Δn_ obtained by a number of the pump laser wavelengths [171].

For instance, bulk reorientation of azobenzene groups in the polymer chains upon exposure produces a birefringence grating which also contributes to the overall DE of the grating [170].

A recent study by N. Nedelcev et al. investigates the dependence of birefringence on the recording wavelength for PAZO – poly[1-[4-(3-carboxy-4- hydroxyphenylazo)benzene sulfon

amido]-1,2-ethanediyl, sodium salt] a commercially available azopolymer shown in Fig. 1.15 [171]. It was observed that a density grating below the film surface can be formed by annealing SRG on an azopolymer [140]. Therefore, for practical applications it is imperative to take into account all the types of gratings.

The great amount of research on photoinduced surface-relief formation has opened up new perspectives of fundamental and applied science by explaining the effect of stable macroscopic changes of the azopolymer below the glass transition temperature. However, until now none of the models accounting for the macroscopic light-induced polymer motions entirely revealed the considerable variations of the azobenzene functionalized polymer systems [173,174]. Current and future photonic applications critically depend on the in-depth understanding of the surface-pattern formation phenomena observed upon illumination with an interference pattern.

1.4 Novelty and contribution of the doctoral thesis

The presented research is of particular interest because it targets a relatively young field and contains research issues that exist internationally. In recent years, there has been an increasing emphasis on the computerization of scientific equipment and devices, and especially the microscope. For the DHM to become competitive with the atomic force microscope (AFM) or electron scanning microscope (ESM), reconstructed results from digital holograms must be viable and the working time with this tool must be reduced. These main requirements depend on the specific experimental constraints, as well as on the reconstruction algorithms and on the knowledge about the physical-electronic processes that take place in the device.

The main problem solved by the DHM technique is the investigation of phase objects that do not absorb or scatter light significantly or transparent objects. Among various techniques used to study phase objects, digital holography stands out through measurements made with nanometer accuracy. The new approach consists in application of DHM for study of optical parameters of DOE. Namely, off-axis and phase-shifting DHM configurations were adopted for the investigation of refractive index and surface relief maps of various DOEs recorded on azopolymers thin films and ChGs nanomultilayers. In addition, other aspect of this approach is that for the improvement and optimization of the optical setup, a liquid crystal variable retarder was integrated in the imaging system of the phase-shifting DHM.

Some new techniques was developed and applied for digital image processing. The algorithm based on SPAR technique was adopted as a noise minimizing approach. The Gaussian noise in the observations (hologram acquisition) was considered. Spatial light modulator (SLM)

39

with appropriate software performed the digital modulation of light was introduced in the DHM optical setup. It is proposed various phase masks, acting as Bessel beam, blazed grating, object adjusted masks, displayed on SLM as adaptive illumination elements for modulating the amplitude and phase of light propagating through the object.

The contribution of this thesis

In the work I present several advances that improve upon this state-of-the art. **First**, in this thesis, the computerization/digitization approach to apply not only processing of digital holograms (software), but to govern of physical experiment (hardware). DHM as a full-field QPI technique is developed and applied for the analysis of refractive index and SR maps of DOEs. For the improvement and optimization of the DHM setup, digital liquid crystal (LC) devices are integrated in the imaging system for increasing the performance of the microscope. Tackling the challenges in 3D imaging by DHM, it is proposed to integrate LC devices into DHM imaging system, making the microscope programmable and customizable with respect to a given sample, thus overcoming the major limitation of current DHM microscopy. Nonetheless, the challenging conditions such as limited resolution of DHM optical setup and meticulous observations of a microscopic sample under study require precise modulation of light. Thus, it is of special interest to perform the digital modulation of light (wavefront shaping operations) by introducing LC devices in the DHM experimental setup and to develop appropriate image processing software for the accurate hologram processing. For this purpose, a numerical algorithm will be developed to process digital image data (holograms), calculate optical phase shifts, and determine the 3D shape of the samples. A major challenge is to perform precise modulation of light. For this purpose, the LC devices are meticulously calibrated.

It is demonstrated the feasibility of the developed DHM for the measurement of refractive index modulation and surface topography of DOEs recorded on azopolymers thin films and ChGs nanomultilayers.

Second, important problem addressed in this thesis is the numerical algorithm for computational reconstruction of the phase of the studied object. Sparse phase and amplitude reconstruction (SPAR) algorithm was applied for minimizing the noise from the phase reconstruction in the off-axis DHM configuration. It is an iterative algorithm based on local least square solution that includes well-known for best filtering data-adaptive block-matching 3D (BM3D) technique to reduce the noise from the observations and maintain high the signal to noise ratio (SNR) [73]. One key advantage of BM3D algorithm is a good ability for noise filtration due to assumption that low dimensional models can be used for phase and amplitude approximations. In order to provide reliable and accurate results for refractive index and relief mapping on

diffraction gratings, and to compensate the distortions of the wavefront that can appear during hologram recording due to the inadequate laboratory conditions (building vibrations, noise, etc.) in the phase-shifting DHM configuration, a special cycle has been developed for the hologram processing algorithm.

Third, the design and development of DOEs is performed via analog and digital PHR on ChGs nanomultilayers and azopolymer thin films. Application of these two approaches allows us to record the DOEs with multifunctional properties. The reconstruction of the phase from a digital hologram maintaining high resolution to provide reliable and accurate results for refractive index and relief mapping on DOEs is the final goal of this work.

Strong suppression of noisy components is enabled by this low dimensionality and the main features of the signals of interest are precisely revealed. The correct combination of the reconstruction technique together with the advanced liquid crystal devices will give rise to a robust instrument for high resolution 3D imaging of innovative optical materials.

2. IMPROVEMENT OF DHM VIA DEVELOPMENT OF COMPUTATIONAL PROCESSING

In the recent years, digital holographic techniques have attracted high interest as a set of full fields, label-free methods for quantitative phase imaging. Development of digital holography (DH) is important for industrial technology and biomedicine, since the surface and the structure of samples can be monitored in real-time from image acquisitions [176-178]. Moreover, advanced optical components, which today are based on emerging computer technologies, can be applied in DH in order to increase the depth of field, resolution, and compensation of aberrations, noises and image distortion introduced by the optical components of the setup (microscope objective, lenses, etc.), which, in turn, require the specific software [179-181]. Besides amplitude and phase imaging (3D imaging) and most importantly the digital wavefront manipulation and quantitative information on thickness and/or height topography of samples are the advantages of computational image reconstruction from digital holograms. Digital holographic imaging with intrinsic high axial resolution has another important advantage in the fact that quantitative imaging of the sample under investigation can be automatically achieved by numerical refocusing of a 2-D hologram acquisition at different object planes. But high axial resolution always simultaneously increases the coherent speckle noise, thus decreasing the quality of the phase reconstruction [72]. The reconstruction of the digital hologram of the object, while maintaining high resolution, and a low signal-to-noise level throughout the object volume is a major challenge.

Digital holographic microscope supplied with the camera combines the high-quality imaging capability of light microscopy and whole-object wavefront recovery and numerical processing capabilities of holography and computers. It is a versatile tool with a huge potential of practical applications in various branches of science and industry including optical metrology, biology, medicine, material science and many others. The main purpose of DHM is the label-free, noninvasive quantitative measurement of the complex amplitude distribution (especially phase information) of the light field in a micro- or hundreds of nanometer scale of transparent samples. This feature is reached by the reference beam, like analog holography, which interferes with the wave that illuminates the object named the object beam. But in digital holography, unlike analog holography, the restoration of a three-dimensional image is carried out by numerical calculations.

Two digital interferometric DHM layouts in transmission mode have been designed and developed for application to nanomultilayed ChG and azopolymer thin films optical studies.

In the **off-axis configuration**, a reference beam, which is introduced into the recording camera plane, is tilted relative to the imaging beam. This configuration is capable of retrieving

whole object wavefront in a single exposure because it is based on the spatial filtering of one of the diffraction orders at the Fourier domain. The single-shot operation is useful for evaluation of, for instance, dynamic processes in live cell imaging, while the influence of external vibrations in the measurements becomes minimized. However, the spectral wide of the reconstructed image is limited due to the overlapping between the different diffraction orders at the Fourier domain. To completely separate of the twin imaging terms from the *dc* term at the Fourier domain, a carrier frequency at least three times the highest spatial frequency of the object wave and a digital sensor bandwidth at least four times the one of the object wave are required. The pixel dimensions of the digital camera define the ratio between the sizes and separation of the different diffraction orders which can yield in significant information loss as a consequence of the space-bandwidth product deterioration.

In-line configuration phase shifting digital holographic microscopy (PS-DHM) has been proposed as an alternative technique that is free from the presence of zero-order and conjugate images. The on-axis interferometric configuration proposes an in-line geometry where the angle between reference and object beams is set to a minimum value close to zero. As a result, the spatial frequency bandwidthof the interferograms becomes narrower, in comparison with the off-axis modality. On-axis methods provide full optimization of the space–bandwidth product up to a maximum achievable resolution imposed by the camera pixel size. Nevertheless, the method requires multiple acquisitions of at least four hologram measurements. In comparison with PS-DHM, the off-axis configuration requires a single acquired hologram, thus allowing dynamic applications despite a lower resolution of the reconstructed wavefront due to the presence of carrier fringes.

Existing solutions for the phase reconstruction improvement of DHM restrict from the dependence of the resolving power on the wavelength and numerical aperture (*NA*) of the microscope objective (MO) described by the Abbe criterion. The spatial resolution of optical imaging systems is established by the diffraction of photons which interfere on image plane.

$NA = $ n·sin(α),

where n is refractive index of the medium between sample and objectiv's front lens and α is the one-half angular aperture of the objective's front lens.

The lateral resolution (resolution in the plane orthogonal to the optical axis) R_{Abbe} given by the Abbe criterion is: $R_{Abbe} = \lambda/2[$n·sin(α)$]$, where λ is wavelength of illumination and as a result $R_{Abbe} = \lambda/2NA$, The axial resolution (resolution along the optical axis) R_{axial} requiring the evaluation of the out of focus image reconstruction can be estimated only approximately and it is: $R_{axial} \approx \lambda/1.4NA^2$. So, when using immersion liquid (n>1), a greater *NA* value can be obtained,

thereby improving the resolution of the objective. The limited *NA* of the microscope restricts the spatial-frequency content of the object arriving at the image plane. Previous attempts to apply a short-wavelength laser (UV range) proved to be destructive and phototoxic for the investigation of biological objects [13]. Other works demonstrated enlarged spatial frequency coverage by creating a synthetic numerical aperture [182,183]. M. Paturzo and P. Ferraro introduced diffraction gratings between the object and the CCD sensor in the lensless DHM setup to augment the NA [184]. Successful integration of spatial light modulators in the DHM optical setup permitted fast and precise operation of the object wavefront for generating the desired structured patterns [44, 184–187].

In this chapter, as a solution for improving the DHM performance, it is proposed the introduction of phase masks in the imaging system of the microscope. A computer simulation of the off-axis and phase-shifting DHM configurations was performed. First, the simulation of the off-axis DHM with a phase mask introduced before the object under study is described. The modulation of the object beam by the phase mask aims to obtain additional information about the object due to the diffraction maximums falling on the camera. A software solution is able to produce high-quality imaging for quite noisy data based on the Sparse Phase and Amplitude Reconstruction (SPAR) algorithm.

A number of modifications have been made to the algorithm according to the features of the experiment and sample under investigation. This algorithm was implemented to ensure of the present noises reduction from the off-axis holograms [73].

The second section/part of this chapter describes the simulation of the phase-shifting DHM with different phase masks introduced in the object arm of the imaging system. The optimal phase mask is determined with its corresponding parameters. The numerical reconstruction algorithm developed for the processing phase-shifting holograms executes the correction of the phase shifts in case of distorted tilt produced during hologram recording. This correction step is important when the real laboratory conditions (inevitable tuning inaccuracy, temperature, mechanical vibrations, etc.) cannot be maintained.

2.1 The off-axis DHM configuration with phase masks

The aim of this study is to demonstrate that a sinusoidal diffraction grating as a phase mask can be successfully applied to lensless digital holographic microscopy for phase reconstruction. Therefore, it is proposed to investigate the influence of sinusoidal phase masks, acting as a modulating element for the light propagating through the object.

For the simplicity of the calculations and reduction of the computational operation time the off-axis lens less DHM is considered with a sinusoidal phase modulation at the object plane. The variational algorithm for phase and amplitude reconstruction is based on the algorithm proposed in the paper [73]. The forward wavefront propagation is modelled using the Fourier transform with the angular spectrum transfer function. The multiple intensities (holograms) recorded by the sensor vary in dependence on the angle of the phase diffraction grating. The independent and identically distributed (i.i.d.) Gaussian noise is added to observations to make them closer to real experimental conditions. The i.i.d. term defines the random variables in signal processing. Specifically, *identically distributed* means that all values in the sample are taken from the same probability distribution and there are no general trends. *Independent* means that the sample values are all independent events. In other words, data about the value of one variable gives no information about the value of the other variable and vice versa. The root mean square error (RMSE) values of the phase reconstructions were compared in two scenarios: with and without the diffraction grating.

In this experiment, the process of digital holographic recording of the wavefront originating from the object with subsequent computer reconstruction of the object's image was modelled. Digital holograms result from the interference between the wave transmitted by the object to be imaged and a plane reference wave in off-axis optical geometry. By placing the diffraction grating (DG) in front of the studied sample, the wavefront reaching the CCD sensor takes in new diffraction orders from the grating. In this case, the digital hologram contains more information about the object if compared to an ordinary holographic system.

The variability of DG features (period, optical phase, number of rotating angles) allows one to adjust the phase modulation for obtaining more accurate results. Furthermore, the flexibility of the numerical reconstruction approach allows one to selectively use the diffraction orders carrying out useful information. This step minimizes the hologram noise. Fig. 2.1 shows the off-axis optical setup operating in transmission mode which is simulated in this section. The computer simulations are performed and executed in MATLAB software. The step-by-step computational procedure implemented for recording off-axis holograms with the object wavefront modulated by the phase mask is presented in Fig. 2.2. The laser beam is split by the beam splitter BS into the reference wave and object wave that illuminates the sample under study.
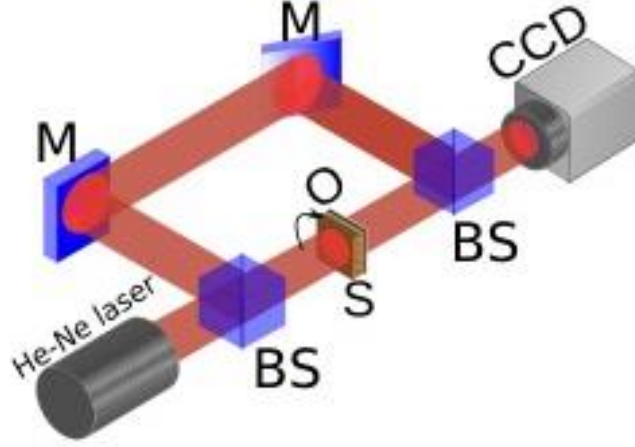
Fig. 2.1. Scheme of the simulated off-axis DHM setup in Mach-Zehnder configuration. He-Ne laser, $\lambda = 633\ nm$, M-mirror, BS-beam splitter, S-sinusoidal DG, O-object. The arrow close to S shows the axial rotation of the DG.

A plane wave was used as the reference source. The center of the CCD sensor is set at the origin of the rectangular coordinate system.Consider a plane reference wave $u_R(x,y) = A_r \exp(j\varphi_r)$, and an object wave $u_o(x,y) = B_0 \exp(j\varphi_0)$. The hologram intensity recorded by the CCD camera is given as:

$$H(x,y) = |u_O(x,y) + u_R(x,y)|^2 = |B_0 \exp(j\varphi_0) + A_r \exp(j\varphi_r)|^2 =$$
$$= B_0^2 + A_r^2 + A_r(\exp(j(\varphi_0 - \varphi_r)) + \exp(-j(\varphi_0 - \varphi_r))), \tag{2.1}$$

where B_0, A_0 are their amplitudes and φ_0, φ_r are phases of the object and reference wavefronts, respectively. Similarly, it can be expressed by

$$H(x,y) = |I_O(x,y)|^2 + |I_R(x,y)|^2 + u_O(x,y)u_R^*(x,y) + u_O^*(x,y)u_R(x,y), \tag{2.2}$$

where I_O, I_R are intensities of the object and reference wavefronts, respectively and * denotes the complex conjugate amplitude. The real and twin image fields are presented by symbols $u_O(x)\ u_R^*(x)\ and\ u_O^*(x)\ u_{R_R}^*(x)$, respectively.

For a correct numerical simulation, it is important to consider the magnification of all DHM optical components including the microscope objective and the lens. The total magnification of the microscope is given by

$$M = \frac{f_L}{f_{MO}}, \tag{2.3}$$

where f_L, f_{MO} represent the focal distance of the lens and the MO, respectively. For a lens less setup M=1.
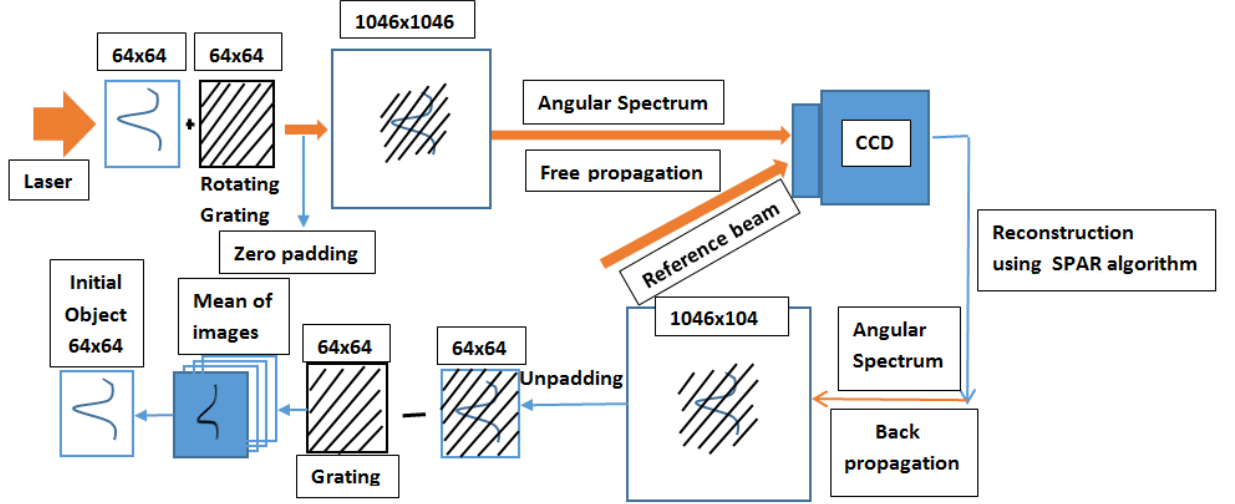
Fig. 2.2. Stages of the MATLAB simulation including off-axis hologram recording and phase reconstruction.

The ***complex-valued object beam*** in the DHM imaging system can be expressed by the convolution between the geometrical image representation of the sample and the point spread function produced by optical systems. The numerical simulation of the complex-valued object wavefront is produced by computing the convolution process between the geometrical optics image prediction and the point spread function produced by the diffraction phenomena:

$$u_O(x,y) = u_{OS}(x,y) \otimes \tilde{g}\left(\frac{x}{\lambda}, \frac{y}{\lambda}\right), \qquad (2.4)$$

where u_{OS} is the complex wavefront at the sample plane and $\tilde{g}\left(\frac{x}{\lambda}, \frac{y}{\lambda}\right)$ is the Fraunhoffer diffraction pattern of the microscope. The first term in equation (2.4) stands for the geometrical estimation of the sample, while the second term denotes the point spread function generated by the optical setup due to diffraction phenomena. The second term can be expressed by

$$\tilde{g}\left(\frac{x}{\lambda}, \frac{y}{\lambda}\right) = \iint_{-\infty}^{\infty} A(x'y') exp\left[-j\frac{2\pi}{\lambda}(x'x + y'y)\right] dx'dy', \qquad (2.5)$$

where $A(x'y')$ is the aperture function of the microscope representing the influence of the optical components of the imaging system on the transmitted light.

Numerical simulation allows the possibility of modelling different geometrical images of the complex wavefront at the object plane. In this simulation, the pure phase object is represented by a Gaussian beam that is coded by the following analytical expression

$$u_{GS}(x,y) = B_{GS} \exp(j\varphi_s), \qquad (2.6)$$

where $B_{GS} = 1$ is the invariant amplitude and $\varphi_s = \pi$ the given phase representing the transmission object, which can be the product of the topography and the refractive index. The numerical algorithm of the described the simulation is shown in Annex 1.

Theoretically, the digital hologram $H(k, l)$ is an array of $R \times P$ 8-bit-encoded numbers that results from the two-dimensional sampling of $H(x, y)$ by the CCD camera [188]:

$$H(k, l) = I_H(x, y) rect\left(\frac{x}{L}, \frac{y}{L}\right) \times \sum_{k=-N/2}^{R/2} \sum_{l=-R/2}^{R/2} \delta(x - k\Delta x, y - l\Delta y), \quad (2.7)$$

where $\Delta = 2.2$ μm is the pixel pitch of CCD camera, $R = 2592$ pixel and $P = 1944$ pixel present the number of CCD pixels along the X and Y axes of the sensor plane, k and l are integers, $L \times L = 4.85mm \times 4.85\ mm$ is the area of the sensitive chip, and Δx, Δy defines the sampling intervals in the hologram plane (pixel size) $\Delta x = L/N$, $\Delta y = L/R$. The digital hologram is discretized by the CCD in such a way that the size of the pixels at the sensor plane $\Delta R' \times \Delta P'$ is expressed by the discretization of the sample plane via the geometrical magnification of imaging system M [188]:

$$\Delta R' \times \Delta P' = \frac{\Delta R}{M} \times \frac{\Delta P}{M}. \quad (2.8)$$

In our experiments M=1.The field-of view of the computed DHM's image is calculated by

$$FOV_x \times FOV_y = \frac{R\Delta R}{M} \times \frac{P\Delta P}{M}. \quad , \quad (2.9)$$

where FOV_x, FOV_y represent the available field-of-view along X and Y-axis, respectively. In this experiment, the FOV of the DHM system corresponds to the FOV of the CCD camera due to the lensless setup. In our experiment the size of the image at the sensor plane is zero-padded, as shown further.
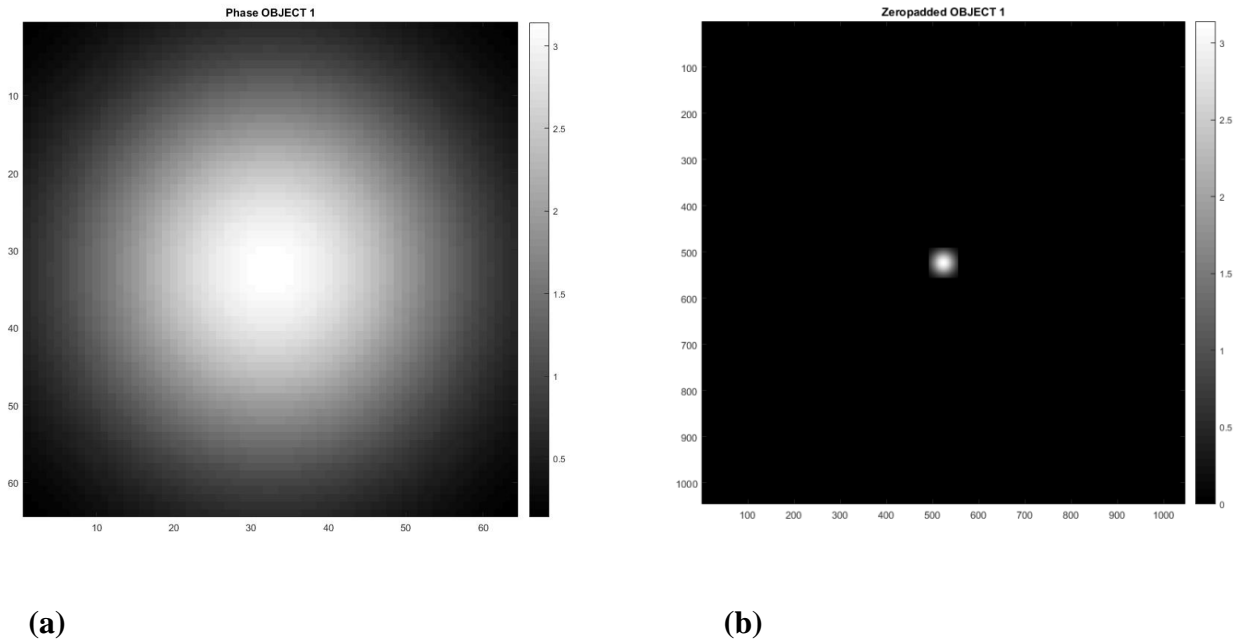

(a)   (b)

Fig. 2.3. 2D Gaussian intensity distribution of the object, zero-padded object

Zero-padding is another important step which presumes that the recorded hologram is numerically extended by adding pixels of zero intensity to it as shown in Fig. 2.3(a). It is important because when the phase reconstruction algorithm processes the pixels on the borders of an image, some of the elements of the masking block or filter kernel may not overlap actual image pixels. For example, if the kernel (small matrix) is 64-by-64 and you are computing the result for a pixel on the top row of the image, some of the elements of the kernel are outside the border of the image. The computational matrix overlaps pixels outside the original image, but the center pixel overlaps a pixel in image. The result is included in the output matrix if the shape parameter is the same or full. So, for an accurate result the initial image is zero-padded from 64x64 to 1046x1046. Fig. 2.3(a) shows the given object and Fig. 2.3(b) the zero-padded object.

Knowing the set distance from the object to CCD sensor $z_{max} = 0,008\,m$, the pixel *computational* size of the CCD pixel $\Delta_c = 2,2 \cdot 10^{-6} m$ and the wavelength λ=0.633nm, the size of zero-padd can be determined by a formula from [72]:

$$z \le z_{max} = \frac{N\Delta_c^2}{\lambda} \rightarrow N = \frac{z\lambda}{\Delta_c^2} = 1046 . \tag{2.10}$$

A object is discretized by computational pixels $\Delta_c \times \Delta_c$. This discretization is necessary both for digital data processing as well as for modeling of wavefront propagation and image formation. N defines the $N \times N$ computational support of zeropadded object and sensor, with the computational apertures size $N\Delta_c \times N\Delta_c$. The key step in the numerical simulation of the complex-valued object wave is the computation of the diffraction effects constituted by the impulse response of the DHM. According to equation (2.5), the Fraunhoffer diffraction pattern of the aperture function represents the impulse response of the imaging system. This step ensures the precise evaluation of the overall performance of the DHM including the resolution or any possible optical aberrations of the instrument by accounting for the complex-valued shape of the aperture function.

The ***computed complex-valued reference beam*** includes both the amplitude and the phase of the wave $u_R(x, y) = A_r \exp(j\varphi_r)$. The control of the waves' amplitude allows the simulation of different types of wavefronts, such as plane or spherical. In our experiment, a plane wavefront which implies constant amplitude of the beam $A_r = 1$ is set.
The phase of the modeled plane reference wave is given by

$$\varphi_r = \frac{2\pi\Delta}{\lambda}(x \sin\alpha_x + y \sin\alpha_y), \tag{2.11}$$

where α_x, α_y the angles between the object and reference beams with respect to the optical axis Z, (x,y) are the coordinates in the sensor plane and Δ= 2.2 μm is the pixel pitch.

49

The wave vector of the plane reference wave is given by

$$w_k = \frac{2\pi}{\lambda(\cos\alpha U_x + \cos\beta U_y)}, \tag{2.12}$$

where U_x and U_y are the unit vectors along X and Y-axes.

In the simulated off-axis DHM configuration the $\alpha \neq 0$ and $\beta \neq 0$, and must be set according to the sampling theorem.

The fulfillment of the **sampling theorem** is one of the essential prerequisites for the recording of digital holograms by CCD arrays. This condition presumes that it is necessary to have at least two-sampled points for each interference fringe. Thus, the digital hologram is set as the amplitude superposition of two plane waves producing the interference image with the period given by $\Delta x = \frac{\lambda}{2\sin\alpha/2}$ and $\Delta y = \frac{\lambda}{2\sin\beta/2}$ along the X and Y-axes of the CCD image plane. The maximum values of the angles defining the wave vector of the reference beam are calculated by

$$\alpha_{max} = \frac{\lambda}{2\Delta N} \text{ and } \beta_{max} = \frac{\lambda}{2\Delta P}, \tag{2.13}$$

This means that the period of the interference line or fringe should be greater than 2Δ (Δ standing for the CCD camera pixel pitch).

Another important prerequisite for off-axis digital hologram simulation is an optimized **space bandwidth**. This precondition arises from the fact that the DC diffraction order has to be separated from the **+1 and -1 diffraction orders,** which encode sample information. For the purpose of separation, a suitable angle of the wave vector (angle between the reference and object waves) is required. A detailed investigation of the influence of the design of the optical arrangement on the size of the space bandwidth was reported in [189]. The space bandwidth must fit the all the diffraction orders that compose the Fourier spectrum of the hologram. It is considered that the space bandwidth is square by setting an equal numbers of identical CCD camera pixels. In consequence, the wave vector has equal angles with respect to the X and Y-axes.

Previous investigations [189, 190] numerically demonstrated the value ratio of the NA and the MO magnification must complete the separation of first orders from DC and for a square digital sensor, the following condition must be satisfied:

$$\frac{NA}{M} \leq \frac{2\sqrt{2}\pi}{3}\sin\phi, \tag{2.14}$$

when $\alpha = \beta = \phi$, where ϕ the maximum angle between the object and reference beam in the off-axis configuration. Nyquist requirements dictate the maximum angle, ϕ_{max}, that can exist between the reference and the object waves when the camera's square pixel size is ΔN, $\phi_{max} = \lambda/2\Delta N$.

Again, as a lens less setup is considered, M=1. By combining last equation and with (2.14) the interbeam angle is obtained that fulfills both the sampling theorem and optimized space bandwidth conditions

$$\sin^{-1}\left(\frac{3}{2\sqrt{2}\pi}\frac{NA}{M}\right) \leq \phi \leq \frac{\lambda}{2\Delta N}, \tag{2.15}$$

When the Eqs. (2.13) and (2.14) are applied, there is sufficient space bandwidth in the Fourier domain for filtering the +1 and −1 diffraction orders without losing spatial frequencies or introducing noise from the DC diffraction order. Also, in this case the DHM operating in transmission mode is considered diffraction limited.

The *simulated hologram* of the Gaussian beam (the object under study) is shown in Fig. 2.4. In the simulated setup it is assumed that the recorded hologram contains noise, similar to real experimental conditions. The intensity Y with noise in the observations is defined by

$$Y = H(x, y) + \sigma\varepsilon, \tag{2.16}$$

where ε is the identically distributed zero-mean Gaussian noise, the plagued Gaussian noise level was set at 5 % from the hologram intensity, σ denotes the standard deviation of the noise and is equal to 5. Gaussian noise is a common term in signal processing indicating a type of noise that takes Gaussian-distributed values. Namely, it is the noise that has a probability density function equal to that of the normal distribution.

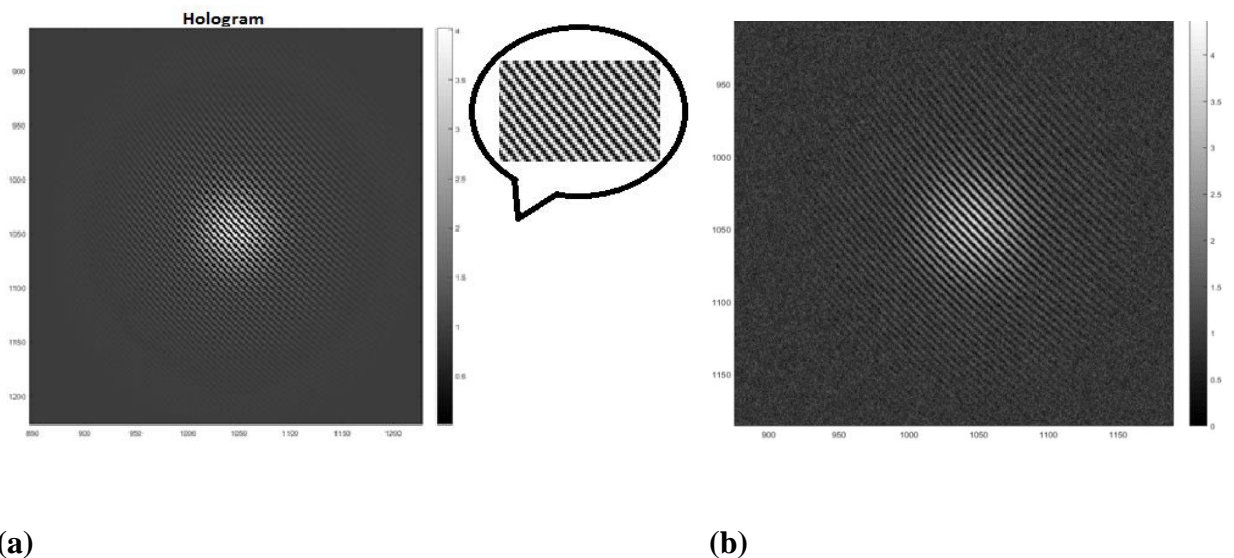(a)   (b)

Fig. 2.4. The simulated digital hologram of the Gaussian beam and the zoomed interference fringes (inset).

In digital images, Gaussian noise occurs during acquisition and is mainly caused by the sensor and electronic circuit noise due to poor illumination, temperature, and optical

transmission [191]. The noise is given by a random array, and to add the same noise to all the simulated experiments, the MATLAB seed function is introduced and included in a loop. An image plane digital hologram is produced when the computed complex-valued object wavefront is superimposed with a reference wavefront in the image plane of the imaging system. The propagation of any wave can be performed using the angular spectrum, Fresnel transform, or Fresnel–Bluestein method. In the present work, Angular Spectrum algorithm was utilized for this purpose, which is described in [72] and given by

$$u(x, y, d) = \kappa \mathcal{F}^{-1} \left\{ H(f_x f_y, z) \cdot \mathcal{F}\{u_0(x, y, 0)\} \right\}, \tag{2.17}$$

$$H(f_x, f_y, z) = \begin{cases} exp\left[i\frac{2\pi}{\lambda}d\sqrt{1 - \lambda^2(f_x{}^2 + f_y{}^2)}\right], f_x{}^2 + f_y{}^2 \leq \frac{1}{\lambda^2}, \\ 0 \end{cases} \tag{2.18}$$

where $u_0(x, y, 0)$ is the initial object plane, which propagates the distance d to achieve the CCD array. The operators $\mathcal{F}^{-1}$, $\mathcal{F}$ are the Fourier and inverse Fourier transforms, $H(f_x, f_y, z)$ is the Angular Spectrum transfer functions depending on the spatial frequencies f_x, f_y and the wavelength λ. 0, otherwise, in 2.18 must be

For processing the off-axis holograms, the Fourier transform method of interference pattern analysis was adapted for the DHM measurements. In the initial step of numerical reconstruction, the first order component of the FT corresponding to $B_0 \exp(j\varphi_0)$ is extracted. The next step involves the inverse FT of this component. Thereafter, the phase $\varphi_O - \varphi_R$ is calculated and the object phase φ_O is reconstructed with the condition that the reference phase φ_R is preliminary known. After the estimate of φ_O is FT filtered, the final estimate is obtained. Taking this into consideration, FT filtering reconstructs the object phase φ_O and furthermore suppresses the noise. The reconstructed complex-valued object wave $u_O(x, y)$ allows us to compute the phase of the Gaussian beam φ_O (object under study) taken as the image sample:

$$\varphi_O(x, y) = \tan^{-1} \frac{Im\{u_O(x,y)\}}{Re\{u_O(x,y)\}} \tag{2.19}$$

For modeling the next steps of the proposed experiment and finding the optimal parameters of the modulated object beam by RMSE criteria, it is important first to reconstruct the object phase. The main off-axis reconstruction approaches include FT, adjustable magnification methods, Fresnel transform (Fresnel-Bluestein transform, Fresnel decomposition), convolution-based methods (digital quadratic lens method), iterative local least square method [192]. The choice of the reconstruction method is driven by the hologram recording conditions. For instance, when dealing with far and extended objects, the single-FFT algorithm will be the most appropriate,

whereas convolution approaches will be suited for the reconstruction of small objects located near the sensor array.

For our purposes, the iterative Sparse Phase and Amplitude Reconstruction (SPAR) technique recently developed for wavefront reconstruction as most efficient for noise suppression [73] is used. The details of the SPAR algorithm are described in the next section.

2.1.1 SPAR algorithm for phase reconstruction of the hologram

SPAR technique is a new algorithm based on the sparse modeling of the object amplitude and phase as functions of the coordinates (x, y). The use of the method makes it possible to significantly reduce the time of matrix calculations and noise suppression due to the assumptions used. The sparsity hypothesis assumes that there are basic functions ("atoms") such that both phase and amplitude can be well approximated by series of small number of these functions. Conceptually, the sparsity is a consequence of the self-similarity of images, what means that it is quite possible to find in them many similar patches in different locations. For sparse modeling of phase and amplitude the non-local block-matching technique is implemented in SPAR. It includes the grouping of similar patches, their joint analysis, synthesis, and filtering [73]. These procedures are produced in parallel for phase and amplitude images.

The SPAR algorithm combines two different ideas: the local least square solution for Gaussian noise in the observations and the sparse modelling of phase and amplitude. The SPAR algorithm is derived from the variational formulation of phase/amplitude reconstruction and in this way, provides the optimal phase/amplitude estimates from noisy observation. The noise suppression in this algorithm is essentially based on the used sparsificafion of the phase and amplitude representations. Furthermore, SPAR is quite efficient for the phase and amplitude reconstruction from off-axis holograms. The robustness of this algorithm with respect to noise is important for the problem considered in DHM. It is because the standard Fourier transform-based techniques do not distinguish between the nature of the small details of the hologram and high frequencies noise.

The key idea of this approach is to minimize the deviation of the estimate from the measurements by optimizing the loss function. From mathematical optimization a loss function represents the error function. The SPAR algorithm for phase reconstruction from digital holograms is shown in Annex 2.

The off-axis hologram is the interference pattern I of the object $u_o = B_o\ exp(j\varphi_o)$ and reference $u_r = A_r\ exp(j\varphi_r)$ wavefronts, registered in the sensor plane as $I = |u_o = B_o\ exp(j\varphi_o) + u_r = A_r\ exp(j\varphi_r)|$. In

case of plane reference wavefront the reference phase φ_r can be wrote as $\varphi_r = 2\pi(x \sin \alpha_x + y \sin \alpha_y)/\lambda$,

where α_x and α_y are angles of the reference beam plane with respect to the optical axis $z(x, y)$ are coordinates in the sensor plane.

Following [73] auxiliary variables U and Z are introduced:

$$U = |B_0|^2 + |A_r|^2 \text{ and } Z = u_0 A_r, \tag{2.20}$$

In this way, the recorded hologram intensity I, which originally quadratic with respect to the amplitudes B_0 and A_r becomes linear function on the new variables U and Z. The intensity of interference pattern in the sensor plane can be rewritten in the new variables as

$$I = U + (V^*Z + Z^*V), \tag{2.21}$$
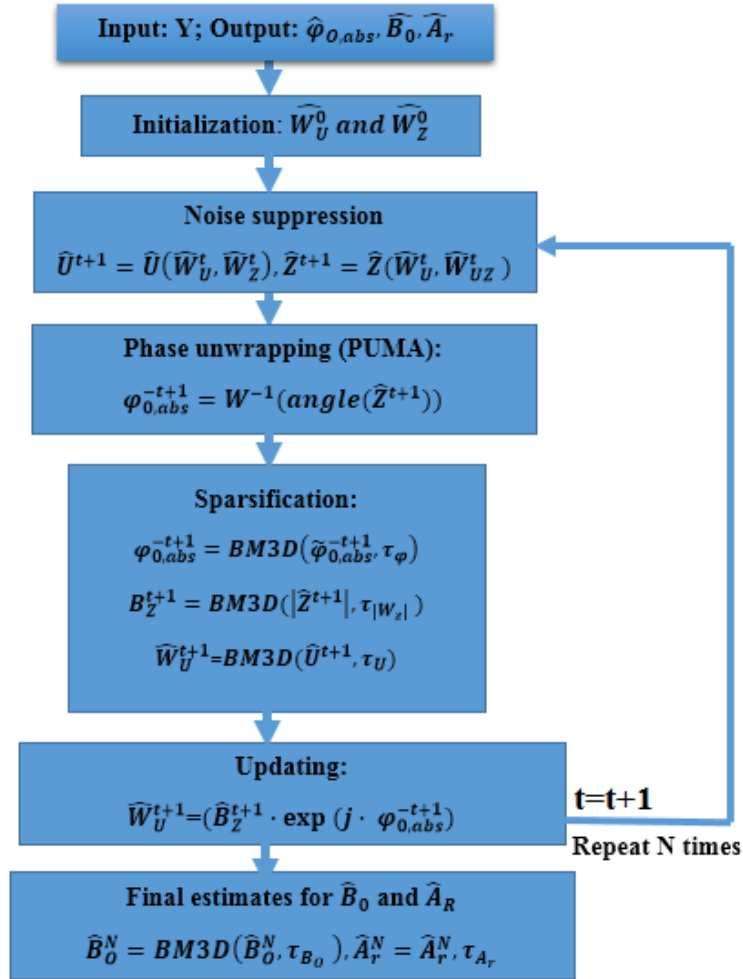
where $V = \exp(j\varphi_r)$.

Fig. 2.5. The block-scheme of the SPAR algorithm for off-axis hologram processing [73]

The amplitude A_r is computed according to the formula from [192]

$$A_r = \left(\frac{U \pm \sqrt{U^2 - 4|Z|^2}}{2}\right)^{1/2}, \tag{2.22}$$

where the plus symbol is used for condition $|u_0| < A_r$ and the minus one for $|u_0| > A_r$. Then the following equation is obtained

$$u_0 = Z/A_r. \tag{2.23}$$

The technique is based on the assumption that the variables B_0, φ_0, A_r are invariant in a small neighborhood x_m of each m -th pixel of the observations and the criterion is of the least square form

$$J_m = \sum_{q \in X_m} w(q)[Y(q) - I]^2, \tag{2.24}$$

where $w(q), \sum_{q \in X_m} w(q) = 1$, is a weight function applied to the variables in the neighborhood of x_m given in the form as presented in Fig. 2.5.

Since SPAR technique is based on multiple estimates:

$$J_m = \sum_{t \in X_m} w(t)[Y(t) - (U + (V^*(t)Z + Z^*V(t))]^2 \tag{2.25}$$

A set of non-symmetric windows (weight functions) different by size and direction are included in the approach. The block-scheme of the algorithm is presented in Fig.2.5 with the next steps.

1. The algorithm is initialized by W_U^0 and W_Z^0, which are the estimates of U and Z for the windowed point-wise least square approximation of the noisy observations.

2. The second step is the phase unwrapping max-flow (PUMA) algorithm. PUMA algorithm described in [193], where W^{-1} defines the unwrapping operation. The algorithm solves integer optimization problem by computing a sequence of binary optimizations. PUMA syntax in MATLAB can be seen in Annex 2.

3. In the third step the sparsity assumption is imposed on the $B_0, \boldsymbol{\varphi_O}$ amplitude and phase of the object wavefront and A_r amplitude of the reference wavefront.

4. The last step of the algorithm an applied nonlocal Block-Matching and 3D (BM3D) filter is computed for the final estimates of the algorithm. The BM3D algorithm is a powerful image denoising method showing state-of-the-art denoising performance. For microscopic investigations, it is especially important to minimize the noise but to preserve important image details. This is possible due to filtering in 3D transform domain by combining sliding-window transform processing with block-matching and by applying a shrinkage operator (e.g. hard thresholding or Wiener filtering) on the transform coefficients. The image blocks are processed in a sliding manner so that blocks that exhibit similarity are matched together to form a 3D array. The high correlation induced along the dimension of the image array is operated by applying a 3D decorrelating unitary transform which produces a sparse representation of the true signal in 3D transform domain. The final

estimate is the weighted average of all matching local block-estimates. Consequently, during the matching process the artifacts are blocked and the estimation ability is improved [72, 21].

Contrary to the Fourier transform methods, the SPAR approach allows one to use full power of the hologram (in Fourier domain it means the use of all orders of the hologram). That is the principal advantage of the variational approach which could potentially guarantee a better accuracy and a better resolution of imaging. According to Abbe, as more diffraction maximums are accepted by the camera, more resolution will be distinguished.

The criterion (2.25) is highly nonlinear with respect to unknown quantities B_0, φ_0, A_r but with introduced auxiliary variables V and Z, the variational problem becomes much simpler [194]. For the experimental conditions presented here several modifications have been made. In contrast to the original algorithm described in [73] a plane and a spherical wavefront was incorporated in (2.25). Additionally, for an accurate reconstruction the optimal values of the window size and direction which essentially uses confidence intervals for the point-wise estimates are determined. For this purpose, a for loop with two conditions was created.

For estimating the performance of the simulated off-axis DHM setup, the root mean squared error (RMSE) is utilized as an appropriate general-purpose error metric for numerical predictions. The RMSE value is calculated by

$$\text{RMSE} = \sqrt{\frac{1}{n}\sum_{j=1}^{n}(y_j - \hat{y}_j)^2}, \tag{2.26}$$

where $\mathbf{y_j}$ are the pixels of the original hologram image and $\hat{y}_j$ are pixels of the reconstructed image In Fig. 2.6 is shown the dependence of RMSE on the widow size and window sigma.
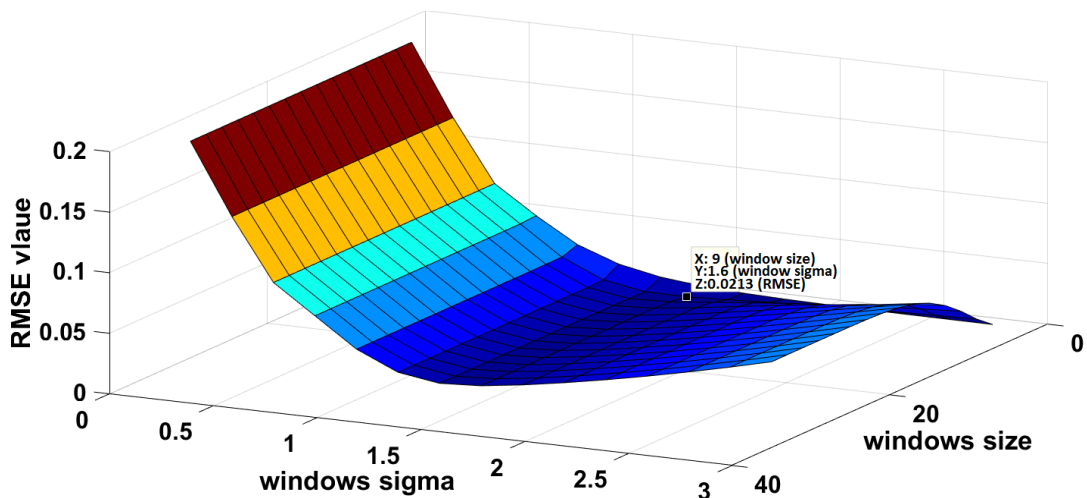

Fig. 2.6. RMSE value dependence on windows sigma and windows size

From Fig. 2.6 can be seen that the optimal value of the windows size constitutes 9-by-9 pixels and windows sigma is 1.6. The window size dimensions 9-by-9 means the calculation of 9×9 = 81 equations in a minimization problem for each pixel. It determines the region (square) for the reconstruction around the pixel of interest.

2.1.2 Simulation and optimization of the phase mask parameters

The applied phase mask is computed using a sinusoidal function with the following parameters: period Λ and phase modulation $\Delta\varphi$ and the rotation angle between two consecutive positions of the grating is denoted by θ. For the modeled setup are found the optimal parameters of the grating: period, phase and number of rotating steps (angles of DG). Period and phase of the grating were selected by visually analyzing the CCD camera images. The optimal number of rotating steps n was selected in regard to the RMSE criterion. Simulation of the diffraction process was performed by computing the propagation of a complex wave through a rotating DG and the object to the sensor plane, which was done using Fourier transform of images and Angular Spectrum (AS) as transfer function (Eqs. 2.17, 2.18). The light generated from a laser with $\lambda = 633\ nm$ was propagated through the DG and the object and projected on CCD camera with pixel sizes of 2.2µm x2.2µm. The sinusoidal phase modulation was introduced by rotation of the DG over 180 degrees with a step of one degree.
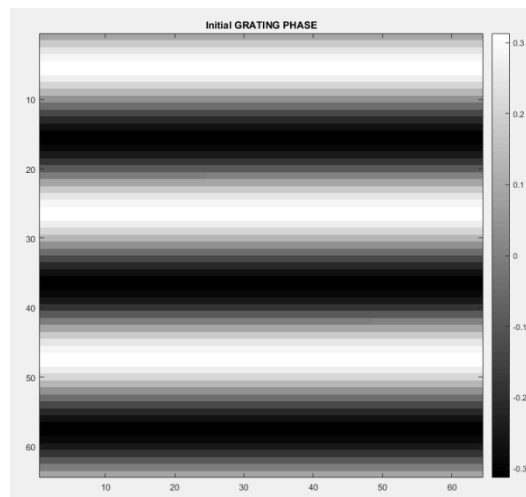
Fig.2.7. The computed sinusoidal DG as a phase mask.

The reference beam as a planar wavefront was used with constant amplitude A_{ref} and flat phase φ_r in the form $I_{ref} = A_{ref} \cdot e^{i\varphi_r}$ The phase grating is defined by the formula

$$G = exp[i\Delta\varphi(1 + \sin\left(\frac{2\pi\sin\theta}{\Lambda} + \frac{2\pi\cos\theta}{\Lambda}\right))] \tag{2.27}$$

where θ - the rotation angle between two consecutive positions of grating, $\Delta\varphi$ – the phase modulation of the grating, Λ - the grating period.

(a)   (b)
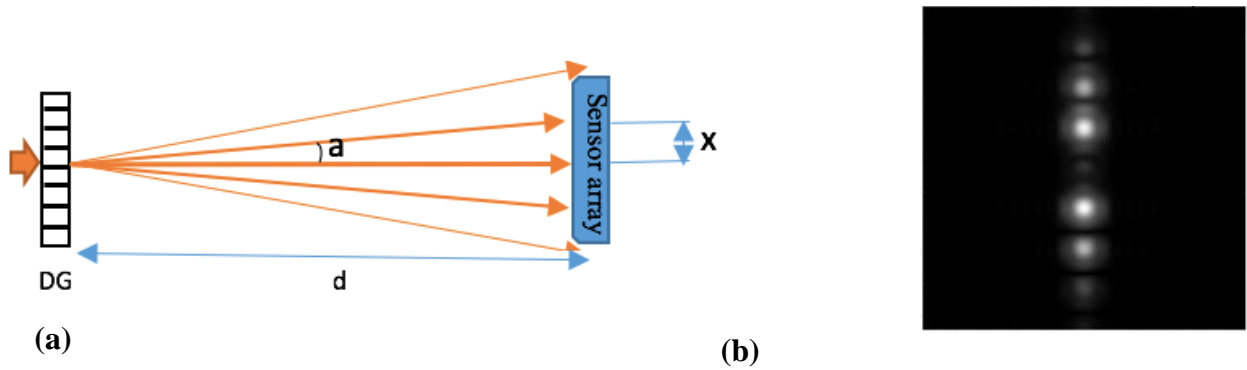
Fig. 2.8. (a) Propagation of grating diffraction orders to the CCD camera sensor, d-propagation distance, a-angle between the diffraction order, x-distance between zero and the first diffraction order. (b) CCD camera image of the propagated light through the DG.

In order for all 1st diffraction orders to reach the CCD sensor, the period Λ, the distance between the camera DG d, and the wavelength λ are taken into account.

First, the optimal period Λ of DG where the Ist diffraction orders fall the sensor array is determined (Fig.2.7):

$$\Lambda = \frac{m\lambda}{\sin\alpha} \sim 44\mu m, \tag{2.28}$$

where $\lambda = 633nm$ is the wavelength, $\alpha=0.82°$, d=4 cm, m=1 is the diffraction order. The diffraction order position on the sensor depends not only on the period of the DG but also on its phase properties. The computed features of initial phase grating is shown in Fig. 2.7.
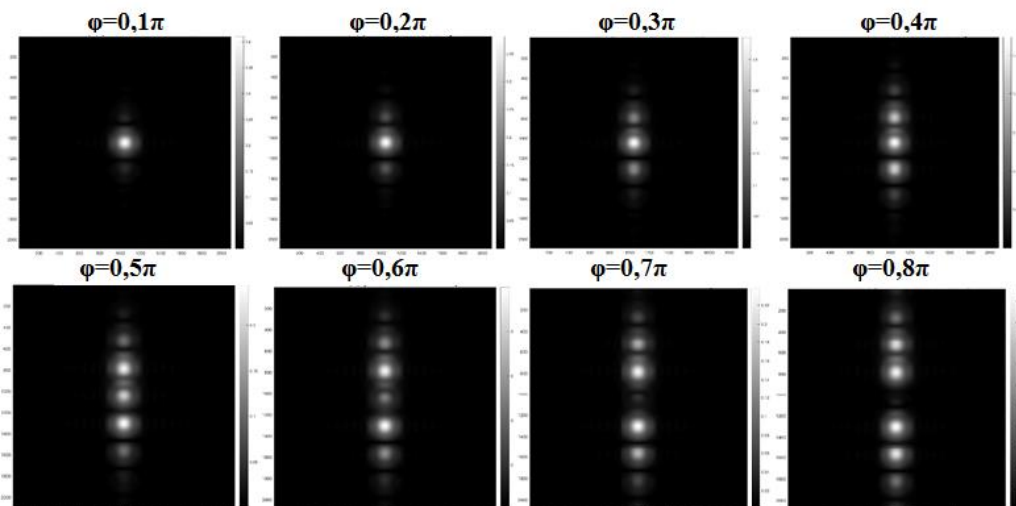
Fig. 2.9. Propagation to CCD of grating diffraction orders for some values of the DG phase

Finding the optimal phase for a better reconstruction after grating rotation is important because an erroneous phase shift may bring to superimposing of DG orders. The best DG phase

58

was found by visually analyzing the CCD camera images of the propagation of the wavefront after the grating Fig. 2.9.
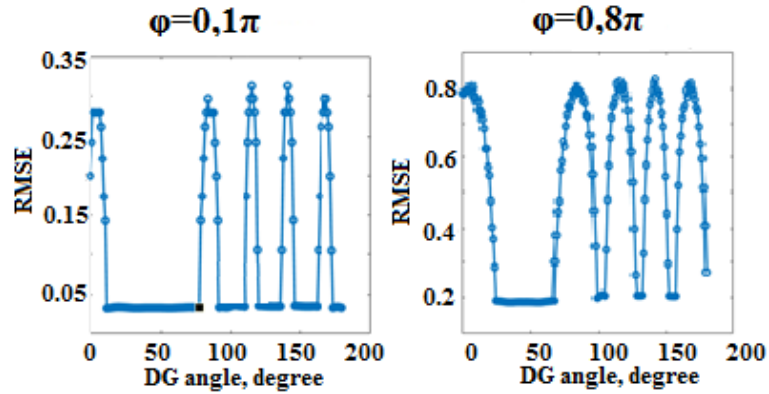
Fig. 2.10. RMSE dependence for different angles and phases of diffraction grating

The optimal value of the DG phase modulation was determined to be $\varphi = 0.1\pi$. It can be seen that the superimposing of diffraction orders starts at $\varphi=0{,}7\pi$ (Fig. 2.9).
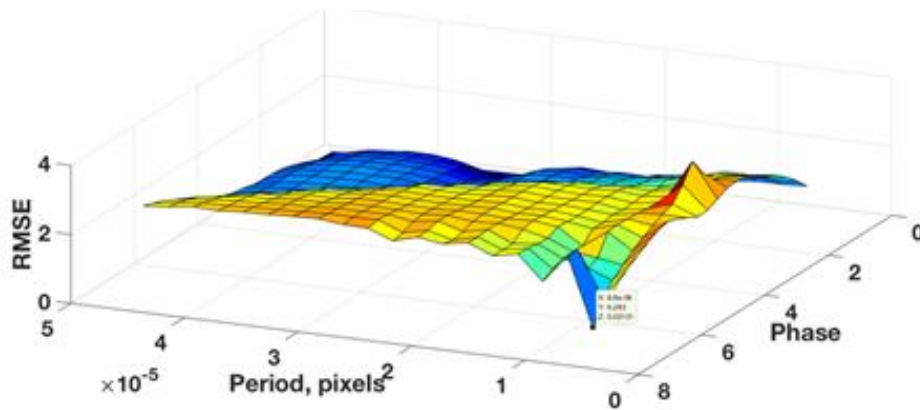
Fig. 2.11. RMSE dependence on grating phase and period. The angle is equal to 90°.

For simultaneous estimation of the optimal period and phase for the phase grating used in the experiment, a for loop with two conditions was created for plotting the dependence of RMSE on the phase and period of the phase grating shown in Fig. 2.11.
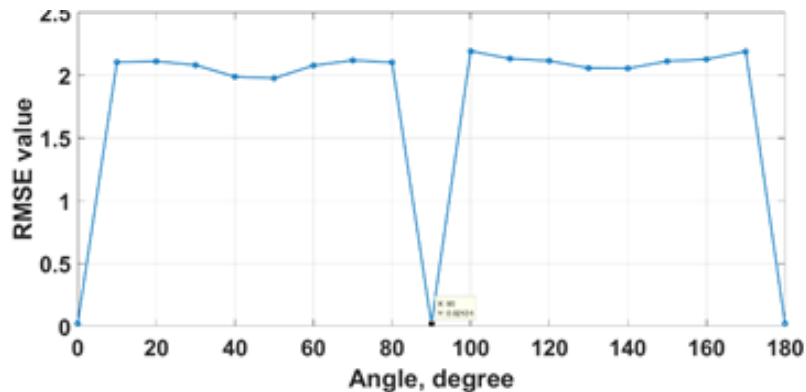
Fig. 2.12. Dependence of RMSE on gratings rotation angle for determining the optimal values of period and phase.

The RMSE is calculated for different angles of the DG with respect to the optical axis of the setup from 1 to 180^0 for $\varphi=0,1\pi$ to $0,8\pi$. The obtained results are shown in Fig. 2. 10.

Next, the dependence of RMSE on gratings rotation angles is evaluated, as shown in Fig. 2.12. Calculation of RMSE for the reconstructed object phase compared to original phase was made to determine the number of required angles for object phase reconstruction improvement. Lower values of RMSE indicate more accurate reconstruction results. It is determined that the best results are obtained for the angles 0°, 90° and 180°. Thus, the phase mask was rotated 2 times starting with 0^0 to 180^0 with an increment of 90^0.

2.1.3 Simulation results for the off-axis DHM with phase mask

In our experiments the application of DG was tested on two objects: first study object was a Gaussian beam generated in the form $A_{obj} \cdot e^{i\varphi_0}$, where A_{obj} is the invariant amplitude of object, $\varphi_0=\pi$ object phase. Second study object was a phase step in the form:

$$Phase\ step = \begin{vmatrix} \frac{\pi}{2} radians, for\ 0 < x < 64 \\ 0\ radians, for\ 64 < x < 128 \end{vmatrix} \qquad (2.29)$$

The object size in pixels was 64 by 64 pixels. The DG and propagation parameters are the same as in Section 2.1. In this experiment, a sequence of intensity patterns was recorded at different angles of the phase DG grating which was placed before the object and rotated from 0° to 180° (0° position means vertical lines, 90° position means horizontal lines). Zero degrees, i.e. vertical grating means that the phase grating lines are parallel to the interference fringes formed by the interference of the object and reference beams. The phase object was added to the phase of the reference beam and then the interference was simulated. The robustness of the DH setup facilitates the presence of noise in the holograms, thus Gaussian noise observations were performed to simulate a process closer to real experiment conditions.

The value of RMSE for case of rating rotation shows better simulation. The multitude of reconstructed object phases after grating rotation where averaged. Fig. 2.13, 2.14 show the reconstructed phase without grating and with the application of DG. The plot of the intensity profile of the reconstructed phase clearly shows the decrease in noise when the sinusoidal phase modulation is performed. On the basis of the obtained RMSE values from the simulated experiment it is determined that the experiment with DG gives $\sim$ 20% less error if compared with the experiment without grating. It can be concluded that phase imaging enhancement can be obtained by adopting a sinusoidal phase modulation to the lensless digital holographic setup.

Fig. 2.13. Simulation results of the experiment with a phase step. After grating rotation value of RMSE$_{phase}$=0.025, without grating RMSE$_{phase}$=0.031.
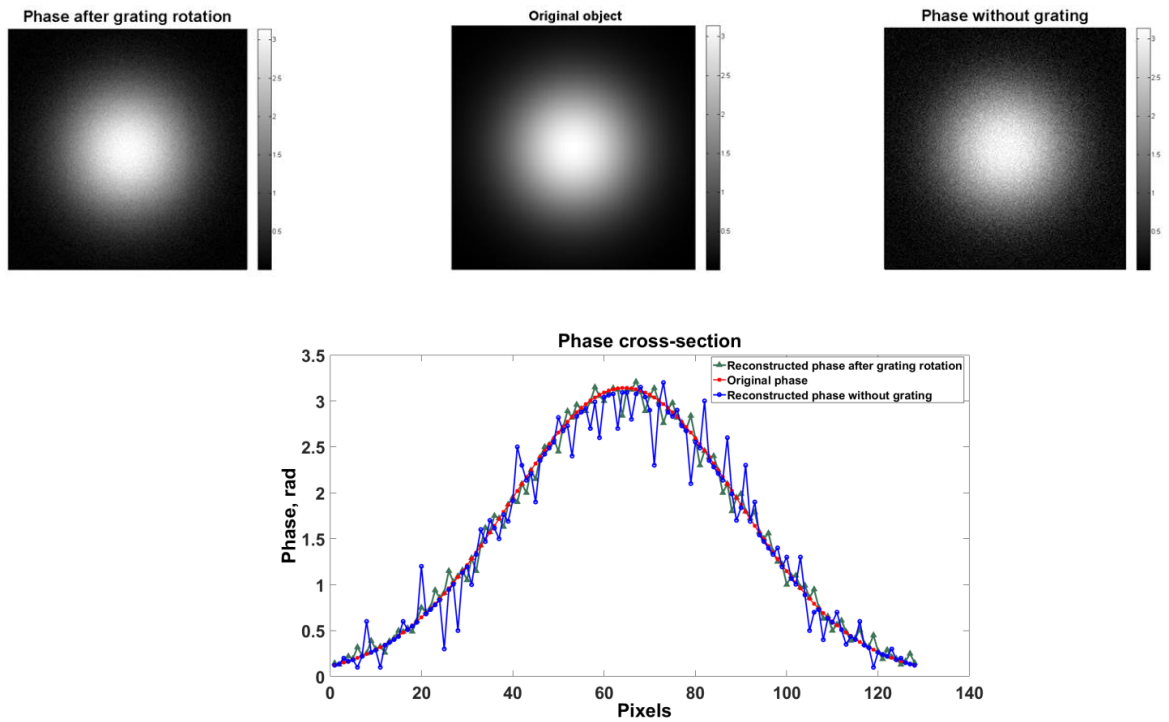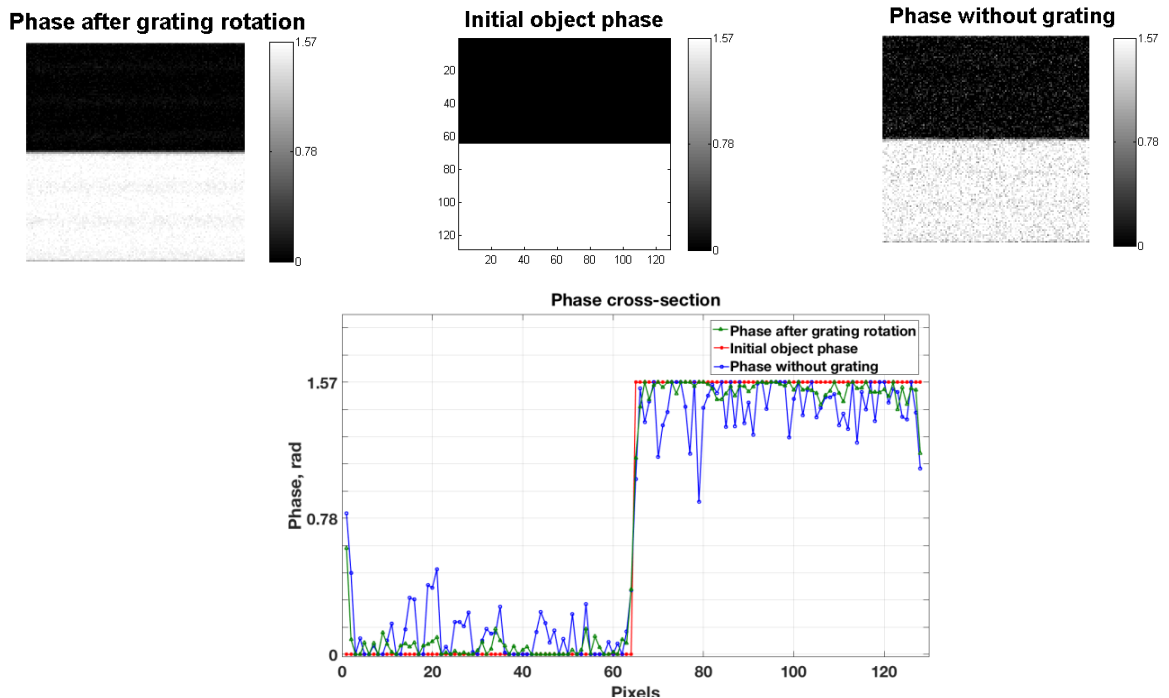

Fig. 2.14. Simulation results of the experiment with a Gaussian object. After grating rotation value of RMSE$_{phase}$=0.0243, without grating RMSE$_{phase}$=0.0292.

Due to the optimized diffraction grating parameters (period, phase and number of rotating steps) more information about the high spatial frequencies of the object spectrum is recorded in

the CCD sensor from the diffracted orders. This is a key point since the diffraction grating can be positioned to find the best experimental angular condition for recording digital holograms. The results are demonstrated for two phase objects and compared with the experiment without the sinusoidal phase mask.

2.2 The phase-shifting DHM in transmissive configuration with phase masks

This section is focused on improving the performance of quantitative phase imaging via phase-shifting digital holographic microscope. The results presented in this section are published by the author of this thesis in [195]. Despite the good performance of off-axis DHM systems, thanks to the possibility of reconstructing the complex wavefield from a hologram, this technique requires careful alignment to achieve no overlapping orders in the Fourier domain. Multiple applications utilize the in-line architecture of the DHM, which ensures minimal computational effort regardless of the fact that the three diffraction orders are overlapped in the Fourier domain. In contrast with the off-axis DHM, the phase-shifting DHM working in on-axis regime, is capable of making use of full CCD camera spatial resolving power and thus can capture finer sample spatial details. In phase-shifting DHM the phase difference between two interfering beams, which is called the reference phase, is modulated in a predetermined manner. The application of phase-shifting techniques to recover the object information without the presence of the other diffraction components implies the recording of a set of holograms with known and controlled phase shifts in the reference wave.

The aim of this part is to achieve compensation of object wavefront deviations in a phase-shifting (P-S) DHM arrangement. For this purpose, the digital modulation of light in the object beam is operated by the SLM. The use of the digital approach to wavefront modulation provided by SLM offered several advantages compared to beam shaping by a phase mask recorded on a thin film. First, it permits accurate control and strikethrough alignment of the required phase modulation. Second, it gives quick access to a variety of pattern parameters and shapes that are difficult, or sometimes impossible, to inscribe on a physical diffraction grating. The optimal modulation shape of the object wave by different phase masks is determined via computer simulations using MATLAB software.

The phase-shifting DHM with three different types of phase masks: sinusoidal and blazed diffraction gratings, and binary Fresnel lens responsible for object wavefront modulation are implemented. The simulated experimental setup is depicted in Fig. 2.15, where the reference wave is adjusted parallel to the object wave. To further test the realistic modeling boards, a phase-shifting experiment was simulated for Barbara test image as a pure-phase object with a size of 128

pixels x 128 pixels and with the phase values ranging between 0 and the maximum value of object phase $\varphi_0 = \pi/2$ shown in Fig.2.15(a). The ideal sample information was taken to be composed of a known phase distribution and unitary amplitude, $A_{obj} = 1$.

(a)   (b)
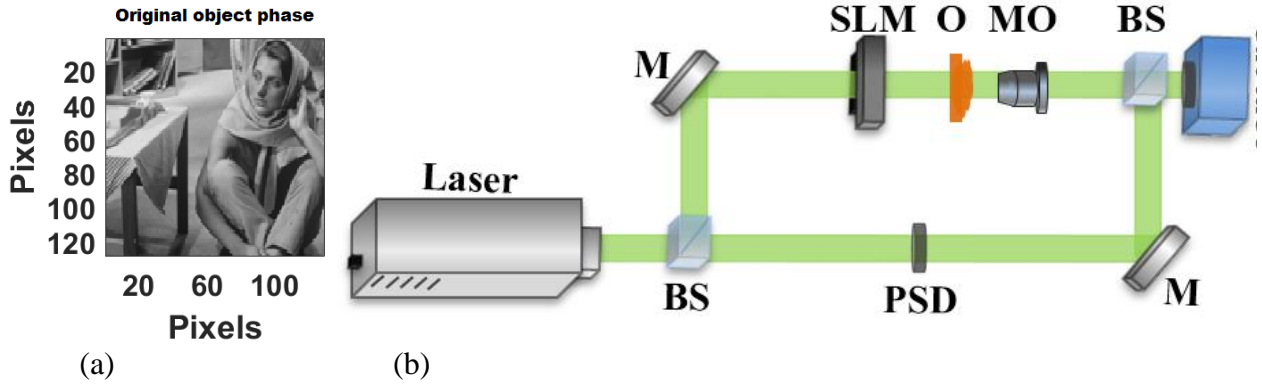
Fig. 2.15. (a) Barbara as phase object; (b) Simulated DHM setup: laser (λ=532nm), BS-beam splitter, M-mirror, MO-microscope objective 20ˣ, NA=0.40, SLM- HoloEye LC2002 spatial light modulator, O-object (Barbara test image), BS-beam splitter, imaging camera –resolution (3.45x3.45 μm pixel size), PSD- phase-shifting device.

For matching the real laboratory conditions a superficial noise in the order of 5% from hologram intensity was introduced to the sample by adding Gaussian-distributed values to the ideal phase. Four simulated phase-shifting holograms obtained by shifting the reference wave with $\pi/2$ are depicted in Fig. 2.16. For an ample explanation, the reconstruction method is revised and adapted to the proposed DHM imaging system. The intensity distributions of the four on-axis holograms with phase shift of $\pi/2$ can be expressed by

$$\begin{cases} I_1 = a(x,y) + b(x,y)[\cos\varphi(x,y) - \varphi_1] \\ I_2 = a(x,y) + b(x,y)[\cos\varphi(x,y) - \varphi_2] \\ I_3 = a(x,y) + b(x,y)[\cos\varphi(x,y) - \varphi_3] \\ I_4 = a(x,y) + b(x,y)[\cos\varphi(x,y) - \varphi_4] \end{cases} \quad , \tag{2.30}$$

where $a(x,y)$ is the background illumination, $b(x,y)$ is the modulation of the fringes $\varphi(x,y)$ is the object phase and $\varphi_1 = 0$, $\varphi_2 = \pi/2$, $\varphi_3 = \pi$, $\varphi_4 = 3\pi/2$ represent the phase steps.

Simulation parameters correspond to the values of the parameters of the optical setup built in the laboratory. The object O , considered to be illuminated by a laser with a wavelength of 532 nm, was then sharply imaged through a microscope composed of a 20ˣ and NA=0.40 objective with 8.4-mm working distance into a rectangular sensor of 8mm x 7mm side lengths, and maximum resolution of 2448 pixels × 2048 pixels. The number of illuminating pixels ona certain plane of the imaging system is determined by the magnification *M* of the MO. The magnification of the

DHM system was experimentally determined using a stage micrometer for calibrating the objective magnification with 1cm scale and 100 μm division. With these parameters, according to Eq. (2.9) the system has a resulting field of view (FOV) in the sample plane of $FOV_x \times FOV_y = 0{,}36$ mm x $0{,}35$mm , and a maximum admissible angle between the object and reference waves of 0.01 rad 0.57°.
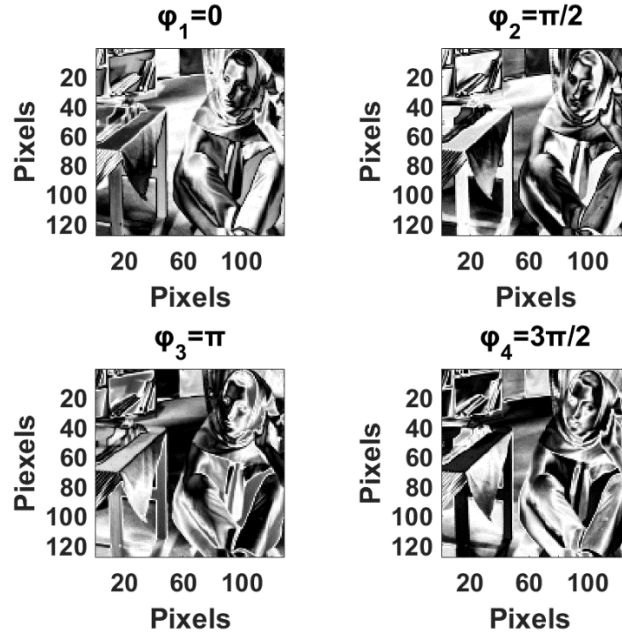
Fig.2.16. Simulated digital holograms obtained from 4 phase-shifting steps φ on DHM.

According to Eq. (2.13). In the sensor plane, the imaged wavefield of the object is superposed in amplitude with a plane reference wave tilted an angle of 0.001 rad 0.057°. The distance between the phase masks (imaged on SLM) and the object was set at 3 cm. At this distance, the diffraction orders are not superimposed.

The sinusoidal modulation of the object wavefront was computed using Eq. (2.28). The blazed grating is defined and computed by

$$G_B = exp[i\Delta\varphi_B(\sin\theta_B + \sin\left(\frac{2\pi\sin\theta}{\Lambda} + \frac{2\pi\cos\theta}{\Lambda}\right))], \qquad (2.31)$$

where θ_B-the blazed angle, θ- the rotation angle between two consecutive positions of grating, $\Delta\varphi_B$ – the phase modulation of the grating, Λ - the grating period. The value of the gratings period $\Lambda\sim44\mu m$ was established by taking into account that all diffraction orders fit in the CCD sensor, similar to previous experiment.

The Fresnel zone lens (FZL) is described and computed by

$$FZL = exp[in\Delta\varphi_{FZL}(\frac{2\pi}{\lambda}\sqrt{f^2 + r^2} - f], \qquad (2.32)$$

where *f*-focal length of the FZL, *r*-radius of the concentric rings, φ_{FZL}-the phase modulation of the mask, n- number of concentric rings.

(a)   (b)   (c)
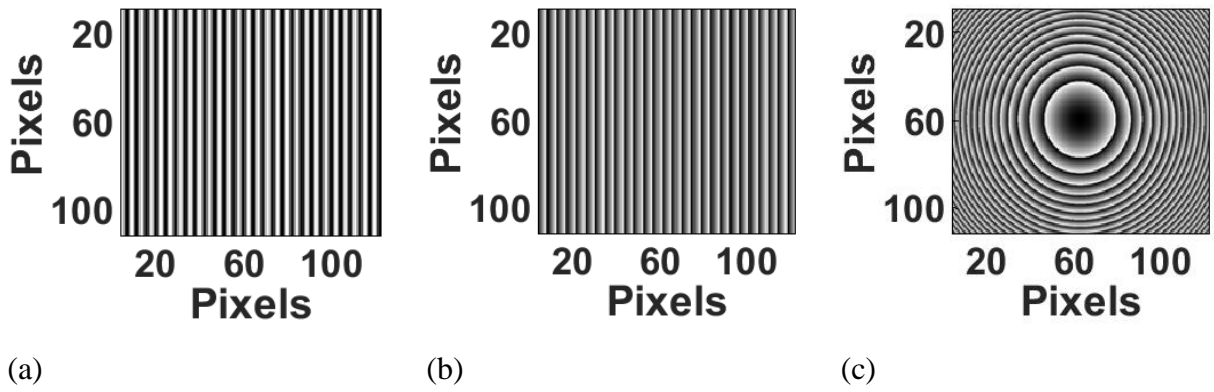
Fig.2.17. (a) Sinusoidal diffraction grating, (b) Blazed diffraction grating and (c) Fresnel zone lens phase-mask.

The optimal phase-masks parameters are determined by varying the diffraction gratings period Λ and angle α in relation to the optical axis of the imaging system and the number of concentric rings in the experiment with a Fresnel zone lens.
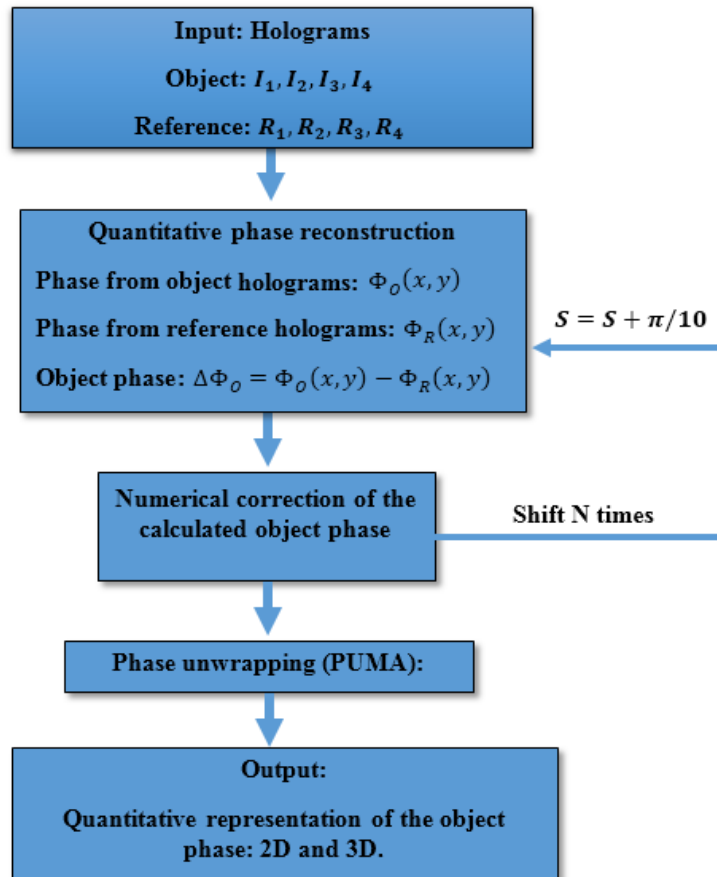
Figure 2.18. Block-scheme of the reconstruction method from phase-shifting holograms.

The reconstruction method for four-step phase-shifting interferometry has been proposed by Yamaguci in [83]. The block-scheme of the phase-shifting algorithm applied to the four aforementioned holograms used for phase map the reconstruction is shown in Fig. 2.18. It executes the correction of the phase shifts in the case of distorted tilt produced by phase-shifting device

65

(wave retarder plates or a piezo mounted mirror). This step is important when the appropriate laboratory conditions (changes of temperature, mechanical vibrations, unstable laser parameters etc.) cannot be maintained.
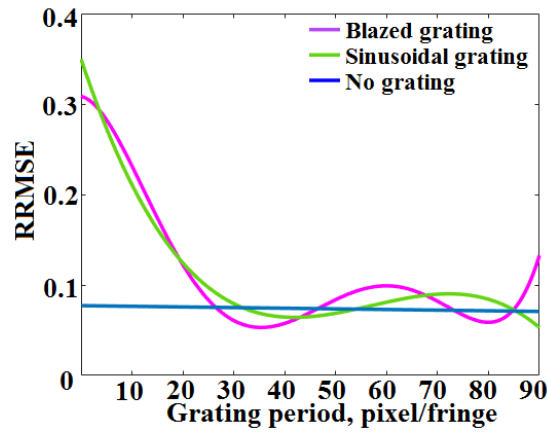
(a)
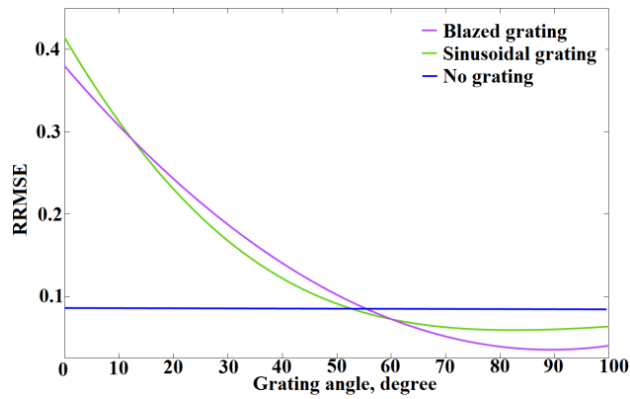
(b)
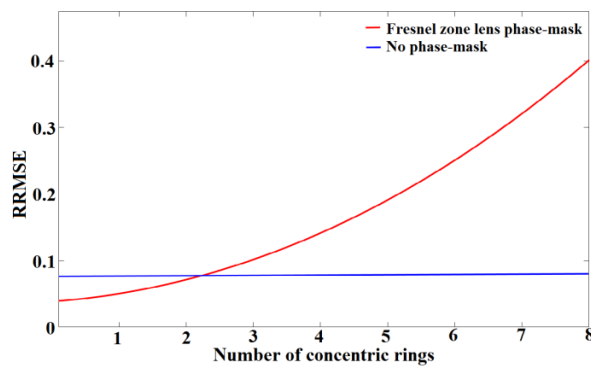
(c)

Fig. 2.19. (a) RMSE dependence on the sinusoidal and blazed gratings period; (b) RMSE dependence on the sinusoidal and blazed gratings angle in relation to the optical axis of the imaging system; (c) RMSE dependence on the number of concentrinc rings of Fresnel zone lens.

A small phase shift is added during the in iterations until the object phase is successfully revealed.

The microscope objective introduced in this setup generates an additional spherical phase term. For suppressing the spherical phase term, the principle of double exposure holography is applied. First, holograms with the object and then without the object are recorded. The holograms without the object carry information of the spherical phase arising from the microscope objective. The phase from the object holograms is calculated by

$$\Phi_O(x,y) = \tan^{-1}\left[\frac{I_1(x,y)-I_3(x,y)}{I_2(x,y)-I_4(x,y)}\right], \tag{2.33}$$

where, I_1, I_2, I_3, I_4 are the four recorded hologram intensities under corresponding phase shifts of the object under study.

The phase from the reference holograms which contains information about the additional phase term is calculated by

$$\Phi_R(x,y) = \tan^{-1}\left[\frac{R_1(x,y)-R_3(x,y)}{R_2(x,y)-R_4(x,y)}\right], \tag{2.34}$$

where, R_1, R_2, R_3, R_4 are the four reference intensities under corresponding phase shifts captured in the region without the object. The object phase is quantitatively reconstructed by subtracting the additional spherical phase term from the calculated reference phase using the formula

$$\Delta\Phi_O(x,y) = \Phi_O(x,y) - \Phi_R(x,y). \tag{2.35}$$

The accuracy of the phase reconstruction is evaluated by the relative root mean square error (RRMSE) between the true and reconstructed object's models,:

$$\text{RRMSE} = \frac{\|\varphi_0 - \Delta\Phi_O\|_F}{\|\varphi_0\|_F}, \tag{2.36}$$

where φ_0 and $\Delta\Phi_0$ are the phases of the true and reconstructed object, and $\|\cdot\|_F$ means the Frobenius norm. When RRMSE<0.11 the reconstruction process is considered to be successful [196].

Through the simulation experiments the optimal shaping of the object wavefront was determined. Fig. 2.19(a) shows that the best reconstruction can be obtained for the blazed grating when a grating fringe is projected on 35 or 80 pixels. At these values, the phase reconstruction quality is improved if compared to the experiment without the wavefront modulation by the blazed grating.

From Fig. 2.19 (b) it can be determined that the optimal angle is $\alpha=90^0$ with respect to the optical axis of the DHM. Also, better reconstruction results are obtained when α is in the range of 60-90^0. The sinusoidal grating with $\alpha=90^0$ with respect to the optical axis of the DHM presents a decrease of the RRMSE of approximately 25%, while the blazed grating under the same angle achieves a decrease of approximately 72%.
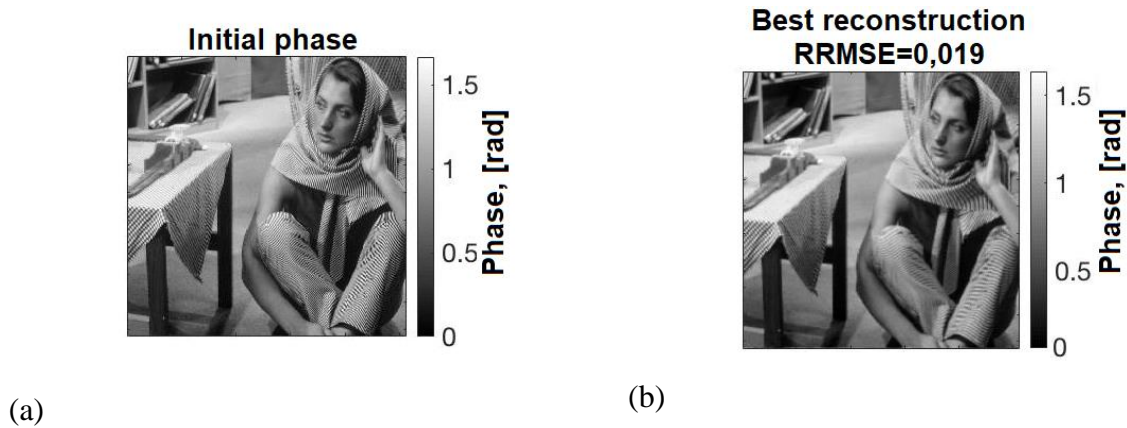
Fig. 2.20. Illustration of (a) initial phase and (b) the best phase reconstruction of Barbara test image resulted from the modulation of the object wavefront by a blazed grating with the period P=90 Pixel/fringe and angle $\alpha = 90^0$, with respect to the optical axis of the DHM.

According to the plot depicted in Fig. 2.19(c), the relation between RRMSE and number of the concentric rings of the Fresnel zone lens is inversely proportional. The most accurate results were obtained in the experiment where the lens creates a single concentric ring, providing an improvement of approximately 35% of the reconstructed phase image.

To sum up, the computational simulation results suggest that application of a blazed wavefront provide the best compensation for the wavefront deviations in the modeled setup. Therefore, with regards to the practical experiments described in this paper a blazed grating with the determined optimal parameters was set on the SLM display. The best reconstruction result the optimal object beam phase mask modulation is illustrated in Fig. 2.20.~~21~~. It is important to point out that the optimization obtained in the computational simulations represents a numerical estimation which cannot fully describe the conditions of an experiment conducted in the laboratory. The standard Gaussian noise was taken into account.

2.3 Conclusions to Chapter 2

1. Off-axis and phase-shifting are the two most commonly applied DHM configurations that have been computationally simulated in MATLAB software. For improving the DHM performance, different phase masks were introduced in the setup for modulating the object wavefront. The developed phase reconstruction, including the SPAR algorithm for off-axis digital hologram processing, was described. For the phase-shifting holograms, an algorithm based on the Yamaguchi approach given in detail in [83, 85] was designed and adopted.

2. It can be concluded that phase imaging enhancement can be obtained by adopting a sinusoidal phase modulation with DG for the off-axis lens less DHM setup. The following optimal

DG parameters were identified: the period $\Lambda = 44\mu m$, the value of phase modulation was $\varphi = 0.1\pi$ and two positions rotation steps of the DG at 0, 90, 180 degrees. Due to the optimized diffraction grating parameters (period, phase and number of rotating steps) more information about the high spatial frequencies of the object spectrum is recorded in the CCD sensor from the diffracted orders. Computational experiments showed that with sinusoidal phase modulation RMSE values are decreased about 20%. These results support the conclusion on the advantage of the proposed phase modulation gratings in off-axis lens less digital holography.

3. In the phase-shifting configuration it was found that by introducing a blazed diffraction grating in the phase-shifting DHM setup the precision of the phase reconstruction can be improved by approximately 72%. Particularly, the simulation showed that the best reconstruction can be obtained for the blazed grating with a period equal to 35 and 80 pixels/fringe and an angle $\alpha=90^0$ with respect to the optical axis of the DHM. The results are demonstrated for two phase objects specifically, a Gaussian beam and a phase step that were selected as experimental samples. The obtained results were compared with the experiment without the phase mask. The standard Gaussian noise was considered. Uncontrollable factors affecting the process of recording holograms are the stability of the laser in spatial coherence, the noise of the video camera, the rigidity of the tables, and the scattering of light by micro particles in the air.

4. It was demonstrated that due to numerical phase control of the object and the reference waves, significantly improved phase images can be obtained. This knowledge and numerical tools developed could be applied to record, reconstruct and process digital holograms.

3. IMPLEMENTATION OF LIQUID CRYSTAL DEVICES TO DIGITAL HOLOGRAPHY

3.1 The importance of liquid crystal devices calibration

Liquid crystal devices are fundamental elements of modern digital holographic systems. These computer-controlled tools use nematic liquid crystal materials to electrically modulate various parameters of electromagnetic radiation. Liquid crystal spatial light modulators (SLM) and variable retarders (LCVR) are two main peripheral gadgets used for the development and innovation of the optical setups. Two types of devices are used in practice, namely, in transmission mode and reflection modes.

SLMs are effective tools for the phase, amplitude control of the laser beams, being the key device in a wide range of optical applications such as, wavefront shaping [197], optical tweezers and manipulation [198], super-resolution imaging in digital holographic microscopy [199], or recording of sophisticated DOEs [200]. The liquid crystals in a SLM can be regarded as an array of variable retarders with fixed fast axis due to the electrically controlled birefringence properties of liquid crystals. Therefore, SLM can also be used to manipulate beam polarization. This opens a window for more structured light applications such as polarization-resolved patterns of beam generation [201], Pancharatnam-Berry device fabrication [202], polarization imaging and data encoding [203, 204]. On these grounds, SLMs turn out to be an important and universal tool that can be applied for polarization holographic recording. SLM can be implemented in digital microscopy to modify sample illumination and for image formation.

The phase and amplitude/intensity modulation generated by the SLM originates from the movement of liquid-crystal cells in different directions of their optical axis as a response to the variation of the gray scale map displayed on the SLM liquid crystal array.

The laser beam phase and amplitude/intensity modulation generated by the SLM originate from the displacements of liquid crystals as a response to the variation of the applied voltages map displayed on the SLM liquid crystal array. Each pixel in the SLM should be able to provide phase shift coverage of at least 2π radians. Theoretically, all the light reflected from or transmitted through the SLM pixels undergoes a phase change corresponding to the gray levels displayed on the SLM. In the practice, due to the effects induced by the geometry of the SLMs as a consequence of the fabrication process, most devices available on the market today do not generate the exactly desired high-resolution phase modulation or produce minor wavefront phase changes. In particular, it is a result of the limited fill factor of the SLM array caused by the presence of the inactive area between the pixels. Due to fabrication limitations, there are always gaps amongst the

70

pixels of a SLM, which may cause undesired diffraction. The fill factor is the ratio between the active pixel surface and the square of the pixel pitch. A higher fill factor value leads to fewer diffraction maximums and higher image quality.

The manufacturer provides calibration files for only specific wavelengths. The non-linear response between the gray scale driven by voltage and the phase modulated by the SLM necessitates calibrations. The birefringence of LC in SLM depends on the applied voltage and laser wavelength. Therefore, to ensure that for the wavelength used, SLM provides the required phase modulation, it is mandatory to know its ratio with the gray scale values on the bitmap, i.e., to perform a calibration.

The LCVR is built out of a transparent cell filled with a solution of Liquid Crystal (LC) molecules. The alignment layer of the LC molecules consists of an organic polyimide coating whose molecules are arranged in the rubbing direction during manufacturing. Due to the birefringence of the LC material, this LC retarder functions as an optically anisotropic wave plate, with its slow axis parallel to the surface of the retarder. A transparent conductive film covers the internal walls of the cell so that a voltage can be applied across the cell. The applied voltage determines the orientation of the LC molecules. Thus, the retardance of the liquid crystal variable retarder is mainly controlled by the applied voltage. A controller supplies a square-wave AC voltage output with an amplitude that can be adjusted. The absence of moving parts provides quick switching times on the order of milliseconds. To minimize effects due to ions in the materials, an LC device must be driven using an alternating voltage. Due to this function of the LCVR it permits the all-optical manipulation (phase-shifting) of light, which is usually required in DHM systems. The LCVR retardance is a nonlinear function of the applied voltage.

LCVR provides optical retardation tuning in transmission mode. Analysis and manipulation of the phase and polarization of light is a tool in many optical setups control via a PC interface. [204, 205]. When included in the optical scheme of the holographic microscope, LCVRs provide electrically controlled phase retardance.

LCVR provides active control over the polarization state and/or phase delay of light depending on the voltage applied to the optical system. Application of the LCVR to phase-shifting DHM configurations is of particular interest, since it is capable of performing phase steps. The merit of the LCVR is that it executes optical phase shifting, by driving voltages. The temperature dependence of LCVR's phase retardance is equal to $0.01\,\pi$ per degree. if compared to mechanical displacement, produced via a piezoelectric transducer. In particular, this is because–LCVR is mounted in-line, vibration free, and produces an uniform retardance in the aperture [200].

When voltage is applied to cell, LCVR produces a nonlinear voltage-retardance relationship. Usually a step-voltage method is generally applied to LCVR. For a successful implementation of the LCVR in different optical configurations it is mandatory to perform its experimental calibration.

This chapter is focused on the calibration of the SLM and LCVR which will be further used in DH setups for recording of DOEs and microscope. The first section of this chapter describes the detailed phase calibration of individual pixels of the SLM for precise spatial control of the laser light. Two different algorithms for phase reconstruction are developed. First, an FFT-based algorithm was used. For a high-accuracy analysis of the SLM phase modulation the SPAR-based algorithm (described in the previous chapter) was implemented. It was further developed as pixel-by-pixel investigation software. Moreover, retardance calibration is performed in order to determine the polarization modulation produced by the SLM. The described methodology includes both hardware and algorithms, that could be built into an interferometric optical system for calibration of both phase and retardance (polarization) modulation. A comparison of the calibration curves in the SLM active phase modulation area and the entire array (including the gaps between pixels) is done. The benefits of the performed calibration method include detailed characterization of the phase in each pixel, phase determination and polarization control of the SLM liquid crystal array. The obtained results show good agreement with the device manual. The proposed calibration set-up including the image processing algorithm provides a comprehensive method for phase and retardance characterization.

The second section of this chapter describes the detailed calibration of the LCVR. The LCVR must be preliminary calibrated to perform a precise phase control. The aim of the calibration is to determine the dependence of the phase retardance on the applied voltage without changing the polarization of the input beam. For this purpose, an off-axis digital holographic registration scheme was used with subsequent restoration of the phase pattern by the Fast Fourier Transform method. The experimental retardance vs. applied voltage curves were compared with the available data provided by the manufacturer.

3.2 Calibration of the SLM Holoeye LC 2012

3.2.1 The hardware DH system for the phase calibration of the SLM

A DH optical setup is used for calibrating the phase modulation of the SLM. The considered modulator is a phase and amplitude SLM based on a translucent liquid crystal

microdisplay of type Holoeye LC 2012 with a resolution of 1024×768 pixels with a pixel pitch of 36 µm². This SLM is based on a twisted nematic liquid crystal display. The fill factor of the SLM is equal 58%. Active area of the modulator: 36.9 x 27.6 mm (1.8" diagonal). The phase modulation is mostly possible as the twist always causes a coupled polarization effect (amplitude modulation). The manual given by the manufacturer of the SLM indicates a phase shift of about 2π at wavelength λ=450 nm, about 1.8 π at λ=543 nm and around π at λ=800 nm. The components (microdisplay and drive electronics) of the device are packed into a compact box for an easy integration into various optical systems. The SLM is addressed using a HDMI interface. The brightness and contrast are adjusted using a USB interface. Phase mostly or amplitude modulation modes depend on the incident polarization and polarizer-analyzer settings of the optical configuration. In the developed DH optical system, to the SLM display is addressed as a second computer monitor. The intensity variation is controlled by loading proper phase screens to the SLM. For operation, the desired phase distribution has to be displayed as an 8-bit grey value pattern on a computer screen. The computer interface that requires 0-255 gray scale level images was used to communicate the phase modulation to the SLM display. Each grey value represents a certain phase shift of the SLM display in the range of 0 to the maximal phase modulation. To maximize efficiency of the phase screens, the pixel values of the screen must be modified based on the characteristics of the SLM. By duplicating and loading the gray value pattern of the computer screen to the SLM, the phase distribution is introduced pixel-wise into the experimental setup.
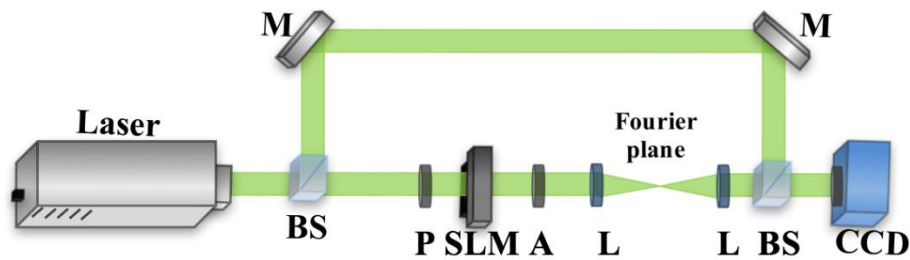
Fig. 3.1. Digital holographic set-up for determination of the phase modulation used for SLM calibration. BS- non-polarized beam-splitter, L- lens, P-polarizer, A- analyzer, SLM-transmissive spatial light modulator "Holoeye" LC2012, M-mirror, Laser-wavelength λ=532nm, CCD camera.

The SLM is operated by the HOLOEYE SLM Pattern Generator Software which is provided by the manufacturer. The detector is a 4000×3000 pixel CCD camera with a pixel pitch of 1.55x1.55 µm². The two-beam holographic set-up is illustrated in Fig. 3.1. In the Mach- Zehnder configured set-up, the laser light passes through a non-polarizing beam splitter such that the beam is divided

into two beams with the same polarization states. One of the beams illuminates the SLM display, while the reference beam illuminates directly the CCD camera.
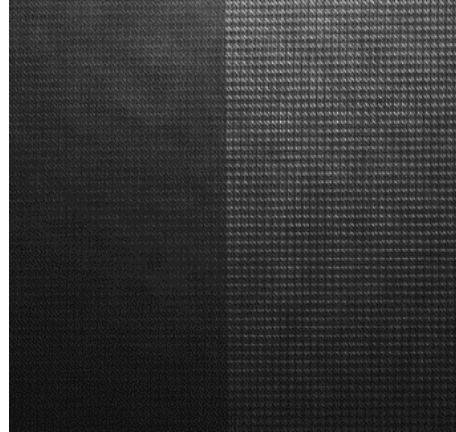
Fig. 3.2. The hologram of the SLM divided screen was recorded by the CCD camera. On the left side the grey level addressed to the SLM display is zero and kept uniform, on the right side of the SLM display the gray level varies from 0 to 255.

Consequently, the phase of the reference beam is kept constant, while the phase of the object beam is varied when it transmitted through the SLM. The 4f lenses system with diaphragm in focus placed in the object arm removes any extra phase terms and trims out diffraction maximums. A computer is used to control the SLM's display parameters as well as the acquisition of the images by the camera. As suggested by the manufacturer, to achieve maximal modulation, the polarizer-P is arranged at 315° and the analyzer-A set at 15° with respect to the vertical axis of the system and are located before and after the SLM, respectively. Also, according to the recommendations, the brightness of the SLM display is set to a value of 45, while the contrast is 63.

The recorded by the SLM the hologram vertically divided screen pattern is shown in Fig. 3.2. The interference fringes at the image plane are obtained on the CCD camera chip. Off-axis hologram alignment is determined by the oblique angle of the reference wave with respect to the object beam. Calibration of the SLM is done by loading a series of vertically divided screen patterns on the SLM display. A half of the screen is the reference zone and has a uniform distributed gray scale equal to 0. The other half is the variable zone and has the gray scale values ranging from 0 to 255.

3.2.2 Fast Fourier Transform algorithm for SLM calibration

The FFT is the first method used to process the interferograms obtained using the optical system described in the previous section. It is a commonly employed signal processing technique

because usually it requires just single interferogram acquisition for extracting the phase information. The interferogram intensity in spatial domain is given by

$$I(x,y) = a(x,y) + b(x,y)\cos(\varphi_r + \varphi_o), \tag{3.1}$$

where φ_r, φ_o denote the reference and initial phase distributions. Let's rewrite it as:

$$I(x,y) = a(x,y) + b(x,y)\cos[(x,y) + 2\pi f_o(x)] = a + ce^{i2f_0(x)} + c * ce^{-i2f_0(x)}, \tag{3.2}$$

where $I(x,y)$ is the intensity in the detection plane (x,y), a(x,y) is the mean intensity in the interference field, b(x,y) is the modulation of the detected interference field, f_o-spatial career frequency*.

$$c = \frac{b(x,y)e^{i\varphi(x,y)}}{2}. \tag{3.3}$$

According to the basic properties of the linear and frequency shifts of the Fourier transform frequency domain, the spectrum can be obtained by

$$\tilde{I}(u,v) = \tilde{a}(u,v) + C(u + f_o, v) + C^*(u + f_o, v), \tag{3.4}$$

where $\tilde{a}(u,v)$ is the zero order in the Fourier spectrum, and represents the spectrum of the background, $C(u + f_o, v)\ and\ C^*(u + f_o, v)$ are the +1 and -1 orders in the Fourier spectrum.
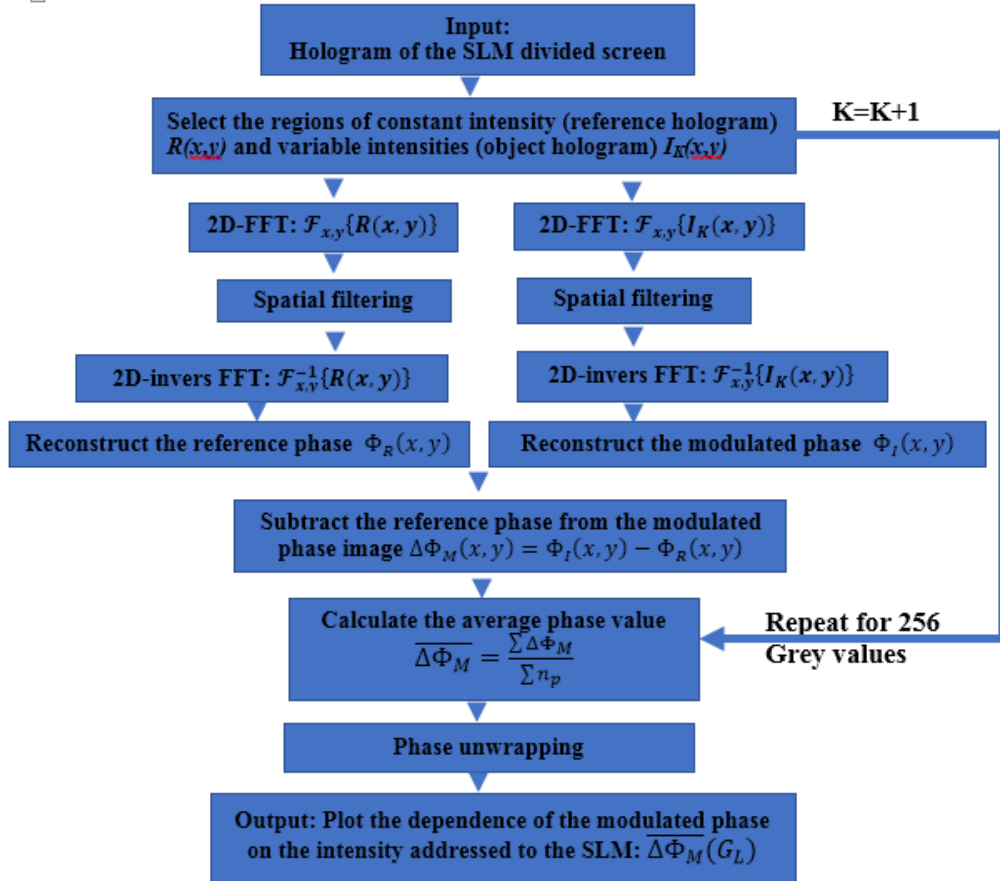
Fig. 3.3. FFT algorithm flowchart for calibration of the SLM's phase.

They are representing the two spectra of the interferogram, being symmetric relative to the origin of the frequency and complex conjugates of each other. The flowchart of the FFT based

algorithm developed in MATLAB is depicted in Fig. 3.3. The algorithm first processes the reference part of the hologram where the gray level addressed to the SLM display is uniform. In the next step, 256 holograms are processed; here the gray level in the variable zone differs for each acquisition. For obtaining the phase modulation performed by the SLM the difference between the variable and reference phase images are calculated for each modulation of the SLM. The adjusted FFT algorithm for SLM calibration is shown in Annex 3 of this thesis.

In Fig. 3.4 are illustrated the sequential steps of the FFT method used for phase calibration of the SLM. The FFT-FFT^{-1} methods are based on the Fourier transform of the intensity distribution of the interference field into frequency domain and back to the intensity domain. The 2D-FFT of the off-axis hologram shown in Fig.3.4 (a) is represented by a Hermitian function when it is complex conjugate is equal to the original function with the variable change of the sign. This procedure is applied separately for the reference and modulated part of the hologram. The resulted Fourier spectrum of both parts of the hologram is shown in Fig. 3.4(b). Here, the spectral peak at zero order (in the center) represents a low frequency spectral component that comes from the background intensity modulation of the interferograms.
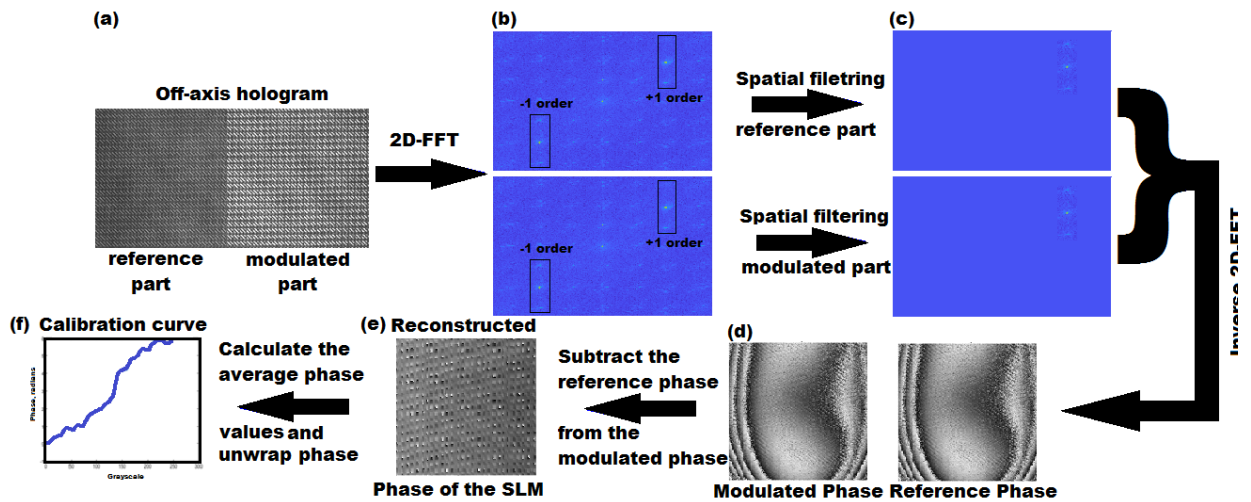
Fig. 3.4. Sequential phase reconstruction steps for SLM calibration (a) off-axis hologram, (b) Fourier transformed spatial frequency domain data, (c) filtered +1 order of the spectrum, (d) reconstructed phase of the reference and modulated part, (e) final reconstructed phase of the SLM after subtraction of the reference and phase unwrapping, (f) the SLM calibration curve shows phase dependence on gray levels.

The two symmetric spectral side lobes marked in black squares are the +1 and -1 orders and carry the same information about the phase values. By spatial filtering, one of the side lobes is extracted (Fig. 3.4(c)). The phase image can be reconstructed by isolating the +1st order of the spectrum through appropriate adaptive band pass filters in the spatial frequency domain and

performing the inverse Fourier transform. Inverse 2D-FFT of the filtered spectrum will offer the wrapped phase values as shown in Fig. 3.4(d). For obtaining the phase modulation generated by the SLM, the phase calculated the reference phase (where the gray level on the SLM display is kept constant at a 0 value) was subtracted from the part of the SLM display where the gray level varied from 0 to 255.

The FFT method for hologram processing and SLM calibration is considered a traditional approach for phase reconstruction. It is relatively simple in implementation for SLM calibration and offers the results using shorter amount of computational steps and time. However, there are still several cautions regarding this technique. In order to choose the appropriate spectrum and remove the hologram's background and noise, hologram processing based on the FFT method needs to use a spatial filtering technique. For this aim the pinhole was mounted inside 4f optics in the focus plane. Even small mistakes in the spectrum region selection, when the first order of the spectrum is chosen by filtering technology, can result in a relatively large phase tilt.

(a)
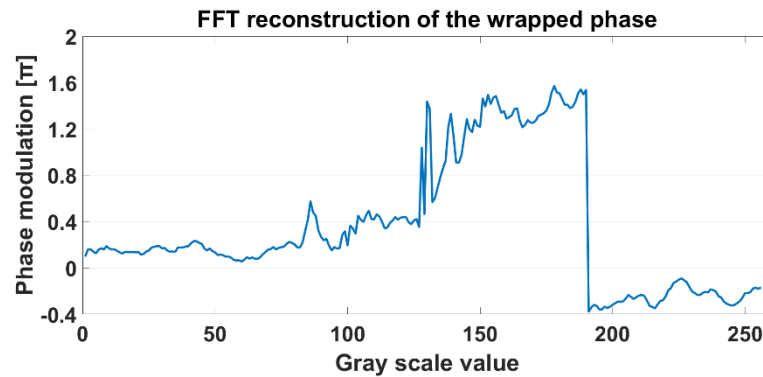
(b)
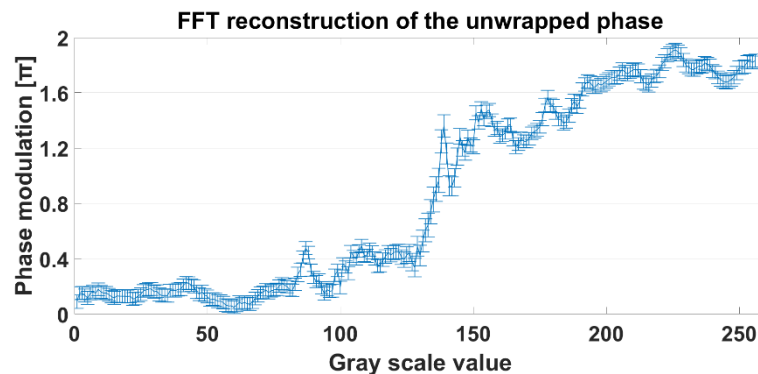
Fig. 3.5. FFT algorithm results of the phase modulation dependent on gray level for the bisected screen of the SLM display. (a) The calculated wrapped phase; (b) The calculated unwrapped phase.

This drawback is also evident in the calibration curve that was obtained, which is shown in Fig. 3.5.It is challenging to estimate the SLM phase modulation accurately because the

illustrated dependence of the SLM phase modulation on the gray levels does not exhibit a smooth curve. In order to remove the noise caused by the phase tilt on the image and achieve precise phase recovery, the obtained phase information must be post-processed. Since the SLM calibration procedure by default requires the acquisition of multiple holograms, they must be acquired as quickly as possible. So, the accuracy of the experiment will be minimally corrupted by the equipment disturbances.

In view of the above, there is a growing need to develop an algorithm for SLM calibration that would be able to process the interferograms with higher level of accuracy.

3.2.3 Local least squares algorithm application for SLM Holoeye LC 2012 calibration

The SPAR algorithm based on local least square (LLS) estimation of the phase data obtained from the interferometer was adjusted for a robust calibration of the SLM from the interferometer in the presence of omnidirectional noises.
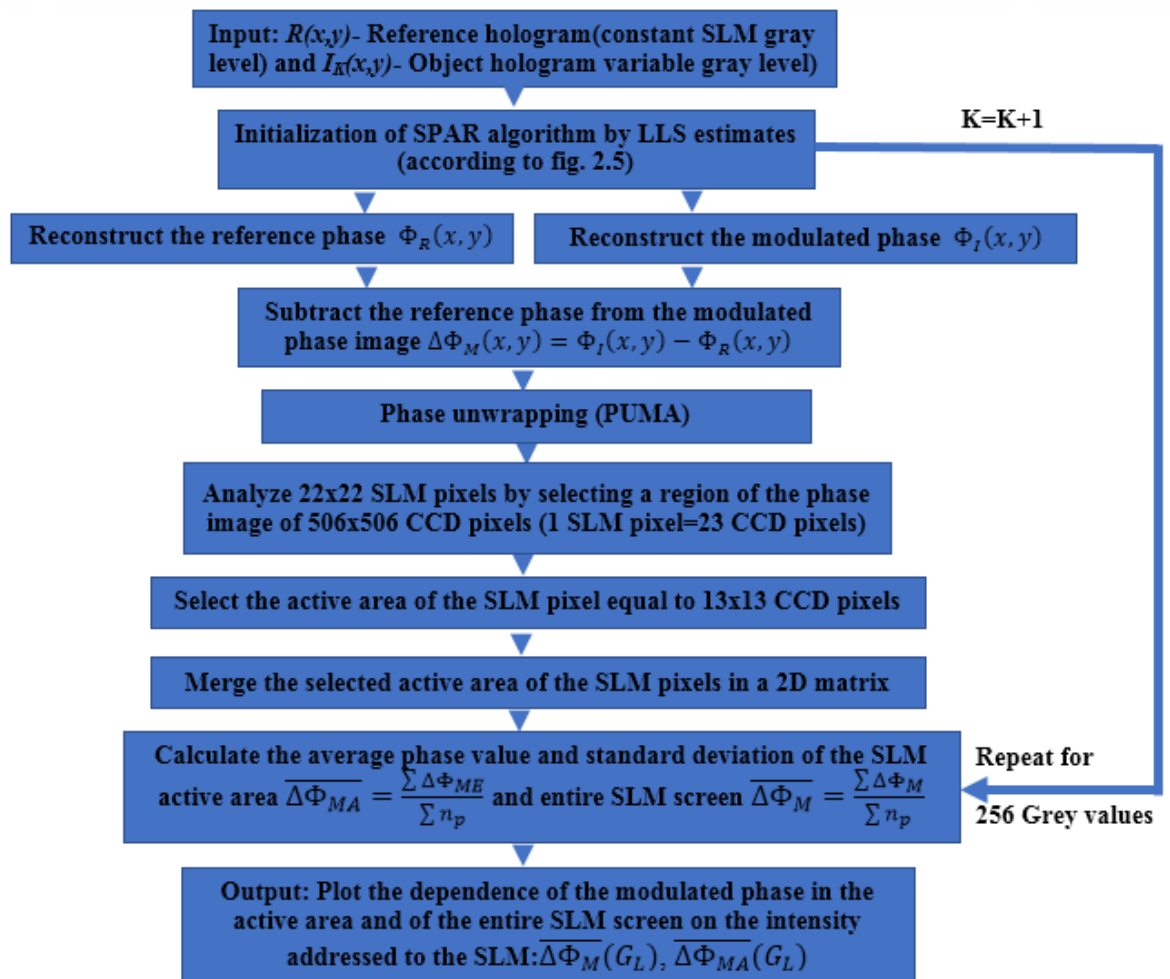
Fig. 3.6. SPAR algorithm flowchart for calibration of the SLM phase.

As mentioned in Chapter 2 of this thesis, it is a noise-minimizing algorithm which permits efficient phase reconstruction from off-axis holograms. This is essential for a correct determination of the SLM phase response. For a more detailed characterization of the SLM the phase was investigated in individual pixels and their active area. The adjusted SPAR algorithm for SLM calibration is shown in Annex 4 of this thesis.

For this purpose, the "dead zones" (non-photosensitive regions) around the pixels representing the driving electronics per pixel were excluded from the phase calculations. The SPAR algorithm flowchart for calculating the SLM phase modulation is depicted in Fig 3.6. The estimation performed by SPAR is complex, and it requires more time and computational effort if compared to FFT algorithm. This is true, especially here when additional loops are included for investigation of individual pixels. In order to solve this issue and reduce the computational time required for revealing the phase in each pixel of the SLM, a 506x506 array image represented by the central CCD pixels was processed for analyzing 22x22 SLM pixels.

(a) (b)

(c)
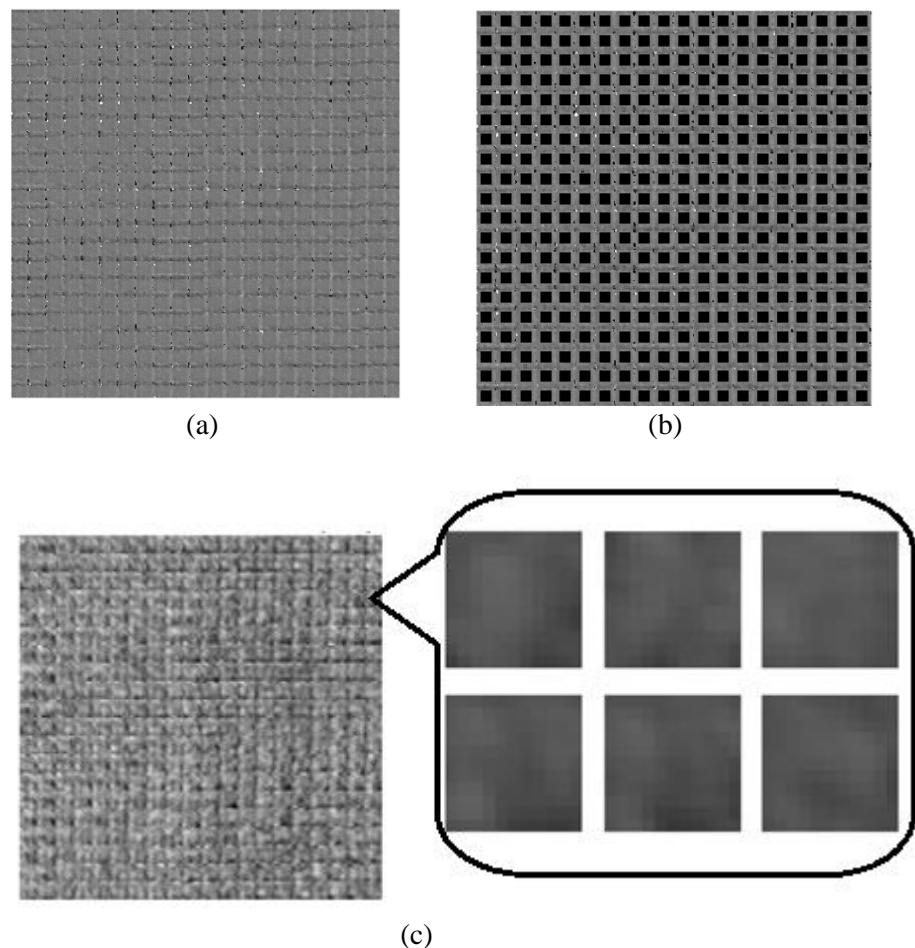
Fig. 3.7. Resulted phase images of (a) entire SLM display, (b) "dead zones" depicted in gray color, and (c) active pixels area (call-out).

In the next step, the active area of the SLM pixels was localized. It was determined that 1x1 SLM pixel equals to 23x23 CCD pixels..

(a)

(b)

(c)
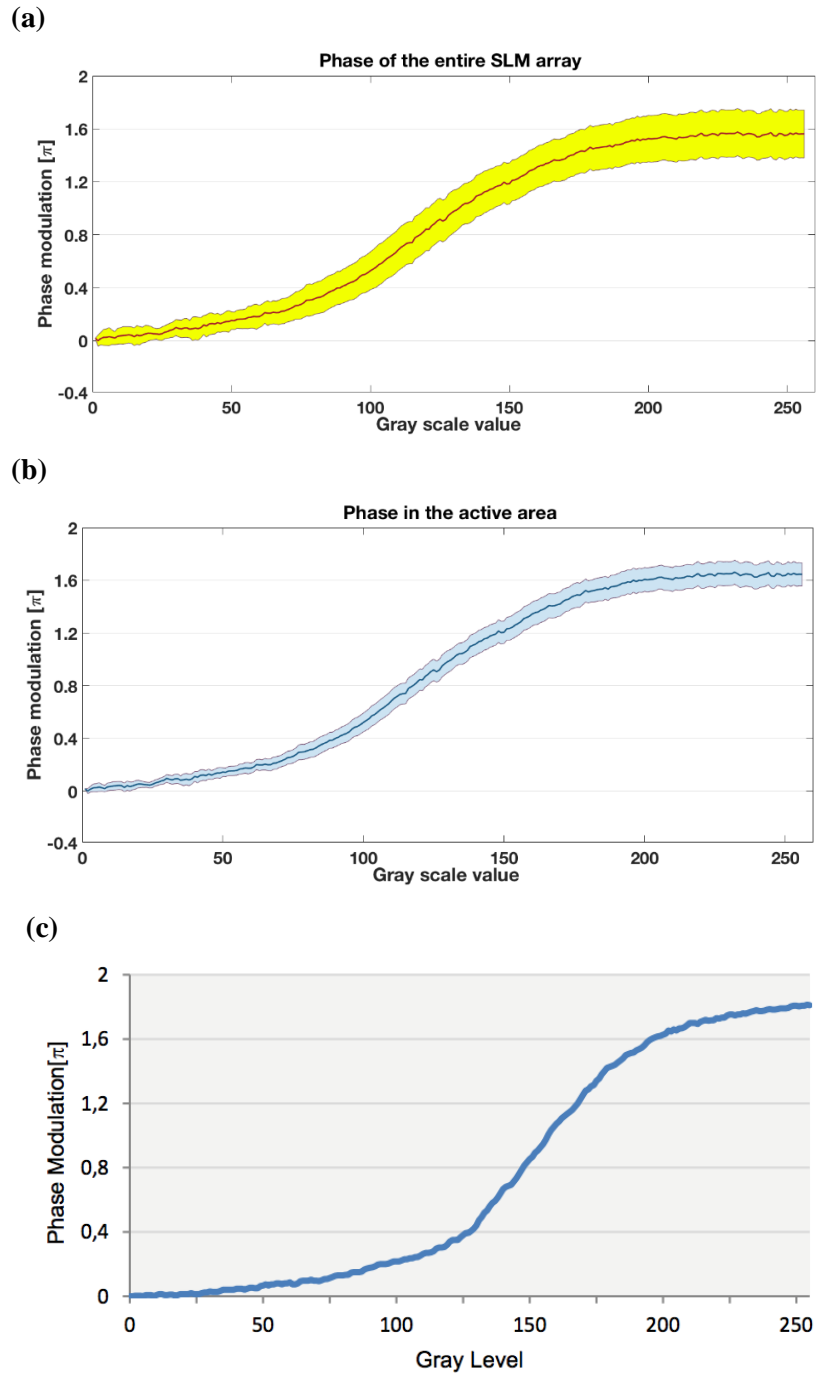
Fig. 3.8. The calibration curve resulted from application of the SPAR algorithm representing the relationship between the SLM phase modulation (blue and red lines), phase standard deviation (yellow and blue areas around the main curves) and the gray scale of (a) the entire SLM array and (b) in the active area of the SLM pixel; (c) the calibration curve given by the manufacturer for λ=543 nm. The plots of dependence on phase modulation for λ=532 nm (a and b) are shown.

The active area of the SLM pixel constitutes 13x13 CCD pixels. The "dead zones" surrounding the active area of the SLM pixel constitute 5 CCD pixels. Fig. 3.7 pictures the phase images resulting from the adjusted SPAR algorithm.

The zoomed in pixels shown in Fig. 3.7(c) demonstrate phase gaps (in white color); thus, it is important to identify the standard deviation and clarify the difference between the phase modulation obtained from the entire SLM and in the active parts of the pixels.

The phase modulation shown in Fig. 3.8, is the result of the difference between the reconstructed phase of the reference hologram where the display is addressed with a constant signal (gray level is 0) and the hologram with one half of the display modulated with gray levels varying from 0 to 255. From the results obtained by the SPAR based algorithm it can be noticed that in the region of maximum phase modulation, the standard deviation of the active part of the SLM pixel is 0.5 radians smaller if compared to the phase of the entire SLM array, as illustrated in Fig. 3.8 (a), (b).

This effect could be the result of the "dead zones" of the SLM array, where the polarization of passed laser beam cannot be controlled. Even though the dependences presented in Fig. 3.8 show similar tendencies, specific differences can be noticed when comparing the calibration curve given by the manufacturer with the curves resulting from the implemented SPAR algorithm. First, the phase response increases at lower rates of gray scale values using the calibration setup and software approach described in this chapter. Particularly, at the 125-gray scale value, the phase modulation of the SLM active pixel area is π; the entire SLM display modulates 0.9π, for λ=532 nm. Also, the maximal phase modulation of the SLM active pixel area is 1.7π and the entire SLM display is 1.6π

The obtained SLM phase modulation by applying post-processing to the SPAR algorithm gives better results. The modulation curve on the gray levels exhibits a smoother curve in comparison with the previous it calibration. The SLM provides a phase shift of about 2π at 450 nm, about 1.8π at 532 nm and around 1π at 800 nm.

3.2.4 Retardence calibration of the SLM Holoeye LC 2002

The polarization state, along with wavelength amplitude and phase, is a crucial property of light. The inclusion of polarization encoding in conventional digital holograms paves the way for the development of polarization holography. Polarization-sensitive holograms for reconstructing polarization holographic images are encoded with the help of polarization-dependent birefringent materials. The use of LC materials in SLMs depends on their optical and electrical anisotropic

properties. The method of polarization holography is based on recording in a photo-induced anisotropic medium the superposition of two monochromatic waves with different polarization states.

Typically, a thin layer of LC material can be described as a birefringent material with two refractive indices along two axes. The orientation of the index ellipsoid depends on the direction of the orientation of LC molecules. The typical alignment of LC molecules of SLMs allows the change only along their one axis while the other orthogonal direction remains invariant. It results in optical anisotropy because of the phase retardation in one of the axis directions inside the SLM. The optimized phase shift for each pixel of the SLM is programmed as a function of 256 gray scales ranging from 0 to 255. Therefore, the typical anisotropic properties of SLM (phase shift and birefringence) can also be interpreted as a function of its gray scales.

(a)

(b)
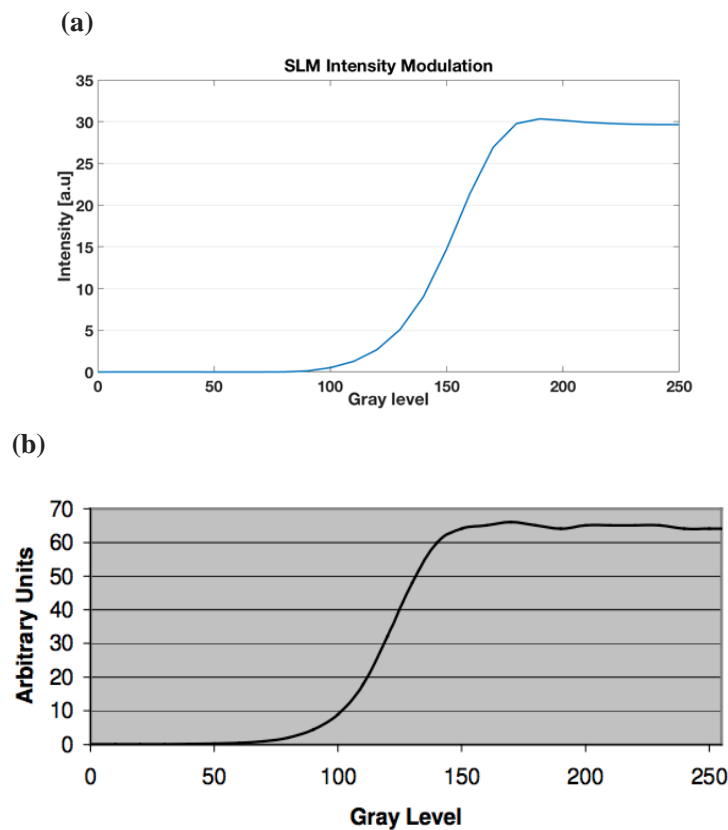
Fig. 3.9. Intensity as a function of gray scale value for the SLM of type Holoeye LC 2002 (a) current experiment at the λ=532 nm, (b) data provided by the manufacturer at the λ=543 nm.

The retardance calibration in this part of chapter was completed for the SLM of type Holoeye LC 2002. The LC2002 is a general purpose device for displaying images by using a monochrome LC display. SLM is designed to be plugged to the graphic board of a PC with a resolution up to

SVGA format, i.e., 832×624 image pixels. The SLM converts color signals into corresponding grey level signals. The following are its characteristics:

- Active area: 26.6 x 20.0mm^2
- Pixel pitch: 32μm
- Gray level image playback
- Fill factor 85%

First, the intensity modulation of SLM is determined. For this purpose, the reference arm of the DH setup shown in Fig. 3.1 was blocked, while the 4f system was replaced with lens and a microscope objective. So the collimated laser beam was formed and directed to SLM display.
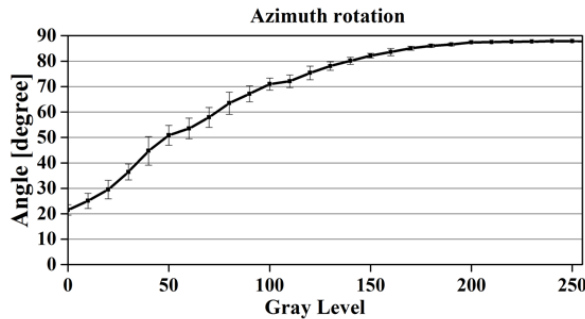
(a)   (b)
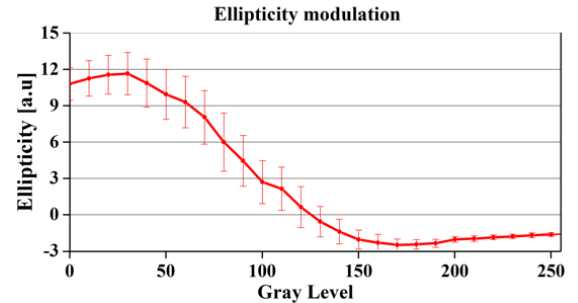
(c)
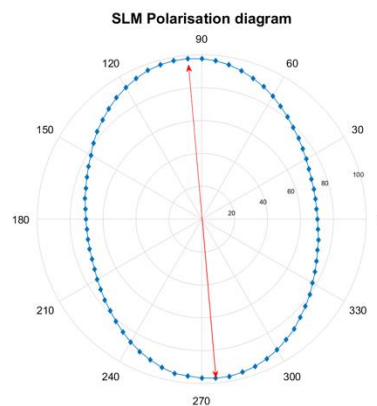
Fig. 3.10. Influence of the SLM's gray levels on the transmitted polarization: (a) azimuth and (b) ellipticity, (c) SLM polarization diagram.

This input beam was linearly polarized light oriented by polarizer P to +45° at the vertical axis. The output light was viewed through a 135° (-45°) oriented analyzer A, as suggested by the manufacturer for the wavelength, λ=543nm. The blank screen pattern was loaded on the SLM display. The addressed gray level values were set up with a range from the minimum of 0 to the

maximum of 255. These patterns represent a uniform gray level screen. The value of the intensity modulation was calculated by averaging the intensity of each SLM pixel for 256 gray levels. The resulting plot of the intensity as a function of gray scale value is shown in Fig. 3.9.

For retardance calibration of the SLM, the polarizer P with transmission axis at +45° (with regard to the vertical axis) was mounted before the SLM. The output light after SLM passes through the analyzer A mounted on the rotation stage, where the polarization axis position was positioned from 0° to 360° with a step of 10°. The maximum 255 gray level value was loaded on the SLM homogeneous display. At this value, the highest intensity modulation is obtained, according to the data obtained in the previous experiment. The polarization modulation performed by SLM is also characterized by azimuth rotation angle and ellipticity of the transmitted beam.

The azimuth rotation angle was identified by measuring the inclination angle between the analyzer position for minimal transmission of light through the SLM (major axis of the ellipse) and the analyzer position for maximal transmission of light through the SLM (in the positive direction to the vertical, by adding 90^0). The azimuth rotation angle defines the orientation of the ellipse in its plane. The plot of the azimuth rotation angle as a function of gray level addressed to the SLM is shown in Fig. 3.10(a).

The ellipticity is calculated by subtracting the minimal intensity value for the maximal transmission of light through the SLM (major axis of the ellipse) and the intensity value for the minimal transmission of light through the SLM. The intensity values in this case are measured by a photodiode. The plot of the ellipticity as a function of gray level addressed to the SLM is shown in Fig. 3.10(b). It can be noticed that SLM output polarization state is typically, elliptical. Only when uniform 125 gray level is loaded on the SLM display it keeps the linear polarization of the input light. Also, this plot shows that the denser the gray level applied to the display, the smaller the light polarization modulation in the output. The MATLAB algorithm for calculating the polarization diagram is shown in Annex 5.

The polarization diagram shown in fig. 3.10(c) was obtained by calculating the average value of the intensity image for every state of polarization set on the analyzer. Figure 3.10(c) was built for 255 gray levels, by the *polarplot* function in MATLAB software. This function creates a polar coordinate plot of the output angle of polarizer A versus the radius and plots them in a Cartesian plane and draws the polar grid on the plane.

3.3 Calibration of the liquid crystal variable retarder

The LCVR is built out of a transparent cell filled with a solution of Liquid Crystal (LC) molecules. The alignment layer of the LC molecules consists of an organic polyimide coating

whose molecules are arranged in the rubbing direction during manufacturing. Due to the birefringence of the LC material, this LC retarder functions as an optically anisotropic wave plate, with its slow axis parallel to the surface of the retarder. A transparent conductive film covers the internal walls of the cell so that a voltage can be applied across the cell. The applied voltage determines the orientation of the LC molecules. Thus, the retardance of the liquid crystal variable retarder is mainly controlled by the applied voltage. A controller supplies a square-wave AC voltage output with amplitude that can be adjusted. The absence of moving parts provides quick switching times on the order of milliseconds.   To minimize effects due to ions in the materials, an LC device must be driven using an alternating voltage. Due to this function of the LCVR it permits the all-optical manipulation (phase-shifting) of light, which is usually required in DHM systems. The LCVR retardance is a nonlinear function of the applied voltage.

The phase retardance of LCVR depends on the laser beam wavelength and the applied voltage to it. The LCVR must be preliminary calibrated to find the exact phase retardance as a function of applied voltage without changing the polarization state of the input beam. Here the phase was reconstructed via the FFT method from off-axis digital holograms.

(a)   (b)
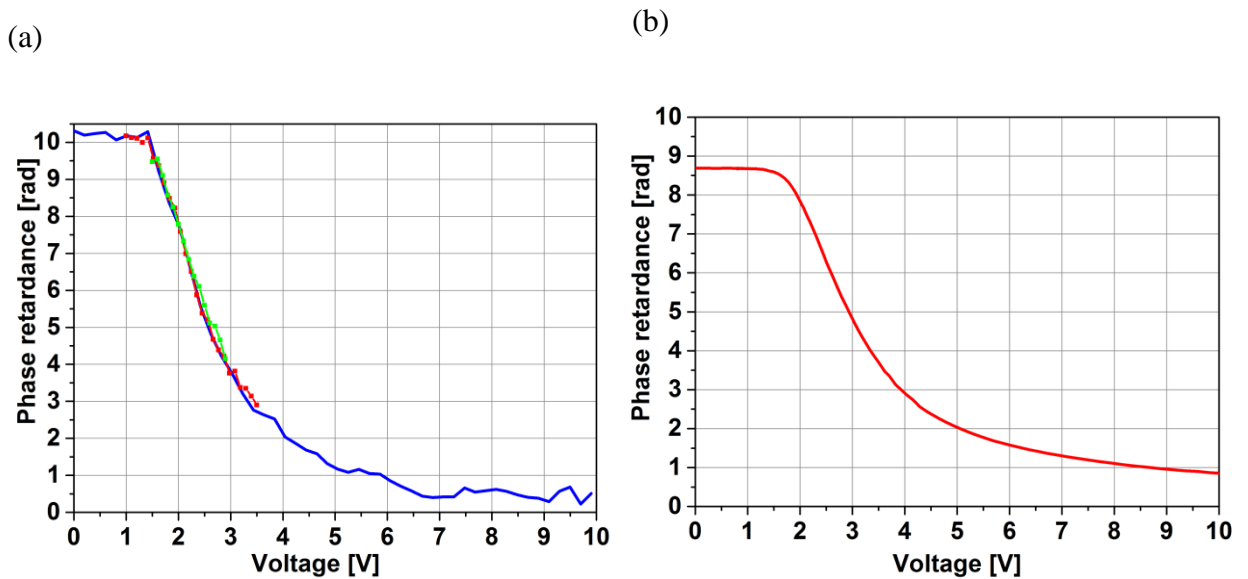
Fig. 3.11. (a) Reconstructed phase retardance for the laser wavelength 532 nm of the LCVR (LCVR-100"Medowlark optics" versus applied voltage., measured for three times (blue, red and green); (b) Phase retardance for the laser wavelength 633 nm given in the device manual.

To control the polarization states for the set of phase shifts, it is necessary to correctly adjust the anisotropy axes of the LCVR. Pure phase modulation was achieved by setting the optical fast (slow) axis of the LCVR at an angle of 0°(90°) with respect to the polarization of the incident

beam. The fine adjustment of the LCVR's axes was performed by Thorlabs' PAX1000VIS Polarimeter (Azimuth and Ellipticity Accuracy of ±0.25°).

The predominantly phase modulation was verified with an additional polarizer placed after the LCVR and intensity analysis on a CMOS camera. When the voltage across the phase plate was changed from 0 to 10 V, the intensity observed on the camera was invariant, which indicates that the phase is modified while the polarization state remains constant.

Fig. 3.11(a) shows the reconstructed phase retardance of the LCVR, depending on the applied voltage (with a step of 0.1 V). A more accurate analysis of the phase retardance was performed in the quasi-linear section $\Delta\varphi$ (V) 1.5-3.5 V with a step of 0.05 V and the dependence for three series of measurements, with a voltage change of 1.5-3.5 V and vice versa 3.5-1.5 V. Fig.3.11(b) illustrates the available data about the phase retardance given by the manufacturer in the technical specifications book. It depicts the dependence of the phase retardance on the applied voltage calibrated at a wavelength of 633 nm. As it can be noticed, the obtained plot for the wavelength 532nm maintains the trend of the retardance vs. voltage curve supplied with the device specifications.
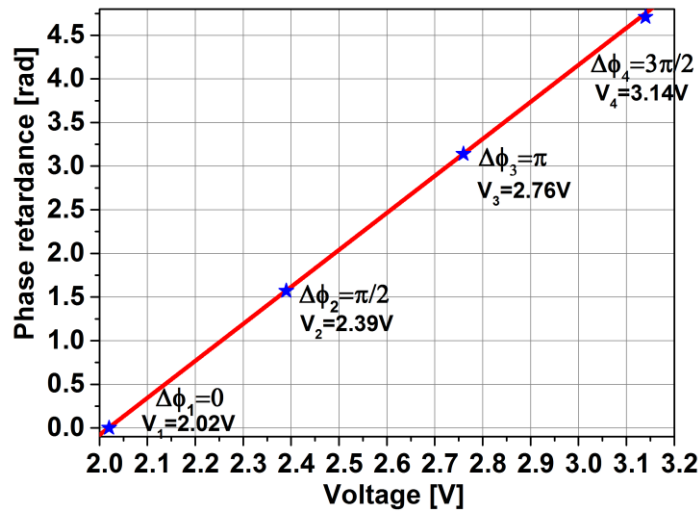
Fig. 3.12. A linear approximation of the LCVR phase shift in the region 2-3.2V vs. the applied voltages.

In addition, it can be noticed that phase retardance for 532 nm is higher at smaller voltages (1-2V) with successive decrease for greater values (3-10V) of the applied voltage. Since the DHM system described in the fifth chapter of this thesis requires to produce particular phase shifts equal to $\varphi_1 = 0$, $\varphi_2 = \frac{\pi}{2}$, $\varphi_3 = \pi$, $\varphi_3 = 3\pi/2$ a linear approximation of the LCVR phase shift in the region 2-3.2V vs. applied voltages was carried out. The calibration results are shown in Fig. 3.12. The initial applied voltage is 2.02 V where the phase shift is considered null. According to the formula $\Delta\varphi_n = a + bV_n$, where a=-8.58 and b=4.25 are constants, V_n is the corresponding

voltage, and n=1,2,3,4. The phase step is equal to $\pi/2$. After calculations, it was determined that the four phase changes pointed out above correspond to the voltages $V_1 = 2.02$ V, $V_2 = 2.39$ V, $V_3 = 2.76$ V, $V_4 = 3.14$ V, respectively.

3.4 Conclusions to Chapter 3

1. Experimental phase and polarization calibration of SLM and LCVR have been discussed in detail. The off-axis DH set-up was described as a hardware part of the phase calibration of optical system. The FFT and SPAR phase reconstruction algorithms were modified for the calibration procedure. If comparing the resulted curves that describe the SLM phase modulation as a function of gray level loaded to the SLM screen, FFT algorithm provides rather noisy data. In contrast, SPAR algorithm demonstrates better effectiveness due to the LLS approximations capable of removing the effects of external phase disturbance. Hence, a SPAR based algorithm was applied for further pixel-wise calibration of the SLM. From the detailed phase information extracted for each pixel, it can be noticed that in the region of maximum phase modulation, the standard deviation of the active part of the SLM pixel is 0.5 radians smaller if compared to the phase of entire SLM array. It can be presumed that, this outcome is the result of the "dead zones" of the SLM display, where the laser beam cannot be controlled. The standard deviation of the phase data from individual pixels and their active area prove the fact that SLM display exhibits spatial variations and the importance of SLMs calibration in precision applications.

2. An *ad hoc* calibration procedure for the SLM polarization modulation was presented. The described method requires a single-beam setup with relatively simple hardware components for evaluating the ellipticity and azimuth rotation angle as a function of gray level addressed to the SLM. The resulted graphs indicate that the SLM output polarization state is typically, elliptical. Only when a 125 gray level blank screen is loaded on the SLM display it keeps the linear polarization of the input light. Also, it shows that the larger the voltage applied to the SLM, the smaller becomes the light polarization modulation.

3. The phase shifting calibration of the LCVR by taking into account the polarization of the incident beam at a wavelength of 532nm is described. The calibration of the LCVR is a mandatory procedure, since detailed data about this device (on this exact wavelength) is not provided by the manufacturer. The phase shifting produced by the LCVR was done by a preliminary fine adjustment of the fast (slow) axis of the liquid crystal with the polarization plane of the incident beam. To produce accurate all-optical phase shifts, via DHM systems containing an LCVR, a linear approximation of the phase shift in the region 2-3.2V of the applied voltages was build.

4. The resulted calibration data shows that non-negligible errors are probable when controlling the phase and polarization of LC devices. For proper application of these devices, prior to use the SLMs, a characterization study must first be performed. The interferometric set-ups presented in this chapter are compatible with in-situ calibration and can be adapted to different optical systems. Furthermore, the software procedures included in the SPAR calibration algorithm compensate the effects of external noise which reduce the requirements for stability of the interferometer. The described procedures for region-by-region calibration of the SLM have valuable implementations in DHM.

4. DESIGN OF DOEs BY ANALOG AND DIGITAL PHR

Holographic recording (HR) is a technique that uses the phenomenon of interference for recording diffractive optical elements (DOEs). In contrast to the scalar holographic process, in which intensity variations in an interference pattern between identically polarized an object and a reference beams are recorded, polarization holography employs beams with two different polarizations states for hologram recording. Polarization holographic recording (PHR) is an effective holographic method that allows you to record holograms using orthogonal states of polarization of recording beams, i.e. phase holograms, which makes it possible to reveal the phase features of the DOE. In comparison to scalar HR techniques, PHR triggers the mass transport mechanism that leads to deeper surface relief formation. As a result, PHR allows pattern formation without extra wet post-processing steps.

Analog and digital PHR are two main techniques that can be distinguished. In general holography involves a two-stage process in which the wave field of the object is recorded in a first step so that it can be reconstructed in a second step. In physics it can be described by the phenomenon diffraction and interference used to record and reconstruct optical wavefields or 3D objects. The connecting element between the recording and reconstruction stages is the hologram. At the beginning, holography was a purely experimental and analog technique, holography was later digitalized step by step. Holograms were first simulated and later reconstructed by computer, the hologram storage medium became discretized optical elements, pixelated sensors, and light modulators.

Analog PHR deals with registration of continuous-space orthogonal two wavefronts and involves recording of light waves diffracted from object such as some physical items or optical components. Analog PHR offers higher resolution of the created DOEs due to the absence of pixelation in analog optical components, so high quality of holograms. It is important for phase holograms which are very noisy due to absence of amplitude image. But evidently, analog PHR is not so flexible, although offers more high-quality holograms, as in the case of complex DOEs.

Digital PHR presumes the utilization of the computational sampling of the recording wave fields. In this case, the amplitude and/or phase of the wave are digitally predetermined, encoded and preset via special software that permits optical control of the wavefront via liquid crystal SLM or other relevant/similar digital devices capable of dynamical and spatial manipulation of the electromagnetic waves. Hence, it is considered a more flexible approach for phase, amplitude or polarization modulation of the outcoming field thanks to the broad range of computer-generated digital holograms that can be used to create various shapes and geometries of DOEs.

The quality of the DOEs is determined not only by the recording techniques but also by the properties of light-responsive media. In fact, for performing successful patterning of DOEs it is important to select an appropriate medium that is both photo- and polarization-sensitive. ChG and azopolymers thin layers possess both properties and are suitable for micro- and nano-patterning via HR and PHR [206, 207]. Moreover, unique optical and structural proprieties of ChGs nanomultilayers and amorphous azopolymer thin films allow one-step formation of complex surface relief structures. Both scalar (photodarkening, photobleaching and photoexpansion) and vectorial (photoinduced anisotropy, photoinduced dichroism, photoinduced light-scattering, birefrigence) photoinduced phenomena can be observed in ChGs thin films as well as in azopolymers. These photo-sensitive media exhibit similar light-induced structural transformations, which are also related to defects creation and atoms diffusion.

Physical and/or chemical effects appear at the initial level of electron-hole excitation. ChGs and azopolymers respond by optical (anisotropy), mechanical (softening) or geometrical (expansion, contraction) changes. In turn, different types of DOEs are generated. Scalar effects such as photodarkening or photoexpansion appear even though all transition dipoles are randomly distributed after the exposure to unpolarized light. The mechanism underlying the vector effects such as dichroism (modification of the optical absorption) or birefringence (change of the refractive index) is based on partial conversion of transition dipoles along the y axis into x axis as a result of material exposure to polarized light along the y axis.

In this chapter analog and digital PHR are implemented as patterning techniques for recording of several types of DOEs on ChG NMLs and azopolymer thin films. The first section presents fabrication procedures of photosensitive ChG As_2S_3-Se and As_2S_3 nanomultilayers (NML) and azopolymer thin films. It includes the classification of DOEs as well as the optical characteristics of the materials. Section two describes analog and digital PHR setups that are built for recording on ChG NMLs including the diffraction efficiency kinetics as a function of the exposure time for every type of the obtained gratings. The second section of this chapter is devoted to analog and digital PHR on azopolymer thin films. It also comprises the schematic description of the mounted recording setups and the first-order diffraction efficiency kinetics for every type of the obtained DOEs. Besides it includes images of the diffraction patterns with are generated by patterned DOEs. The third section presents the conclusion to this chapter.

4.1 Fabrication technique of photosensitive ChGs NML and azopolymer thin films

4.1.1 Fabrication technique of ChGs NML

NML's of ChG were prepared by computer controlled successive cyclic thermal vacuum deposition of bulk As_2S_3 and Se from two separated boats. The glass substrate at room temperature was continuously rotated over the boats [12]. The structural stability at interfaces and in the nanomonolayer is critical for any superlattice, including NML. The direct determination of the periodicity and roughness of the interfaces of NML As_2S_3–Se deposited by cyclic thermal evaporation was performed in [208] by low-angle X-ray diffraction, where the author has shown the good quality of this NML. The deposition of the materials on the glass substrate was implemented through two separate windows. The offset windows over the boats have form of fragments of ring limited by two radiuses of a circular.

The technology allows film deposition control within the whole sample thickness range of 0.005 up to 3.0 µm. The monitoring and determination of the total NML film thickness during the thermal evaporation were carried out. Two interference thickness laser sensors at $\lambda = 0.95$ µm in transmission mode were applied in-situ. The total measured thickness of each composition on the substrate was measured by microinteferometer after deposition. The thickness of each nanomonolayer was calculated by dividing the total measured thickness by the number of complete revolutions of the sample. In Fig. 4.1, the photograph and the cross-section sketch are shown below.
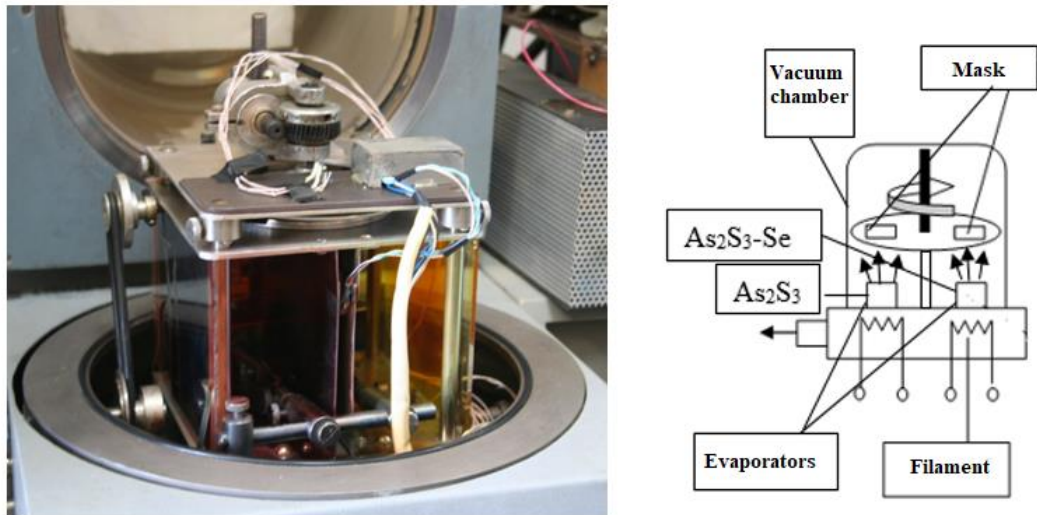
Fig. 4.1. Computer controlled cyclic thermal vacuum deposition technique.

The following deposition conditions were ensured for NML formation: boats temperatures of 400-600°C (this is considered a rather low temperature to prevent decomposition), residual

pressure in the vacuum chamber of at least 10^{-3} Pa, deposition rate of 10-20 nm/min, polished glass substrate keeping up at room temperature during the deposition of layers.

The developed equipment for PC controlled cyclic thermal vacuum deposition is illustrated in Fig. 4.1. Continuously rotating the condensed zones of NML sample over heaters decreases the local sample temperature and prevents interlayer components diffusion during the NML deposition. Otherwise, the deposited nanolayers under continuous heating turn into monolayer with a homogeneous composition.

The overlaying part of the sample contains alternating nanolayers of Se and As_2S_3, i.e., two wide rings overlap in the central part of the substrate, forming NML of As_2S_3–Se. The outside and internal rings of layers on the substrate contain pure compositions of As_2S_3 and Se, respectively. The layers of As_2S_3 and Se were obtained at the same time onto the same substrate, consequently through the windows, and used to check the composition and calculate the ratio of the layer thicknesses in one modulation period N (the total thickness of one As_2S_3 and one Se nanolayers). To prevent the possible crystallization of Se layers, which are rather structurally unstable under heating and/or illumination, the heating of layers during the deposition is minimized by virtue of substrate rotation and reduced boat temperature.

As a result, NML samples of As_2S_3–Se type structures with a total thickness of 1.5–3.5 µm and a total number of nanolayers up to 300 in the modulation period N = 10–50 nm range can be obtained.

(a)   (b)
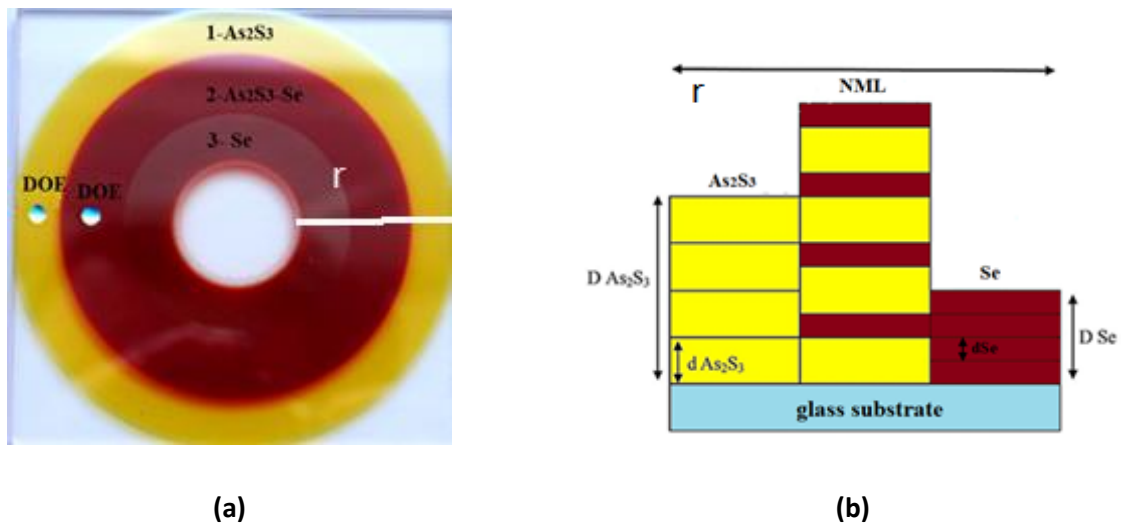
Fig. 4.2. (a) Picture of the obtained NML sample with the recorded DOEs, (b) cross-section of the deposed NML structure. The symbol "r" indicates the cross-section of the NML

The resulting samples were NML As_2S_3–Se structure with a total thickness of 2500 nm and a composition modulation period N = 12+13=25 nm. The NML structure has a number of nanolayers of 100 $_{As2S3}$ + 100 $_{Se}$.

The NML sample contained alternating As_2S_3 nanolayers with thickness of 12 nm and Se nanolayers of 12 nm. The total number of nanolayers was about 250, thickness's modulation period of pair As_2S_3+Se layers was about 24 nm. The total thickness of NML was 12 nm x 250 =3.0 µm. The last-mentioned parameter is critical in the recording process for obtaining high quality surface reliefs. The picture and sketch cross-section of the deposed NML structure is depicted in Fig. 4.2. The internal ring in Fig. 4.2 (a) contains pure Se; the middle ring is composed of overlapped nanolayers of As_2S_3 with nanolayers of Se, and the external ring consists of nanolayers of As_2S_3. Transmission spectra in the region 450–900 nm with the use of the spectrophotometer Specord M40 in order to determine separately the refractive index, the thickness, and the optical band-gap energy of As_2S_3, Se layers, and NML As_2S_3–Se were measured.

(a)   (b)
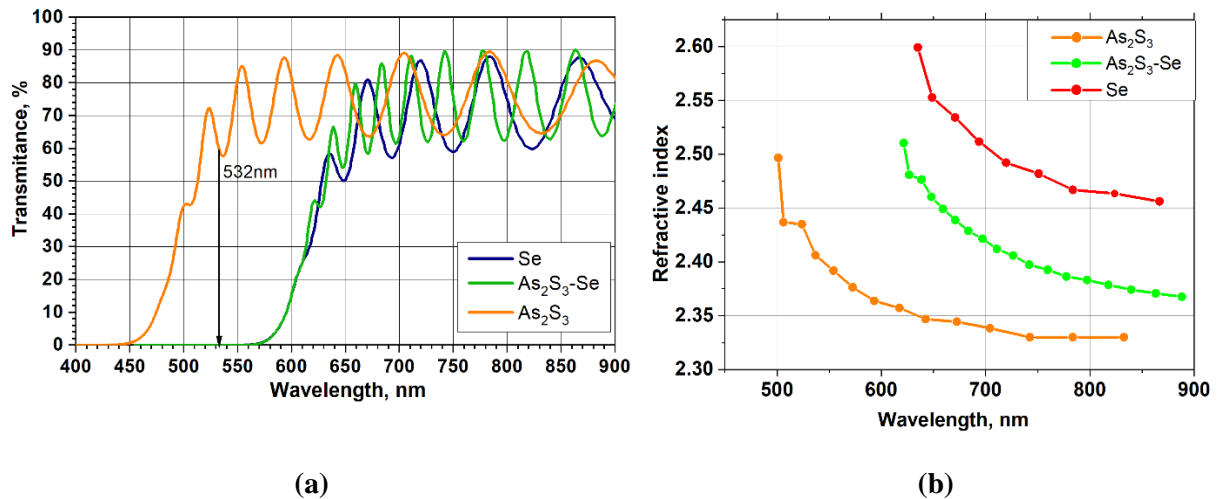
Fig. 4.3. (a) The optical transmittance spectrum of ChGs NML, (b) The spectral dependence of the calculated refractive index of ChGs NML.

The Swanepoel's method was used for refractive index calculation [209] by analyzing the transmission spectra of the obtained samples. The calculated refractive index for As_2S_3–Se NML and As_2S_3 at wavelength 632.8 nm was 2.46 and 2.40 respectively.

The transmittance spectrum curves presented in Fig. 4.3(a), indicate strong absorption at short wavelengths whilst at long wavelengths side there is a significant drop in absorption. The As_2S_3 NML s strongly in the region of 400–460 nm, the As_2S_3–Se and Se NML the region of absorption is extended to 580 nm. Based on the spectral dependence of refractive index shown in Fig. 4.3(b) a normal dispersion of the refractive index values of the NMLs is observed. The

calculated spectrum of refractive index of As_2S_3-Se NML is arranged between the spectra of the As_2S_3 and Se.

4.1.2 Fabrication technique of azopolymer thin films

The photo-sensitive azopolymer was synthesized by the polymerization of the poly-n-epoxypropyl carbazole (PEPC) with azo dye Solvent Yellow 3 (SY3) chromophore. Solvent Yellow 3 (4'-amino-2,3'-dimethylazobenzene) with dye content 90% is manufactured by Sigma-Aldrich Company, and was used without further purification. Azopolymers were obtained by the reflux method presented in Fig. 4.4, 0.3 g of PEPC and 0.1 g of SY3, which were dissolved in toluene and refluxed for 8 hours. The reaction of the azo dye attachment to the PEPC polymer matrix was carried out through the epoxy group.
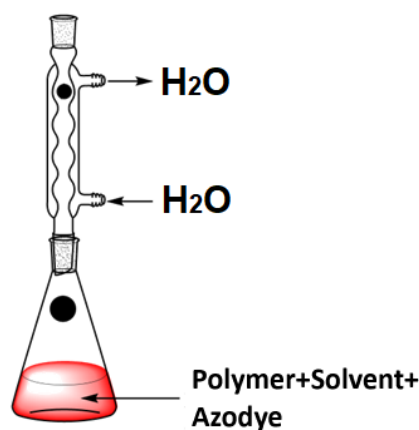
Fig. 4.4. Schematic diagram of the reflux method for obtaining azopolymers.

Taking into account the functional groups of the azo dye as well as the functional groups of the polymer matrix, the chemical bonding proceeds through different reaction mechanisms, which are interdependent with the functional groups. One of these mechanisms is the chemical bonding between the epoxy functional group and the primary amine functional group. This mechanism involves the chemical reaction shown schematically in fig. 4.5(a) and drives the polymerization of the poly-n-epoxypropyl carbazole (PEPC) with azo dye Solvent Yellow 3 (SY3) chromophore.

After the end of the reaction, the azopolymer solution was cooled and filtered. A polymerization reaction was utilized for chemical bonding of SY3 to PEPC polymer. A chemical structure of PEPC-co-SY3 (3:1) is presented in Fig. 4.5(b). According to the transmittance spectrum presented in Fig. 4.6(a), for 473 nm wavelength the absorption is about 80%. A laser working at this wavelength was used for DE recording. It can be seen that because film absorption at HeNe laser wavelength of 633 nm is small, this laser can be used for recording control.

Fabrication of the azopolymer based thin films was done via spin-coating (using programmable spin-coater "SGS Spincoat G3P-8"). This method offers uniformity as well as high spinning speed resulting in deposition of thin layers in the range of micrometers.

(a)

(b)
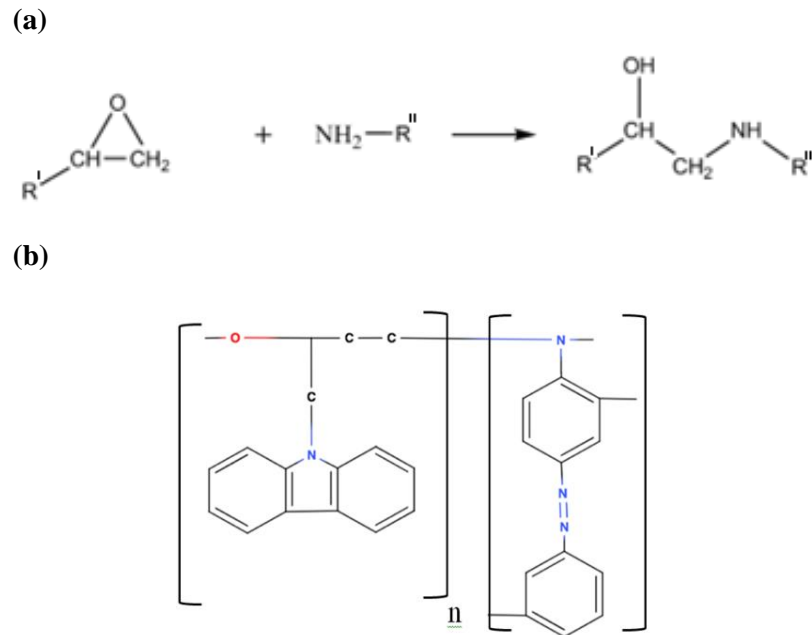
Fig. 4.5. (a) The chemical reaction between the epoxy functional groups and the primary amine functional group; (b) Chemical structure of the synthesized PEPC-co-SY3 azopolymer.

The set rotation speed benefits uniform evaporation of the solvent [210]. The coating material PEPC-co-SY3 (10wt.% homogeneous azopolymer) dissolved in toluene is deposited onto the glass substrate, which is made to rotate and distribute the solution by centrifugal force. In the final step, the applied thin film is dried in the oven at 60°C for 6 hours.

The obtained film thickness was determined by using the modified digital MII-4 interference microscope in the reflection mode with magnification of 530^x and a depth resolution of 15 nm [207]. The interference patterns of light reflected from the region of the deposed azopolymer and region of the glass substrate were recorded. The developed OpticMeter software was applied for high-accuracy processing of the interferograms [210]. The thickness of the films is equal to 1.0±0.027μm, and is calculated by measuring the corresponding line shifts. The spectral dependence of the refractive index was calculated from the reflectance spectra, which was determined from the relationship:

$$n = \left(\frac{1+R}{1-R}\right) + \sqrt{\frac{4R}{(1-R)^2} - k^2}, \qquad (4.1)$$

where R is the reflectance and k is the extinction coefficient, defined as k= λα/4π.
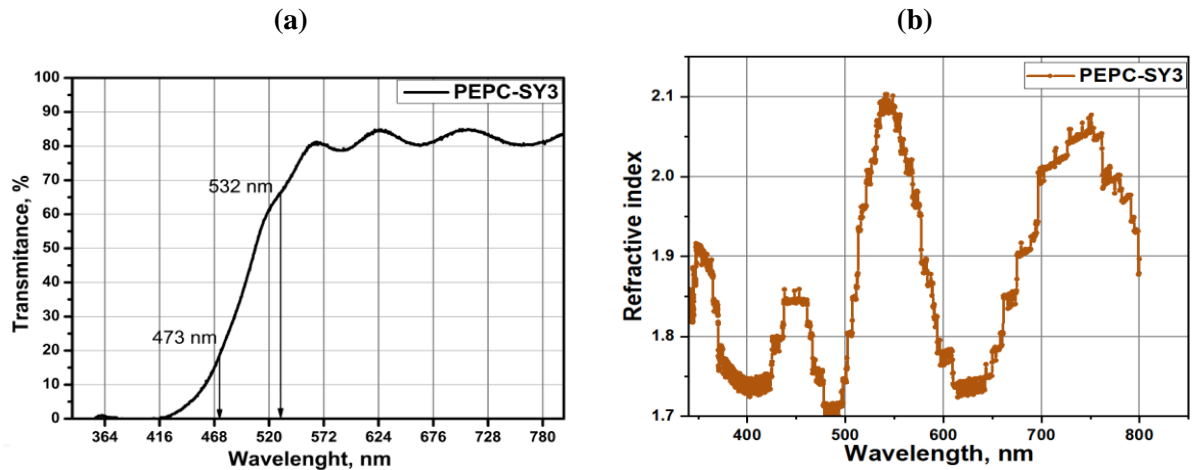
Fig. 4.6. (a) Transmittance spectrum of the synthesized PEPC-co-SY3 azopolymer thin film thickness 1.0 μm; (b) The spectral dependence of the calculated refractive index of PEPC-co-SY3 azopolymer thin film azopolymer thin film.

The spectral dependence of refractive index shown in Fig. 4.6(b) indicates a continuous increase of the refractive index values of the azopolymer thin film starting from 500 nm, with a maximal value at 532 nm and a subsequent drop of a refractive index until 633 nm.

4.2 Recording of DOEs on ChGs nanomultilayers

4.2.1 Analog PHR on ChGs nanomultilayers

The DOE is inherently a complex interferogram formed from diffraction gratings. A DOE is formed when the interference formed by the laser beams with photon energy equal or above the band gap energy irradiates the photosensitive thin film and strong absorption of the light takes place in the material [12, 211]. Due to the photosensitivity of the ChGs different photo/thermo-induced structural transformation occur under laser irradiation. The induced structural transformation depends on the material properties, photon energy, intensity, and polarization state of the laser beam. As an initial step for studying these media and all parameters of polarization recording processes, the diffraction gratings are recorded. They serve as preliminary recording examples. Three main types of diffraction gratings can be distinguished according to the recording media changes that occur during analog or digital PHR [208], as shown in Fig. 4.7:

1. RIG, due to the refractive index changes Δn.
2. SRG, resulting from the changes of thickness Δd.
3. Amplitude gratings, resulting from the change of the absorption coefficient Δα.

Types 1 and 2 represent phase gratings. In this thesis, only these types of gratings: RIG and SRG are investigated.
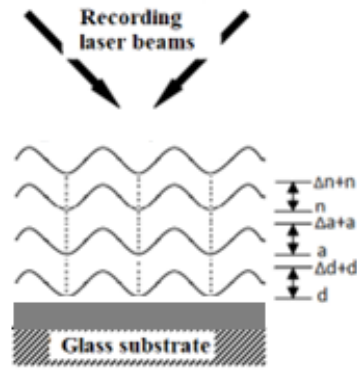
Fig. 4.7. Types of DOEs.

The purpose of our research is to investigate the optical and physical characteristics of the nanostructures formed on As_2S_3 and As_2S_3-Se NML. Specifically, it is aimed at identifying the differences between the recording properties of these materials. First, the analog PHR was implemented on ChGs NML for patterning a sinusoidal DOEs- a transmission diffraction grating. Unlike intensity holographic recording, PHR requires two different states of polarizations of the recording beams. As a result, the polarization state of the formed interference pattern is recorded on the photosensitive material. The two interfering beams independently pass through phase turning half-wave plates to provide a control over the polarization state of the writing beams. Interfering beams with P:P, S:S, ±45° polarization combinations were used for DOE recording. Figure 4.8(a) shows the experimental setup used to record sinusoidal gratings on As_2S_3 and As_2S_3-Se NML.

The recording arrangement was located on vibration isolated table in order to be insensitive to the environmental perturbation. The period of the gratings is determined by the following equation:

$$\Lambda = \lambda/(2\sin\frac{\alpha}{2}), \tag{4.2}$$

where λ is the recording wavelength and α is the angle between the two beams. A power density of 270 mW/cm^2 was used for the recording. Holographic relief gratings having period of 1 μm were recorded by laser beams having different polarization configurations. The angle was $\alpha = 30^O$ and equal intensities of the laser beams were used to achieve maximum contrast of the interference fringes. The intensity modulation of the formed interference pattern was evaluated by the interference contrast C calculated by the relation $C = \left|\frac{I_{max}-I_{min}}{I_{max}+I_{max}}\right| * 100\%$, where I_{max} and I_{min} are the maximum and minimum of the light intensities in the interference pattern.

In order to investigate the kinetics of the photo-induced gratings patterning, the DE in dependence on the exposure time is measured by a laser diode (LD) and two photodiodes for the intensity measurement at zero I_0 and first I_1 diffraction orders.

(a)
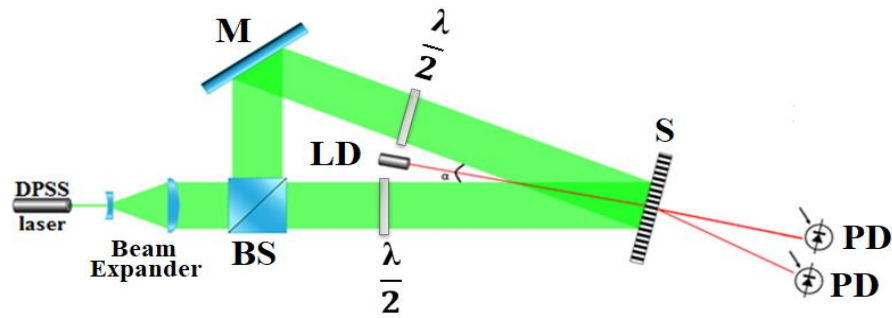
(b)
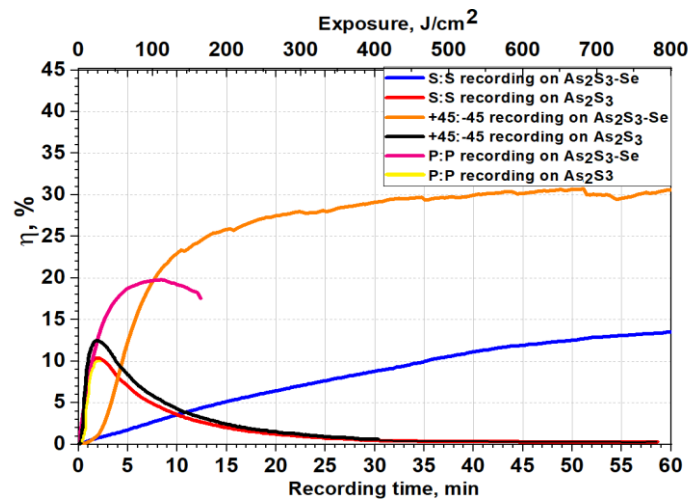
Fig. 4.8. (a) Holographic recording setup: single mode laser DPSS (λ=532nm, 100 mW),
beam expander, BS-beam splitter 50/50, PD-photo diodes, M-mirror, LD-laser diode
(λ=650 nm, 1 mW), sample of As_2S_3 film or As_2S_3-Se NML, α-angle between incident
beams, λ/2-half wave plate on the rotation stage; (b) Kinetics of the first-order
diffraction efficiency of the recorded DOEs with different polarizations of the recording
beams.

The DE of the gratings was measured for the $\lambda = 650$ nm since this wavelength does not
influence the recording process. The DE in the first order was calculated by: $\eta = I_1/(I_0 + 2I_1)$. I_1
and I_0 represent the light intensities in the first and zero orders of diffraction, recorded by the
photodiodes, as shown in Fig. 4.8 (a). Series of holographic gratings with different DE were
obtained by varying the exposure time. Figure 4.8(b) shows the evolution of the diffraction
efficiency as a function of the exposure time. The DE changes were observed in real time during
the holographic recording process. The kinetics shows that the DE behavior with the increasing of
the exposure time is different for two types of structures, namely As_2S_3 and As_2S_3-Se NML. The
As_2S_3 samples exhibit DE maxima in all used polarization combinations, with subsequent decrease
of DE values.

For the S:S polarization states configuration, the DE of As_2S_3 thin films reaches the maximum of 10.7% at exposure of 70 J/cm^2 and recording time of 2 min. The DE of As_2S_3-Se NML increases constantly without saturation, reaching ~14% as shown by the blue curve from Fig. 4.7(b).

The orange curve in Fig.4.8 (b) illustrates the kinetics for the grating formation in As_2S_3-Se NML, in ±45° polarization configuration. It is remarked that a significant increase of the η to a maximum value of 31%, is reached within 50 minutes of recording. It can be seen that S:S polarization states configuration is most effective from the point of view of DE value. The DE for the DOE obtained on As_2S_3 NML reaches a maximum of 13.5% in about two minutes, as shown by the black curve in Fig. 4.7(b).

For the P:P polarization configuration a rapid increase of the η for the As_2S_3 NML thin films reaching a maximum of 13% in the second minute of the recording process, shown by the yellow curve in Fig. 4.7(b). It is followed by a decrease of the η caused by the overexposure which is producing a reduction of the volume of the grating. The DE of As_2S_3-Se NML reaches a maximum of about 20% in 7 minutes of exposure followed by a decrease, as shown by the pink curve from Fig. 4.7(b).

It is assumed that in the As_2S_3 film, two opposite processes take place: the RIG patterning and amplitude grating formation on the base of absorption coefficient changes. Whereas in As_2S_3-Se NML the mass transfer phenomenon of grating recording occur, this is inertial and predominate over others.

4.2.2 Digital dual-beam PHR of sinusoidal DOE on ChGs nanomultilayers

A SLM was integrated in the recording setup for performing digital PHR. The essence of SLM utilization for PHR is the computer-generated hologram, which involves numerical calculation of the pattern rather than producing it photographically. Since SLM is a typical digital optical component, to stimulate its diffraction of the light waves, it must be considered the specific SLM parameters such as actual size, pixel dimension, sampling in spatial domain and phase levels. The phase SLM acts as a sophisticated diffraction grating which transforms the phase of the transmitted light beam into a specific pattern. The phase modulator, in contrast to amplitude one, is more efficient as it completely redirects the incoming light to the outcome image. Almost no laser intensity is lost. A complex DOE was imprinted simultaneously by means of two different recording modes, operating in a parallel regime. The first recording mode functions as a single beam setup, with the SLM display located in the object arm of the PHR system. The dynamic

phase range of the SLM (LC2002 HOLOEYE) used in our experiment depends on the wavelength of incident light and is less than 2π for $\lambda=532$ nm. A sinusoidal grating was displayed on the SLM. The period of the sinusoidal grating addressed to the SLM was set 20 µm and cannot have a smaller value due to the pixelated nature that affects the generated digital hologram. Particularly, electric field overlapping across the neighboring pixels results in a blurring effect on the sharp edges between pixels. A long focus AR coated lens (+700 mm) and short focus lens (+60 mm) for creating almost paraxial beam were mounted after SLM. For avoiding diffraction orders caused by the SLM screen pixelation, a diaphragm was places between these lenses. The sample was placed in the collimated zone. The pixel pitch of the SLM is equal to $32\mu m$, which is the sampling interval of the SLM in the spatial domain for the hologram.

The DOE is patterned on the As$_2$S$_3$-Se NML by an incident beam that passes through a digital sinusoidal grating addressed to the SLM display. The dual-beam PHR setup is pictured in Fig. 4.9 (a). The first polarizer placed before the SLM ensures high extinction ratio of the linear polarization of the input beam.
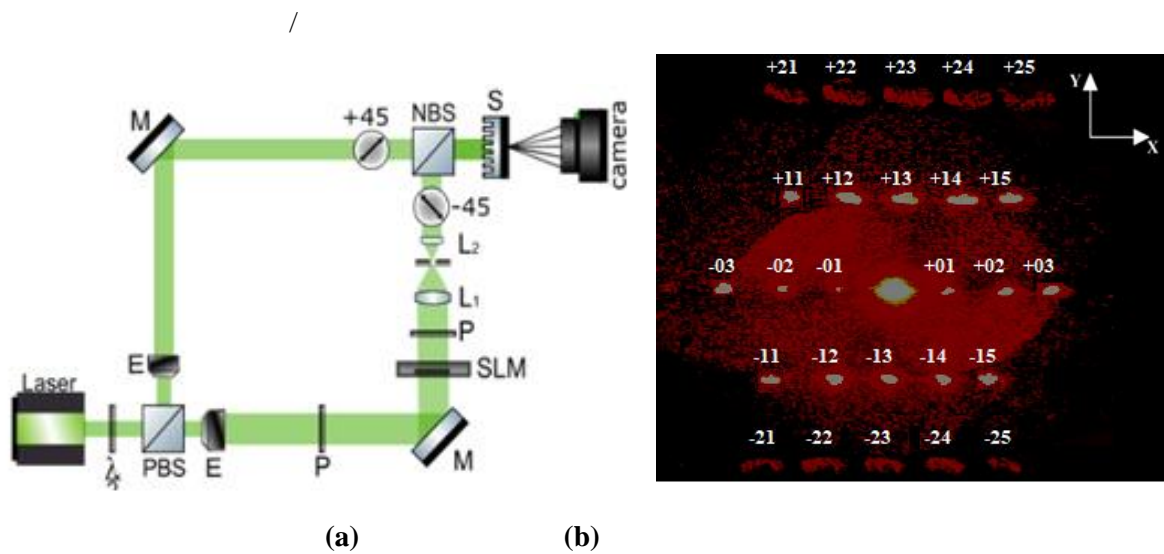
Fig. 4.9. (a) Digital dual-beam PHR setup for micro-patterning complex DOE. CW DPSS laser (λ=532 nm, power =2W, TEM00 mode), M – mirror, PBS – polarized beam splitter, NBS- non-polarized beam splitter, E-beam expander, SLM-spatial light modulator LC-2002 with a resolution of 800 × 600 pixels and a pixel pitch of 32 µm, S – sample; λ/2- half wave plate, P-polarizer, L1, L2-lenses, (b) the spatial multiplexed diffraction pattern generated by the DOE obtained via dual-beam digital PHR on ChGs nanomultilayers.

Since SLM changes the polarization of the input beam, to select proper polarization of the output beam the second polarizer is placed after the SLM. When the SLM-generated hologram is illuminated by an incident Gaussian beam, a diffraction pattern is created in the output signal. For

avoiding the redundant diffraction order caused by SLM screen pixelation, a diaphragm between these lenses was placed.

The second recording mode functions as a Mach-Zehnder interferometric recording set-up due to adding of the reference arm to the patterning system. The complex DOE is formed when the object beam passing through the SLM and possessing -45^0 polarization and the plane Gaussian reference beam possessing +45^0 polarization states (with regard to the plane of interfering beams) interfere. In this way, the angle between polarization states of the interfering beams is 90^0. The complex DOE generates diffraction maxima, as shown in Fig. 4.9(b). The diffraction image has a 2D space distribution. The distribution of diffraction maxima along X-axis coincides with the space distribution maxima obtained by the single-beam recording mode that includes a SLM. The diffraction maxima along Y-axis are significantly bigger and brighter.
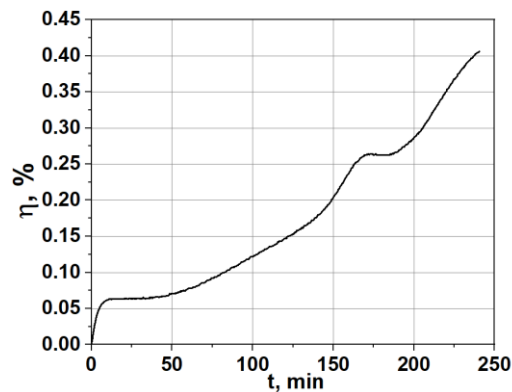
Fig. 4.10 Kinetics of the first-order diffraction efficiency DOE obtained on $As_2S_3 - Se$ NML by digital PHR

It can be supposed that the recorded DOE consists of two surface gratings in X and Y directions of the sample plane. The grating period on the X-axis resulting from the first recording mode is 20.0 µm and is tuned by the frequency of the hologram fringes displayed on the SLM. The grating period on the Y-axis resulting from the second recording mode is 5.0 µm, and is determined by the angle θ≈60 between reference and the object wave beams of the optical setup. The black curve in Fig. 4.10 shows the DE evolution measured online in the +01-diffraction order obtained by dual-beam recording setup and coincides with the +01-diffraction order obtained. The DE value in +01 diffraction order is about 0.4%, reached within 240 minutes of exposure. It is important to note that the DE measured from the obtained DOE represents a relative value because it is measured after the exposure. The DE's kinetics being approximated by calculations from the +01-diffraction order was measured during the recording process. The real efficiency might be higher if considering all the diffraction maxima.

4.3 Recording of DOEs on azopolymer thin films

4.3.1 Analog PHR on azopolymer thin films

The intensive research in the field of optical materials has shown that light-induced surface deformation in azopolymers is based on the molecular reorientation of the azo-chromophores perpendicular to the electric field vector of light by a series of *trans–cis–trans* isomerization cycles. There are still no models fully describing the photo-induced processes in azopolymers, due to the large number of factors that must be considered, such as the reorientation of molecules, changes in polymer matrices, the influence of surface forces, mass transfer, changes in optical properties, and the redistribution of light energy in the formed relief. But, as confirmed by most of researchers, the polarization states of the object and reference beams strongly influence the formation of photo-induced surface gratings. In this section, analog PHR setups used for obtaining sinusoidal, hexagonal superimposed DOEs and DOEs capable of generating optical vortices on carbazole-based azopolymer thin films is described.

Sinusoidal DOEs

The setup configuration used for analog recording of sinusoidal single and superimposed DOEs is shown in Fig. 4.11(a). The recording laser is single mode DPSS laser, $\lambda = 473$ nm, with a power density of 1700 mW/cm^2. The polarization states of the incident beams were LCP: RCP were obtained by $\lambda/4$ quarter-wave plates also known as wave retarders. The interfering beams formed a sinusoidal pattern on the azopolymer surface. The angle between interfering beams is $\theta \approx 4^0$ and the period of the grating on the X-axis is about 7 μm (Fig. 4.11(a) inset). To evaluate the performance of the obtained DOEs the DE evolution has been measured by two photodiodes and a laser diode with a wavelength of $\lambda = 650$ nm, P=5 mW which features is not actinic to the azopolymer film.

For obtaining a superimposed DOE the azopolymer film is mounted on a fine ($\pm 1°$) rotation stage. The sample was exposed to the interference pattern for a fixed period of time. After each exposure, the sample was rotated twice (60^0, 120^0) around the optical axis to achieve the required orientation of the grating vector relative to the previous one. By this way hexagonal form of diffracted beam in XY plane with sinusoid in Z axis is obtained.

To fabricate a superimposed structure with n-fold rotation symmetry, the rotation angle was π/n and n exposure steps were required. The time period for each exposure was constant and equal to 60 min. For obtaining a hexagonal DOE the stage was rotated 2 times. The DE exhibited by the obtained sinusoidal DOE reaches 33% in 50 minutes of exposure.

102
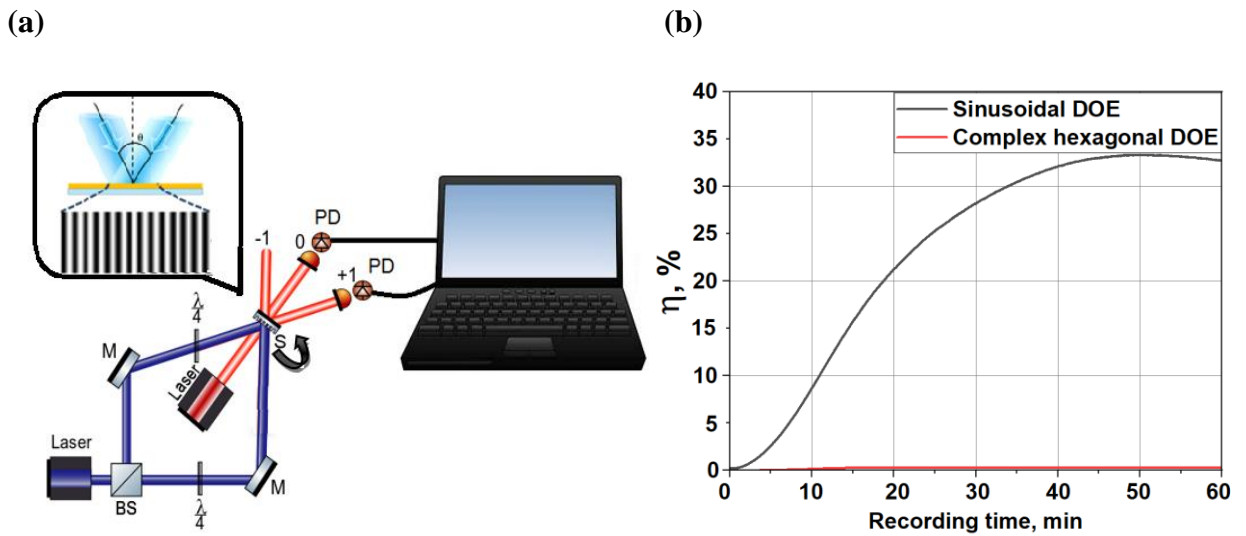
Fig. 4.11. (a) Polarization holographic recording setup for recording sinusoidal and superimposed DOEs: Laser-single mode DPSS (λ =473 nm, P=100 mW), BS-polarized beam splitter, M-mirrors, λ/4-quarter wave plate, Laser Diode (λ =650 nm, power =5 mW), S-azopolymer thin film placed on a rotating stage, PD-photodiodes for DE registration, (b) Kinetics of the first-order diffraction efficiency of the recorded DOEs.

The DE exhibited by the obtained hexagonal DOE barely reaches 0.1% during the entire exposure time. It can be explained by the fact that the measured DE of the hexagonal DOEs is relative value as it comprises multiple generated maxima making. Fig. 4.12 illustrates the diffraction maxima of generated by the sinusoidal and superimposed hexagonal DOEs.

(a)

(b)
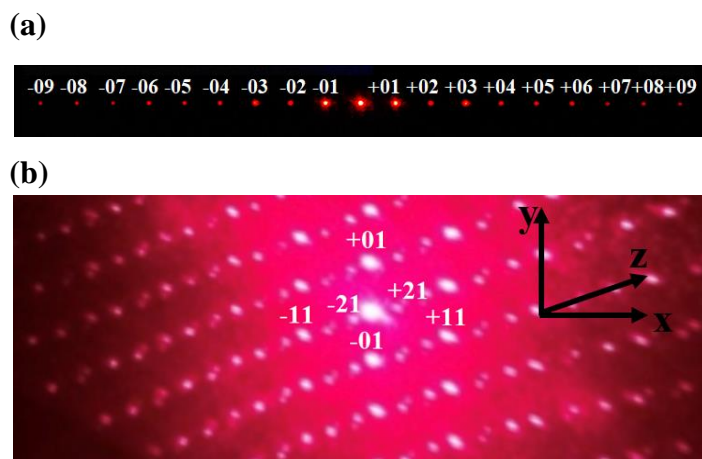
Fig. 4.12. Picture of the diffraction pattern of (a) sinusoidal DOE, (b) the superimposed hexagonal DOE.

The sinusoidal grating generates a typical diffraction pattern that includes diffractions maxima aligned along a single line. The hexagonal grating generates a spatial multiplex diffraction

pattern with maxima arranged in multiple lines. The maxima obtained along Y-axis are indicated by +01, -01 in Fig. 12(b). After rotation of the stage to 60^0 are recorded the maxima recorded aligned along the X-axis, indicated by +11, -11 in Fig. 12 (b). Finally, after the second rotation of the stage by 600°, the maxima recorded along the z axis are registered, designated +21, -21 in Fig. 12. (b).

Vortex DOE

The vortex DOE was patterned on azopolymer thin films via analog PHR using a vortex phase retarder (VPR) as a vortex mask. The VPR (half-wave plates WPV10L-532, topological charge TC=1 from Thorlabs) generates non-diffracting Bessel beams. It changes the azimuthal and radial polarization of the optical field. Specifically, this retarder is a polarization-sensitive plate which transforms the incident Gaussian beam into a "donut hole" shaped Laguerre-Gaussian mode. It has been determined that only the circular polarization of light preserves the same polarization state after the VPR. So, to ensure the recording of orthogonal polarization states, the right and left circular polarizations (RCP: LCP) of the object and reference beams are used, respectively.
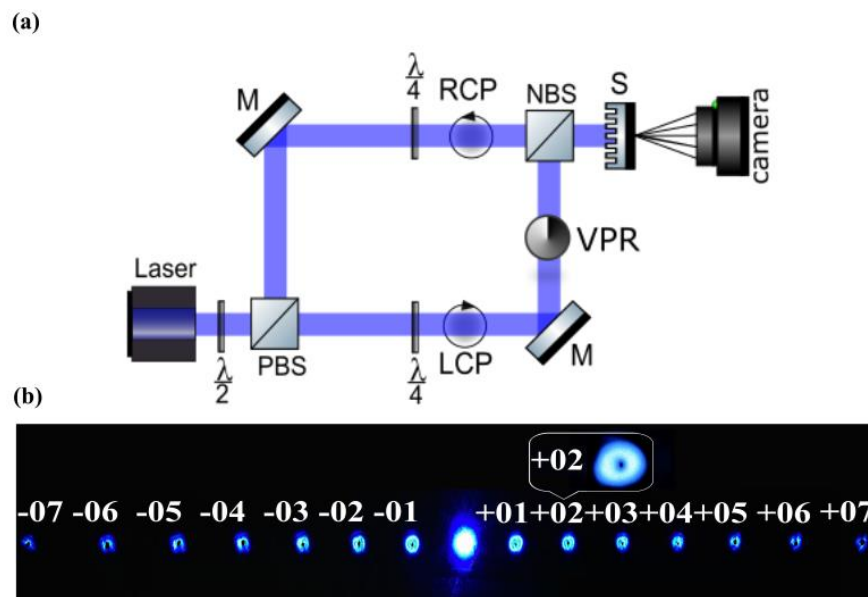
Fig.4.13. (a) Analog interferometric arrangement for vortex DOE recording via VPR. The components of the setup are: CW DPSS laser (λ=473 nm, power =100 mW), M – mirror, PBS – polarized beam splitter, NBS- non-polarized beam splitter, VPR-vortex phase retarder plate, S – sample; λ/4- quarter wave plate, λ/2- half wave plate, camera - 12MPxs camera; (b) diffraction image of the phase singularities (donuts) displayed in the diffraction pattern.

104
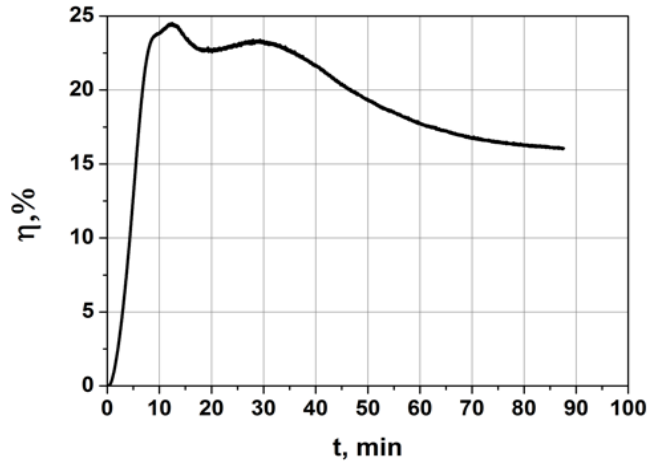
Fig. 4.14. Kinetics of the first-order diffraction efficiency of the recorded vortex DOE obtained by VPR-based PHR.

The sketch of the PHR setup based on a VPR is illustrated in Fig. 4.13(a). The laser beam polarization state is inclined at 45^0 by a half-wave plate. Two quarter-wave plates with fast axes reciprocal angles at 90^0($+45^0$ and -45^0 to vertical axis) create RCP and LCP. The DOE is produced by interference between a spiral wavefront formed after a laser beam passes through the VPR and a plane wavefront of the reference beam. The VPR generates an OAM with a TC equal to 1. Both interfering beams pass through quarter-wave plates for obtaining a polarized DOE. The angle between interfering beams is approximately $\theta \approx 3.6°$.

This angle determines the period of the grating on the X-axis of approximately 7.5μm. It can be underlined that the DOEs that are used to create optical vortices are fabricated in a one-step recording process. The resulted diffraction pattern projected on the camera is pictured in Fig.4.13 (b). The collinearly aligned phase singularities can be observed on the diffraction image.

The presence of numerous diffraction maximums (at least ±7) points out to the thin grating regime of diffraction. To estimate the performance of the vortex DOE, the diffraction efficiency (DE) evolution was monitored and measured during the recording process, as shown in Fig. 4.14. It can be noted that DE represents an integral characteristic of the diffracted power, that does not take into account its spatial distribution. Nevertheless, DE is one of the main characteristics of the DOE that measures the amount of optical power diffracted into a selected direction (given diffraction order) in comparison with the power of the incident beam. The value of DE was measured by the low intensity laser beam with a wavelength λ= 473 nm. The DE exhibited by the obtained vortex DOE reaches 24% in 12 minutes of exposure. It was measured in the first diffraction order +01 which is shown in Fig. 4.13(b).

The applied VPR for PHR provides high diffraction efficiency vortex beams, VPR is a passive optical component that restricts the geometrical variation of azopolymer surface modulation in addition to the limited number of dimensions where the diffraction orders can be spatially distributed. For ensuring dynamic changes in the optical characteristics of the beam shape a SLM was incorporated in the single-beam and dual-beam digital PHR setups.

4.3.2 Digital PHR of vortex DOEs on azopolymer thin films

Single-beam PHR via SLM

Computer-generated holograms of vortex displayed on SLM panel were used. It is another powerful method for generating beams with a desired singular phase distribution and topological charges TC=1 and TC=2. The two-dimensional intensity distribution, which would be observed as a result of interference was calculated.

For performing digital PHR of vortex DOEs a SLM was integrated in the recording optical systems. The essence of SLM utilization for PHR is the computer-generated hologram that involves numerical calculation of the pattern rather than producing it photographically. The phase SLM panel acts as a sophisticated diffraction grating which transforms the phase of the transmitted light beam into a specific pattern. The phase modulator, in contrast to amplitude one, is more efficient as it completely redirects the incoming light to the outcome image. The dynamic phase range of the SLM (LC2002 HOLOEYE) used in our experiment depends on the wavelength of incident light and is less than 2π for wavelength of λ=532 nm. Therefore, a fork-shaped grating (FSG) is displayed on the SLM panel instead of a vortex phase mask. Another issue is that the SLM's panel pixelated nature affects the generated digital hologram. Particularly, electric field overlapping across the neighboring pixels results in a blurring effect on the sharp edges between pixels. The digital FSG image is incorrectly reconstructed if this limitation is not appropriately solved. Consequently, in our experiment the periodic pattern displayed on the SLM panel cannot have a period smaller than pixel pitch 32~~0~~-µm.

The DOE is patterned on the azopolymer thin film by an incident beam that passes through a digital FSG with a TC equal to 2 that was addressed to the SLM panel. The laser beam was expanded as much as the diagonal of the SLM panel. The PHR setup is pictured in Fig. 4.15(a). The first polarizer placed before the SLM ensures high extinction ratio of the linear polarization of the input beam. Since SLM panel changes the polarization of the input beam, to select proper polarization of the output beam the second polarizer is placed after the SLM. When the SLM-generated hologram is illuminated by an incident Gaussian beam, a vortex is created in the output

signal. For avoiding the redundant diffraction order caused by SLM panel pixelation, a diaphragm between these lenses was placed. When the SLM-generated hologram will be illuminated by an incident Gaussian beam, a donut is created in the output diffraction pattern.
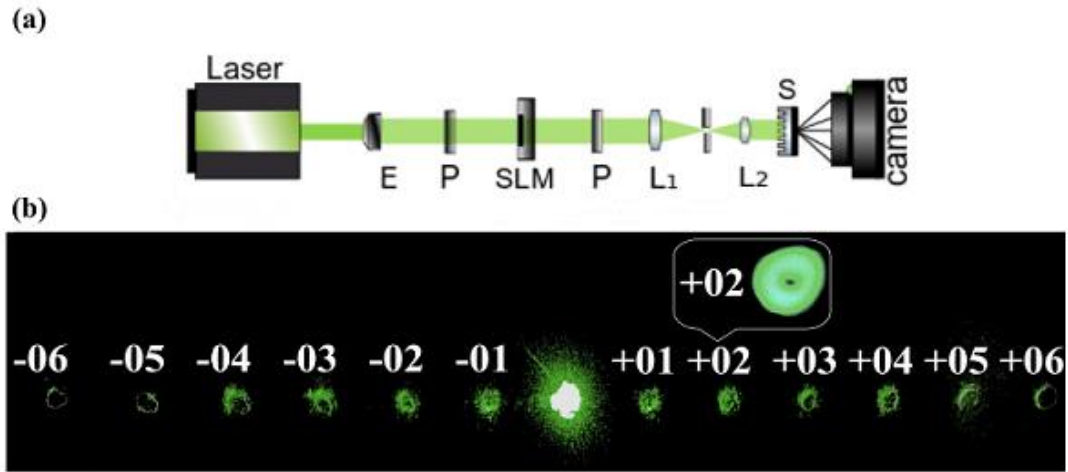
Fig. 4.15. (a) Digital PHR setup with a single beam. CW DPSS laser (λ=532 nm, power =2W, TEM00 mode), E-beam expander, SLM-spatial light modulator LC-2002 with a resolution of 832 × 624 pixels and a pixel pitch of 32 μm, P-polarizer, L1, L2-lenses, S-sample; (b) image of the phase singularities displayed in the diffraction pattern generated by the vortex DOE recorded by the single-beam PHR via SLM.

Low-intensity phase singularities arranged in a single line can be observed in the diffraction image in Fig.4.15 (b). From the diffraction pattern formed by the vortex DOE recorded on PEPC-co-SY3 thin film it can be observed that the space distribution of light intensity is "donut-hole" with reduced uniformity of the diffraction maximums. This is proved by DE kinetics which is presented by the black curve in Fig. 4.17. The maximum DE measured in the first diffraction order +1 is only 0.1% after 180 minutes of exposure. It is clear that all laser beam energy is distributed to in 0at least 12 orders.

Dual-beam polarized holographic recording via SLM

Dual-beam polarized holographic recording via SLM was implemented on azopolymer thin films for obtaining spatially multiplexed phase singularities. The complex vortex DOE was imprinted simultaneously by means of two different recording modes, operating in a parallel regime. The first recording mode functions as the single-beam PHR described previously, with the SLM display located in the object arm of the optical setup, as pictured in Fig. 4.15(a). The second recording mode functions as a Mach-Zehnder interferometric recording setup due to the addition of the reference arm to the patterning system. The dual-beam PHR setup is shown in Fig. 4.9 (a).

The vortex DOE is formed when the object beam passing through the SLM and possessing -45^0 polarization and the plane Gaussian reference beam possessing +45^0 polarization (with regard to the plane of interfering beams) interfere. In this way, the angle between polarization states of the interfering beams is 90^0. As a result, only the phase pattern was recorded on the thin film, and amplitude was not recorded.
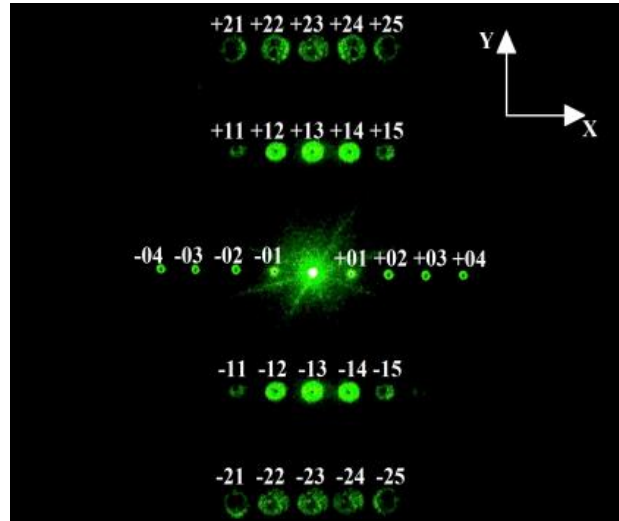
Fig. 4.16. The spatial multiplexed diffraction pattern in donut-shape was obtained via dual-beam digital PHR.

As shown in previous investigations [207] on digital PHR recording on azopolymer thin films, cross-polarized states of light beams controlled by half-wave plates facilitate the maximum surface relief modulation. The half-wave plate placed immediately after the laser controls the polarization direction of the incident beam with regard to the beam splitter. The polarized beam-splitter provides 30:70 intensity ratio with a minimal dependence on the polarization state of the incident light. For covering the entire SLM matrix, the incident beams were expanded. To scale the hologram transmitted through SLM in correspondence to the recording spot on the film, two lenses with different focal lengths were used.

The photo-induced vortex DOE generates multi-channel vortex beams, as shown in Fig. 4.16. The phase singularities arranged in multiple lines can be observed in the diffraction pattern displayed on the camera. The diffraction image has a 2D spacial distribution. The distribution of diffraction maxima along the X-axis coincides with the space distribution maxima obtained by single-beam recording via SLM as described in Fig. 4.15 (b). The diffraction maxima along the Y-axis are significantly bigger and brighter, and the distance between them corresponds to the 5.0 μm grating period.
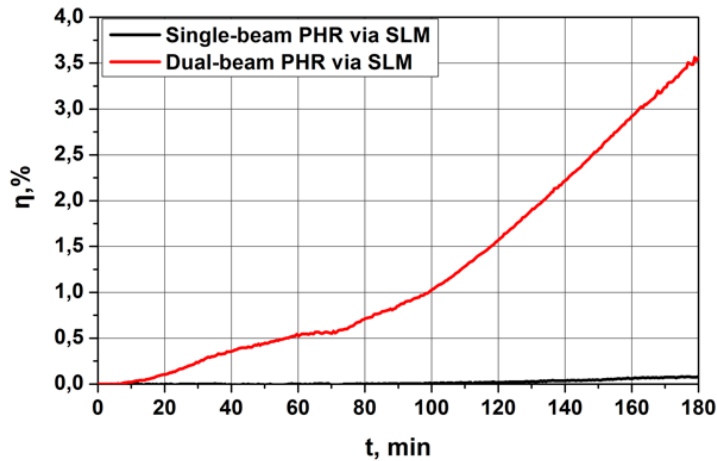
Fig. 4.17. Kinetics of the diffraction efficiency in the +01 order of the recorded vortex DOEs obtained by digital PHR via SLM.

It can be supposed that the recorded DOE consists of two surface gratings in X and Y directions of the sample plane. The grating period on the X-axis resulting from the first recording mode is 20.0 µm and is conditioned by the frequency of the hologram fringes displayed on the SLM panel. The grating period on the Y-axis resulting from the second recording mode is 5.0 µm, and is determined by the angle $\theta \approx 60^0$ between the reference and the object ~~waves~~ beams of the optical setup. The black curve in Fig. 4.17 shows the DE evolution measured online in the +01-diffraction order obtained by a dual-beam recording setup and coincides with the +01-diffraction order obtained via a single-beam recording setup. The DE value in +01 diffraction order is about 0.1%. The red curve describes the DE evolution in the +13-diffraction order. The DE value reaches 3.5% after 180 minutes of exposure. It is important to note that the value of DE's measured from the obtained DOEs represent a relative value because it comprises the entire "donut-hole" including the isolated intensity zero present in the phase singularity. Thus, when excluding the regions with zero intensity, the real efficiency might be higher.

4.4 Conclusions to Chapter 4

1. Analog and digital polarization holographic methods were exploited for obtaining multifunctional DOEs with different geometries on ChGs NML and azopolymer thin films. The investigation of the diffraction efficiency kinetics for different polarizations of the recording beams was made for every DOE.

2. Analog PHR with S:S, P:P, ±45° and RCP:LCP polarization configurations were implemented on ChGs NML and a series of SRG and RIG were obtained. The highest DE was obtained for DOE recorded by ±45° polarization configuration reaching 31% for As_2S_3-Se NML

and 13.5% for As_2S_3 NML. Digital dual-beam PHR was applied on As_2S_3-Se NML producing a complex sinusoidal DOE that generated special multiplexed diffraction maxima. It can be supposed that the recorded DOE consists of two orthogonal surface gratings in the X and Y directions of the sample plane. The grating period on the X-axis resulting from the first recording mode is tuned by the period of the hologram fringes displayed on the SLM. The grating period on the Y-axis resulting from the second recording mode is determined by the interference produced by the reference and the object waves beams of the optical setup. The obtained DE value is about 0.4%, which is a relative value as it is estimated from a single diffraction maximum. The real efficiency is higher if considering all the diffraction maxima.

3. Analog PHR in LCP:RCP polarization configuration was implemented on azopolymer thin films for patterning sinusoidal, superimposed hexagonal and vortex DOEs. The DE exhibited by the obtained sinusoidal DOE reaches a maximum of 33%. The DE exhibited by the obtained superimposed hexagonal DOE barely reaches 0.1% during the entire exposure time. Similar to previously evaluated DE on ChG NMLs, it can be explained by the fact that the measured DE of the superimposed hexagonal DOEs is relative value as it comprises multiple generated maxima making it difficult to evaluate the real efficiency. In addition, DE of DOE recorded on azopolymer thin films does not describe entirely of DOE's form due to closeness of refractive index azopolymer and air.

4. The designing process of vortex DOEs on carbazole-based azopolymers is described for analog as well as digital PHR. The patterned vortex DOEs are capable of generating single-channel and spatial multiplexed phase singularities. The spiral wavefront generated by analog PHR via VPR produces DOEs that create vortex beams with high diffraction efficiency, however the variability of the spatial distribution of the diffraction pattern is limited. In contrast, the digital generation of the spiral wavefront by SLM introduced in the PHR system is a more flexible source that permits to record DOEs that generate 2D and 3D spatial distribution of the diffraction patterns.

5. The specific advantage of the presented results is the combination of PHR with a new polarization-sensitive azopolymer, which permits to obtain DOEs with a deep surface relief of about 40% with respect to the total thin film thickness. The implemented analog and digital PHR in different optical setups have proven to be an applicable one-step method for patterning vortex DOEs that generate phase singularities. Although it seems that both approaches permit to fabricate DOEs that produce similar fields, the variation of the vortex beams parameters must be considered. The fast axis angle orientation over the surface of an analog vortex is complex (rotates from 0^0 to 180^0). It is working as a half-wave retarder and needs a polarization camera to characterize it. The highest diffraction efficiency of 24% is exhibited by the DOE patterned via an analog VPR, while

the DOE obtained by the digital single-beam interferometric setup with an embedded SLM produces vortices with a low diffraction efficiency of only 0.1%. It must be taken into account that in the first case the number of observed maxima are 12, while in the second case there are 28 maxima.

6. Analog and digital PHR are proven to be efficient methods for patterning a wide variety of DOEs on ChGs NMLs and azopolymer thin films. As a final observation analog PHR produces DOEs with high diffraction efficiency, while digital PHR enabled designing of DOEs with complex geometries capable of generating spatially multiplexed patterns. The quantitative investigation of the surface and refractive index maps of the imprinted gratings will give a more ample understanding of the photoinduced processes that took place in these materials.

5. DEVELOPED DHM FOR THE INVESTIGATION OF DOES

Among different microscopic techniques used for quantitative phase imaging, DHM is regarded as a non-contact optical method that allows optical thickness measurement with nanometers accuracy [12]. DHM performs non-destructive imaging and provides 3D information without impairing the integrity of the object under study. Due to digitalization of this microscope technique, investigations can be performed with frequent image acquisition making it suitable for live monitoring. It is very important for biomedical samples in vivo. When the digital hologram is computationally processed the phase and amplitude of the sample are reconstructed. In other words, the distribution of the refractive indices(birefrigency) and the topography of the surface are restored. Owing to the quantitative phase data, obtained by DHM, it allows a detailed visualization of DOE, otherwise difficult to investigate via current commercial light microscopes. From the phase information, physical and optical parameters such as thickness, volume, shape, and refractive index can be quantified. This is a full-field imaging technique and is essential for understanding the evolution of complex three-dimensional (3D) structures created inside transparent materials, where the scanning microscopes such as atomic force microscope (AFM) or scanning electron microscope cannot be applied. Despite the higher surface measurement accuracy provided by the AFM, the line scanning method takes much more time, as much as ten minutes for one square centimeter surface. In this regard, DHM is a suitable tool for surface and shape examination of DOEs patterned on photosensitive materials.

The diffraction efficiency of DOEs is the main parameter determining their possibility to be used for practical applications. Since the diffraction efficiency is defined both by refractive index and thickness modulations, it is very important to determine accurately the map of these changes. A topography map of surface relief gratings is conventionally measured by AFM, but this is a scanning technique with restricted field of view. Moreover, revealing the refractive index map of RIG is still a problem. Optical techniques such as refracted near-field measurements [32], imaging ellipsometry [33,34], and lateral shearing interferometry [35] are used for refractive index mapping. The drawback of these methods is the complicated mechanical arrangement required. As mentioned previously, DHM is full-field, and in this chapter it will be demonstrated how it can be used for the measurement of refractive index modulation and surface topography. Furthermore, it will be shown that DHM combined with sparse phase and amplitude reconstruction (SPAR) algorithms provides reliable and accurate results for refractive index and relief mapping on DOEs.

This chapter is organized as follows. The first section describes the developed off-axis setup including the SPAR technique applied as a software solution for suppressing the noise in the

phase reconstruction process. The investigation results of the designed DOEs on ChG NML and azopolymer thin films are also presented in this section. The second section presents the developed PS-DHM system with an embedded liquid crystal variable retarder (LCVR). Results of the phase reconstruction and topography characterizing the inscribed vortex DOEs are discussed.

5.1 Off-axis DHM configuration developed for the investigation of DOEs on ChGs NML

For analyzing the DOEs imprinted on ChGs an off-axis DHM bright-field configuration in transmission mode was used. The developed setup is illustrated in Figure 5.1. The light emitted by a laser was coupled into a single-mode fiber and divided into two beams by a Y splitter. One beam is directed towards the surface of the grating; the other one is the reference beam which is coming at the registration plane at a small angle. The diameter of the light spot on the sample was adjusted by the fiber to sample distance. The object and reference beams intensities were adjusted in order to increase the contrast of the interference fringes in the digital hologram. An oil immersion objective with magnification 100x and NA=1.25 has been used. Oil was introduced between the cover slip (0.13 mm thickness) and the first objective lens. The CCD sensor was located at a distance of 190 mm from microscope objective (MO) for reducing the aberrations in the image. The angle between the object and the reference beams was α= 4.50 and the carrier frequency was 3.5 pixel or $\sim$ 8 μm. The He-NE laser has a wavelength $\lambda = 632.8\ nm$, thus considering Abbe formula $d = \dfrac{\lambda}{2NA}$, the resolution or the smallest resolvable object detail visible to the built microscope is about 253 nm. The resolution of the CCD camera is 2592 pixels x 1944 pixels with pixel size 2.2 μm x 2.2μm. The period of the investigated DOEs is $\Lambda = 1\ \mu m$, thus it is 4 times larger than the resolution limit.

The complex-valued wavefront at the sensor plane is given as:

$$u_s = B_0\ exp\ exp\ (j\varphi_0)\ + A_r exp\ (j\varphi_r), \tag{5.1}$$

where $u_0 = B_0\ exp\ exp\ (j\varphi_0)$ and $u_r = A_r exp\ (j\varphi_r)$ are the object and reference wavefronts, respectively. Here B_0, A_0 are their amplitudes and φ_0, φ_r are phases [212].

In our experiments, a spherical reference wavefront is generated by the single-mode optical fiber used and the recorded intensity is given by:

$$I = |B_0\ exp\ exp\ (j\varphi_0)\ + A_r\ exp\ exp\ (j\varphi_r)\ |^2 =$$
$$= B_0^2 + A_r^2 + A_r(exp\ exp\ (j(\varphi_0 - \varphi_r))\ (-j(\varphi_0 - \varphi_r)\ )), \tag{5.2}$$

The recorded data is noise and can be written as:

$$Y = I + \sigma\varepsilon, \tag{5.3}$$

where I is the true intensity, σ is the noisy standard deviation of noise and ε is a random noise. It is assumed in this section that the noise is zero-mean i.i.d. standard Gaussian, $\varepsilon \sim N(0,1)$. The reconstruction of the surface relief and refractive index of DOEs is carried out from the phase and amplitude values obtained from the observation Y.

For the recorded off-axis digital holograms, the iterative Sparse Phase and Amplitude Reconstruction (SPAR) technique is used. It was recently developed in MATLAB software for the reconstruction of the wavefront phase with efficient noise suppression. A more detailed description of the SPAR algorithm can be found in Chapter 2 and in [73]. Several adjustments were made in the code according to the experiment features and nature/properties of the investigated DOEs.
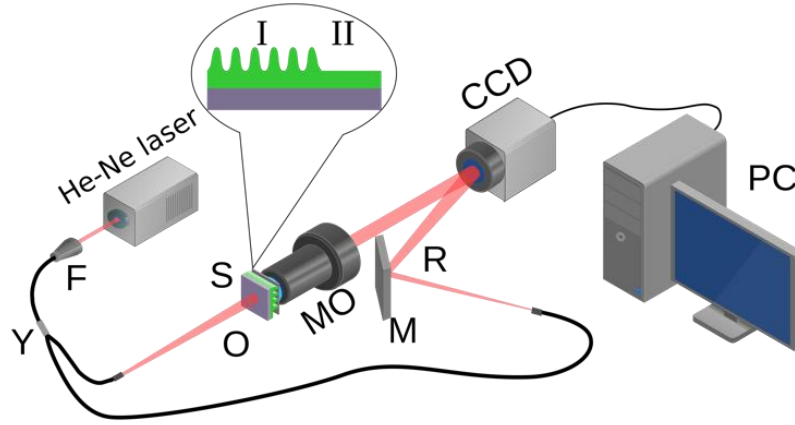
Fig. 5.1. Setup of the off-axis DHM: He-Ne laser ($\lambda = 632.8\ \mu m,\ power = 10mW$) F-micropositioner for coupling light into a single-mode fiber; Y-2x2 single-mode fiber optic coupler, O-object beam, R- reference beam, S-sample with diffraction grating and coverslip on top with immersion liquid (n=1.51); MO- immersion microscope objective, M- mirror and CCD camera, PC-computer, I, II show two illumination beams positions on the sample, namely I- through the grating and II-outside of the grating.

First, a spherical reference wavefront as well as a plane one are incorporated in (2.25) contrary to the linear wavefront (2.11) which is only exploited in [73]. Second, the operating window dimensions x_m are 20-by-20 pixels, and the Gaussian standard deviation is 5, which have been tested to provide improved the reconstruction results.

The phase map $\Delta\varphi(x,y)$ of DOEs was determined from the reconstructed wavefront by the following equation

$$\Delta\varphi(x,y) = \varphi_{01}(x,y) - \varphi_{02}(x,y). \tag{5.4}$$

where φ_{01} is the phase calculated from the reconstructed object hologram of the exposed DOE and φ_{02} is the phase calculated from the reconstructed reference hologram of the unexposed area.

5.1.1 Refractive index and surface map reconstruction of DOEs recorded on As₂S₃-Se NML

Investigation of ChG films optical parameters during and after DOE formation is necessary for a better understanding of the photoinduced phenomena that take place at the microscopic level [12]. As mentioned above, different methods can be used for the reconstruction of the refractive index map such as phase contrast, refracted near-field measurements, imaging ellipsometry, lateral shearing interferometry or DHM [12, 32-35]. An advantage of the DHM with SPAR is that it can be used for the study of small variations of the refractive index mapping while ellipsometry is a relatively slow scanning technique, effectuated in reflective mode and involves a cumbersome process.

The phase map of the inscribed DOEs contains two components: a first constituent describing the refractive index modulation and a second constituent describing the thickness modulation. The phase map $\Delta\varphi(x, y)$ can be expressed mathematically as:

$$\Delta\varphi(x, y) = \frac{2\pi}{\lambda}[d_0\Delta n(x, y) + (n_0 - 1)\Delta d(x, y)] \qquad (5.5)$$

where d_0 is the thickness of the film, Δd the change in thickness, n_0 is the refractive index of the film, Δn is the photoinduced change in refractive index, and λ is the wavelength. Here, $\frac{2\pi}{\lambda}d_0\Delta n(x, y)$ represents the refractive index change and $\frac{2\pi}{\lambda}(n_0 - 1)\Delta d(x, y)$ expresses the change in thickness.

Let us consider the parameters $\Delta\varphi$, Δn and Δd as local average values of the corresponding $\Delta\varphi(x, y), \Delta n(x, y)$ and $\Delta d(x, y)$, as a result the following equation is obtained

$$\Delta\varphi = \frac{2\pi}{\lambda}[d_0\Delta n + (n_0 - 1)\Delta d] \qquad (5.6)$$

It should be remarked that the fluctuations in the phase map $\Delta\varphi(x, y)$, of the digital holograms are due to variations in both thickness and refractive index. From the phase map $\Delta\varphi(x, y)$ retrieved by DHM, the DOEs phase profile and the local average values of the phase $\Delta\varphi$ can be extracted. When the thickness change $\Delta d (x, y)$ of the grating is known (measured it by AFM) it is possible to extract from (5.6) the average refractive index modulation Δn.

The maximum refractive index fluctuation is 0.004 while the mean refractive index modulation of 0.001 (Fig.5.2), and from AFM the mean value of Δd for grating is 90 nm. Hence,

the influence of refractive index Δn and thickness Δd modulation in the average range on the phase $\Delta \varphi$ is about 1:10.

1
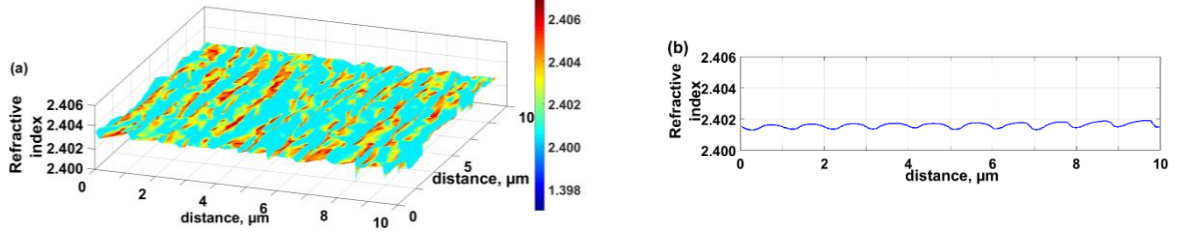
2
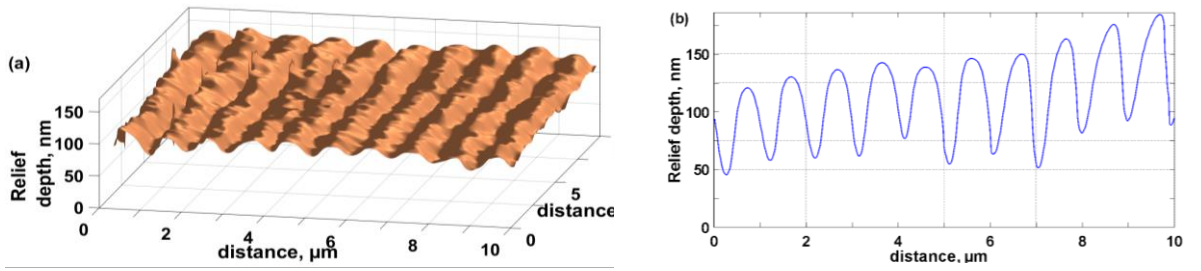
3
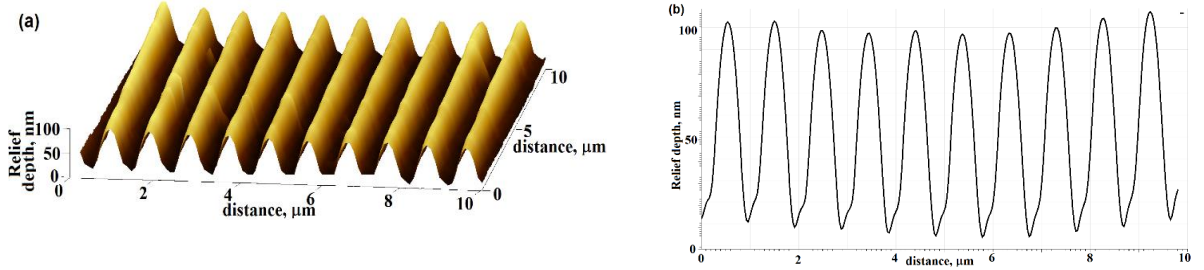
Fig. 5.2. 1(a) Refractive index map obtained via DHM and 1(b) mean cross-section for DOE recorded on As₂S₃-Se NML, 2(a) The topography map and 2(b) mean cross-section of DOE formed on NML As₂S₃-Se and obtained by DHM with SPAR technique, 3(a) 3(b) The topography map and cross-section of DOE formed on NML As₂S₃-Se and measured by AFM.

It is also shown in the refractive index map (fig. 5.2) that the modulation of the refractive index is comparable to the noise of the DHM. Thus, it can be considered that the DOE recorded on As₂S₃-Se is determined mostly by the relief thickness modulation.

Therefore, the topography of the grating was obtained from $\Delta \varphi(x, y)$ by using the relation deduced from (4), taking into account that the impact of refractive index is negligible:

$$\Delta d(x, y) = \frac{\Delta \varphi(x, y)}{2\pi(n_0 - 1)} \lambda \tag{5.7}$$

where $\lambda = 632.8 \ nm$ is the wavelength and $n_0 = 2.46$ the refractive index [12, 209].

Figure 5.2, 1(a) represents the three-dimensional refractive index distribution of the DOE on As2S3-Se NML and Fig. 5.2, 1(b) represents the mean cross-section that corresponds to the surface topography shown in Fig. 5.2, 1(a). The topography and cross-section of DOE with the diffraction efficiency of 13.4% obtained by DHM with SPAR technique Fig. 5.2, 2(a), (b) were compared with measurements done by AFM shown in Fig. 5.2.3 (a), (b).

The cross-section mean values of DHM data (Fig. 5.2.2(b)) match generally with the cross-section mean values of AFM data (Fig. 5.2.3(b)). The differences are more visible in the topography maps. The noisier 3D map in DHM may be as a result of speckle noise and of different spaces of data presentation in these methods. The difference is caused by type of analysis and the accuracy of AFM depends on the radius of the tip whereas DHM is a contactless optical method if compared to AFM. The SPAR reconstructs the phase map from a hologram provided by DHM while the AFM measures the surface directly. In our DHM configuration the object beam passes through the glass substrate volume and residual thickness of the DOE (2.5 μm) thereby embedding total phase (volume and surface) and uncontrolled noises in topography map of SRG unlike the AFM procedure, thus achieving lower resolution can be achieved on the y-axis.

From Fig. 5 it can be concluded that the DHM with SPAR reconstruction algorithm can be successfully used as an alternative for the phase reconstruction of SRG and it shows only small visual differences from the AFM cross-sections. According to the measurements by AFM and DHM the groove depth of DOE with DE 13.4% is about 90 nm. For DOEs with DE's from 8-12% the groove depth of SRG increases from 75 to 85 nm.

5.1.2 Reconstruction of refractive index map of DOEs recorded on As$_2$S$_3$ NML

Before reconstructing the refractive index map $\Delta n(x, y)$, the thickness changes Δd from AFM measurements are determined. AFM scanning (Fig. 5.3) showed that the investigated DOE formed on As$_2$S$_3$ thin film had low thickness modulation (1-3 nm). The real refractive index map after DOE recording consists of refractive index of the NML and the modulation of the refractive index: $n(x, y) = n_0 + \Delta n(x, y)$.

Thus, the relation between the phase $\Delta \varphi(x, y)$ obtained by DHM and the refractive index map $n(x, y)$ is expressed by:

$$n(x, y) = \frac{\Delta \varphi(x, y)}{2\pi \cdot d_0} \lambda + n_0. \tag{5.8}$$

Since the measured phase map can be a combination of both the refractive index and the thickness modulation of the film, this formula should be used in conjunction with a known depth.
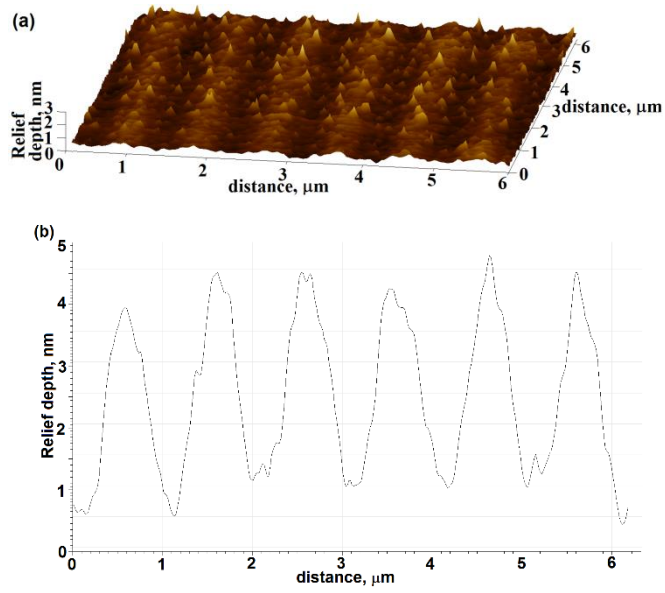
Fig. 5.3. (a) The surface relief map (a) and cross-section (b) of holographic grating recorded on As₂S₃ film and measured by AFM.

The cross-section and the refractive index profile of the patterned DOEs prove the feasibility of DHM indirect measurements.
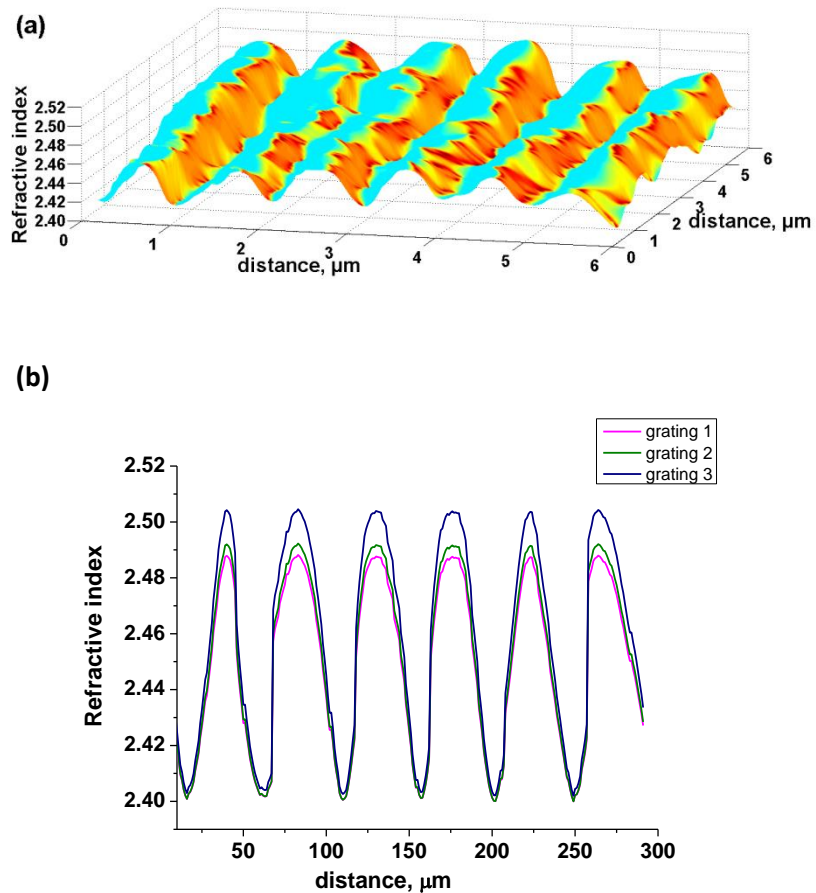
Fig. 5.4 (a) Refractive index map of DOE recorded on As₂S₃ thin films . and (b) cross-section refractive index of gratings with different diffraction efficiencies

From Fig. 5.4 it can be seen that the refractive index modulation of DOE N°3 with DE 10.4% (Fig. 4.8(b)) is about 0.1. The refractive index modulation of DOEs (N°1-3) recorded on As_2S_3 varies in dependence on the DE (8-10.4%) and the exposure time from 0.08 to 0.1. The obtained results match with the photoinduced changes in refractive index measured by a lateral shearing interferometer in [35].

It was demonstrated that by using off-axis DHM and the SPAR algorithm the topography and refractive index map of DOEs recorded on As_2S_3-Se NML and on As_2S_3 thin films can be obtained. Moreover, the type of patterned DOEs can be determined. For As_2S_3-Se NML a SRG is obtained as it is determined mostly by surface thickness modulation of 90 nm.

For As_2S_3 thin films, a RIG is obtained as it is determined mostly by refractive index modulation 0.1. In this way, by using DHM with the SPAR reconstruction algorithm quantitative information about the origin of DOE's is obtained (surface relief modulation or refractive index modulation).

5.2 Phase-shifting DHM configuration developed for the investigation of the DOEs recorded on azopolymer thin films

The PS-DHM system was upgraded with the LCVR to perform phase shifts in the reference beam. The microscope was applied for investigating sinusoidal DOEs obtained using different exposure doses and vortex DOEs obtained via analog and digital PHR on azopolymer thin films. The merit of the developed PS-DHM is that LCVR executes optical phase shifting, by driving voltages, with higher accuracy if compared to mechanical displacement, produced via a piezoelectric transducer. In particular, this is because LCVR is mounted in-line, vibration free, and functions more stable by producing high retardance uniformity [213]. Furthermore, automatic control of the LCVR adopted in LabVIEW software permits the holograms frame registration within 30 milliseconds. Thus, fast hologram acquisition minimizes the periodic background noise and temperature variation typically influencing the image quality. The calibration of the LCVR is mandatory in order to perform a precise phase control.

The aim of the calibration is to determine the dependence of the phase retardance on the applied voltage without changing the polarization of the input beam. The detailed description of the calibration procedure can be seen in Chapter 3.

The upgraded phase-shifting digital holographic microscope (PS-DHM) with a LCVR for producing all-optical phase-shifts is depicted in Fig. 5.5. In the experiment, the single-mode laser beam is divided by a non-polarized beam-splitter into the undisturbed reference wave-Rw and the scattering from the vortex DOE- Ow.
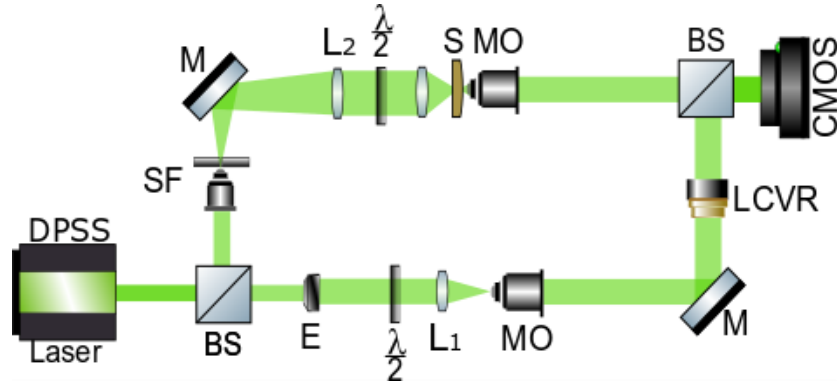
Fig. 5.5 DHM setup:CW DPSS laser (λ=532nm, 100 mW, TEM00), BS-non-polarized beam splitter, λ/2- half-wave plates, M-mirror, MO-microscope objective (20x, NA=0.40), S-sample, L1, L2-lenses, CMOS- digital camera "DMK33UX264", resolution 2,448×2,048 (5 MPxs), LCVR- "Meadowlark optics" liquid crystal variable retarder LCVR-100, SF-spatial filter, E-beam expander.

The laser beam is expanded by a microscope objective and lens L2. Thus, the beam was collimated. The collimated object beam passes through a half-wave plate to adjust the polarization states of the object and reference beams.
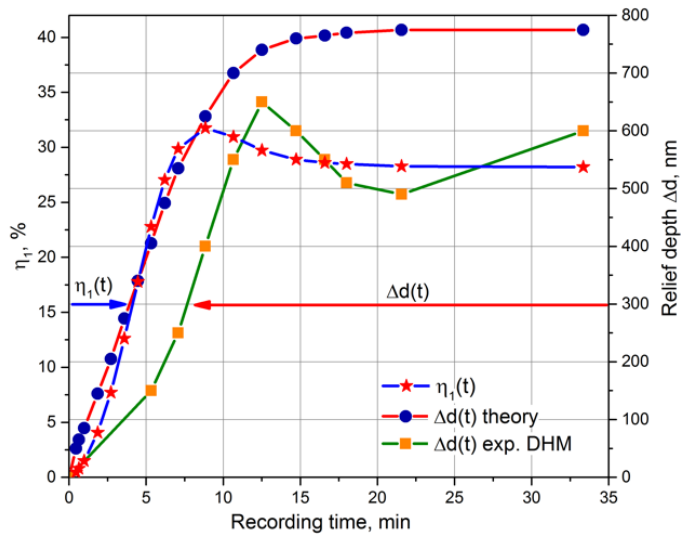
Fig. 5.6.: Kinetics of the first-order DE of the recorded DOEs(blue), relief depth calculated theoretically (red), relief depth measured experimentally obtained by phase-shifting DHM(green curve)[214].

The second lens, as a collimator, focuses light on the sample. The CMOS camera acquires digital holograms via identical microscopic systems in both paths. The microscope magnification was evaluated by preliminary calibration using a 1 mm linear stage micrometer with 10 µm divisions. It was determined that each CMOS pixel acquires 160x160nm of the sample area. The

phase of the reference beam is shifted sequentially by the LCVR. Nematic liquid crystals producing the phase retardations exhibit optical birefringence properties. Therefore, half-wave plates are introduced in each arm to maintain similar polarization of both beams and to achieve high-contrast interference patterns. The object wave is superposed with the reference wave after a non-polarized beam splitter, and then the combined beams form the in-line hologram on the CMOS camera.

The digital hologram recorded by the CMOS camera is a result of the interference of the object beam $O_w = A_O \exp(i\Phi_O)$ and reference beam $R_w = A_R \exp i(\Phi_R + \varphi_N)$, whose intensity is given by

$$I_N = |O_W + R_W|^2, \tag{5.9}$$

where A_O, A_R and Φ_O, Φ_R are the amplitudes and the phases of the object and reference waves, respectively, and φN represents the phase changes in the reference arm created by the LCVR, where N=1, 2, 3, 4.

(a)

(b)
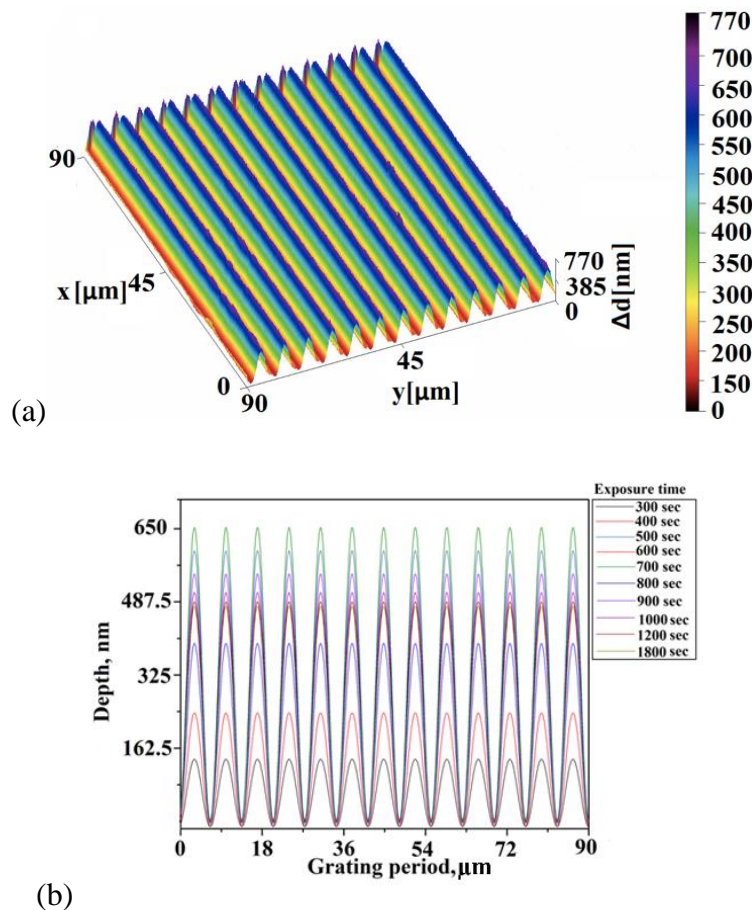
Fig. 5.7. (a) 3D topography map of the DOE which has the maximal depth (b) Cross-sections taken across X-axis of the DOEs.

The phase can be quantitatively reconstructed from the four recorded interferograms using the procedure described in Section 2.2 of Chapter 2. Specifically, the phase from the object

121

holograms is calculated by Eq. 2.33 and the phase from the reference holograms which contains information about the additional phase term is calculated by Eq. 2.34.

For reconstructing the phase map of the DOEs, four object holograms are captured within the DOE recorded area in the azopolymer film. Another four reference holograms are recorded on the unprocessed area of the film for minimizing the background effect and the modulation fluctuations.

Finally, the phase map of the DOE is calculated by:

$$\Delta\Phi(x,y) = \Delta\Phi_O(x,y) - \Delta\Phi_R(x,y), \tag{5.10}$$

where $\Delta\Phi_O(x,y)$, $\Delta\Phi_R(x,y)$ are reconstructed phase maps from the object and reference holograms, respectively. The reconstruction algorithm executes the numerical compensation of the PS in case of a misaligned shift produced by the LCVR. This step is important when the environmental disturbances influence the laboratory conditions (temperature changes, mechanical vibrations, etc.). A small phase shift is added during the phase reconstruction stage until the object phase is successfully revealed.
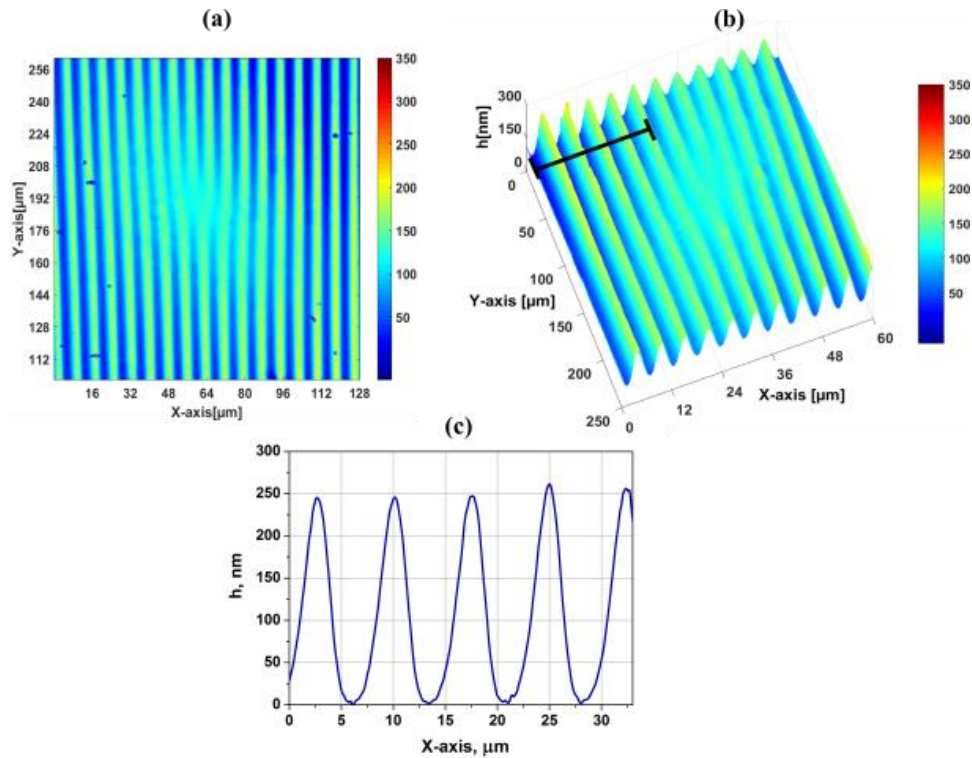
Fig. 5.8. (a) 2D phase image TC=1, (b) 3D topography map and (c) X-axis cross-section of vortex DOE recorded via analog PHR setup.

After the PS compensation, phase unwrapping is performed by the PUMA unwrapping algorithm based on energy minimization. Generally, based on reference data, two kinds of phenomena govern the formation of diffraction gratings in azopolymers: 1. Volume birefringence

due to photo-induced modulation of the refractive index; 2. Surface relief modulation caused by the mass movement, triggered by structural photo-induced modifications in the bulk of the azopolymer [31].

Even though the obtained DOEs can be considered as birefringence gratings, the contribution of the refractive index to the overall DE of azopolymer thin films is relatively small [108]. On this basis, it is important to mention that only the surface relief modulation is considered while the refractive index changes in azopolymers are not taken into account in our calculations. The reconstructed phase map from the PS-DHM holograms includes both bulk and surface phase modulation of the azopolymer films.
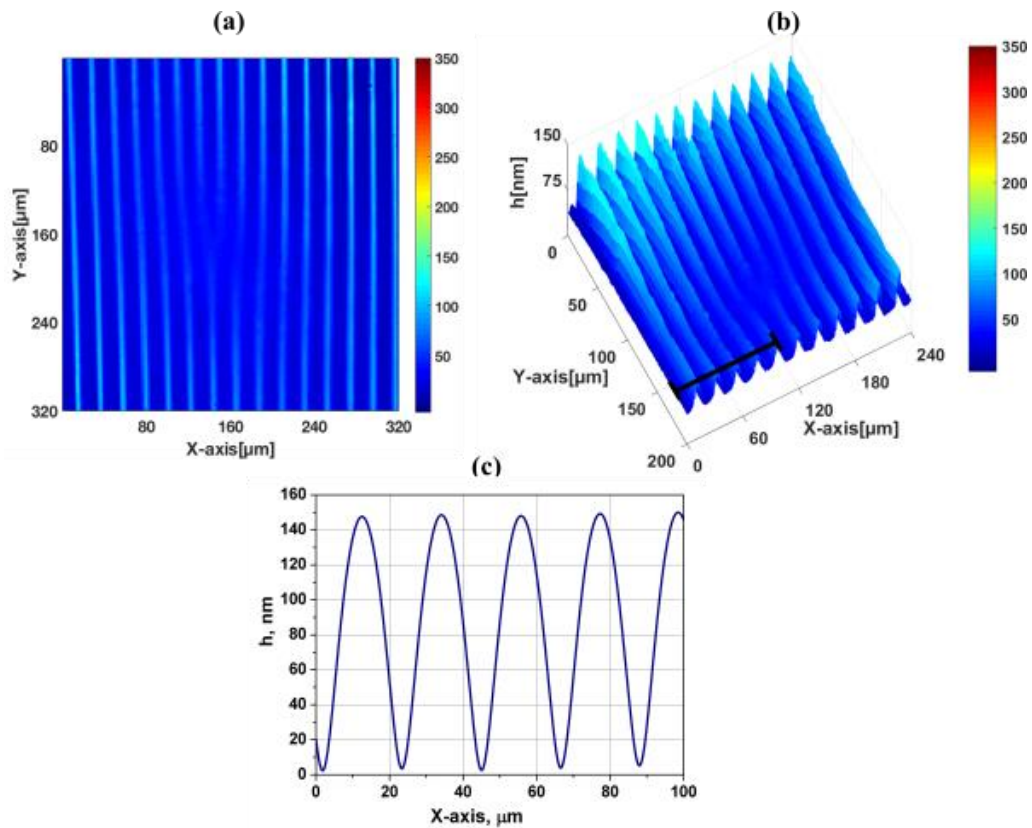
Fig. 5.9. Results of the DHM investigations of vortex DOE obtained via single-beam PHR. (a) 2D phase image of vortex DOE with TC=2, (b) 3D topography map, (c) X-axis cross-section of the vortex DOE recorded via digital single-beam PHR setup.

Theoretical calculations and experimental DHM measurement results of the sinusoidal DOEs obtained using different exposure doses are illustrated in Figure 5.6 and Figure 5.7. The investigations confirm the sinusoidal form of the gratings. The maximal height modulation according to theoretical calculations is reached when the azopolymer is exposed for 30 minutes.

The measured height for this DOE is equal to 780 nm as shown by the red curve in Figure

5.6. However, according to the DHM measurements the maximal modulation constitutes 650 nm corresponding to 12 minutes recording time [214].

Discrepancies are also observed in the evolution of the relief depth. DHM measurements indicate that the height of the relief decreases after 12 minutes and starts to increase again after 27 minutes of exposure, while theoretical calculations show a constant growth, until a certain point of saturation.
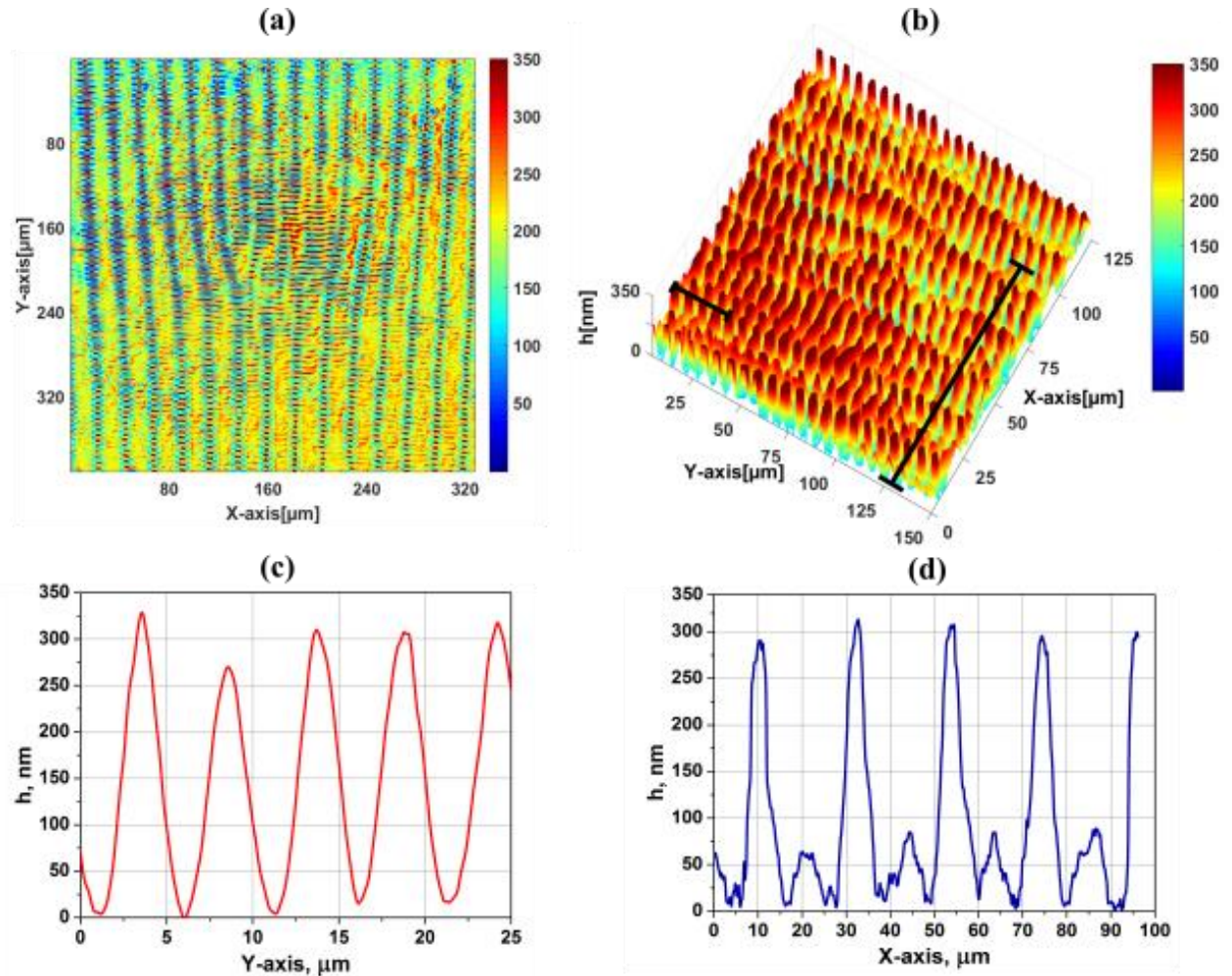
Fig. 5.10. (a) 2D phase image of vortex DOE with TC=2, (b) 3D topography map (c) Y-axis cross-section (d) X-axis cross-section of the complex vortex DOE patterned by digital dual-beam PHR.

Remarkably, the evolution of the relief modulation defined by DHM corresponds to the kinetics of the first-order DE measured by the photo-diodes during the recording process and represented by the blue curve in Fig. 5.6. The kinetics reveals that maximal DE is achieved within 8 minutes of exposure. Figure 5.7(a) illustrates the 3D topography map obtained from DHM measurements of the DOE with the maximal relief height equal to 650 nm.

According to the cross-sections of the DOEs, illustrated in Fig. 5.7(b) the grating period is approximately 7μm, which corresponds to the experimental recording conditions.

Knowledge of deposited azopolymer thin film behavior under the influence of light interference is valuable for determining the quality of the formed patterns, as well as for measuring surface photo-induced deformations in different directions of the vortex DOEs, the following results were published in [200]. The topography ($\Delta d(x, y)$) of the vortex DOEs is calculated numerically from the unwrapped phase by Eq. 5.7, where λ=532nm is the wavelength and n is the refractive index of the azopolymer films.

The PS-DHM measurement results of the vortex DOE obtained using the analog PHR setup based on a VPR are illustrated in Figs.5.8 (a) and 5.8 (b). It has the form of a FSG with one groove bifurcation and topological charge is equal to 1, respectively. The mean value of height for this DOE is equal to 250 nm as shown in the cross-section depicted in Fig. 5.8(c). The grating period is approximately 7.5 µm, which corresponds to the experimental recording conditions. The highlighted black line on the 3D topography map denotes the line along which the cross-section was extracted.

Figure 5.9 shows the DHM result images of the vortex DOE patterned using the digital single-beam PHR setup (Fig.4.15) based on a SLM. In Fig. 5.9 (a) and Fig. 5.9 (b) is shown the topography map of the FSG with the topological charge equal to 2. According to the cross-section depicted in Fig. 5.9 (c), the mean value of surface relief height is 157 nm and the period of the grating is about 20 µm.

The reconstructed full-field surface of the complex vortex DOE inscribed via dual-beam SLM-based setup is pictured in Fig. 5.10. The central part of complex vortex DOE is seen more clearly if compared to the DOE obtained via single-beam PHR. Two-fold symmetrically spaced fringes along the X- and Y-directions of the relief map result from the one-step PHR of two orthogonal modes. The cross-section built across the Y-axis, shown in Fig. 5.10 (c), reveals the relief slopes with a height of 300 nm and a frequency of 5.0 µm, created by the intersection of the SLM modulated beam and the object wave with polarization states of $+45^0 : -45^0$, respectively. Surface profile extracted across the X-axis presented in Fig. 5.10 (d) denotes the azopolymer films structured by the digital fork-shaped hologram addressed to the SLM. A grating with two peaks was observed on the X-axis: the major peak with depth about 300 nm, and additional minor peaks with a height of 50 nm. The period of the patterned fringes is 20.0 µm and corresponds to the fork grating displayed on the SLM. The origin of minor peaks could be the result of the refractive index modulation in the azopolymer films.

5.3 Conclusions to chapter 5

1. The off-axis DHM is applied for the quantitative phase imaging of a series of DOEs recorded on As_2S_3 thin films and As_2S_3-Se NMLs. The separated contribution of topography and refractive index maps of recorded gratings in diffraction efficiency is estimated.

2. The applicability of DHM combined with SPAR reconstruction algorithm for the determination of DOEs parameters is proved. The recently developed variational algorithm is able to produce high-quality phase imaging from quite noisy data of DHM. Comparison of the topography maps recovered by DHM with the SPAR and AFM data shows that our results qualitatively and quantitatively match with the AFM data. To sum up, DHM together with the SPAR algorithm are applicable for proper reconstruction of both the topography map of SRG and the refractive index modulation of RIG recorded on As_2S_3–Se NML and As_2S_3 thin films, and may be an effective complementary method to AFM. Full-field image acquisition by DHM covers a larger investigated area of the sample under study and is more time efficient.

3. The advanced PS-DHM with the incorporated LCVR was developed and implemented for non-contact, all-optical investigation of the phase and surface relief transformations on azopolymer thin films. Sinusoidal and complex vortex DOEs were investigated.

4. In order to realize the full potential of the sinusoidal DOEs and understand their formation dynamics and response to different exposure doses theoretical calculations versus experimental measurements obtained via PS-DHM are used. The influence of the exposure doze on the diffraction efficiencies and topography of sinusoidal DOEs was established. The comparison between the obtained experimental and theoretical parameters of the recorded DOEs show particular differences in the relief depth values. The maximal height modulation according to theoretical calculations is reached when the azopolymer is exposed for 30 minutes, the measured height for this DOE is equal to 780 nm as shown by the red curve in Figure 5.6. However, according to the DHM measurements the maximal modulation constitutes 650 nm corresponding to 12 minutes of recording time. Differences are also observed in the growth of the relief depth. DHM measurements indicate that the height of the relief decreases after 12 minutes and starts to increase again after 27 minutes of exposure, while theoretical calculations show a constant growth, until a certain point of saturation.

5. Based on the PS-DHM results obtained from complex vortex DOEs analysis, it could be concluded that the variation of the surface relief height and diffraction efficiency of the DOEs obtained by analog and digital PHR is explained by different periods of the vortex DOEs that also influences these parameters. In addition, the absorption of the azopolymer at a wavelength of 473nm is higher than at the 532nm wavelength of the recording beam. Slightly increased

roughness of the complex DOE may be the outcome of increased sensitivity to the pixelated nature of SLM, and external vibrations of the patterning setup. Additional investigations of the surface deformation have to be performed for exact an estimation of the surface and volume contributions in the phase image of the grating.

6. The proposed PS-DHM configuration was proven to be successfully used as a versatile metrological tool for 3D quantitative measurements of complex structures of DOEs including transparent surface relief deformations on a nanometer scale. On the bases of these results two assumptions have been made. First, it is assumed that the variations in the results may be due to the refractive index changes also arising in azopolymer thin films during exposure. Second, the non-uniform modulations of the relief depth of the DOEs caused by the Gaussian beam distribution makes it difficult to investigate the patterns in the area with maximal depth modulation. Therefore, further investigations in this field would increase the knowledge on the mechanisms of photoinduced phenomena in azopolymer thin films as well as the photonic applications of these materials.

7. It is anticipated that in the future, extended research on the input of surface relief and refractive index changes into the phase modulation of the azopolymer thin films would further facilitate complete understanding of the behavior as well as the photonic applications of these materials. The development of DHM in reflection mode would allow more complete examination of films and opaque objects.

CONCLUSIONS AND RECOMANDATIONS

The development of digital holographic microscopy as an optical instrument has an important role in the exploration, understanding and advancement/breakthrough of nanotechnology and innovative optical materials. At present, continuous enhancement of microscopic tools is mandatory in order to support the needs of micro-nanotechnology. In this regard, the main focus of this thesis was the improvement of the digital holographic microscope including hardware and software components for quantitative investigation of the diffractive optical elements on a nanometer scale. Another emphasis was the design of complex diffractive optical elements using analog and digital methods for polarization holographic recording on chalcogenide glasses nanomultilayers and azopolymer thin films. For both purposes, new digital devices were introduced in optical setups, thus a detailed calibration of digitally controlled liquid crystal devices was necessary to be implemented.   Direct one step recording of DOEs makes it possible to preserve original calculated pattern, in contrast to etching procedures. The plasma and wet etching methods often used to create the relief distort, in one way or another, both the calculated drawing, the grooves form, and the depth of the designed relief. Laser power and the time of direct recording holography are more easily controlled than a number of etching parameters. The notable properties of DOEs recorded by polarization holography are that they diffraction efficiency is higher than ones recorded by scalar holography, and they are ready for use in an optical setup. As analog of free form optics with new, never seen before optical functionalities is a remarkable direction for DOEs in modern optical devices.

In the following paragraphs the main conclusions drawn from the research results are presented:

1. The results of the computational simulations of off-axis DHM configuration have proved that phase imaging enhancement can be obtained by adopting a sinusoidal phase grating mask to the off-axis lens less DHM setup. Due to the optimized diffraction grating parameters (period, phase and number of rotating steps) more information about the high spatial frequencies of the object spectrum is recorded in the CCD sensor from the diffracted orders. The root mean square error values of the phase reconstruction decreased with about 20%. At the same time, the results of the computational simulations of the phase-shifting DHM configuration show that by inserting a blazed diffraction grating in the optical setup the error of the phase reconstruction decrease by approximately 72%. This knowledge and the developed numerical tools could then be applied to record, reconstruct and process digital holograms. %. (Conclusions driven from the experiments described in Chapter 2 of the thesis)

2. Integration of liquid crystal devices in digital holographic optical systems presume the mandatory and important procedure of detailed phase and polarization calibration for each specific configuration. The calibration of LC devices shows that non-negligible errors are probable when controlling the phase and polarization of LC devices. Furthermore, the software procedures included in the SPAR calibration algorithm applied in this thesis demonstrate a compensation of the effects of external noise which reduce the requirements for stability of the interferometer. (Conclusions driven from the experiments described in Chapter 3 of the thesis)

a.   The standard deviation of the phase data from individual pixels and their active area proves the fact that SLMs exhibit spatial variations the standard deviation of the active part of the SLM pixel is 0.5 radians smaller if compared to the phase of entire SLM array. This is the result of the spacing between pixels (the "dead zones") present on the SLM display, where the incident laser beam cannot control the phase modulation. The ad hoc calibration procedure of the SLM polarization modulation was implemented for evaluating the ellipticity and azimuth rotation angle of output beam as a function of gray level addressed to the SLM. The results point that SLM output polarization state is typically, elliptical. Only when 125 gray level blank screen is loaded on the SLM display it keeps the linear polarization of the input light. Also, it shows that the larger voltage applied to the SLM, the smaller becomes the light polarization modulation.

b.   The calibration of the LCVR indicates that the phase shifting produced by the LCVR was possible by fine adjustment of the fast (slow) axis of the liquid crystal with the polarization plane of the incident beam without rotating the polarization plane. The obtained phase shift-volt characteristic of the LCVR is nonlinear. To produce accurate all-optical phase shifts, via DHM systems containing an LCVR, a linear approximation of the phase shift in the region 2-3.2V of the applied voltages was build. The advanced PS-DHM with the incorporated LCVR was developed and implemented for non-contact, all-optical investigation of the phase and surface relief transformations on azopolymer thin films and ChG NML.

3. Through analog and digital PHR, the direct (one-step) method of forming multifunctional DOEs on the surface of ChGs nanomultilayers and azopolymer thin films was achieved, which is the result of the mass transfer induced by the vectorial character of holography in polarized light (vectorial). Analog PHR produces DOEs with a high diffraction efficiency with a maximum of 33% achieved in this thesis on azopolymer thin films, while digital PHR enabled designing of DOEs with vortex geometries capable of generating spatially multiplexed beams with

phase singularities, but the diffraction efficiency of these DOEs is not more than 1%. (Conclusions driven from the experiments described in Chapter 4 of the thesis)

4. Off-axis and phase-shifting DHM configurations are applicable for the investigation of refractive index and surface relief maps of various DOEs recorded on azopolymers thin films and ChGs nanomultilayers. A hologram processing algorithm with SPAR reconstruction was developed and applied for the off-axis and phase-shifting digital holographic setups, capable of reconstructing the phase from noisy data (holograms). A liquid crystal variable retarder was integrated in the imaging system of the phase-shifting DHM for the enhancing the performance and stability of the microscope. (Conclusion driven from the experiments described in Chapter 5 of the thesis)

5. The proposed PS-DHM configuration was proven to be successfully used as a versatile metrological tool for 3D quantitative measurements of complex structures of DOEs including transparent surface relief deformations on a nanometer scale. On the bases of these results two assumptions have been made. First, we assume that the variations in the results may be due to the refractive index changes also arising in bulk of azopolymer thin films and ChG NML during exposure. Second, the non-uniform modulations of the relief depth of the DOEs caused by the Gaussian beam distribution makes it difficult to investigate the patterns in the area with maximal depth modulation. Therefore, further investigations in this field would increase the knowledge on the mechanisms of photoinduced phenomena in azopolymer thin films as well as the photonic applications of these materials. (Conclusion driven from the experiments described in Chapter 5 of the thesis)

Considering the conclusions above, the following recommendations for further research are highlighted:

1) Automatization of the phase reconstruction process, by excluding manual/individual introduction of the digital holograms in the MATLAB software and adjustment of algorithm parameters. Implementation of artificial intelligence algorithms is recommended for these procedures.

2) Implementation of multiwavelength DHM for broadening the application of the advanced optical system as it will expand absolute distance/phase measurements and diversify the objects under study. In addition, multiwavelength DHM allows changing the resolution of microscope.

3) The development of a complex optical system (a combination of DHM with a PHR setup) capable of simultaneous and real time DOE recording and investigation of phase, surface relief growth and diffraction efficiency would facilitate a profound understanding of photoinduced

phenomena and increase the accuracy of the investigations. The development of DHM in reflection mode would allow more complete examination of films and opaque objects.

4) Extended research on the input of surface relief and refractive index changes into the phase modulation of the azopolymer thin films and ChGs NML would further facilitate complete understanding of the light-matter interactions as well as the photonic applications of these materials.

5) Development of a compact DHM system for easier transportation and capable of adapting to various measurement tasks. This can be achieved by implementing advanced digital devices as SLM and LCVR (suggested in this thesis) that are capable to efficiently execute tasks and replace analog optical components.

REFERENCES

1.   GABOR, D. A new microscopic principle. In: *Nature*. 1948, vol. 161, pp. 777–778. ISSN 1476-4687 (online). Disponible: DOI: 10.1038/161777a0

2.   MAIMAN, T. H. Stimulated optical radiation in ruby. In: *Nature*. 1960, vol. 187, pp. 493–494. ISSN 1476-4687 (online). Disponible: DOI: 10.1038/187493a0

3.   LEITH, E. N. and UPATNIEKS, J. Reconstructed wavefronts and communication theory. In: *Journal of the Optical Society of America*. 1962, vol. 52, pp. 1123–1130. ISSN 1520-8532 (online). Disponible: https://opg.optica.org/josa/abstract.cfm?URI=josa-52-10-1123

4.   KIM, M. K. Principles and techniques of digital holographic microscopy. In: *SPIE Reviews*. 2010, vol. 10, pp. 51-50. ISSN 1946-3251 (online). Disponible: DOI: 10.1117/6.0000006

5.   CUCHE, E., BEVILACQUA, R., and DEPEURSINGE, C. Digital holography for quantitative phase contrast imaging. In: *Optics Letters.* 1999, vol. 24, pp. 291–293. ISSN 1539-4794 (online). Disponible: DOI: 10.1364/OL.24.000291

6.   TAKAKI, Y., KAWAI, H., and OHZU, H. Hybrid holographic microscopy free of conjugate and zero-order images. In: *Applied Optics.* 1999, vol.38, pp. 4990–4996. ISSN 2155-3165 (online). Disponible: DOI: 10.1364/AO.38.004990

7.   OSTEN, W., et al. Recent advances in digital holography, In: *Applied Optics.* 2014, vol. 53, no. 27, pp.44-63. ISSN 2155-3165 (online). Disponible: DOI: 10.1364/AO.53.000G44

8.   EL-SCHICH, Z., LEIDA MÖLDER, A., GJÖRLOFF WINGREN, A. Quantitative Phase Imaging for Label-Free Analysis of Cancer Cells-Focus on Digital Holographic Microscopy. In: *Applied Sciences*. 2018, vol. 8, pp.1027-1043. ISSN 2076-3417 (online). Disponible: DOI: 10.3390/app8071027

9.   SCHMEIDER, F., KLAPPER, S.D., KOUKOURAKIS, N.; BUSSKAMP, V., CZARSKE, J.W. Optogenetic Stimulation of Human Neural Networks Using Fast Ferroelectric Spatial Light Modulator—Based Holographic Illumination. In: *Applied Sciences*. 2018, vol.8, nr. 7, pp. 1180. ISSN 2076-3417(online). Disponible: DOI: 10.3390/app8071180

10.   XIAO, Y., JISOO, H., CHANGGENG, L., MYUNG, K., Review of digital holographic microscopy for three-dimensional profiling and tracking. In: *Optical Engineering*. 2014, vol.53, iss.11, paper nr. 112306. ISSN 1560-2303 (online). Disponible: DOI: 10.1117/1.OE.53.11.112306

11.   REKOLA, H., BERDIN, A., FEDELE, C. et al. Digital holographic microscopy for real-time observation of surface-relief grating formation on azobenzene-containing films. In: *Scientific Reports*. 2020, vol. 10, paper nr. 19642. ISSN 2045-2322 (online). Disponible: DOI: 10.1038/s41598-020-76573-6

12.   **CAZAC V.**, MESHALKIN, A. ACHIMOVA, E. ABASHKIN, V. KATKOVNIK, V.

SHEVKUNOV, I. CLAUS, D. PEDRINI, G. Surface relief and refractive index gratings patterned in chalcogenide glasses and studied by off-axis digital holography. In: *Applied Optics.* 2018, vol.57, nr 3, pp. 507-513. ISSN 2155-3165 (online). Disponible: DOI:10.1364/AO.57.000507

13.   FARIDIAN, A., HOPP, D., PEDRINI, G., EIGENTHALER, U., HIRSCHER, M., OSTEN, W. Nanoscale imaging using deep ultraviolet digital holographic microscopy. In: *Optics Express.* 2010, vol. 18, pp.14159–14164. ISSN 1094-4087 (online). Disponible: DOI: 10.1364/OE.18.014159

14.   SOMKUWAR, A. S., DAS, B., VINU, R. V., PARK, Y., SINGH, R. K. Holographic imaging through a scattering layer using speckle interferometry. In: *Journal of Optical Society of America* A. 2017, vol. 34, nr 8, pp. 1392-1399. ISSN 1520-8532 (online). Disponible: DOI: 10.1364/JOSAA.34.001392

15.   JESACHER, A., RITSCH-MARTE, M. Synthetic holography in microscopy: opportunities arising from advanced wavefront shaping. In: *Contemporary Physics.* 2016, vol. 57, nr. 1, pp. 46–59. ISSN 1366-5812 (online). Disponible: DOI: 10.1080/00107514.2015.1120007

16.   MUFFOLETTO, R. P., TYLER, J. M. AND TOHLINE, J. E. Shifted Fresnel diffraction for computational holography. In: *Optics Express.* 2007, vol. 15, nr. 9, pp. 5631-5640. ISSN 1094-4087 (online). Disponible: DOI: 10.1364/OE.15.005631

17.   YU-CHIH LIN, HAN-YEN TU, XIN-RU WU, XIN-JI LAI, AND CHAU-JERN CHENG. One-shot synthetic aperture digital holographic microscopy with non-coplanar angular-multiplexing and coherence gating. In: *Optics. Express.*2018*,* vol.26, pp.12620-12631. ISSN 1094-4087 (online). Disponible: DOI: 10.1364/OE.26.012620

18.   HUSSAIN, A., MARTÍNEZ, J. L., LIZANA, A., CAMPOS, J. Super resolution imaging achieved by using on-axis interferometry based on a Spatial Light Modulator. In: *Optics Express.* 2013, vol.21, nr 8, pp.9615–9623. ISSN 1094-4087 (online). Disponible: DOI: 10.1364/OE.21.009615

19.   KUJAWINSKA, M., WOJCIAK, J. High accuracy Fourier transform fringe pattern analysis. In: *Optics and Lasers in Engineering.* 1991, vol. 14, nr. 4, pp.325-339. ISSN 1873-0302 (online). Disponible: DOI: 0143-8166(91)90056-Y

20.   SHAOHUI LI, JUN MA, CHENLIANG CHANG, SHOUPING NIE, SHAOTONG FENG, AND CAOJIN YUAN. Phase-shifting-free resolution enhancement in digital holographic microscopy under structured illumination. In: *Optics Express.* 2018, vol. 26, pp. 23572-23584. ISSN 1094-4087 (online). Disponible: DOI: 10.1364/OE.26.023572

21.   TRUSIAK, M., PICAZO-BUENO, J., ZDANKOWSKI, P., MICÓ, V. DarkFocus: numerical autofocusing in digital in-line holographic microscopy using variance of computational

dark-field gradient. In: *Optics and Lasers in Engineering*. 2020, vol. 134, pp. 106195. ISSN 1873-0302 (online). Disponible: DOI: 10.1016/j.optlaseng.2020.106195

22.   SHEN, Y., WANG, X., XIE, Z., MIN, C., FU, X., LIU Q., GONG, M., YUAN, X. Optical vortices 30 years on: OAM manipulation from topological charge to multiple singularities. In: *Light: Sci. and Appl.* 2019*,* vol. 8, nr. 90. ISSN 2047-7538 (online). Disponible: DOI: 10.1038/s41377-019-0194-2

23.   VAYALAMKUZHI, P. et. al. Direct patterning of vortex generators on a fiber tip using a focused ion beam. In: *Optics Letters.* 2016, vol.41, pp.2133-2136. ISSN 1539-4794 (online). Disponible: DOI: 10.1364/OL.41.002133

24.   FERNANDEZ, R., GALLEGO, S., MARQUES, A., NEIPP, C., CALZADO, E. M., FRANCES, J., MORALES-VIDAL, M., BELENDEZ, A. Complex Diffractive Optical Elements Stored in Photopolymers. In: *Polymers.* 2019, vol. 11, nr. 1920. ISSN 2073-4360 (online). Disponible: DOI: 10.3390/polym11121920

25.   KRYSHENIK, V. M., AZHNIUK, Y. M., KOVTUNENKO, V. S. All-optical patterning in azobenzene polymers and amorphous chalcogenides. In: *Journal of Non-Crystaline Solids.* 2019, vol. 512, pp.112-131. ISSN 1873-4812 (online). Disponible: DOI: 10.1016/j.jnoncrysol.2019.02.019

26.   ZAKERY, A., ELLIOTT, S.R. Optical properties and applications of chalcogenide glasses: a review. In: *Journal of Non-Crystaline Solids.* 2003, vol. 330, pp. 1–12. ISSN 1873-4812 (online). Disponible: DOI: 10.1016/j.jnoncrysol.2003.08.064

27.   ELLIOTT, S. R. Medium-range structural order in covalent amorphous solids. In: *Nature.* 1991, vol. 354, pp. 445-452. ISSN 1476-4687 (online). Disponible: DOI: 10.1038/354445a0

28.   ZAKERY, A., ELLIOTT, S.R. *An Introduction to Chalcogenide Glasses. In: Optical Nonlinearities in Chalcogenide Glasses and their Applications*. Springer Series in Optical Sciences, vol 135. Berlin; Heidelberg: Springer, 2007. ISBN 978-3-540-71068-4. Disponibil: https://link.springer.com/chapter/10.1007/978-3-540-71068-4_1

29.   STRONSKI, A. et.al. Nanomultilayer structures on the base of chalcogenide glasses: properties and application in optical elements fabrication, In*: Collection of scientific papers "Fullerenes and nanostructures in condensed matter"*, 6-9sept. 2009. Minsk: Institute of thermal & mass transfer NAS Belarus, 2016. pp. 412–418.

30.   YADAVALLI, N. S., SANTER, S. In-situ atomic force microscopy study of the mechanism of surface relief grating formation in photosensitive polymer films. In: *Journal of Applied Physics* 2013, vol. 113, nr. 224304. ISSN 1089-7550 (online). Disponible: DOI: 10.1063/1.4809640

31.   MOUJDI, S. et.al. Azo-polymers for holographic recording: photo-assisted holography and surface relief gratings, In: *Proceedings of SPIE Opto conference: Practical Holography XXXIII: Displays, Materials, and Applications.* February 2-7, 2019. San Francisco, California, United States, nr. 1094403. ISSN 1605-7422 (online).

32.   YANG, Z., ANHEIER JR., N. C., QIAO, H. A., LUCAS, P. Sub-wavelength imaging of photo-induced refractive index pattern in chalcogenide glass films. In: *Optics Communications* 2009, vol. 282, pp. 4370–4373. ISSN 1873-0310 (online). Disponible: DOI: 10.1016/j.optcom.2009.08.014

33.   TOMPKINS, H. G. *A User's Guide to Ellipsometry.* [online]. Elsevier Science, 1993. ISBN: 9780323140003.

34.   RÖLING, C., THIESEN, P., MESHALKIN, A., ACHIMOVA, E., ABASKIN, V., PRISACAR, A., TRIDUH, G. Imaging ellipsometry mapping of photo-induced refractive index in As$_2$S$_3$ films. In: *Journal of Non-Crystaline Solids.* 2013, vol. 365, pp.93-98. ISSN 1873-4812 (online). Disponible: DOI: j.jnoncrysol.2013.01.037

35.   KRISHNASWAMI, K., BERNACKI, B. E., HÔ, N., ALLEN, P. J., ANHEIER, N. C. Lateral shearing interferometer for measuring photoinduced refractive index change in As2S3. In: *Review of Scientific Instruments.* 2008, vol. 79, nr. 095101. ISSN 1089-7623 (online). Disponible: DOI: 10.1063/1.2973640.

36.   SÁNCHEZ-ORTIGA, E., DOBLAS, A., SAAVEDRA, G., MARTÍNEZ-CORRAL, M., GARCIA-SUCERQUIA, J. Off-axis digital holographic microscopy: practical design parameters for operating at diffraction limit. In: *Applied Optics*. 2014, vol.53, nr. 10, pp. 2058-2066. ISSN 2155-3165 (online). Disponible: DOI: 10.1364/AO.53.002058

37.   MIHAILESCU, M., PAUN, I. A., VASILE, E., POPESCU, R. C., BALUTA, A. V., ROTARU, D. G. Digital off-axis holographic microscopy: from cells visualization to phase shift values, ending with physiological parameters evolution. In: *Romanian Journal* of *Physics.* 2016, vol. 61, nr. 5, pp. 1009–1027. ISSN 1221-146X (print). Disponible: https://rjp.nipne.ro/2016_61_5-6/RomJPhys.61.p1009.pdf

38.   SIRICO, D.G. et al. Compensation of aberrations in holographic microscopes: main strategies and applications. In: *Applied Physics B.* 2022, vol. 128, nr. 78. ISSN 1432-0649 (online). Disponible: DOI: 10.1007/s00340-022-07798-8

39.   MANN, C., YU, L., LO, C.-M., KIM, M. High-resolution quantitative phase-contrast microscopy by digital holography. In: *Opt. Express.* 2005, vol. 13, pp. 8693–8698. ISSN 1094-4087 (online). Disponible: DOI: 10.1364/OPEX.13.008693

40.   COLOMB, T., MONTFORT, F., KÜHN, J., ASPERT N., CUCHE, E., MARIAN, A.,

CHARRIÈRE, F., BOURQUIN, S., MARQUET, P., DEPEURSINGE, C. Numerical parametric lens for shifting, magnification, and complete aberration compensation in digital holographic microscopy. In: *Journal of Optical Society of America A*. 2006, vol. 23, pp. 3177–3190. ISSN 1520-8532 (online). Disponible: DOI:10.1364/JOSAA.23.003177

41.   CUCHE, E., MARQUET, P., DEPEURSINGE, C. Simultaneous amplitude-contrast and quantitative phase-contrast microscopy by numerical reconstruction of Fresnel off-axis holograms. In: *Applied Optics.* 1999, vol. 38, pp. 6994–7001 ISSN 2155-3165 (online). Disponible: DOI:10.1364/AO.38.006994.

42.   VELLEKOOP, I.M., MOSK, A. Focusing coherent light through opaque strongly scattering media. In: *Optics Letters.* 2007, vol.32, nr.16, pp. 2309-2311. ISSN:1539-4794 (online). Disponible: DOI: 10.1364/OL.32.002309

43.   VELLEKOOP, I.M, Feedback-based wavefront shaping. In*: Optics Express.* 2015, Vol. 23, nr.9, pp. 12189-12206. ISSN 1094-4087 (online). Disponible: DOI: 10.1364/OE.23.012189

44.   MOSK, A., LAGENDIJK, A., LEROSEY, G., FINK, M. Controlling waves in space and time for imaging and focusing in complex media. In: *Nature Photonics.* 2012, vol. 6, pp. 283–292. ISSN 1749-4885 (online). Disponible: DOI: 10.1038/NPHOTON.2012.88

45.   HORSTMEYER, R., RUAN, H., YANG,C.   Guidestar-assisted wavefront-shaping methods for focusing light into biological tissue. In: *Nature Photonics.* 2015, vol. 9, pp. 563–571. ISSN 1749-4885 (online). Disponible: DOI:10.1038/nphoton.2015.140

46.   YU, H., PARK, J., LEE, K., YOON, J., KIM, K., LEE, S., PARK, Y. Recent advances in wavefront shaping techniques for biomedical applications. In: *Current Applied Physics*. 2015, vol. 15,   pp.   632–641. ISSN 1567-1739   (online).   Disponibile: https://arxiv.org/ftp/arxiv/papers/1502/1502.05475.pdf

47.   CONKEY, D.V., BROWN, A., N., CARAVACA-AGUIRRE, A.M., PIESTUN, R. Genetic algorithm optimization for focusing through turbid media in noisy environments. In*: Optics Express.* 2012, vol. 20, nr.5, pp. 4840–4849. ISSN 1094-4087 (online). Disponible: DOI: 10.1364/OE.20.004840

48.   KONG, F., SILVERMAN, R.H., LIU, L., CHITNIS, P.V., LEE, K.K., CHEN, Y.C. Photoacoustic-guided convergence of light through optically diffusive media. In: *Optics Letters.* 2011, vol. 36, nr.11, pp. 2053-2055. ISSN:1539-4794. Disponible: DOI: 10.1364/OL.36.002053

49.   CONKEY, D.V., CARAVACA-AGUIRRE, A.M., DOVE, J.D., JU, H.Y., MURRAY, T.W., PIESTUN, R. Super-resolution photoacoustic imaging through a scattering wall. In: *Nature Communications*. 2015, vol. 6, nr. 1. ISSN 2041-1723 (online). Disponible: DOI: https://arxiv.org/ftp/arxiv/papers/1310/1310.5736.pdf

50. VELLEKOOP, I.M., MOSK, A. Phase control algorithms for focusing light through turbid media. In: *Optics Communications*. 2008, vol. 281, nr. 11, pp.3071-3080. ISSN 0030-4018 (online). Disponible: DOI: 10.1016/j.optcom.2008.02.022

51. DEÁN-BEN X.L., ESTRADA, H., RAZANSKY, D. Shaping volumetric light distribution through turbid media using real-time three-dimensional opto-acoustic feedback. In: *Optics Letters*. 2015, vol. 40, nr.4, pp. 443-446. ISSN 1539-4794 (online). Disponible: DOI: 10.1364/OL.40.000443

52. KATZ, O., SMALL, E., GUAN, Y., SILBERBERG, Y. Noninvasive nonlinear focusing and imaging through strongly scattering turbid layers. In: *Optica*. 2014, vol. 1, nr.3, pp. 170–174. ISSN 2334-2536 (online). Disponible: DOI: 10.1364/OPTICA.1.000170

53. YU, H., LEE, K., PARK, Y. Ultrahigh enhancement of light focusing through disordered media controlled by mega-pixel modes. In: *Optics Express*. 2017, vol. 25, pp. 8036–8047. ISSN 1094-4087 (online). Disponible: DOI: 10.1364/OE.25.008036

54. KATZ, O., RAMAZ, F., GIGAN, S., FINK, M. Controlling light in complex media beyond the acoustic diffraction-limit using the acousto-optic transmission matrix. In: *Nature Communications*. 2019, vol. 10, nr. 717. ISSN 2041-1723 (online). Disponible: DOI: 10.1038/s41467-019-08583-6

55. WANG, D.; ZHOU, E.H.; BRAKE, J.; RUAN, H.; JANG, M., YANG, C. Focusing through dynamic tissue with millisecond digital optical phase conjugation. In: *Optica*. 2015, vol. 2, nr.8, pp. 728–735. ISSN 2334-2536 (online). Disponible: DOI: 10.1364/OPTICA.2.000728

56. LIU, Y., MA, C., SHEN, Y., SHI, J., WANG, L.W. Focusing light inside dynamic scattering media with millisecond digital optical phase conjugation. In: *Optica*. 2017, vol. 4, nr.2, pp. 280–288. ISSN 2334-2536 (online). Disponible: DOI: 10.1364/OPTICA.4.000280

57. JI, N., MILKIE, D.E., BETZIG, E. Adaptive optics via pupil segmentation for high-resolution imaging in biological tissues. In: *Nature Methods*. 2010, vol. 7, pp. 141–147. ISSN 1548-7091 (online). Disponible: DOI: 10.1038/nmeth.1411

58. VELLEKOOP M., AEGERTER, C.M. Scattered light fluorescence microscopy: imaging through turbid layers. In: *Optics Letters*. 2010, vol. 35, nr. 8, pp. 1245-1247. ISSN 1539-4794 (online). Disponible: DOI: 10.1364/OL.35.001245

59. HSIEH, C., PU, Y., GRANGE, R., PSALTIS, D. Digital phase conjugation of second harmonic radiation emitted by nanoparticles in turbid media. In: *Optics Express*. 2010, vol. 18, nr.12, pp. 12283-12290. ISSN 1094-4087 (online). Disponible: DOI: 10.1364/OE.18.012283

60. CHAIGNE, T., KATZ, O., BOCCARA, A.C., FINK, M., BOSSY, E., GIGAN, S. Controlling light in scattering media non-invasively using the photoacoustic transmission matrix.

In: *Nature Photonics*. 2014, vol. 8, pp. 58–64. ISSN 1749-4885 (online). Disponible: DOI: 10.1038/nphoton.2013.307

61.   KONG, F., SILVERMAN, R.H., LIU, L., CHITNIS, P.V., LEE, K.K., CHEN, Y.C. Photoacoustic-guided convergence of light through optically diffusive media. In: *Optics Letters*. 2011, vol. 36, nr. 11, pp. 2053-2055. ISSN 1539-4794 (online). Disponible: DOI: 10.1364/OL.36.002053

62.   TZANG, O., NIV, E., CARAVACA-AGUIRRE, A.M., PIESTUN, R. Thermal expansion feedback for wave-front shaping. In: *Optics Express*. 2017, vol. 25, nr.6, pp. 6122-6131. ISSN 1094-4087 (online). Disponible: DOI: 10.1364/OE.25.006122

63.   LAI, P., WANG, L., TAY, J.W., WANG, L.V. Photoacoustically guided wavefront shaping for enhanced optical focusing in scattering media. In: *Nature Photonics*. 2015, vol. 9, pp. 126–132. ISSN 1749-4885 (online). Disponible: DOI: 10.1038/nphoton.2014.322

64.   JANG, J., LIM, J., YU, H., CHOI, H., HA, J., PARK, J.-H., OH, W.-Y., JANG, W., LEE, S., PARK, Y. Complex wavefront shaping for optimal depth-selective focusing in optical coherence tomography. In: *Optics Express*. 2013, vol. 21, nr.3, pp. 2890–2902. ISSN 1094-4087 (online). Disponible: DOI: 10.1364/OE.21.002890

65.   XU, X., LIU, H., WANG, L.V. Time-reversed ultrasonically encoded optical focusing into scattering media. In: *Nature Photonics*. 2011, vol.5, pp. 154–157. ISSN 1749-4885 (online). Disponible: DOI: 10.1038/nphoton.2010.306

66.   WANG, Y.M., JUDKEWITZ, B., DIMARZIO, C.A., YANG, C. Deep-tissue focal fluorescence imaging with digitally time-reversed ultrasound-encoded light. In: *Nature Communications*. 2012, vol. 3, pp. 928. ISSN 2041-1723 (online). Disponible: DOI: 10.1038/ncomms1925

67.   SI, K., FIOLKA, R., CUI, M. Fluorescence imaging beyond the ballistic regime by ultrasound pulse guided digital phase conjugation. In: *Nature Photonics*. 2012, vol. 6, nr. 10, pp. 657-661. ISSN 1749-4885 (online). Disponible: DOI: 10.1038/nphoton.2012.205

68.   RUAN, H., JANG, M., JUDKEWITZ, B., YANG, C. Iterative Time-Reversed Ultrasonically Encoded Light Focusing in Backscattering Mode. In: *Scientific Reports*. 2014. vol. 4, pp. 7156. ISSN 2045-2322 (online). Disponible: DOI: 10.1038/srep07156

69.   TAY, J., LAI, P., SUZUKI, Y., WANG, L.V. Ultrasonically encoded wavefront shaping for focusing into random media. In: *Scientific Reports*. 2014. vol. 4, pp. 3918. ISSN 2045-2322 (online). Disponible: DOI: 10.1038/srep03918

70.   RUAN, H., JANG, M., YANG, C. Optical focusing inside scattering media with time-reversed ultrasound microbubble encoded light. In: *Nature Communications*. 2015, vol. 6, pp.

8968. ISSN 2041-1723 (online). Disponible: DOI: 10.1038/ncomms9968

71.   DABOV, K., FOI, A., KATKOVNIK, V., EGIAZARIAN, K. Image Denoising by Sparse 3-D Transform-Domain Collaborative Filtering. In: *IEEE Transactions on Image Processing*. 2007. vol. 16, nr. 8, pp. 2080-2095. ISSN: 1941-0042 (online). Disponible: DOI: 10.1109/TIP.2007.901238

72.   KATKOVNIK, V., SHEVKUNOV, I., PETRO, N.V., EGIAZARIAN, K. Computational super-resolution phase retrieval from multiple phase-coded diffraction patterns: simulation study and experiments. In: *Optica*. 2017, vol. 4, nr.7, pp. 786-794. ISSN 2334-2536 (online). Disponible: DOI: 10.1364/OPTICA.4.000786

73.   KATKOVNIK, V., SHEVKUNOV, I.A., PETROV, N.V., AND EGIAZARIAN, K. Wavefront reconstruction in digital off-axis holography via sparse coding of amplitude and absolute phase. In: *Optics Letters.* 2015, vol.40, nr.10, pp. 2417-2420 (2015). ISSN 1539-4794 (online). Disponible: DOI: 10.1364/OL.40.002417

74.   SÁNCHEZ-ORTIGA, E., DOBLAS, A., MARTÍNEZ-CORRAL, M., SAAVEDRA, G., GARCIA-SUCERQUIA, J. Aberration compensation for objective phase curvature in phase holographic microscopy: comment. In: *Optics Letters*. 2014, vol. 39, pp. 417. ISSN 1539-4794 (online). Disponible: DOI: 10.1364/OL.39.000417

75.   FERRARO, P., DE NICOLA, S., FINIZIO, A., COPPOLA, G., S. GRILLI, MAGRO, C., PIERATTINI, G. Compensation of the inherent wave front curvature in digital holographic coherent microscopy for quantitative phase-contrast imaging. In: *Applied Optics.* 2003, *vol.* 42, pp. 1938–1946. ISSN 2155-3165 (online). Disponible: DOI: 10.1364/AO.42.001938

76.   TAHARA, T., QUAN, X., OTANI, R., TAKAKI, Y., MATOBA, O. Digital holography and its multidimensional imaging applications: a review. In: *Microscopy*. 2018, vol. 67, pp.55–67. ISSN 2050-5698 (online). Disponible: DOI: 10.1093/jmicro/dfy007

77.   DOBLAS, A., SÁNCHEZ-ORTIGA, E., MARTÍNEZ-CORRAL, M., SAAVEDRA, G., ANDRÉS, P., GARCIA-SUCERQUIA, J. Shift-variant digital holographic microscopy: inaccuracies in quantitative phase imaging. In: *Optics Letters.* 2013, vol. 38, pp. 1352–1354. ISSN: 1539-4794 (online). Disponible: DOI: 10.1364/OL.38.001352

78.   COLOMB, T. et.al. Automatic procedure for aberration compensation in digital holographic microscopy and applications to specimen shape compensation, In: *Applied Optics*. 2006, vol. 45, pp. 851-863. ISSN 2155-3165 (online). Disponible: DOI: 10.1364/AO.45.000851

79.   KEMPKESET, M. et. al. Three dimensional digital holographic profiling of micro-fibers. In: *Optics Express*, 2009, vol. 17, nr. 4, pp. 2938 –2943. ISSN 1094-4087 (online). Disponible: DOI:10.1364/OE.17.002938

80.   ROSTYKUS, M., SOULEZ, F., UNSER, M., MOSER, C. Compact in-line lensfree digital holographic microscope. In: *Methods.* 2018, vol. 136, pp. 17-23. ISSN: 1095-9130 (online). Disponible: DOI: /10.1016/j.ymeth.2017.11.008

81.   SCHNARS, U., JUEPTNER, W. *Digital Holography* [online]. Berlin: Springer-Verlag, 2005.164 p. ISBN 978-3-540-26911-3. Disponible: DOI: https://doi.org/10.1007/b138284

82.   GARCIA-SUCERQUIA, J., XU, W., JERICHO, S. K., KLAGES, P., JERICHO, M. H., JÜRGEN KREUZER, H. Digital in-line holographic microscopy. In: *Applied optics*. 2006, vol. 45, nr. 5, pp. 836-850. ISSN 2155-3165 (online). Disponible: DOI: 10.1364/AO.45.000836

83.   YAMAGUCHI, I., ZHANG, T., Phase-shifting digital holography. In: *Optics Letters*. 1997, vol. 22, nr. 16, pp. 1268-1270. ISSN 1539-4794 (online). Disponible: DOI: 10.1364/OL.22.001268

84.   GAO, P., YAO, B., HARDER, I., MIN, J., GUO, R., ZHENG, J., YE, T. Parallel two-step phase-shifting digital holograph microscopy based on a grating pair. In: *Journal of Optical Society of America A*. 2011, vol. 28, pp. 434-440. ISSN 1520-8532 (online). Disponible: DOI: 10.1364/JOSAA.28.000434

85.   YAMAGUCHI, Ichirou. Phase-Shifting Digital Holography. In: Poon T.-C., eds. *Digital Holography and Three-Dimensional Display* [online]. Boston; Massachusetts: Springer New York, 2006. ISBN 978-0-387-31397-9. Disponible: https://link.springer.com/book/10.1007/0-387-31397-4

86.   XU, X. F. et. al. Simple direct extraction of unknown phase shift and wavefront reconstruction in generalized phase-shifting interferometry: algorithm and experiments. In: *Optics Letters.* 2008, vol. 33, pp. 776-778. ISSN 1539-4794 (online). Disponible: DOI: 10.1364/OL.33.000776

87.   DU, H., HE, Z., MA, P., CHEN, X., YIN, P. Phase-shift extraction of multiple-frame randomly phase-shifted interferograms by analysis of the amplitude of the analytic signal. In: *Applied Optics. 2020, vol.* 59, pp. 9844-9849 ISSN 2155-3165 (online). Disponible: DOI: 10.1364/AO.405445.

88.   MORIMOTO, Y., NOMURA, T., FUJIGAKI, M., YONEYAMA, S., TAKAHASHI, I. Deformation measurement by phase-shifting digital holography. In: *Experimental Mechanics.* 2005, vol. 45, pp. 65–70. ISSN 1741-2765 (online). Disponible: DOI: 10.1007/BF02428991

89.   XIA, P., WANG, Q., RI, S., TSUDA, H. Calibrated phase-shifting digital holography based on a dual-camera system. In: *Optics Letters*. 2017, vol. 42, nr. 23, pp. 4954-4957. ISSN 1539-4794 (online). Disponible: DOI: 10.1364/OL.42.004954

90.   LARKIN, K. G. A self-calibrating phase-shifting algorithm based on the natural

demodulation of two-dimensional fringe patterns. In: *Optics Express.* 2001, vol. 9, nr. 5, pp. 236-253. ISSN: 1094-4087 (online). Disponible: DOI: /10.1364/OE.9.000236

91. WANG, Z. AND HAN, B. Advanced iterative algorithm for phase extraction of randomly phase-shifted interferograms. In: *Optics Letters*. 2004, vol. 29, nr. 14, pp. 1671-1673. ISSN: 1539-4794. Disponible: DOI: 10.1364/OL.29.001671

92. YOSHIKAWA, N. Phase determination method in statistical generalized phase-shifting digital holography. In: *Applied Optics*. 2013, vol. 52, pp. 1947-1953. ISSN 2155-3165 (online). Disponible: DOI: 10.1364/AO.52.001947

93. KOLLAROVA, V., COLLAKOVA, J., DOSTAL, Z., VESELY, P., CHMELIK, R. Quantitative phase imaging through scattering media by means of coherence-controlled holographic microscope. In: *Journal of Biomedical Optics*. 2015, vol. 20, nr. 11, pp. 1-9. ISSN: 1560-2281 (online). Disponible: DOI: 10.1117/1.JBO.20.11.111206

94. WATANABE. K., NOMURA, T. Recording spatially incoherent Fourier hologram using dual channel rotational shearing interferometer. In: *Applied Optics.* 2015, vol. 54, pp. A18–A22. ISSN 2155-3165 (online). Disponible: DOI: 10.1364/AO.54.000A18

95. PATURZO, M., MEROLA, F., GRILLI, S., DE NICOLA, S., FERRARO P. Digital holography in combination with diffraction grating to get super-resolution. In: *Proceedings of SPIE Conference on Optical Micro-and Nanometrology in Microsystems Technology II*, 20 May 2008, Strasbourg, France, pp. 1-8. Disponible: DOI: 10.1117/12.782111

96. FRERICHS, R. New optical glasses transparent in the infrared up to 12μ. In: *Physical Reviews*. 1950, vol. 78, nr. 5, pp. 643. ISSN 1050-2947 (print). Disponible: DOI: 10.1103/PhysRev.78.637

97. FRERICHS, R. New optical glasses with good transparency in the infrared. In: *Journal of Optical Society of America*. 1953, vol. 43, pp. 1153-1157. ISSN 0030-3941 (print). Disponible: DOI: 10.1364/JOSA.43.001153

98. SANGHERA, J. S., SHAW, L. B., AGGARWAL, I. D. Applications of chalcogenide glass optical fibers. In: *Comptes Rendus Chimie*. 2002, vol. 5, pp. 873-883. ISSN 1878-1543 (online). Disponible: DOI: 10.1016/S1631-0748(02)01450-9

99. Calvez, L. Chalcogenide glasses and glass-ceramics: Transparent materials in the infrared for dual applications. In: *Comptes Rendus Physique*. 2017, vol.18, nr. 5–6, pp. 314-322. ISSN 1631-0705 (online). Disponible: DOI: 10.1016/j.crhy.2017.05.003

100. Manifacier, J. C., Gasiot, J., Fillard, J. P. A simple method for the determination of the optical constants n, k and the thickness of a weakly absorbing thin film. In: *Journal of Physics E: Scientific Instruments.* 1976, vol. 9, pp.1002–1004. ISSN 0022-3735 (print). Disponible: DOI:

10.1088/0022-3735/9/11/032

101.   SWANEPOEL, R. Determination of the thickness and optical constants of amorphous silicon. In: *Journal of Physics E: Scientific Instruments.* 1983, vol. 16, nr.12, pp.1214–1222. ISSN 0022-3735 (print). Disponible: DOI: 10.1088/0022-3735/16/12/023

102.   SWANEPOEL, R. Determination of surface roughness and optical constants of inhomogeneous amorphous silicon films. In: *Journal of Physics E: Scientific Instruments.* 1984, vol. 17, pp. 896–903. ISSN 0022-3735 (print). Disponible: DOI: 10.1088/0022-3735/17/10/023

103.   BUREAU, B. et. al. Recent advances in chalcogenide glasses. In: *Journal of Non-Crysaline Solids*. 2004, vol. 345, pp. 276-283. ISSN 1873-4812 (online). Disponible: DOI: 10.1016/j.jnoncrysol.2004.08.096

104.   HAMMAM, M., ABDEL HARITH, M., OSMAN, W. H. Optical constants of thermally evaporated arsenic triselenide using only transmission spectrum. In: *Solid State Communications.* 1986, vol. 59, pp. 271–274. ISSN 1879-2766 (online). Disponible: DOI: 10.1016/0038-1098(86)90406-0

105.   RAMIREZ-MALO, J. B., MARQUEZ, E., CORRALES, C., VILLARES, P., JIMENEZ-GARAY, R. Optical characterization of As_2S_3 and As_2Se_3 semiconducting glass films of non-uniform thickness from transmission measurements. In: *Materials Science and Engineering B*. 1994, vol. 25, pp. 53–59. ISSN 1873-4944 (online). Disponible: DOI: 10.1016/0921-5107(94)90201-1

106.   MARQUEZ, E., RAMIREZ-MALO, J. B., VILLARES, P., JIMENEZ-GARAY, R., SWANEPOEL, R. Optical characterization of wedge-shaped thin films of amorphous arsenic trisulphide based only on their shrunk transmission spectra. In: *Thin Solid Films.* 1995, vol. 254, pp. 83–91. ISSN 1879-2731 (online). Disponible: DOI: 10.1016/0040-6090(94)06267-O

107.   INCI, M.N., YARADANAKUL, M.A., GÜLŞEN, G., AKTAŞ, G. Characterization of the optical constants of As2Se3 thin films using a fiber optic technique. In: *Infrared Physics and Technology.* 1997, vol. 38, pp. 227–232. ISSN 1879-0275 (online). Disponible: DOI: 10.1016/S1350-4495(97)00010-8

108.   VAN POPTA, A. C., et.al. Photoinduced refractive index change in As2Se3 by 633nm illumination. In: *Optics Express.* 2002, vol. 10, pp. 639-644. ISSN 1094-4087. Disponible: DOI: 10.1364/OE.10.000639

109.   BOOLCHAND, P. GEORGIEV, D. G., GOODMAN, B. Discovery of the intermediate phase in chalcogenide glasses. In: *Journal of Optoelectronics and Advanced Materials.* 2001, vol. 3, pp. 703-720. ISSN 1841 - 7132 (online). Disponible: https://old.joam.inoe.ro/arhiva/Pdf3_3/Boolchand.pdf

110.   ZAKERY, S.R. ELLIOTT, A. Optical properties and applications of chalcogenide glasses: a review. In: *Journal of Non-Crystaline Solids.* 2003, vol. 330, pp.1-12. ISSN 1873-4812 (online). Disponible: DOI: 10.1016/j.jnoncrysol.2003.08.064

111.   KOLOBOV, A.V., FONS, P., TOMINAGA, J. Understanding Phase-Change Memory Alloys from a Chemical Perspective. In: *Scientific Reports*. 2015, vol. 5, nr. 13698. ISSN 2045-2322 (online). Disponible: DOI: 10.1038/srep13698.

112.   TANAKA K. Photoinduced processes in chalcogenide glasses. In: *Current Opinion in Solid State Materials Science.* 1996, vol. 1, nr. 4, pp. 567-571. ISSN 1879-0348 (online). Disponible: DOI: 10.1016/S1359-0286(96)80074-X

113.   OVSHINSKY, S. R. Reversible electrical switching phenomena in disordered structures. In: *Physical Review Letters.* 1968, vol. 21, pp. 1450-1453. ISSN 1079-7114. Disponible: DOI: 10.1103/PhysRevLett.21.1450

114.   TANAKA K., SHIMAKAWA, K. Chalcogenide glasses in Japan: A review on photoinduced phenomena. In: *Physica Status Solidi B*. 2009, vol. 246, nr. 8, pp. 1744–1757. ISSN 1521-3951 (online). Disponible: DOI: 10.1002/pssb.200982002

115.   SHIMAKAWA, K., KOLOBOV, A., ELLIOTT, S.R. Photoinduced effects and metastability in amorphous semiconductors and insulators. In: *Advances in Physics*. 1995, vol. 44, pp. 475-588. ISSN 1460-6976 (online). Disponible: DOI: 10.1080/00018739500101576

116.   TANAKA, Keiji, SHIMAKAWA, Koichi. *Amorphous Chalcogenide Semiconductors and Related Materials.* In: New York: Springer NY, 2011. 242 p. ISBN: 978-1-4939-0232-3

117.   KOLOBOV, Alexander, TOMINAGE, Junji. *Chalcogenides: Metastability and Phase Change Phenomena*. In: New York: Springer NY, 2012. 300 p. ISBN: 978-3-6422-8704-6

118.   ANDERSON, P. W. Model for the Electronic Structure of Amorphous Semiconductors. In: *Physical Review Letters.* 1975, vol. 34, pp. 953. ISSN 1079-7114 (online). Disponible: DOI: /10.1103/PhysRevLett.34.953

119.   STREET, R. A., MOTT N. F. States in the Gap in Glassy Semiconductors. In: *Physical Review Letters.* 1975, vol. 35, pp. 1293-1296. ISSN 1079-7114 (online). Disponible: DOI: 10.1103/PhysRevLett.35.1293

120.   KASTNER, M. Bonding bands, lone-pair bands, and impurity states in chalcogenide semiconductors. In: *Physical Review Letters.* 1972, vol. 28, pp. 355-357. ISSN: 1079-7114 (online). Disponible: DOI: doi.org/10.1103/PhysRevLett.28.355

121.   MOTT, Nevill Francis, DAVIS, Edward. *Electron processes in non-crystalline materials*. In: Oxford: Clarendon Press, 1979. 608 p. ISBN 978-0-1996-4533-6

122.   BRODSKY, H. Marc. *Amorphous semiconductors*. In: Berlin, Heidelberg: Springer

Verlag, 1979, 347 p. ISBN 978-3-540-16008-3

123.   FRITZSCHE, H. Optical anisotropies in chalcogenide glasses induced by band-gap light. In: *Physical Reviews B*. 1995, vol. 52, pp. 15854-15861. ISSN 2469-9969 (online). Disponible: DOI: 10.1103/PhysRevB.52.15854

124.   TIKHOMIROV, V. K., ADRIAENSSENS, G. J., ELLIOTT, S. R. Temperature dependence of the photoinduced anisotropy in chalcogenide glasses: Activation energies and their interpretation. In: *Physical Reviews B*. 1997, vol. 55, pp. 660-663. ISSN 2469-9969 (online). Disponible: DOI: 10.1103/PhysRevB.55.R660

125.   TANAKA, K. Photoinduced deformations in chalcogenide glasses: Scalar and vectoral. In: *Journal of Optoelectronics and Advanced Materials*. 2005, vol. 7, pp. 2571-2580. ISSN 1841 - 7132 (online). Disponible: DOI: 10.1201/b15599-4

126.   ASATRYAN, K.E., FREDERICK, S., GALSTIAN, T., VALLEE, R. Recording of polarization holograms in photodarkened amorphous chalcogenide films. In: *Applied Physics Letters*. 2004, vol. 84, pp. 1626-1628. ISSN 1077-3118 (online). Disponible: DOI: 10.1063/1.1666999

127.   ELLIOTT, S.R., TIKHOMIROV, V.K. Vectoral and scalar photoinduced effects in chalcogenide glasses. In: *Journal of Non-Crystalline Solids*. 1996, vol. 198, pp. 669-674. ISSN 1873-4812 (online). Disponible: DOI: 10.1016/0022-3093(96)00002-6

128.   GRIGOROVICI, R., VANCU, A., GHITA, L. A Unitary Model for Reversible Vectorial and Scalar Photostructural Transformations in Amorphous-Chalcogenide Films. In: *Journal of Non-Crystalline Solids*. 1983, vol.59-60, pp. 909-912. ISSN 1873-4812 (online). Disponible: DOI: 10.1016/0022-3093(83)90316-2

129.   LYUBIN, V. M., TIKHOMIROV, V. K. Novel photo-induced effects in chalcogenide glasses. In: *Journal of Non-Crystalline Solids*. 1991, vol. 135, nr. 37, pp. 37-48. ISSN 1873-4812 (online). Disponible: DOI: 10.1016/0022-3093(91)90440-H

130.   LEE, J. M., PAESLER, M. A. Kinetics of laser-induced phenomena in glassy As_2S_3. In: *Journal of Non-Crystalline Solids*. 1987, vol. 97-98, part 2, pp. 1235-1238. ISSN 1873-4812 (online). Disponible: DOI: 10.1016/0022-3093(87)90295-X

131.   FRITZSCHE, H. The origin of photo-induced optical anisotropies in chalcogenide glasses. In: *Journal of Non-Crystalline Solids*. 1993, vol. 164-166, part 2, pp. 1169-1172. ISSN 1873-4812 (online). Disponible: DOI: 10.1016/0022-3093(93)91207-J

132.   DUNSTAN, D. J. Kinetics of distant-pair recombination: Application to amorphous silicon. In: *Physica B+C*. 1983, vol. 117–118, part 2, pp. 902-904. ISSN: 0378-4363 (online). Disponible: DOI: 10.1016/0378-4363(83)90689-7

133.   EGGLETON, B. J., LUTHER-DAVIES, B., RICHARDSON, K. Chalcogenide photonics. In: *Nature Photonics*, Vol. 5, pp. 141-148, (2011). ISSN 1749-4893 (online). Disponible: DOI: 10.1038/nphoton.2011.309

134.   ANDERLE, K., BIRENHEIDE, R., EICH, M., WENDROFF, J. H. Laser-induced reorientation of the optical-axis in liquid-crystalline sidechain polymers. In: *Macromolecular Rapid Communications*. 1989, vol. 10, nr. 9, pp. 477-483. ISSN 1521-3927 (online). Disponible: DOI: 10.1002/marc.1989.030100907

135.   ANGOLINI, F., GAY, F.P. Synthesis and Properties of Azoaromatic Polymers. In: *Macromolecules.* 1970, vol. 3, pp. 349. ISSN 1520-5835 (online). Disponible: DOI: 10.1021/ma60015a015

136.   HO, M.S., BARRETT, C., PATERSON, J., ESTEGHAMATIAN, M., NATANSOHN, A., ROCHON P. Synthesis and optical properties of poly{(4-nitrophenyl)-[3-[N-[2-(methacryloyloxy)ethyl]- carbazolyl]]diazene}. In: *Macromolecules*. 1996, vol.29, nr.13, pp. 4613-4618. ISSN 1520-5835. Disponible: DOI: 10.1021/ma951432a

137.   NATANSOHN, A., ROCHON, P., GOSSELIN, J., XIE, S. Azo polymers for reversible optical   storage.   1.   Poly[4′-[[2-(acryloyloxy)ethyl]ethylamino]-4-nitroazobenzene].   In: *Macromolecules*. 1992, vol. 25, nr.8, pp. 2268-2273. 1520-5835 (online). Disponible: DOI: 10.1021/ma00034a031

138.   MITSCHERLICH, E. Ueber das Stickstoffbenzid. In: *Annalen der Physik*. 1834, vol. 108, nr.15, pp. 225-226. ISSN 1521-3889 (online). Disponible: DOI: /10.1002/andp.18341081502

139.   HARTLEY, G. The cis-form of azobenzene. In: *Nature*. 1937, vol. 140, nr.3537, pp.281. ISSN 1476-4687 (online). Disponible: DOI: 10.1038/140281a0

140.   PRIIMAGI, A. AND SHEVCHENKO, A. Azopolymer-based micro- and nanopatterning for photonic applications. In: *Journal of Polymer Science B*. 2014, vol. 52, nr.3, pp.163–182. ISSN 1099-0488 (online). Disponible: DOI: 10.1002/polb.23390

141.   TODOROV, T., NIKOLOVA, L., TOMOVA, N. Polarization Holography. A new high-efficiency organic material with reversible photoinduced birefringence. In: *Applied Optics*. 1984, vol. 23, pp. 4309-4312. ISSN 2155-3165 (online). Disponible: DOI: 10.1364/AO.23.004309

142.   EICH, M., WENDORFF, J.H., RECK, B., RINGSDORF, H. Reversible digital and holographic optical storage in polymeric liquid crystals. In*: Die Makromolekulare Chemie, Rapid Communications.* 1987. vol. 8, nr.1, pp.59-63. ISSN 1521-3927 (online). DOI: 10.1002/marc.1987.030080111.

143.   FIORINI, C., PRUDHOMME, N., DE VEYRAC, G., MAURIN, I, RAIMOND, P., NUNZI, J.M. Molecular migration mechanism for laser induced surface relief grating formation.

In: *Synthetic Metals.* 2000, vol.115, pp. 121– 125. ISSN 0379-6779 (online). Disponible: DOI: 10.1016/S0379-6779(00)00332-5

144. ZETTSU, N., OGASAWARA, T., MIZOSHITA, N., NAGANO, S., SEKI, T. Photo-Triggered Surface Relief Grating Formation in Supramolecular Liquid Crystalline Polymer Systems with Detachable Azobenzene Unit. In: *Advance Materials.* 2008, vol.20, nr.3, pp. 516-521. ISSN 1521-4095 (online). Disponible: DOI: 10.1002/adma.200701110

145. DELAIRE, J.A., NAKATANI, K. Linear and Nonlinear Optical Properties of Photochromic Molecules and Materials. In: *Chemical Reviews.* 2000, vol. 100, nr. 5, pp. 1817-1845. ISSN 1520-6890 (online). Disponible: DOI:10.1021/cr980078m

146. AHMAD, N. M., BARRETT, C. J. Novel Azo Chromophore-Containing Polymers: Synthesis and Characterization. In: *Proceedings of the American Chemical Society Division of Polymeric Materials: Science and Engineering*. August 26-30, 2001, Chicago, United States, vol. 85, pp. 607–608. ISBN 978-0841238022

147. MEKELBURGER, H.B., RISSANEN, K., VOEGTLE, F. Repetitive-Synthesis of Bulky Dendrimers – A Reversibly Photoactive Dendrimer with Six Azobenzene Side Chains. In: *Chemische Berichte*. 1993, vol. 126, pp. 1161. ISSN 0365-9496 (online). Disponible: DOI: 10.1002/cber.19931260516

148. JUNGE, D.M., MCGRATH, D.V. Photoresponsive dendrimers. In: *Chemical Communications*. 1997, vol. 9, pp. 857-858. ISSN 1364-548X (online). Disponible: DOI: 10.1039/A700292K

149. MARTINEZ-PONCE, G., PETROVA, T., TOMOVA, N., DRAGOSTINOVA, V., TODOROV, T., NIKOLOVA, L. Bifocal-polarization holographic lens. In: *Optics Letters*. 2004, vol. 29, nr.9, pp. 1001–1003. ISSN 1539-4794 (online). Disponible: DOI: 10.1364/ol.29.001001

150. TODOROV, T., NIKOLOVA, L., STOILOV, G., HRISTOV, B. Spectral stokesmeter. 1. Implementation of the device. In: *Optics Letters*. [online]. 2007, vol. 46, nr. 27, pp. 6662-6668. ISSN 1539-4794 (online). Disponible: DOI: 10.1364/AO.46.006662.

151. RAMANUJAM, P.S., DAM-HANSEN, C., BERG, R.H., HVILSTED, S., NIKOLOVA, L. Polarisation sensitive optical elements in azobenzene polyesters and peptides. In: *Optics and Lasers in Engineering.* 2006, vol. 44, nr. 9, pp. 912-925. ISSN 0143-8166 (online). Disponible: DOI: 10.1016/j.optlaseng.2005.06.015

152. KIM, D.Y., LI, L., JIANG, X.L., SHIVSHANKAR, V., KUMAR, J., TRIPATHY, S.K. Polarized laser induced holographic surface relief gratings on polymer films. In: *Macromolecules.* 1995. vol. 28, nr. 26, pp. 8835–8839. ISSN 0141-8130 (online). Disponible: DOI: 10.1021/ma00130a017

153.   BERENDT, J., TEIXEIRA, J.M., GARCÍA-GARCÍA, A., RAPOSO, M., RIBEIRO, P.A., DUBOWIK, J., KAKAZEI, G.N., SCHMOOL, D.S. Tunable magnetic anisotropy in permalloy thin films grown on holographic relief gratings. In: *Applied Physics Letters.* 2014, vol. 104, pp. 082408. ISSN 0141-8130 (online). Disponible: DOI: 10.1063/1.4867162

154.   BERBEROVA, N., DASKALOVA, D., STRIJKOVA, V., KOSTADINOVA, D., NAZAROVA, D., NEDELCHEV, L., STOYKOVA, E., MARINOVA, V., CHI, C.H., LIN, S.H. Polarization holographic recording in thin films of pure azopolymer and azopolymer based hybrid materials. In: *Optical Materials*. 2017, vol. 64, pp. 212-216. ISSN 0925-3467 (online). Disponible: DOI: 10.1016/j.optmat.2016.12.002

155.   LIAN L., NEDELCHEV, A. S., MATHARU, S., HVILSTED, S., RAMANUJAM, P.S. Photoinduced anisotropy in a family of amorphous azobenzene polyesters for optical storage. In: *Applied optics.* 2003. vol. 42, nr. 29, pp. 5918–5927. ISSN 2155-3165 (online). Disponible: DOI: 10.1364/AO.42.005918

156.   GERBREDERS, A., ALEKSEJEVA, J., GERTNERS, U., TETERIS, J. The synthesis of different variants of azo-polyurethane polymers for optical recording. In: *Journal of Optoelectronics and Advanced Materials.* 2011, vol.13, nr.11, pp.1559-1562. ISSN 1841 – 7132(online). Disponible: file:///C:/Users/dioni/Downloads/37Gerbreders.pdf

157.   ROCHA, L., PAIUS, C., LUCA-RAICU, A., RESMERITA, E., RUSU, A., MOLEAVIN, I., HAMEL, M., BRANZA-NICHITA, N., HURDUC, N. Azobenzene based polymers as photoactive supports and micellar structures for applications in biology. *Journal of Photochemistry and Photobiology A: Chemistry*. 2014, vol. 291, pp.16-25. ISSN 1873-2666 (online). Disponible: https://cea.hal.science/cea-01820327/document

158.   WANG, X. *Azo Polymers: Synthesis, Functions and Applications.* Berlin: Springer-Verlag GmbH Germany, 2017. 238 p. ISBN 978-3-662-53422-9.

159.   VISWANATHAN, N.K., BALASUBRAMANIAN, S., LI, L., TRIPATHY, S.K., KUMAR, J. A detailed investigation of the polarization-dependent surface-relief-grating formation process on azo polymer films. In: *Japanese Journal of Applied Physics. Part 1.* 1999, vol. 38, nr.10, pp. 5928– 5937. ISSN 1347-4065 (online). Disponible: DOI: 10.1143/JJAP.38.5928

160.   SOBOLEWSKA, A., BARTKIEWICZ, S. Surface relief grating in azo-polymer obtained for *s-s* polarization configuration of the writing beams. In: *Applied Physics Letters*. 2012, vol. 101, nr.19, pp. 193301. ISSN 1077-3118 (online). Disponible: DOI 10.1063/1.4764950

161.   TSUTSUMI, N., YABUHARA, Y., KINASHI, K., SAKAI, W. Advantage of the circular polarization of light in the updatable holographic response in an azo-carbazole monolithic dye

dispersed acrylate matrix. In: *Optical Materials Express*. 2017, vol. 7, nr. 5, pp. 1647-1655. ISSN 2159-3930 (online). Disponible: DOI: 10.1364/OME.7.001647

162.   GARROT, D., LASSAILLY, Y., LAHLIL, K., BOILOT, J.P., PERETTI, J. Real-time near-field imaging of photoinduced matter motion in thin solid films containing azobenzene derivatives. In: *Applied Physics Letters.* 2009, vol. 94, nr.3, pp. 033303.   ISSN 1077-3118 (online). Disponible: DOI: 10.1063/1.3073742

163.   F. FABBRI, D. GARROT, K. LAHLIL, J. P. BOILOT, Y. LASSAILLY, J. PERETTI, *J.* Evidence of Two Distinct Mechanisms Driving Photoinduced Matter Motion in Thin Films Containing Azobenzene Derivatives. In: *The Journal of Physical Chemistry*. 2011, vol. 115, nr. 6, pp. 1363–1367. ISSN 1520-5207. Disponible: DOI: 10.1021/jp110567z

164.   NATANSOHN, A., ROCHON, P. Photoinduced Motions in Azo-Containing Polymers. In: *Chemical Review and Letters.* 2002, vol. 102, nr. 11, pp. 4139–4175. ISSN 2645-4947(online). Disponible: DOI: 10.1021/cr970155y

165.   KIM, D.Y., TRIPATHY, S.K., LI, L., KUMAR, J. Laser-induced holographic surface relief gratings on nonlinear optical polymer films. In: *Applied Physics Letters.* 1995, vol. 66, nr.10, pp. 1166-1168. ISSN 1077-3118 (online). Disponible: DOI: 10.1063/1.113845

166.   MOTE, R.G., YU, S.F., NG, B.K., ZHOU, W., LAU, S.P. Near-field focusing properties of zone plates in visible regime – New insights. In*: Optics Express,* vol. 16, nr.13, pp. 9554-9564. ISSN 1094-4087 (online). Disponible: DOI: 10.1364/OE.16.009554

167.   Yu, H., Ikeda, T. Photocontrollable Liquid-Crystalline Actuators. In: *Advanced Materials.* 2011, vol.23,   nr.19,   pp. 2149-2180.   ISSN   1521-4095   (online).   Disponible: DOI: 10.1002/adma.201100131

168.   SEKKAT, Z., YASUMATSU, D., KAWATA, S. Pure photo-orientation of azo dye in polyurethanes and quantification of orientation in spectrally overlapping isomers. In: *The Journal of Physical Chemistry B*. 2002, vol. 106, pp. 12407– 12417. ISSN 1520-5207 (online). Disponible: DOI: 10.1021/jp020132

169.   HOLME, N. C. R., RAMANUJAM, P.S., HVILSTED, S. 10,000 optical write, read, and erase cycles in an azobenzene sidechain liquid-crystalline polyester. In: *Optics Letters.* 1996, vol. 21, nr.12, pp. 902-904. ISSN 1539-4794 (online). Disponible: DOI: 10.1364/OL.21.000902

170.   HONG, J.C., PARK, J.H., CHUN, C., KIM, D.Y. Photoinduced tuning of optical stop bands in azopolymer based inverse opal photonic crystals. In: *Advanced Functional Materials.* 2007,   vol.17,   pp.   2462-2469.   ISSN   1616-3028   (online).   Disponible: DOI: 10.1002/adfm.200600773

171.   NEDELCEV, N., IVANOV, D., BLAGOEVA, B., NAZAROVA, D. Optical anisotropy

induced at five different wavelengths in azopolymer thin films: Kinetics and spectral dependence. In: *Journal of Photochemistry and Photobiology A: Chemistry*. 2019, vol. 376, nr.45, pp. 1-6. ISSN 1010-6030 (online). Disponible: DOI: 10.1016/j.jphotochem.2019.02.009

172. GEUE, T.M., SAPHIANNIKOVA, A.G., HENNENBERG, O., PIETSCH, U., ROCHON, P.L., NATANSOHN, A. L. Formation mechanism and dynamics in polymer surface gratings. In: *Physical Review Research*. 2002. vol. 65, pp. 052801. ISSN 2643-1564 (online). Disponible: DOI: 10.1103/PhysRevE.65.052801

173. JUAN M.L., PLAIN J., BACHELOT R., ROYER P., GRAY S.K., WIEDERRECHT G.P. Multiscale model for photoinduced molecular motion in azo polymers. In: *ACS Nano*. 2009, vol.3, nr.6, pp. 1573–1579. ISSN 1936-086X (online). Disponible: DOI: 10.1021/nn900262e

174. AMBROSIO, A., MADDALENA, P., MARRUCCI, L. Molecular Model for Light-Driven Spiral Mass Transport in Azopolymer Films. In: *Physical Review Research*. 2013, vol.110, 146102. ISSN 2643-1564 (online). Disponible: DOI: 10.1103/PhysRevLett.110.146102

175. EMERY, Y. et.al. Digital Holographic Microscopy (DHM) for metrology and dynamic characterization of MEMS and MOEMS. In: *Proceedings of SPIE Photonics Europe Conference, April 3-7, 2006*, Strasbourg, France, 2006, vol. 6186, pp.1-5. ISSN: 1996-756X (online). Disponible: DOI: 10.1117/12.660029

176. MIR, M., BHADURI, B., WANG, R., ZHU, R., POPESCU, G. Quantitative Phase Imaging. In: WOLF, E., eds. *Progress in Optics*[online]. Oxford, United Kingdom: Elsevier Science, 2012, vol.57, pp. 134-214. ISBN 978-0444594228

177. OSTEN, W. et.al. Recent advances in digital holography. In: *Applied Optics*. 2014, vol. 53, nr. 27, pp. 44-63. ISSN 2155-3165. Disponible: DOI: 10.1364/AO.53.000G44

178. PATURZO, M., MEROLA, F., GRILLI, S., DE NICOLA, S., FINIZIO, A., FERRARO, P. Super-resolution in digital holography by a two- dimensional dynamic phase grating. In: *Optics Express*. 2008, vol. 16, nr. 21, pp. 17107-17118. ISSN 1094-4087 (online). Disponible:10.1364/OE.16.017107

179. LIU, C., LIU, Z., BO, B., WANG, Y., ZHU, J. Super-resolution digital holographic imaging method. In: *Applied Physics Letters*. 2002, vol. 81, nr.17, pp. 3143-3145. ISSN 1077-3118 (online). Disponible: DOI: 10.1063/1.1517402

180. PATURZO, M., MEROLA, F., FERRARO, P. Multi-imaging capabilities of a 2D diffraction grating in combination with digital holography. In: *Optics Letters*. 2010, vol.35, pp. 1010-1012. ISSN:1539-4794 (online). Disponible: DOI: 10.1364/OL.35.001010

181. KATKOVNIK, V., SHEVKUNOV, I., PETROV, N., EGIAZARIAN, K. Computational wavelength resolution for in-line lensless holography: phase-coded diffraction patterns and

wavefront group-sparsity. In: *Proceedings of SPIE Digital Optical Technologies*, *June, 26, 2017*. Munich, Germany, vol. 10335, pp. 1-13, 2017. ISSN: 1996-756X (print). Disponible: doi:10.1117/12.2269327

182.   GUSTAFSSON, M. G. Surpassing the lateral resolution limit by a factor of two using structured illumination microscopy. In: *Journal of Microscopy*. 2000, vol. 198, pp. 82-87. ISSN: 1365-2818 (online). Disponible: DOI: 10.1046/j.1365-2818.2000.00710.x

183.   GRANERO, L., MICÓ, V., ZALEVSKY, Z., GARCÍA, J. Superresolution imaging method using phase-shifting digital lensless Fourier holography. In: *Optics Express*. 2009, vol. 17, nr. 21, pp. 15008-15022. ISSN 1094-4087 (online). Disponible: DOI: 10.1364/OE.17.015008

184.   PATURZO, M., FERRARO, P. Correct self-assembling of spatial frequencies in super-resolution synthetic aperture digital holography. In: *Optics Letters*. 2009, vol. 34, nr.23, pp. 3650-3652. ISSN 1539-4794 (online). Disponible: DOI:10.1364/OL.34.003650

185.   O'CONNOR, T., DOBLAS, A., JAVIDI, B. Structured illumination in compact and field-portable 3D-printed shearing digital holographic microscopy for resolution enhancement. In: *Optics Letters*. 2009, vol. 44, nr.9, pp. 2326-2329. ISSN 1539-4794 (online). Disponible: DOI: 10.1364/OL.44.002326

186.   ZHENG, J., GAO, P., YAO, B., YE, T., LEI, M., MIN, J., DAN, D., YANG, Y., YAN, S. Digital holographic microscopy with phase-shift-free structured illumination. In: *Photonics Research*. 2014, vol. 2, nr.3, pp. 87-91.   ISSN 2327-9125 (online). Disponible: DOI: 10.1364/PRJ.2.000087

187.   JANG, J., LIM, J., YU, H., CHOI, H., HA, J., PARK, J-H., OH, W-Y., JANG, W., LEE, SD., PARK, YK. Complex wavefront shaping for optimal depth-selective focusing in optical coherence tomography. In: *Optics Express*. 2013, vol. 21, nr. 3, pp. 2890-2902. ISSN 1094-4087 (online). Disponible: DOI: 10.1364/OE.21.002890

188.   BUITRAGO-DUQUE, CA., GARCIA-SUCERQUIA, J. Realistic modeling of digital holographic microscopy. In: *Optical Engineering*. 2020, vol. 59, nr. 10, pp.1-14. ISSN 1560-2303 (online). Disponible: DOI: 10.1117/1.OE.59.10.102418

189.   SÁNCHEZ-ORTIGA, E., SAAVEDRA, A., MARTINEZ-CORRAL G. Off-axis digital holographic microscopy: practical design parameters for operating at diffraction limit. In. *Applied Optics*. 2014, vol. 53, nr. 10, pp. 2058–2066. ISSN 2155-3165 (online). Disponible: DOI: 10.1364/AO.53.002058

190.   KARRAY, M., SLANGEN, P., PICART, P.   Comparison between digital Fresnel holography and digital image-plane holography: the role of the imaging aperture. In: *Experimental Mechanics*. 2012, vol. 52, nr.9, pp. 1275–1286. ISSN 1741-2765 (online). Disponible: DOI:

10.1007/s11340-012-9604-6

191.   CATTIN, P. Image Restoration: Introduction to Signal and Image Processing [online]. MIAC, *University of Basel*. 19 April 2016. Disponible: https://dokumen.tips/documents/image-restoration-biomedical-engineering-image-restoration-introduction-to-signal.html?page=1

192.   LIEBLING, M., BLU, T., UNSER, M. New Multiresolution Wavelet Bases for Digital Holography. In: *IEEE Transactions on Image Processing*. 2003, vol. 12, nr. 1, pp. 29-43. ISSN: 1057-7149 (online). Disponible: DOI: 10.1109/TIP.2002.806243

193.   BIOUCAS-DIAS, JM., VALADAO, C. Phase Unwrapping via Graph Cuts In: *IEEE Transactions on Image Processing*. 2007, vol. 6, nr. 3, pp. 698-709. ISSN: 1057-7149 (online). Disponible: DOI: 10.1109/tip.2006.888351

194.   KUJAWINSKA M, WÓJCIAK J. High accuracy Fourier transform fringe pattern analysis. In: *Optics and Lasers in Engineering*. 1991, vol. 14, nr. 4-5, pp. 325-339. ISSN 0143-8166 (online). Disponible: DOI: 10.1016/0143-8166(91)90056-Y

195.   **CAZAC, V**. Improved 3D imaging of phase shifting digital holographic microscope by compensation for wavefront distortion. In: *Journal of Physics: Conference Series*, *vol. 1745, 6th International Conference on Information Technology and Nanotechnology, 26-29 May 2020,* Samara, Russia, pp. 1-7. ISSN 1742-6596 (online). Disponible: DOI: 10.1088/1742-6596/1745/1/012020

196.   KOCSIS, P., SHEVKUNOV, I., KATKOVNIK, V., EGIAZARIAN, K. Single exposure lensless subpixel phase imaging: optical system design, modelling, and experimental study. In: *Optics Express*. 2020, vol. 28, nr. 4, pp. 4625-4637. ISSN 1094-4087 (online). Disponible: DOI: 10.1364/OE.379785

197.   TZANG, O., NIV, E., SINGH, S., LABOUESSE, S., MYATT, G., PIESTUN, R. Wavefront shaping in complex media with a 350 kHz modulator via a 1D-to- 2D transform. Nat. Photonics, Vol.13, pp. 788–793, (2019) In: *Nature Photonics.* 2019, vol. 13, nr. 11, pp. 788–793. ISSN 1749-4885 (online). Disponible: DOI: 10.1038/s41566-019-0503-6

198.   ERIKSSON, E., KEEN, S., LEACH, J., GOKSOR, M., PADGETT, MJ. The effect of external forces on discrete motion within holographic optical tweezers. In*: Optics Express.* 2007, vol. 15, nr. 26, pp. 18268-18274. ISSN 1094-4087 (online). Disponible: DOI:10.1364/OE.15.018268

199.   HUSSAIN, A., MARTINEZ, J.L. CAMPOS, J. Holographic superresolution using spatial light modulator. In: *Journal of the European Optical Society Rapid Publications.* 2013, vol. 8, nr. 13007, pp.1-6. ISSN: 1990-2573 (online). Disponible: DOI:10.2971/jeos.2013.13007

200.   **CAZAC, V.**, ACHIMOVA, E., ABASHKIN, V., PRISACAR, A., LOSHMANSCHII, C.,

MESHALKIN, A., EGIAZARIAN, K. Polarization holographic recording of vortex diffractive optical elements on azopolymer thin films and 3D analysis via phase-shifting digital holographic microscopy. In*: Optics Express.* 2021. Vol. 29, nr. 6, pp. 9217-9230. ISSN 1094-4087 (online). Disponible: DOI: 10.1364/OE.415639

201.   LU, T. H., HUANG, T. D., WANG, J. G., WANG, L. W., ALFANO, L. W. Generation of flower high-order Poincaré sphere laser beams from a spatial light modulator. In: *Scientific reports.* 2016, vol. 6, nr. 396756, pp. 1-6. ISSN 2045-23227 (online). Disponible: DOI: 10.1038/srep39657

202.   LI, Y., LIU, Y., LI, S., ZHOU, P., ZHAN, T., CHEN, Q., SU, Y., WU, S.-T. Single-exposure fabrication of tunable Pancharatnam-Berry devices using a dye-doped liquid crystal. In*: Optics Express.* 2019, vol. 27, nr. 6, pp. 9054–9060. ISSN 1094-4087 (online). Disponible: DOI: 10.1364/OE.27.009054

203.   SOLOMON, J. E. Polarization imaging. In. *Applied Optics.* 1981, vol.20, nr. 9, pp. 1537–1544. ISSN 2155-3165 (online). Disponible: DOI: 10.1364/AO.20.001537

204.   DAVIS, J. A.G., EVANS, H., MORENO, I. Polarization-multiplexed diffractive optical elements with liquid crystal displays. In. *Applied Optics.* 2005, vol.44, nr. 19, pp. 4049-4052. ISSN 2155-3165 (online). Disponible: DOI: 10.1364/AO.44.004049

205.   MAURER, C., JESACHER, A., BERNET, S., RITSCH-MARTE, M. In: What spatial light modulators can do for optical microscopy. In: *Laser and Photonics Reviews.* 2011, vol.5, nr.1, pp. 81–101. ISSN: 1863-8899 (online). Disponible: DOI: 10.1002/lpor.200900047

206.   VISWANATHAN, N. K., BALASUBRAMANIAN, S., LI, L., TRIPATHY, S. K., KUMAR, J. A Detailed Investigation of the Polarization-Dependent Surface-Relief-Grating Formation Process on Azo Polymer Films. In: *The Japanese Journal of Applied Physics.* 1999, vol.38, nr. 10, pp. 5928–5937. ISSN 1347-4065 (online). Disponible: DOI:10.1143/jjap.38.5928

207.   MESHALKIN, A., ROBU, S., ACHIMOVA, E., PRISACAR, A., SHEPEL, D., ABASHKIN, V., TRIDUH G. Direct photoinduced surface relief formation in carbazole-based azopolymer using polarization holographic recording. In: *Journal of Optoelectronics and Advanced Materials.* 2016, vol. 18, nr. 9-10, pp. 763–768. ISSN 1841-7132 (online). Disponible: https://old.joam.inoe.ro/index.php?option=magazine&op=view&idu=4016&catid=98

208.   ACHIMOVA, E., STRONSKI, A., ABASKIN, V., MESHALKIN, A., PAIUK, A., PRISACAR, A., OLEKSENKO, P., TRIDUH, G. Direct surface relief formation on As_2S_3–Se nanomultilayers in dependence on polarization states of recording beams. In: *Optical Materials.* 2015, vol. 47, pp. 566-572. ISSN 0925-3467 (online). Disponible: DOI: 10.1016/j.optmat.2015.06.044

209.   POELMAN, D., SMET, P. F. Methods for the determination of the optical constants of thin films from single transmission measurements: a critical review. In: *Journal of Physics D: Applied Physics.* 2003, vol. 36, nr. 15. pp. 1850–1857 ISSN 1361-6463 (online). Disponible: DOI: 10.1088/0022-3727/36/15/316

210.   MESHALKIN, A., ABASHKIN, V., PRISACAR, A., TRIDUH, G., ANDRIES, I., BETS, L., ACHIMOVA, E. High precision interferometric thickness analysis of submicrometers spin-coated polyepoxupropylcarbazole films. In: *Sensor Electronics and Microsystem Technologies*. 2012, vol. 3, pp. 62–69. ISSN 2415-3508 (online). Disponible: DOI: 10.18524/1815-7459.2012.3.114659

211.   KIKINESHI, A. Light-stimulated structural transformations and optical recording in amorphous nano-layered structures. In: *Journal of Optoelectronics and Advanced Materials*. 2001, vol. 5, nr. 2, pp. 377–382. ISSN 1841-7132 (online). Disponible: DOI: https://apps.dtic.mil/sti/tr/pdf/ADP011528.pdf

212.   KATKOVNIK, V., SHEVKUNOV, I., PETROV, N., EGIAZARIAN, K. Sparse approximations of phase and amplitude for wave field reconstruction from noisy data. In: *Proceedings of SPIE Optic+Optoelectronic*, *May, 8, 2015*. Prague, Czech Republic, 2015, vol. 9508, pp.1-13. ISSN: 1996-756X. Disponible: DOI: 10.1117/12.2177657

213.   BOUCHAL, P., CELECHOVSK, R., BOUCHAL, Z. Polarization sensitive phase-shifting Mirau interferometry using a liquid crystal variable retarder. In: *Optics Letters*. 2015, vol. 40, nr.19, pp. 4567–4570. ISSN 1539-4794 (online). Disponible: DOI: 10.1364/OL.40.004567

214.   **CAZAC, V.**, LOSMANSCHII, C., ACHIMOVA, E., MESHALKIN, A., ABASHKIN, V., PODLIPNOV, V. Characterization of Polarization Holographic Gratings Obtained on Azopolymer Thin Films by Digital Holographic Microscopy. In: *Journal of Biomedical Photonics and Engineering*. 2021, vol. 3, nr. 7, pp. 1-5. ISSN 2411-2844 (online). Disponible: DOI: 10.18287/JBPE21.07.030306

Annex 1. MATLAB simulation of the off-axis DHM with sinusoidal phase mask

```matlab
1. close all; clear all; clc;
%% Generate the object wavefront

2. lambda=633e-9;
3. delta_y_0=2.2e-6;
4.      obj1=(fspecial('gauss',[64,64],18));
5.      obj1=obj1/max(obj1(:))*pi;
6.      ampl1=(fspecial('gauss',[64,64],18));
7.      ampl1=ampl1/max(ampl1(:));
8.      O1=1.5*ampl1.*exp(1j*obj1);
%Grating parameters

9. Z=zeros(9);%initializing the matrix with 9x9 zeros
10.     e=1; %integer correlated with Phase
11.     % for Phase=0.1*pi:0.1*pi:2*pi
12.        indx12=0;
13.        for Angle=90
14.           indx12=indx12+1;
15.     Period=21*delta_y_0;
16.     [Ay,Ax]=size(obj1);
17.     [V,T] = meshgrid(1:Ax,1:Ay);
18.     Phase=0.1*pi;
19.     % Angle=90;
20.     %  indx12=indx12+1;
21.     rad=Angle*pi/180;
22.     % Period=3*delta_y_0;
23.     % Phase=pi;
24.     grating=exp(1j*(Phase*sin(1/Period*2*pi*T*sin(rad)*delta_y_0+1/Pe
   riod*2*pi*V*cos(rad)*delta_y_0)));
25.     figure(2); set(gcf, 'Position', get(0,'ScreenSize'));
26.     imagesc(angle(grating)); colormap(gray); axis square; colorbar;
   title('Initial GRATING PHASE');
27.     %Adding grating to the object
28.           Er=O1.*grating;%*exp(1j*Shift);
%start Padding

29.     N=1046*2; %zeropaded size of the image
30.     Si=64; %size of the image
31.     M=(N-Si)/2; %calculated number for the padarray function
32.           Pad_obj=padarray(Er, [M M],'both');
33.     figure(4); set(gcf, 'Position', get(0,'ScreenSize'));
34.     imagesc(angle(Pad_obj)); colormap(gray); axis square; colorbar;
   title('Zeropadded Object + Grating');
35.     S=Pad_obj;
36.     d1=0.04  %%m
37.     [O1toholo] = AngularSp2((S),d1,lambda,delta_y_0,delta_y_0);
   %propagation to the sensor array
38.     F=figure(5); set(gcf, 'Position', get(0,'ScreenSize'));
39.     imagesc((abs(O1toholo))); colormap(gray); axis square; colorbar;
   title(['propagation O1 to CCD= ', num2str(Period)]);
%% Reference wavefront generation

40.     x=0.15;
41.     y=0.15;
42.     [Xa,Ya] = meshgrid(1:N,1:N);
```

```matlab
43.        kSinTheta_x=2*pi*x;  %% the point of the first order is equal to
   .25
44.        kSintheta_y=2*pi*y;
45.             ref_phase=exp(1j*(kSinTheta_x*Xa-Ya*kSintheta_y));   %
   reference signal projected on a plane perpendicular to the propagation
   axis of the signal wavefront
46.        % figure(6); set(gcf, 'Position', get(0,'ScreenSize'));
%Hologram generation

47.             Holo = abs(ref_phase+O1toholo).^2; %Hologram of both
   objects
48.        % figure(7),set(gcf, 'Position', get(0,'ScreenSize'));
49.        % imagesc(Holo); colormap(gray); axis square; colorbar;
   title('Hologram');
%% Hologram reconstruction using SPAR algorythm

50.        window_sigma=1.6; window_size=9;
51.             [Z_est0,Z_est1,Ar_est]
   =Phase_Ampl_NoiseFiltering_Liebling_Initial(Holo,conj(ref_phase),window
   _size,window_sigma);
52.             Reconstr=(Z_est1);%reconstructed hologram
53.             [Z_est1_backprop] = AngularSp2((Z_est1./Ar_est),-
   d1,lambda,delta_y_0,delta_y_0);
%Unpadding

54.             Unpad=Z_est1_backprop(M+1:end-M,M+1:end-M);
   %unzeropadding
55.             G=Unpad;
%grating substraction

56.             H=G./grating;
57.        % figure(8);set(gcf, 'Position', get(0,'ScreenSize'));
58.        % imagesc(angle(H)); colormap(gray); axis square; colorbar;
   title('Un-Zeropadded OBJECT 1');
59.             A=angle(O1);
60.             B1=angle(H);
61.        C1=(A-B1).^2;
62.             D=A.^2;
63.             D1=C1./D;
64.             RMSE1=norm((obj1-B1),'fro')/sqrt(64*64);
65.             maxi1=max(B1(:));
66.             PSNR=10*log(maxi1/RMSE1);
67.          angl(indx12)=Angle;
68.          rmsev1(indx12)=RMSE1;
69.        end
70.          Z(e, 1:20)=rmsev1; %collects all the RMSE data, 2D matrix
71.          e=e+1; %incrimentation
72.        end
73.        figure (123);
   surf([3*delta_y_0:delta_y_0:22*delta_y_0],[0.1*pi:0.1*pi:2*pi], Z);
74.        figure(12); plot(angl, rmsev1, '-o', 'LineWidth', 2); grid on,
   title(' RMSE dependance on grating angle, optimal Period and Phase');
75.        figure(9); set(gcf, 'Position', get(0,'ScreenSize'));
76.         subplot(1,2,1); plot(RMSE1, '-o', 'LineWidth', 2); grid on;
   title('RMSE value');
```

```
77.        subplot(1,2,2); plot(PSNR, '-o', 'LineWidth', 2); grid on;
   title('PSNR value');
```

Annex 2. SPAR algorithm for phase reconstruction from off-axis holograms

```matlab
% close all
% clear all

RRR=200;
% load MatlabWorkspace
sample=2;
switch(sample)
    case 1
        holo_195=double(imread('grationg12.tif'))/255;
        %holo_195=double(holo_195)/255;
        ref_195=double(imread('ref3.tif'))/255;
    case 2
        holo_195=double(imread('gr82withref.tif'))/255;
        %holo_195=double(holo_195)/255;
        ref_195=double(imread('refgr82.tif'))/255;
end


pp=380;
gg=380;
holo_195=holo_195(pp+[0:511],gg+[0:511]);
ref_195=ref_195(pp+[0:511],pp+[0:511]);

%%  holo_195, ref_195
[yN,xN]=size(holo_195);
% imwrite(uint8(ref_195*255), gray(256), 'ref_195test.bmp');
% imwrite(uint8(holo_195*255), gray(256), 'holo_195test.bmp');
%%[Xa,Ya] = meshgrid(1:xN,1:yN);
[Xa,Ya] = meshgrid(-xN/2:xN/2-1,-yN/2:yN/2-1);

%% Angles of the reference wavefront
k_theta_x=1.605/2/pi;     %1.4957


k_theta_y=0.470/2/pi;       %0.5074
%%%%%%%% REFERENCE PHASE LINEAR
%%Er_phase=exp(1i*2*pi*(k_theta_x*Xa-k_theta_y*Ya)); %% linear wavefront
%%delta=2*10^(-9);   %%%%% pixel size
lambda=633*10^(-9);
R=0.178; delta_R=0;    %0.178
R=R*(1+delta_R);
delta=2.2*10^(-6);   %% pixels
% Er_phase_quadratic=exp(1i*pi*(Xa.^2+Ya.^2)*delta^2/lambda/R);
%
% Er_phase=(Er_phase.*Er_phase_quadratic);
% delta=2.2*10^(-6);             %% m
delta_x=0; % .015%     for 267 it should be multiplied by -17;
delta_y=0;  % -.05%  for 267 it should be multiplied by 6;
xo=k_theta_x*R*lambda/delta*(1+delta_x);  %% m
yo=k_theta_y*R*lambda/delta*(1+delta_y);  %% m

t=-1.745;  %0.92
a=0;  %0.865
delta_xr=.015*t;
delta_yr=-.05*a;
xor=k_theta_x*R*lambda/delta*(1+delta_xr);  %% m
yor=k_theta_y*R*lambda/delta*(1+delta_yr);  %% m
%%% SPHERICAL REFERENCE
Er_phase=exp(1i*2*pi/lambda*(sqrt((Xa*delta+xo).^2+(Ya*delta-yo).^2+R^2)-
sqrt((xo).^2+(yo).^2+R^2))); %%reference for object
Er_phase_r=exp(1i*2*pi/lambda*(sqrt((Xa*delta+xor).^2+(Ya*delta-yor).^2+R^2)-
sqrt((xo).^2+(yo).^2+R^2))); %%reference withiout object

Er_r=conj(exp(1i*2*pi/lambda*(sqrt((Xa*delta).^2+(Ya*delta).^2+R^2))));
%% Initiation of the SPAR algorithm by Liebleing estimates
%% Liebling estimator
```

```matlab
%% Parameters of the Liebling estimator
window_sigma=5.;
window_size=floor(3*window_sigma+15);
%% window_size=[10 30];  %% for rectangular mean
%%window_size=floor(2*3*window_sigma+5);
%%[Z_est0_holo,Z_est1_holo,Ar_est_holo]
=Phase_Ampl_NoiseFiltering_Liebling_Initial(holo_195,(Er_phase),window_size,window_sig
ma);
[Z_est0_holo,Z_est1_holo,Ar_est_holo]
=Phase_Ampl_NoiseFiltering_Liebling_Initial_New(holo_195,conj(Er_phase),window_size,wi
ndow_sigma);

[Z_est0_ref,Z_est1_ref,Ar_est_ref]
=Phase_Ampl_NoiseFiltering_Liebling_Initial_New(ref_195,conj(Er_phase_r),window_size,w
indow_sigma);

Z_est1_holo=Z_est1_holo*exp(-1i*pi*0.7);
Z_est1_ref=Z_est1_ref.*exp(-1i*pi*1.5);    %Z_est1_ref.*exp(-1i*pi*1.2);
%%%Substract reference phase from the object phase
PHASEEEE=angle(Z_est1_holo./(Z_est1_ref));
MAXX=max(max(PHASEEEE));
phase_diff1=angle(Z_est1_holo./Z_est1_ref);
phase_diff2=angle(Z_est1_holo./Er_r);
figure(2201), subplot(2,3,1), surfl(double(phase_diff1));shading
interp;colormap(gray); title(['Difference Results,
window=',num2str(window_size)]),zlabel('rad'),...
    subplot(2,3,4),surfl(double(phase_diff2));shading interp;colormap(gray);
title('Difference Results,'), zlabel('rad'),...
    subplot(2,3,2),plot(double(phase_diff1(:,250))); title('dif crossection 250'),grid
on,ylabel('rad'),...
    subplot(2,3,5),plot(double(phase_diff2(:,250))),grid on,ylabel('rad'),...
 subplot(2,3,3),surfl(double(angle(Z_est1_holo)));shading interp;colormap(gray);
title('obj Results'), zlabel('rad'),...
 subplot(2,3,6),surfl(double(angle(Z_est1_ref)));shading interp;colormap(gray);
title('ref Results'), zlabel('rad')

% return

figure(38),  plot(double(phase_diff1(:,RRR))), grid on, title(' Cross-section 250')

 figure(56),
 surfl(double(phase_diff1));shading interp;colormap(gray); title(['Difference Results,
window=',num2str(window_size)]),zlabel('rad'),

%  figure(6),
%  imshow(double(holo_195*255),[]);shading interp;colormap(gray); title(['Difference
Results, window=',num2str(window_size)]),zlabel('s'),

%FFT calculations
%imwrite(uint8((double(phase_diff1)+pi)/2/pi*255), gray(256), 'diff_195test.bmp');
if 0
TTTT=out_195uwp(pp+[0:511],gg+[0:511]);
figure(45), subplot(131), surfl(out_195uwp(pp+[0:511],gg+[0:511]));shading
interp;colormap(gray); title('FFT result'),...
 subplot(132), imshow(out_195uwp(pp+[0:511],gg+[0:511]),[]);  title('FFT Difference')
subplot(133), plot(TTTT(:,250)), grid on, title(' Cross-section 250')
end


%  return

%% START Phase unwrapping by PUMA
if 1
    'unwrapping...'
potential.threshold = .5;
potential.quantized = 'no';
verbose='no';
```

```matlab
%%phi_u0_puma= puma_ho(angle(Z_est1(1:3:end,1:3:end)),2,
'potential',potential,'verbose',verbose); %% for demo PEARLS unwrapping and input for
SPAR
phi_u0_puma_holo= puma_ho(angle(Z_est1_holo),2,
'potential',potential,'verbose',verbose); %% for demo PEARLS unwrapping and input for
SPAR


phi_u0_puma_ref= puma_ho(angle(Z_est1_ref),2,
'potential',potential,'verbose',verbose); %% for demo PEARLS unwrapping and input for
SPAR
 phi_u0_puma_ref_ref= puma_ho(angle(Er_r),2, 'potential',potential,'verbose',verbose);

phi_u0_puma_phase_diff1= puma_ho(phase_diff1,2,
'potential',potential,'verbose',verbose);
figure(2), subplot(121), surfl(double(phi_u0_puma_ref));shading interp;colormap(gray);
title('Unwrapped Ref')

subplot(122), surfl(double(phi_u0_puma_holo));shading interp;colormap(gray);
title('Unwrapped Holo')

figure(22), subplot(2,2,1),surfl(-lambda/2/pi*10^9*double(phi_u0_puma_ref(15:end-
15,15:end-15))+lambda/2/pi*10^9*double(phi_u0_puma_holo(15:end-15,15:end-15)));shading
interp;colormap(gray); title('Difference Results'),...
    zlabel('nm'),...
    subplot(2,2,2),plot(-
lambda/2/pi*10^9*double(phi_u0_puma_ref(:,250))+lambda/2/pi*10^9*double(phi_u0_puma_ho
lo(:,250))),grid on,ylabel('nm'),...
    subplot(2,2,3), imagesc(-
lambda/2/pi*10^9*double(phi_u0_puma_ref)+lambda/2/pi*10^9*double(phi_u0_puma_holo)),..
.
    subplot(2,2,4),plot(lambda/2/pi*10^9*mean(double(-
phi_u0_puma_ref+double(phi_u0_puma_holo)),2)),ylabel('nm'), grid on

%% ee=double(phi_u0_puma_ref-phi_u0_puma_holo);

end

if 1
    figure(1),   subplot(231), imshow(angle(Er_r),[]), title('reference phase'),...
               subplot(232), imshow(angle(Z_est1_ref),[]), title('ref wrapped'),...
                    subplot(233), imshow(angle(Z_est1_holo),[]), title('holo
wrapped'),...
                    subplot(234),surfl(double(phi_u0_puma_ref_ref));shading
interp;colormap(gray); title('reference'),...
                    subplot(235), surfl(double(phi_u0_puma_ref)); shading
interp;colormap(gray); title('ref wrapped'),...
                    subplot(236), surfl(double(phi_u0_puma_holo)); shading
interp;colormap(gray); title('holo wrapped'),

end
  return
%%%%%%%%%%%%%%%%%%%%%%%%%%%%%%%%
%% PARAMETERS of BM3D-FRAME FILTER: FIXED
Nstep = 3;  N11=8;  N22=32; %% BM3D group size
threshType='h';          %% Type of the threshold parameter in BM3D

%% PARAMETERS of ITERATIVE ALGORITHM
IterNum=10/2;             %% ITERATION NUMBER
filtering=1;              %% 1 - means that BM3D filtering is on;  0 - means that
BM3D filtering is off, "output==input"
unwrapping=1;             %% 1 -means unwrapping of phase filtering, 0- means
unwrapping off

threshold_ampl=2;     %% threshold parameters of the SPAR algorithm
threshold_phi=1;
%%%%%%%%%%%% ITERATION %%%%%%%%%%%%%%%
for SS=[1 2]
```

159

```matlab
    SS
if SS==1
Wz=Z_est1_holo;
Wu=Z_est0_holo;
II=holo_195;
end
if SS==2
Wz=Z_est1_ref;
Wu=Z_est0_ref;
II=ref_195;
end

LAMBDAz=zeros(size(Wz));   %% Lagrange multipliers is not used in this version

for ss=1:IterNum; %IterNum
ss
gamma_1=.05/(1+(ss-1)*0); %% FOR OBJECT WAVEFRONT
gamma_0=gamma_1;          %% FOR U
gamma_2=10;    %% FOR LAMBDA

gamma=gamma_1;

[Z_est0,Z_est1,Ar_est]
=Phase_NoiseFiltering_Liebling_Gaussian_corrections_Dec08(II,(Er_phase),Wz,Wu,
LAMBDAz, gamma_0, gamma_1, gamma_2);



%% Phase_NoiseFiltering_Liebling(II,Eo,Er,Wz,LAMBDA, gamma_1 )
%%%%%%%%%%%%%%%%%%%%%%%%%%%%%%%%%%%%%%%%%%%%%%%%%%%%%%%%%%%%%%%%%%%%%
%%%%%%%%%%%%%%%%%%%%%%%%%%%%%%%%%%%%%%%%%%%%%%%%%%%%%%%%%%%%%%%%%%%%%
%% PUMA Phase unwrapping for object phase

if unwrapping==1
potential.threshold = .5;
potential.quantized = 'no';
verbose='no';
phi_u0_puma = puma_ho(angle(Z_est1),2, 'potential',potential,'verbose',verbose); %%
for demo PEARLS unwrapping and input for SPAR
else
    phi_u0_puma=angle(Eo_est);
end

if ss<4  %% BM3D groups are formed for ss<2
    ss0=ss;
end
%% BM3D object phase filtering

dev_phi=function_stdEst2D(double(phi_u0_puma),2)
% figure, subplot(121), surfl(double(phi_u0_puma(5:end-5,5:end-5)));shading
interp;colormap(gray), title('before')

phi_u0_SPAR=BM3D_SPAR_UNWRAP_PHI_ELENA(double(phi_u0_puma),threshType, threshold_phi,
N11, N22, Nstep,filtering,ss,ss0);
%%
% subplot(122), surfl(double(phi_u0_SPAR(5:end-5,5:end-5)));shading
interp;colormap(gray), title('after')
% pause(.3)

figure, surfl(double(phi_u0_SPAR(5:end-5,5:end-5)));shading interp;colormap(gray),
title('after')
dev=function_stdEst2D(double(abs(Z_est0)),2);

[abs_Z0_SPAR] = BM3D_SPAR_UNWRAP_ABS_ELENA(abs(Z_est0),threshType, threshold_ampl,
N11, N22, Nstep,filtering,ss,ss0);


dev=function_stdEst2D(double(abs(Z_est1)),2);
```

```matlab
[abs_Z1_SPAR] = BM3D_SPAR_UNWRAP_ABS_ELENA(abs(Z_est1),threshType, threshold_ampl,
N11, N22, Nstep,filtering,ss,ss0);
Wu=abs_Z0_SPAR;
Wz=abs_Z1_SPAR.*exp(sqrt(-1)*phi_u0_SPAR);   %% Update of W


end
if SS==1
  Ar_holo=Ar_est;
  phi_u0_SPAR_holo=phi_u0_SPAR;
  abs_Z1_SPAR_holo=abs_Z1_SPAR;

  figure(22), surfl(double(phi_u0_SPAR_holo));shading interp;colormap(gray);
title('Phase unwrapped holo')

end
if SS==2
    Ar_ref=Ar_est;
  phi_u0_SPAR_ref=phi_u0_SPAR;
  abs_Z1_SPAR_ref=abs_Z1_SPAR;
 figure(33), surfl(double(phi_u0_SPAR_ref));shading interp;colormap(gray); title('phi-
u0_SPAR-ref')

end

end
 figure(44),  subplot(221),surfl(double(-phi_u0_SPAR_ref(5:end-5,5:end-5)+
phi_u0_SPAR_holo(5:end-5,5:end-5)));shading interp;colormap(gray); title('DIFF of ABS
PHASES'),...
  subplot(223),surfl(double( phi_u0_SPAR_holo(5:end-5,5:end-5)));shading
interp;colormap(gray); title('ABS PHASES HOLO'),...
  subplot(224),surfl(double(phi_u0_SPAR_ref(5:end-5,5:end-5)));shading
interp;colormap(gray); title('ABS PHASES REF'),...
subplot(222), plot(double(-phi_u0_SPAR_ref(:,256)+ phi_u0_SPAR_holo(:,256))), grid,
title('CROSS-Section')
```

Annex 3. FFT algorithm for SLM calibration

```matlab
clear all;
% close all;
clc;
potential.threshold = .5;
potential.quantized = 'no';
verbose='no';
%read sequence of images
%Examples of Digital Hologram Reconstruction Programs book to read
nr_of_images=26;
%nr_of_images=2;
 indx1=1;
%read reference image to substract
holo_gram=double(imread('25', 'tif'));
% x1=700;
% x2=x1+300;
% y1=400;
% y2=y1+300;
 y1=700;
 y2=y1+500;
 x1=10;
 x2=x1+1000;

[N M]=size(holo_gram);
c=single(zeros(N, M));
hologram=holo_gram(x1:x2,y1:y2);

ref_erence=double((imread('reference_nosLM','tif')));% 1.tif is one of 25 images
% xh1=x1-300;
% xh2=x1;
% yh1=y1;
% yh2=y1+300;
yh1=y1-500;
yh2=y1;
xh1=x1;
xh2=x1+1000;
[Nh Mh]=size(ref_erence);
c=single(zeros(Nh, Mh));
reference=ref_erence(xh1:xh2,yh1:yh2);
[out,out_holo]=DividFourierfilter(holo_gram,ref_erence,5.3,532,0.01,0,0,0,0,0,0);%0.01
is the propagation distance
 figure(6), imshow(angle(out)); colormap('gray'); colorbar;
 holo_out=out(x1:x2,y1:y2);
 ref_out=out(xh1:xh2,yh1:yh2);
 final_resul=holo_out./ref_out;
 %figure(6), imshow((final_resul)); colormap('gray'); colorbar;
%Phase determination using FFT
for k = 1 : nr_of_images
    holo_gram=double(imread([num2str(k), '.tif']));
%FFT using Claus subprogram
    [out,out_holo]=Fourierfilter_divid(holo_gram,ref_erence,5.3,532,0.01,0,0,0,0,0,0);
%figure out the distence in the current set up?
Phase=angle(out);
%Set the mean phase values in a vector for plot
Mean_phase(k)=mean2(Phase(303:565,430:821));% a central part of the image is cutted
303:565,430:821
if Mean_phase(k)<0
    Mean_phase(k)=Mean_phase(k)+2*pi
else
    disp('All values are above 0')
end
Mean_phase(Mean_phase<0)=-Mean_phase(Mean_phase<0);

Mean_phase(indx1,:,:)
%Set the values of the gray level in a vector after every 10 shades
```

```
gray_scale(indx1)=[0 10 20 30 40 50 60 70 80 90 100 110 120 130 140 150 160 170 180
190 200 210 220 230 240 250 255]*(1+Phase);
%*(1+Mean_phase);(k+1)
figure(1), imagesc(angle(out)); colormap('gray'); colorbar;
end
unwrap_phase=unwrap(Mean_phase);
gray_scale=[1:10:251];
%Plot the dependance of phase(grayscale)
figure(100), plot(gray_scale,unwrap_phase);
xlabel('Grayscale'); ylabel('PHASE, radians');title('Plot of phase dependant on gray
levels')
figure(101), plot(gray_scale,Mean_phase);
xlabel('Grayscale'); ylabel('PHASE, radians');title('Plot of phase dependant on gray
levels 1st new order')
%second version of loading images, gray_scale
% for i=1:5 %reading 25 images
%
% file_name=dir(fullfile('\\intra.tut.fi\home\cazac\My Documents\Desktop\holo
report\Finland\fin_march_apr_2018\SLM_calibration\FFT'));
%  im=imread(fullfile('\\intra.tut.fi\home\cazac\My Documents\Desktop\holo
report\Finland\fin_march_apr_2018\SLM_calibration\FFT', file_name(i).name ) );
%
% end

% % for a = 1:5
% %    filename = ['' num2str(a,'%d') '.tif'];
% %    img =  double(imread(filename));
% %    % do something with img
% %
% % end
% % image(squeeze(img));
% % holo_gram=double(imread('graylevel_255','tif'));
% % [out,out_holo]=Fourierfilter(holo_gram,ref_erence,5.3,532,0.01,0,0,0,0,0,0);
% % figure(1), imagesc(angle(out)); colormap('gray'); colorbar;
% % % [pixelCounts, grayLevels] = imhist(grayImage, 256);
```

FFT divid function

```
%function [x1,x2,y1,y2]=Fourierfilter(holo,pz, lambda,dist,sx,sy);
function [out,out_holo]=Fourierfilter(holo,ref,pz, lambda,dist,sx,sy,rx,ry,sx2,sy2);
%%function out=Tomorecon(image,pz,dist_low, dist_high, dist_step, lambda);
%% image ist der Name des Hologramms, z.B. rotation0.png
% pz ist die Pixelgrï¿½ï¿½e der Kamera in ï¿½m
%dist ist der Refocusing distance in mm
% lambda ist die verwendete Wellenlï¿½nge in nm
% 1. um die function durchfï¿½hren zu kï¿½nnen musst Du sie in den Ordner der
% Hologramme laden oder diesen in der imread function kenntlich machen
% (Pfad angeben)
%% Phasenkeil zur Zentrierung basierend auf Fouriershifttheorem
[N,M] = size(holo);
m1 = -M/2:M/2 - 1;
n1 = -N/2:N/2 - 1;
[m1,n1]=meshgrid(m1,n1);
phase=exp(-1i*2*pi*(m1/M*sx+n1/N*sy));
%% Ermittlung der Fouriertransformierten
a_holo=fftshift(fft2(fftshift(holo)));
%a_holo=a_holo.*phase;
a_ref=fftshift(fft2(fftshift(ref)));
figure(1), imagesc(brighten(abs(a_holo),0.8));
% H=imrect;
% pos=getPosition(H)
% pos=wait(H);
% pos=round(pos);
% x1=pos(2)
% x2=pos(2)+pos(4)
% y1=pos(1)
% y2=pos(1)+pos(3)
% x1=141;%should be square!!!!
```

```matlab
% x2=341;
% y1=893;
% y2=1093;
%300x300 square cut
x1=95;%should be square!!!!
x2=395;
y1=837;
y2=1137;

[N M]=size(a_holo);
c=single(zeros(N, M));

%c(x1:x2,y1:y2)=a_holo(x1:x2,y1:y2);
%coordinates of the center
c(N/2-(x2-x1)/2:N/2+(x2-x1)/2,M/2-(y2-y1)/2:M/2+(y2-y1)/2)=a_holo(x1:x2,y1:y2);
out_holo=ifftshift(ifft2(ifftshift(c)));
out_holo = AngularSpectrum(out_holo,pz,pz,lambda,10^100,dist,1,sx,sy);
c(N/2-(x2-x1)/2:N/2+(x2-x1)/2,M/2-(y2-y1)/2:M/2+(y2-y1)/2)=a_ref(x1:x2,y1:y2);
%c(x1:x2,y1:y2)=a_ref(x1:x2,y1:y2);
out_ref=ifftshift(ifft2(ifftshift(c)));
out_ref = AngularSpectrum(out_ref,pz,pz,lambda,10^100,dist,1,rx,ry);
%% Phasenkeil zur Zentrierung basierend auf Fouriershifttheorem
phase2=exp(-1i*2*pi*(m1/M*sx2+n1/N*sy2));
%% Abzug Phase des Referenzhologrammes vom Objekthologramm
out=out_holo./out_ref.*phase2;
% figure(21),imshow(angle(out_holo));
%figure(2),imagesc(abs(out_holo));
% figure(3),imagesc(abs(out_ref));
% figure(4),imagesc(angle(out));
% a=double(angle(out));
%
% a=2.*pi.*a/0.633; %generate topography data in microns
%   figure(5),mesh(a)
%   b=real(a.^2); figure(6), mesh(b);

% v=[dist_low:dist_step:dist_high];
% out=AngularStack(c,v,lambda,pz)
```

Annex 4. SPAR algorithm for SLM calibration

```
%%SLM Phase_determination using Local least square
%close all
clear all
%%Set up parameters
lambda=405e-9;%%%%% wavelengh
delta=1.55e-6; %%%%% pixel size
%%Number of graylevels
nr_of_images=256;
ref_erence = double(imread('ref1.png'));%%load reference image for graylevel 0
%ref_erence = imrotate(double(imread('ref_high_exposure.tif')),0.28);
%holo_gram=double(imread('20.tif',1));
%imag = imrotate(double(imread('image.png')),0.20);
%figure(1221), imshow(imag,[]);
%%load sample images for graylevels higher than 0
%k=256
for k = 1 : nr_of_images
    holo_gram=double(imread([num2str(k), '.png']));
    %holo_gram=holo_gram/max(holo_gram(:))*4;
%holo_gram=imrotate(double(imread('10.tif',1)),0.28);
pp=1;
gg=1;
% holo_gram=holo_gram(pp+(0:511),gg+(0:511));
% ref_erence=ref_erence(pp+(0:511),pp+(0:511));
    % figure(1), imshow(holo_gram,[])
%cut central part of the image
% ref_erence_holo=holo_gram(170:630,170:630)%(,620:560);
% holo_gram_obj=holo_gram(250:710,720:1180);
%   figure(2), imshow(ref_erence_holo,[])
%    figure(3), imshow(holo_gram,[])

    %return

[yN,xN]=size(holo_gram);
[Xa,Ya] = meshgrid(-xN/2:xN/2-1,-yN/2:yN/2-1);

%% Angles of the reference wavefront
%for k_theta_x=94.0000*pi/180:0.0500*pi/180:98.0000*pi/180
k_theta_x=88.0775*pi/180; %87.6400 %401 15 425
k_theta_y=90.4140*pi/180;%93.7190 %209 97  200
k_theta_xr=88.0729*pi/180;%87.6395 402
k_theta_yr=90.4142*pi/180;%93.7194 180 175
% k_theta_x=87.6415*pi/180; %87.6400 %401 15 425
% k_theta_y=93.7204*pi/180;%93.7190 %209 97  200
% k_theta_xr=87.6395*pi/180;%87.6395 402
% k_theta_yr=93.7180*pi/180;%93.7194 180 175

%%%%%%%% GIVE REFERENCE PHASE LINEAR
Er_phase=exp(1i*2*pi/lambda*[Ya*delta*cos(k_theta_y)+Xa*delta*cos(k_theta_x)]);
Er_phase_r=exp(1i*2*pi/lambda*[Ya*delta*cos(k_theta_yr)+Xa*delta*cos(k_theta_xr)]);
   % figure(4), imshow(angle(Er_phase));
delta_x=0;
delta_y=0;
xo=k_theta_x*lambda/delta*(1+delta_x);  %% m
yo=k_theta_y*lambda/delta*(1+delta_y);  %% m
t=-0.3;
a=0;
delta_xr=.015*t;
delta_yr=-.05*a;
xor=k_theta_x*lambda/delta*(1+delta_xr);  %% m
yor=k_theta_y*lambda/delta*(1+delta_yr);  %% m

%% Initiation of the SPAR algorithm by Liebleing estimates
%% Liebling estimator
%% Parameters of the Liebling estimator
tic
```

```matlab
%%window_size=29;
window_sigma=4; %Vary, smaller better
window_size=12;
[Z_est0_holo,Z_est1_holo,Ar_est_holo]
=Phase_Ampl_NoiseFiltering_Liebling_Initial_New(holo_gram,conj(Er_phase),window_size,w
indow_sigma);
window_sigma_ref=8; %Vary, smaller better
window_size_ref=18;
[Z_est0_ref,Z_est1_ref,Ar_est_ref]
=Phase_Ampl_NoiseFiltering_Liebling_Initial_New(ref_erence,conj(Er_phase_r),window_siz
e_ref,window_sigma_ref);
%Phase_whole=angle(Z_est1_holo./Z_est1_ref);
Phase_whole=imrotate(angle(Z_est1_holo./Z_est1_ref),0.20);
Phase_whole2=imrotate((Z_est1_holo./Z_est1_ref),0.20);
 Z=angle(Z_est1_ref);
  Zhol=angle(Z_est1_holo);
% figure(565), imshow(Z_est1_holo,[]);
% figure(516), imshow(Z,[]);
% figure(515), imshow(Zhol,[]);
phase1=figure(52), imshow(Phase_whole,[]);
saveas(phase1, sprintf('phase%d.png',k));
% figure(54),PHASE=imshow(angle(Z_est1_holo),[]);b
  CS_y= (Phase_whole(1800,:));
  CS_x=(Phase_whole(:,2050));
% figure(207),plot(CS_y), title('cut Phase y')
% figure(209),plot(CS_x), title('cut Phase x')
%%cut phase image in 506x506 CCD pixels for analysing 20x20 SLM pixels
y1=1231;
y2=y1+505;
x1=1590;
x2=x1+505;
[N M]=size(Phase_whole);
c=single(zeros(N, M));
Z_est1_ref_cut=Phase_whole(y1:y2,x1:x2);
Z_est1_holo_cut2=Phase_whole2(y1:y2,x1:x2);
%figure(35), imshow(Z_est1_ref_cut,[]);
yh1=279;
yh2=yh1+505;
xh1=x1;
xh2=x2;
[Nh Mh]=size(Phase_whole);
c=single(zeros(Nh, Mh));
Z_est1_holo_cut=Phase_whole(yh1:yh2,xh1:xh2);
Z_est1_ref_cut2=Phase_whole2(yh1:yh2,xh1:xh2);
%figure(37), imshow(Z_est1_holo_cut,[]);
%PHASE=Z_est1_holo_cut-Z_est1_ref_cut; %%phase difference
PHASE2=Z_est1_holo_cut2./Z_est1_ref_cut2;
vero_phase=Z_est1_holo_cut2;
%   CS_y= (PHASE(1500,:));
%   CS_x=(PHASE(:,2050));
% figure(207),plot(CS_y), title('cut Phase y')
% figure(209),plot(CS_x), title('cut Phase x')
cuttie1=angle(PHASE2);
%cuttie1=angle(PHASE2);%(974:2134,1400:2560,:);
   %  figure(5), imshow(cuttie1,[]);
%      figure(6), plot(PHASE(500,:));
%phase_diff2(:,250))
potential.threshold = .5;
potential.quantized = 'no';
verbose='no';
cuttie= puma_ho(cuttie1,2, 'potential',potential,'verbose',verbose);

%% cut SLM pixels 23x23 than cutting active area 13x13
c = [];
c1=zeros(260,260);
c_dead=zeros(460,460);
dead_z=zeros(23,23);
i_add=0;
```

```matlab
for i = 1:20
    if rem(i,5)==0
        i_add=i_add+1;
    end
    j_add=0;
    for  j=1:20
        if rem(j,5)==0
            j_add=j_add+1;
        end
    M = cuttie(23*(j-1)+1+j_add:23*(j-1)+23+j_add,23*(i-1)+1+i_add:23*(i-1)+23+i_add);
%%cut SLM pixels 23x23
    c = cat(3, c, M(6:18,6:18));%concatenate in a 3D-matrix 13x13x400

%% cutting SLM pixel active area 13x13
c1(j*13-12:j*13,i*13-12:i*13)=M(6:18,6:18);%arrage 13x13 CCD pixels in 2D matrix
290x290 CCD pixels (20x20 SLM pixels)

%%calculating mean values NO PUMA unwrapping
M1(j,i)=mean2(M(6:18,6:18)); %20x20 matrix mean value of the pixel on each row and
column
M2(j*i)=mean2(M(6:18,6:18)); % 1x 400 vector of all mean values for slm pixels
    % activ_pix_phase=figure(665),imshow(c1,[],'InitialMagnification','fit');
S1(j,i)=std2(M(6:18,6:18));%%calculating standard deviation for each pixel on all rows
and columns

%% Select SLM pixel dead zone
Md = cuttie(23*(j-1)+1+j_add:23*(j-1)+23+j_add,23*(i-1)+1+i_add:23*(i-1)+23+i_add);
Md(6:18,6:18)=NaN(13,13);
M1_dead(i,j)=mean(nanmean(Md));
c_dead(23*(j-1)+1:23*(j-1)+23,23*(i-1)+1:23*(i-1)+23)=Md(1:23,1:23);
%c_dead(23*(jd-1)+1+jd_add:23*(jd-1)+23+jd_add,23*(id-1)+1+id_add:23*(id-
1)+23+id_add)=Md(1:23,1:23);
    end
%end
  % dead_grid=figure(7), imshow(c_dead,[],'InitialMagnification','fit');%visualize 2D
matrix 464x464 CCD pixels of SLM pixel dead zones(20x20 SLM pixels)
%        saveas(dead_grid, sprintf('dead_grid%d.png',k));
%% PUMA unwrapping for phase of SLM active zones of the pixel

    %puma_phase=figure(8),imshow(phi_c1_puma_holo,[],'InitialMagnification','fit');
%     xlabel('20 SLM Pixels'); ylabel('20 SLM Pixels'); title('Phase of Active Zone of
the SLM Pixels(Puma)')
%        saveas(puma_phase,sprintf('phaseSLM_actv_pix_puma%d.png',k));
%%calculating mean values of SLM phase for pixel active zone
% Mean_puma= mean2(phi_c1_puma_holo);
%
%mean_puma_phase=figure(9),imshow(Mean_puma,[],'InitialMagnification','fit'),title('Me
an Phase of Pixel Active Zone of the SLM Pixels(puma)');
% for ii=1:20
%   for jj=1:20
%      ccc=phi_c1_puma_holo(jj*13-12:jj*13,ii*13-12:ii*13);
% M1_puma(ii,jj)=mean2(ccc);%20x20 matrix mean value of the pixel on each row and
column
% M2_puma(ii*jj)=mean2(ccc); % 1x 400 vector of all mean values for slm pixels
% S1_puma(jj,ii)=std2(ccc); %standard deviation for each pixel on all rows and columns
%        end
% end
%     activ_pixphase_mean=figure(10), imshow(M1_puma,[],'InitialMagnification','fit');
%     xlabel('20 SLM Pixels'); ylabel('20 SLM Pixels'); title('Mean Phase of Pixel
Active Zone of the SLM Pixels(puma)')
%        saveas(activ_pixphase_mean,sprintf('phase_mean_actv_pix_puma%d.png',k))

%% NO puma unwrapping
%%ploting a mesh for each pixel standard deviation
%  img_std_pixel=figure(11),subplot(1,2,1),imshow(S1,[],'InitialMagnification','fit');
colorbar
%                          title('Puma before cut Phase STD SLM each pxl act
zn'),xlabel('20 SLM pixels'), ylabel('20 SLM pixels'),
```

```matlab
%                                    subplot(1,2,2),surfl(S1); shading interp,colorbar;
%                                    title('Puma before cut Mesh STD SLM each pxl act
zn'),xlabel('20 SLM pixels'), ylabel('20 SLM pixels'),
%          saveas(img_std_pixel, sprintf('img_std_pixel%d.fig',k))%%save the mesh for
pixel standard deviation for each gray level

    %figure(12), imshow(meanArray,[]);
%% PUMA unwrapping
%ploting a mesh for each pixel standard deviation
%   img_std_pixel_puma=figure(13),subplot(1,2,1),imshow(S1_puma,[],'InitialMagnificatio
n','fit');
%                                    title('Puma Phase STD SLM each pxl act
zn'),colorbar, xlabel('20 SLM pixels'), ylabel('20 SLM pixels'),
%                                    subplot(1,2,2),surfl(S1_puma);
%                                    title('Puma Mesh STD SLM each pxl act
zn'),xlabel('20 SLM pixels'), ylabel('20 SLM pixels'), shading interp,colorbar;
%          saveas(img_std_pixel_puma, sprintf('puma_img_std_pixel%d.fig',k))%%save the
mesh for pixel standard deviation for each gray level
%
%% Collecting mean and STD of phase of SLM pixels in dependance to gray levels

%% SLM Pixel Active Zones NO PUMA
%% Mean data
meanArray= mean(c,3);%%for c as a 3D-matrix c/ 13x13 mean array of all active zones of
400 pixels
%figure(11), imshow(meanArray,[]);
Mean_phase(k)=mean2(cuttie); %calculating phase mean value of the whole 506x506 phase
image
second_mean(k)=mean2(meanArray);%%26 mean values of the pixel active zone phase for
all the gray levels
mean_c1(k)=mean2(c1);%% mean value of all active zones of 400 pixels from 2D-matrix c
% STD data
standard_dev(k)=std(M2,1);;%%normalisation by 1
M_std(k)=std(M2);
mean_M2std(k)=mean(std(M2));
std_c1(k)=std2(c1);
% hist_mean_phase=figure('Position', get(0, 'Screensize')), subplot(1,2,1),
histogram(M1)
%                                    title('Pixel active area phase(puma bef. cut'),
xlabel('Mean phase'); ylabel('Nr of occurences');
%                                    subplot(1,2,2), histogram(S1),
%                                    title('Phase STD of pixel active area(puma bef.
cut)'),xlabel('Phase std'); ylabel('Nr of occurences');
%      %saveas(hist_mean_phase_puma,sprintf('no_puma_hist_mean_phase_act%d.png',k))
%      F1= getframe(hist_mean_phase);
%    imwrite(F1.cdata,sprintf('bef_cut_puma_hist_phi_act%d.png',k))
%% PUMA SLM Pixel Active Zones
%% Mean data
% puma_unwr(k)=Mean_puma;
% std_puma(k)=std2(phi_c1_puma_holo); %%STD of the unwrapped phase of actv zone after
puma from 260x260 matrix
% std_for_hist=std2(phi_c1_puma_holo);
% %% STD data
% standard_dev_p(k)=std(M2_puma,1);%%normalisation by 1 ??
% M_std_p(k)=std(M2_puma); %%??
% mean_M2std_p(k)=mean(std(M2_puma)); %%??

%% SLM Pixel Dead Zones
Dead_mean=mean(nanmean(c_dead));
vect_dead_mean(k)=Dead_mean;
std_dead1(k)=std(c_dead(:),'omitnan');
std_hist_dead=mean(std(c_dead(:),'omitnan'));
fff=std(c_dead(:),'omitnan');
%plot histograms

% hist_mean_phase_puma=figure('Position', get(0, 'Screensize')),subplot(1,3,1),
histogram(M1_puma)
```

```
%                                    title('SLM phi of pxl act zone(puma)'),
xlabel('Mean phase'); ylabel('Nr of occurences');
%                                    legend(['STD=' num2str(std_for_hist)]);
%                                      subplot(1,3,2), histogram(S1_puma),
%                                    title('SLM Phi STD of pxl actve
zn(puma)'),xlabel('Phase std'); ylabel('Nr of occurences');
%                                        subplot(1,3,3), histogram(M1_dead)
%                                    title('SLM phi of pxl dead zone'),
xlabel('SLM Mean Pixel Phase STD'); ylabel('Nr of occurences');
%                                    legend(['STD='
num2str(std_hist_dead)]);
    %saveas(hist_mean_phase_puma,sprintf('puma_hist_phi_act%d.png',k))
    %F= getframe(hist_mean_phase_puma);
    %imwrite(F.cdata,sprintf('puma_hist_phi_act%d.png',k))
    mean_cuttie1(k)=mean2(cuttie1);
    mean_cuttie(k)=mean2(cuttie);
end
end
gray_scale=[1:1:256]; %% grayscale set for 26 holograms

unwrap_cuttie1=unwrap(mean_cuttie1);
figure(160), plot(gray_scale,unwrap_cuttie1,'LineWidth',1.5),title('Phase dependant on
gray levels active and dead zones, no puma');



%% NO PUMA pixel Active zone phase unwrapping
unwrap_phase=unwrap(Mean_phase); %%Phase of active+dead pixel zone
unwrap_phase_pixel=unwrap(second_mean);%%Phase of active pixel mean calculated from
array of 13x13 of 400 pixels
unwrap_c1_mean=unwrap(mean_c1);%%Phase of active pixel zone mean calculated from
matrix of 260x260 pixels
%% PUMA pixel Active zone phase unwrapping
%unwrp_puma=unwrap(puma_unwr);
%figure(168), plot(gray_scale,unwrap_c1_mean,'LineWidth',1.5);
%% Pixel Dead zone phase unwrapping
uwrap_mean_dead=unwrap(vect_dead_mean);

figure(91),plot(gray_scale,unwrap_cuttie,'g',gray_scale,unwrap_c1_mean,'b',
gray_scale,uwrap_mean_dead,'r','LineWidth',2)
title('Phase dependant on gray levels(pumabfcut)'), xlabel('Grayscale');
ylabel('Phase, radians');
legend('Pixel active and dead zones','Pixel active zones','Pixel dead zone');
%% Plot phase(graylevel) dependances
%% SLM PIXEL ACTIVE ZONE
% %% PUMA
%     figure(16), subplot(2,2,1), plot(gray_scale,unwrp_puma,'LineWidth',1.5); %%PHASE
active and dead zones
%     title('Phase of SLM pixels active
zone(puma)','FontSize',15),xlabel('Grayscale','FontSize',14); ylabel('Phase,
radians','FontSize',14);
%                 subplot(2,2,2), boundedline(gray_scale,unwrp_puma,std_puma);
%     title('Phase of SLM pixel active zone and STD(puma)','FontSize',15),
xlabel('Grayscale','FontSize',14); ylabel('Phase, radians','FontSize',14);
%                 subplot(2,2,3), plot(gray_scale, std_puma,'LineWidth',1.5);
%     title('Phase STD of SLM pixel active zone(puma)','FontSize',15),
xlabel('Grayscale','FontSize',14); ylabel('PHASE, radians','FontSize',14);
%                 subplot(2,2,4), plot(gray_scale, mean_M2std_p,'LineWidth',1.5);
%     title('Mean Phase STD of 400 SLM pixels active zones,(puma)','FontSize',15),
xlabel('Grayscale','FontSize',14); ylabel('Phase, radians','FontSize',14);

%% NO PUMA
    figure(17), subplot(2,2,1), plot(gray_scale,unwrap_phase,'LineWidth',1.5); %%PHASE
active and dead zones
    title('Phase of SLM pixel active and dead
zones','FontSize',15),xlabel('Grayscale','FontSize',14); ylabel('Phase,
radians','FontSize',14);
                subplot(2,2,2), plot(gray_scale,Mean_phase,'LineWidth',1.5);
```

```matlab
        title('Wrapped phase mean of whole pixel(active and dead zones)with
puma','FontSize',15), xlabel('Grayscale','FontSize',14); ylabel('Phase,
radians','FontSize',14);
                subplot(2,2,3), errorbar(gray_scale,unwrap_c1_mean, std_c1);
    title('Unwrapped phase of pixel active zone and STD','FontSize',15),
xlabel('Grayscale','FontSize',14); ylabel('Phase, radians','FontSize',14);
        %savefig('fig21.fig')
                subplot(2,2,4), errorbar(gray_scale,uwrap_mean_dead,std_dead1);
title('Unwrapped phase of pixel dead zones and STD (gray levels)'),
xlabel('Grayscale'); ylabel('Phase, radians');
%% SLM PIXEL DEAD ZONE
%               subplot(2,2,3), boundedline(gray_scale,unwrap_c1_mean,
%               std_c1,'LineWidth',1.5); !!!!!!!!!!!!
%     title('Unwrapped phase of pixel active zone and STD','FontSize',15),
xlabel('Grayscale','FontSize',14); ylabel('Phase, radians','FontSize',14);
% %
% %%PHASE active and dead zones
%
figure(91),plot(gray_scale,unwrap_phase,'g',gray_scale,unwrap_c1_mean,'y',gray_scale,u
nwrp_puma,'b', gray_scale,uwrap_mean_dead,'r','LineWidth',2)
% title('Phase dependant on gray levels'), xlabel('Grayscale'); ylabel('Phase,
radians');
% legend('Pixel active and dead zones','(NOPUMA)Pixel active zones','(PUMA)Pixel
active zones','Pixel dead zone');
figure(19),boundedline(gray_scale,uwrap_mean_dead,std_dead1);
title('Unwrapped phase of pixel dead zones and STD (gray levels)'),
xlabel('Grayscale'); ylabel('Phase, radians');
% %% Other usefull stuff
% %
figure(434),plot(gray_scale,uwrap_mean_dead,'r',gray_scale,std_dead1,'b','LineWidth',2
)
% % legend('unwrapped dead zone phase','Phase STD of pixel dead zone');
%
% % % % figure(27), plot(gray_scale, uwrap_mean_dead,'color','r',),
% % % % xlabel('Grayscale','FontSize',20); ylabel('Phase, radians','FontSize',20);
% % % % title('Phase of Pixel dead zone','FontSize',20);
% % % % hold on;
% % % % plot(gray_scale,std_dead1,'color','b','LineWidth',2);
% % % % figure(2201), subplot(2,3,1), surfl(double(phase_diff1));shading
interp;colormap(gray); title(['Difference Results,
window=',num2str(window_size)]),zlabel('rad'),...
% % % %     subplot(2,3,4),surfl(double(phase_diff2));shading interp;colormap(gray);
title('Difference Results,'), zlabel('rad'),...
% % % %     subplot(2,3,2),plot(double(phase_diff1(:,250))); title('dif crossection
250'),grid on,ylabel('rad'),...
% % % %     subplot(2,3,5),plot(double(phase_diff2(:,250))),grid on,ylabel('rad'),...
```

Annex 5. Algorithm for polarization calibration

```matlab
% x=imread('analyser_45','png');
% c=mean2(x);
% Phase_cross_ref_x=x(1024,:);
% plot(Phase_cross_ref_x);
% v=histogram(x);
% plot(v);

y=0;
for k = 0:10:360
y=y+1;
H1=imread([num2str(k), 'analyser.png']);
% x=imread('analyser','png');
c=mean2(H1);
% Phase_cross_ref_x=x(1024,:);
% plot(Phase_cross_ref_x);
% v=histogram(x);
% plot(v);
Mean_phase(y)=c;
end
% x=imread('0analyser','png');
% c=mean2(x);
radians=pi/180;
polaris=[0*radians:10*radians:360*radians];
figure(101), plot(polaris, Mean_phase);
xlabel('polaris'); ylabel('Intensity, radians');title('Intensity(polarisation)')
polar (polaris, Mean_phase);
```

RESPONSIBILITY DECLARATION

I, hereby, confirm that the scientific results presented in the thesis refer to my investigations. I understand, that in the contrary case I have to face the consequences.

Cazac Veronica

Date 23.10.2023

CURRICULUM VITAE

Veronica CAZAC

Current position: scientific researcher
Professional Address: Laboratory of Photovoltaics and Photonics
                          Institute of Applied Physics,
                          5, Academiei str., Chisinau, Moldova.

Date of birth: 21 April 1994
Nationality: Moldavian, Romanian
Phone Number: +373 (0) 68801110
E-mail: veronica.cazac@phys.asm.md
Web page: www.phys.asm.md/en/personalpages/vceban

Employment history:

Scientific researcher at the Institute of Applied Physics   (in present - since 2016)

Project Assistant at Institutum Virtutes Civilis (NGO)   (2021-2023)

Studies:

Ph.D. student at State University of Moldova, Moldova   (2018-2023)
Thesis "Quantum behaviors of optical and optomechanical systems possessing articial atoms"
Master degree at Moldova State University, Chisinau, Moldova   (2015-2017)
Master in Exact Sciences (*Semiconductor Physics and Engineering*)
Bachelor degree at Moldova State University, Chisinau, Moldova   (2012-2015)
Bachelor's Degree in Exact Sciences (*Physics*)
Bachelor degree at Technical University of Moldova, Chisinau, Moldova   (2012-2016)
Bachelor's Degree in Accounting

Internships:

Tampere University of Technology, Tampere, Finland   (2018,2017)
Signal Processing Department, "Computational Imaging" group, duration: 4 months
Technische Universität Stuttgart, Stuttgart, Germany   (2016, 2017)
Investigation of DOEs via digital holographic microscopy, duration: 4 months

Participation to scientific projects:

- European project, Horizon 2020, H2020 687328 project   (2016-2018)
- Bilateral Moldo-Belarous Project ANCD 19.80013.50.07.04A/BL   (2019-2020)

- National Institutional Project ANCD 20.70086.16/COV   (2020-2021)
- National Institutional Project 20.80009.5007.03   (2020-2023)
- International Project ANCD 21.80013.5007.1M   (2021-2023)

Publications: _

International journals:

- **Cazac, V.**, Achimova, E., Abashkin, V., Meshalkin, A., Losmanschii C., Egiazarian, K. *"Polarization holographic recording of vortex diffractive optical elements on azopolymer thin films and 3D analysis via phase-shifting digital holographic microscopy"*, Optics Express, Vol. 29, nr. 6, pp. 9217–9230, (2021)
- **Cazac, V.,** Losmanschii, C., Achimova, E., Meshalkin, A., Abashkin, V., Podlipnov, V. *"Characterization of Polarization Holographic Gratings Obtained on Azopolymer Thin Films by Digital Holographic Microscopy"*, Journal of Biomedical Photonics & Engineering, Vol. 7, nr. 3, (2021)
- **Cazac, V.,** Meshalkin, A., Achimova, E., Abashkin, V., Katkovnik, V., Shevkunov, I., Claus, D., Pedrini, G. *"Surface relief and refractive index gratings patterned in chalcogenide glasses and studied by off-axis digital holography"*, Applied Optics, Vol. 57, pp. 507-513, (2018)

National Journals and Conference Proceedings:

- Achimova, E., Abaskin, V., **Cazac, V.,** Meshalkin, A., Loshmanschii, C. *"The Anisotropy of Light Propagation in Biological Tissues"*, Conference on Nanotechnologies and Biomedical Engineering. Chisinau, Republic of Moldova, pp. 149–156, (2021)
- **Cazac, V.** *"Improved 3D imaging of phase shifting digital holographic microscope by compensation for wavefront distortion"*, Journal of Physics: Conference Series, Volume 1745, The VI International Conference on Information Technology and Nanotechnology, (2020)
- Meshalkin, A., Achimova, E., Losmanschii, C., Podlipnov,V., **Cazac, V.** *"Analysis of diffraction efficiency of phase gratings in dependence of grooves number"*, IEEE Proceedings of VI International Conference on Information Technology and Nanotechnology 2020, pp. 143-146, (2020)
- **Cazac, V.** *"Spiral illumination applied for extended performance of the digital holographic microscope"*, Tendințe contemporane ale dezvoltării științei: viziuni ale tinerilor cercetători. Ediția 9, Vol. 1, pp.55-60, (2020)
- Meshalkin, A., Achimova, E., Losmanschii, C., Podlipnov, V., **Cazac, V.** *"Analysis of diffraction efficiency of phase gratings in dependence of grooves number"* Proceedings of VI International Conference on Information Technology and Nanotechnology (ITNT-2020), pp. 143-146, (2020)
- **Cazac, V.,** Achimova, E., Abashkin, V., Meshalkin, A., Katkovnik, V., Shevkunov I. *"Noise minimizing by harmonic phase diffraction gratings in off-axis lensless digital holography"*, The 9th edition of the International Conference "ATOM". Proc. of SPIE, (2018)

- **Cazac, V.,** Achimova, E. Application of bessel beam for digital holographic microscopy. In: Conferința Tendințe contemporane ale dezvoltării științei: viziuni ale tinerilor cercetători. Ediția 7, Chisinau, Republic of Moldova, pp.27-31, (2018)
- Loshmanschii, C., Meshalkin, A., Achimova, E., Abashkin, V., Prisacar, A., **Cazac, V.**, Pogrebnoi, S., Macaev, F. *"Influence of thickness and polarization on diffraction efficiency of direct patterned diffraction gratings in carbazole-based azopolymer films"*, Microelectronics and Computer Science Conference, Chisinau, Republic of Moldova, pp. 84-87, (2017)

Conferences: _

Talks:
- **Cazac, V.,** Achimova, E., Katkovnik, V., Shevkunov, I., Egiazarian, K. Pixel-Wise Calibration of the Spatial Light Modulator. *OSA Frontiers in Optics and Laser Science (online),* (2020)
- **Cazac, V.** Imaging complex superimposed gratings by digital holographic microscopy, *9th International Conference on Amorphous and Nanostructured Chalcogenides,* (2019)
- **Cazac, V.,** Achimova, E., Abaskin, V., Meshalkin, A., Pedrini, G., Claus, D., Shevkunov, I., Katkovnik, V. Surface topography studied by off-axis digital holography. *OSA Advanced Photonics Congress, Zurich, Switzerland,* (2018)
- **Cazac, V.**, Meshalkin, A., , Achimova, E., Abashkin, V., A., Katkovnik, V., Shevkunov,I. Phase grating application for digital holographic imaging, *9th International Conference on Microelectronics and Computer Science & the 8th Conference of Physicists of Moldova*, , Chisinau, Republic of Moldova, (2017).
- **Cazac, V.,** Meshalkin, A., Achimova, E., Abashkin, V., A., Katkovnik, V., Shevkunov, I. Phase retrieval of diffractive optical elements from off-axis digital holograms using SPAR technique*, 17th International Young conference: Optics and high technology Material Science SPO 2016,* October, Kiev, Ukraine, (2016).
- Meshalkin, A., **Cazac, V.**, Achimova, E., Abashkin, V., A., Katkovnik, V., Shevkunov, I. Application of diffraction gratings for phase imaging enhancement in digital holographic microscopy. *3rd International Conference: Health Technology Management HTM-2016*, October, Chisinau, Republic of Moldova, (2016).

Scholarships: _

- World Federation of Scientists Moldovan Scholarship for the research related to the WFS Plenary Emergency "Medicine&Biotechnology", topic "DHM Technology" (2020-2021).
- Nominal Government Award Scholarship for PhD students in the domain of Physics in the name of "Sergiu Radauteanu" (2018).
- Scholarship in the framework of the XX edition of the "Bursa de Merit 2014" (2014).

Other information:

Scientific interests: digital holography, optics, signal processing, laser physics.
Programming languages: Matlab.
Languages: Romanian (native), English (TOEFL score: 95), German (beginner), Russian.